EBM Experimental Biology and Medicine

Volume 251 | Issue 5

Experimental Biology and Medicine

Editor-in-Chief

Nicola Conran
University of Campinas, Brazil

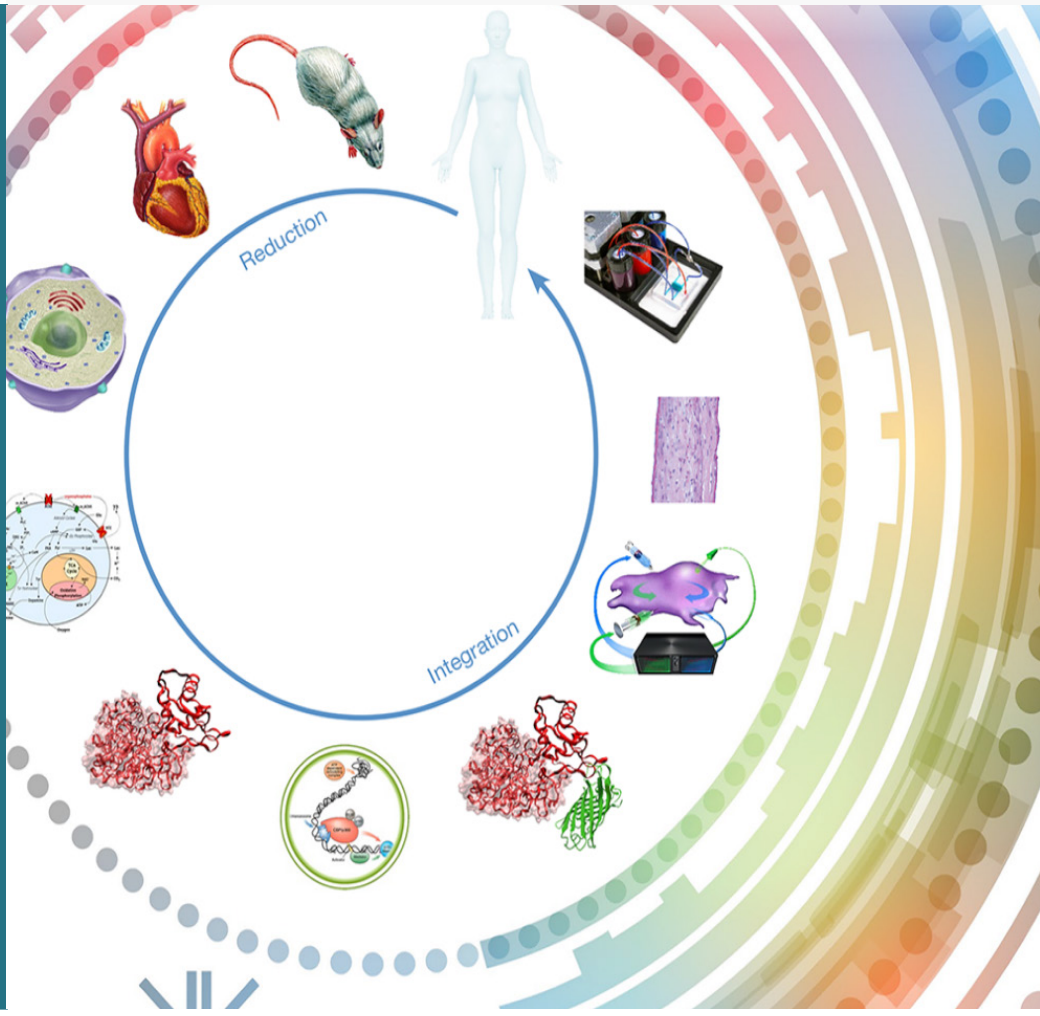

ISBN 978-2-8325-8334-0
DOI 10.3389/978-2-8325-8334-0

frontiers | Publishing Partnerships

Society for Experimental Biology and Medicine
3220 N Street NW, #179
Washington DC 20007, USA
Executive Director – ed@sebm.org

www.sebm.org

EBM Experimental Biology and Medicine

Editorial Board

ISSN 1535-3699
ISBN 978-2-8325-8334-0
DOI 10.3389/978-2-8325-8334-0

Generative AI statement
Any alternative text (Alt text) provided alongside figures in the articles in this ebook has been generated by Frontiers with the support of artificial intelligence and reasonable efforts have been made to ensure accuracy, including review by the authors wherever possible. If you identify any issues, please contact us.

EBM Experimental Biology and Medicine

2026 | Volume 251 | Issue 5 | ISSN 1535-3699

Table of contents

EBM Experimental Biology and Medicine

TYPE Original Research
PUBLISHED 12 May 2026
DOI 10.3389/ebm.2026.10945

OPEN ACCESS

*CORRESPONDENCE
Lirong Wu,
hedgehog4556@gmail.com

RECEIVED 23 December 2025
REVISED 26 March 2026
ACCEPTED 28 April 2026
PUBLISHED 12 May 2026

CITATION
Li Y, Fan J and Wu L (2026) Antibody-mediated immune responses and cardiovascular disease: a Mendelian randomization study.
Exp. Biol. Med. 251:10945.
doi: 10.3389/ebm.2026.10945

Antibody-mediated immune responses and cardiovascular disease: a Mendelian randomization study

Yi Li, Jiuqi Fan and Lirong Wu*

Department of Cardiology, Guiqian International General Hospital, Guiyang, China

Abstract

Cardiovascular diseases represent the leading cause of global mortality and disability, posing a severe threat to human health. Accumulating evidence suggests that antigen–antibody–mediated immune responses may be involved in the pathogenesis of various cardiovascular conditions; however, whether these associations reflect causal relationships has long remained unclear. To address this question, we conducted a bidirectional two-sample Mendelian randomization study leveraging summary-level data from genome-wide association studies. In this analysis, 46 antibody-mediated immune traits were evaluated as exposures, and 11 cardiovascular outcomes, including aortic aneurysm, aortic valve stenosis, atrial fibrillation, coronary artery disease, dilated cardiomyopathy, atrioventricular block, heart failure with reduced ejection fraction, hypertrophic cardiomyopathy, infective endocarditis, myocarditis, and pericarditis, were examined as outcomes. Our results revealed several significant causal associations: genetically predicted higher levels of Epstein–Barr virus EBNA-1 antibodies were associated with increased risks of myocarditis and aortic valve stenosis, while elevated VCA p18 antibody levels were linked to a higher risk of myocarditis. Furthermore, increased antibody levels against BK polyomavirus VP1 were causally associated with greater risks of aortic valve stenosis and dilated cardiomyopathy. In contrast, higher levels of antibodies against varicella-zoster virus glycoproteins and human herpesvirus 6 IE1B were associated with reduced risks of myocarditis and aortic aneurysm, respectively. These findings not only help clarify the causal role of immune-mediated mechanisms in cardiovascular pathogenesis but also provide a theoretical foundation for the future development of immune-targeted strategies for prevention and treatment.

KEYWORDS
antibody-mediated immune responses, cardiovascular diseases, infectious agents, Mendelian randomization, immune traits

Impact statement

Our findings deepen the understanding of immune-mediated mechanisms of cardiac injury and provide genetic evidence supporting precision-medicine interventions. However, the clinical feasibility of targeting antibody responses requires further validation in future studies.

Introduction

Cardiovascular disease (CVD) is a principal driver of global mortality and disability. The Global Burden of Disease study indicates that CVD generally represents about 30%–35% of total deaths worldwide [1]. Therefore, identifying factors that influence the progression of CVD is of paramount importance. Current evidence implicates viral infections, dysregulated immune function, genetic predisposition, lifestyle factors and environmental exposures as important contributors to CVD risk [2–5]. Histopathological studies show increased infiltration of immune cells in CVD pathological tissue suggesting that immune-response–driven matrix injury is implicated throughout the course of CVD development [6–9]. A Mendelian randomization (MR) studies have shown that various antibody-mediated immune responses are risk factors for myocarditis [10]. Immune cells recognize antigens and produce specific antibodies that limit viral spread and clear pathogens via neutralization, opsonization, complement activation, and Fc receptor–mediated effector functions [11, 12]. As key effector molecules of the immune response, antibody levels can serve both as biomarkers of infectious exposure and as pathophysiological clues linking infection to noncommunicable diseases (for example, molecular mimicry, immune complex deposition, and dysregulated immune modulation) [13–15]. Nevertheless, the potential pathophysiological links between infectious agents and CVD remain unclear, and whether a true causal relationship exists is still unclear. Guillaume Butler-Laporte et al. identified genetic variants related to antibody-mediated immune responses through genome-wide association studies [16]. Unlike polygenic risk scores—which aggregate genetic susceptibility for risk prediction but cannot discern directionality or causality.MR is a genetic epidemiological approach specifically designed for causal inference, leveraging genetic variants as instrumental variables to estimate the causal effect of an exposure on an outcome while minimizing confounding and reverse causation bias [17, 18]. Thus, applying MR creates a new opportunity to investigate causal relationships between antibody-mediated immune responses and CVD. In this study, we performed bidirectional, two-sample Mendelian randomization analyses to systematically assess causal links between antibody-mediated immune responses and eight CVD, with the aim of advancing understanding of immune-mediated cardiovascular injury mechanisms and offering genetic evidence to support future precision immunotherapy strategies.

Materials and methods

We first obtained summary-level data from published genome-wide association studies (GWAS), comprising 46 antibody-mediated immune response traits and eleven common cardiovascular diseases (aortic aneurysm, aortic valve stenosis, coronary artery disease, hypertrophic cardiomyopathy, dilated cardiomyopathy, infective endocarditis, myocarditis, pericarditis, atrial fibrillation, heart block, and reduced ejection fraction heart failure) (Table 1). We then applied two-sample MR to systematically evaluate the potential causal effects of antibody-mediated immune responses on these cardiovascular outcomes (Figure 1).

Data sources

The summary data of antibody mediated immune response comes from the antibody characteristic GWAS study by Butler Laporte et al [16]. This is the largest and only publicly available GWAS to date that systematically characterizes genetic determinants of antigen-specific antibody levels across a broad panel of infectious agents. The study analyzed 46 serological phenotypes—derived from mean fluorescence intensity measurements of serum antibodies against 13 pathogens—in approximately 8,735 White British participants from the UK Biobank. Genetic instruments for our Mendelian randomization analyses were drawn exclusively from this comprehensive resource[1]. Summary statistics for the cardiovascular disease outcomes were retrieved from the OpenGWAS platform[2].

Instrumental variable selection

The validity of causal inference in this Mendelian Randomization (MR) study is grounded on three fundamental assumptions regarding genetic variants: (1) the instrumental variables (IVs) are robustly associated with the exposure (antibody-mediated immune responses); (2) the IVs are independent of any confounding factors; (3) the IVs influence the outcome (various cardiac diseases) solely through the exposure pathway, without pleiotropic effects.

To identify appropriate IVs, single nucleotide polymorphisms (SNPs) associated with antibody-mediated immune traits were selected based on a genome-wide significance threshold of $P < 5 \times 10^{-5}$. Independent SNPs were retained after performing LD clumping with an r^2 threshold of 0.1 within a 10,000 kb window.

To mitigate horizontal pleiotropy and reduce bias, the MR-PRESSO (Mendelian Randomization Pleiotropy RESidual Sum and Outlier) test was employed. SNPs identified as outliers ($P < 0.05$) were iteratively removed until the global pleiotropy test indicated no residual pleiotropic effect ($P > 0.05$). Furthermore, SNPs directly associated with the outcome at $P < 0.05$ were excluded to prevent confounding. Only SNPs with F-statistics greater than 10 were retained to avoid weak instrument bias.

Statistical analysis

Causal effects were estimated using five complementary MR methods: inverse variance weighted (IVW) as the primary approach due to its statistical efficiency, supplemented by maximum likelihood, MR-Egger regression, weighted median, and weighted mode methods to ensure robustness. Reverse MR analyses were conducted using identical procedures to evaluate potential reverse causal relationships.

All analyses were performed in R software (version 4.3.1) utilizing the TwoSampleMR (version 0.5.7) and MR-PRESSO (version 1.0) packages.

1 https://www.ebi.ac.uk/gwas/studies/GCST90006909-GCST90006884

2 https://gwas.mrcieu.ac.uk/

TABLE 1 GWAS traits used as exposures (antibody responses) and outcomes (cardiovascular diseases) in the MR analysis, with corresponding GWAS Catalog IDs (GCST).

Category	GWAS ID	Trait name
Exposure	GCST90006909	Human herpes virus 7 U14 antibody levels
Exposure	GCST90006910	Anti-helicobacter pylori IgG seropositivity
Exposure	GCST90006911	*Helicobacter pylori* CagA antibody levels
Exposure	GCST90006912	*Helicobacter pylori* Catalase antibody levels
Exposure	GCST90006913	*Helicobacter pylori* GroEL antibody levels
Exposure	GCST90006914	*Helicobacter pylori* OMP antibody levels
Exposure	GCST90006915	*Helicobacter pylori* UREA antibody levels
Exposure	GCST90006916	*Helicobacter pylori* VacA antibody levels
Exposure	GCST90006917	Anti-herpes simplex virus 1 IgG seropositivity
Exposure	GCST90006918	Herpes simplex virus 1 mgG-1 antibody levels
Exposure	GCST90006919	Anti-herpes simplex virus 2 IgG seropositivity
Exposure	GCST90006920	Herpes simplex virus 2 mgG-1 antibody levels
Exposure	GCST90006921	Anti-polyomavirus 2 IgG seropositivity
Exposure	GCST90006922	Polyomavirus 2 JC VP1 antibody levels
Exposure	GCST90006923	Anti-merkel cell polyomavirus IgG seropositivity
Exposure	GCST90006924	Merkel cell polyomavirus VP1 antibody levels
Exposure	GCST90006925	Anti-toxoplasma gondii IgG seropositivity
Exposure	GCST90006926	Toxoplasma gondii p22 antibody levels
Exposure	GCST90006927	Toxoplasma gondii sag1 antibody levels
Exposure	GCST90006928	Anti-varicella zoster virus IgG seropositivity
Exposure	GCST90006929	Varicella zoster virus glycoproteins E and I antibody levels
Exposure	GCST90006885	BK polyomavirus VP1 antibody levels
Exposure	GCST90006886	Anti-chlamydia trachomatis IgG seropositivity
Exposure	GCST90006887	*Chlamydia trachomatis* momp A antibody levels
Exposure	GCST90006888	*Chlamydia trachomatis* momp D antibody levels
Exposure	GCST90006889	*Chlamydia trachomatis* pGP3 antibody levels
Exposure	GCST90006890	*Chlamydia trachomatis* PorB antibody levels
Exposure	GCST90006891	*Chlamydia trachomatis* tarp-D F1 antibody levels
Exposure	GCST90006892	*Chlamydia trachomatis* tarp-D F2 antibody levels
Exposure	GCST90006893	Anti-cytomegalovirus IgG seropositivity
Exposure	GCST90006894	Cytomegalovirus pp28 antibody levels
Exposure	GCST90006895	Cytomegalovirus pp52 antibody levels
Exposure	GCST90006896	Cytomegalovirus pp150 antibody levels
Exposure	GCST90006897	Anti-Epstein-barr virus IgG seropositivity
Exposure	GCST90006898	Epstein-barr virus EA-D antibody levels
Exposure	GCST90006899	Epstein-barr virus EBNA-1 antibody levels
Exposure	GCST90006900	Epstein-barr virus VCA p18 antibody levels
Exposure	GCST90006901	Epstein-barr virus ZEBRA antibody levels

(*Continued*)

TABLE 1 Continued

Category	GWAS ID	Trait name
Exposure	GCST90006902	Anti-human herpes virus 6 IgG seropositivity
Exposure	GCST90006903	Anti-human herpes virus 6 E1A IgG seropositivity
Exposure	GCST90006904	Human herpes virus 6 IE1A antibody levels
Exposure	GCST90006905	Anti-human herpes virus 6 IE1B IgG seropositivity
Exposure	GCST90006906	Human herpes virus 6 IE1B antibody levels
Exposure	GCST90006907	Human herpes virus 6 p101k antibody levels
Exposure	GCST90006908	Anti-human herpes virus 7 IgG seropositivity
Exposure	GCST90006884	Anti-BK polyomavirus IgG seropositivity
Outcome	GCST90480203	Aortic aneurysm
Outcome	GCST90480118	Aortic stenosis
Outcome	GCST90624411	Atrial fibrillation
Outcome	GCST90480129	Coronary heart disease
Outcome	GCST90018834	Dilated cardiomyopathy
Outcome	GCST90480159	Heart block
Outcome	GCST90018861	Hypertrophic cardiomyopathy
Outcome	GCST90480146	Infective endocarditis
Outcome	GCST90436090	Myocarditis
Outcome	GCST90480145	Pericarditis
Outcome	GCST90480182	Reduced ejection fraction heart failure

Results

Relationship between antigen–antibody responses and aortic aneurysm

This study identified two antibody-mediated immune responses with causal associations to aortic aneurysm at the nominal significance level ($P < 0.05$). Both associations showed no evidence of significant heterogeneity or horizontal pleiotropy in sensitivity analyses (Supplementary Tables S2, S3). Specifically, genetically predicted higher levels of Cytomegalovirus pp52 antibody were associated with an increased risk of aortic aneurysm (OR = 1.05, 95% CI 1.02–1.09, P = 0.005). Conversely, higher levels of Human herpes virus 6 IE1B antibody were associated with a reduced risk of aortic aneurysm (OR = 0.95, 95% CI 0.90–0.99, P = 0.028) (Figures 2, 3; Supplementary Table S1). The Wald ratio estimates for individual SNPs are presented in Supplementary Table S4.

Relationship between antigen–antibody responses and aortic valve stenosis

This study identified three antibody-mediated immune responses with causal associations with aortic valve stenosis at the nominal significance level ($P < 0.05$). All three showed no evidence of significant heterogeneity or horizontal pleiotropy in sensitivity analyses (Supplementary Tables S2, S4). Specifically, genetically predicted higher levels of BK polyomavirus VP1 antibody (OR = 1.23, 95% CI 1.01–1.50, P = 0.037), Epstein-Barr virus EBNA-1 antibody (OR = 1.12, 95% CI 1.04–1.20, P = 0.001), and Human herpes virus 6 p101k antibody (OR = 1.13, 95% CI 1.02–1.25, P = 0.015) were associated with an increased risk of aortic valve stenosis (Figures 2, 3; Supplementary Table S1). The Wald ratio estimates for individual SNPs are presented in Supplementary Table S4.

Relationship between antigen–antibody responses and coronary artery disease

This study identified five antibody-mediated immune responses with causal associations to coronary heart disease at the nominal significance level ($P < 0.05$). Sensitivity analyses indicated that four of these associations showed no evidence of significant heterogeneity or horizontal pleiotropy (Supplementary Tables S2, S3). Specifically, genetically predicted higher levels of Merkel cell polyomavirus VP1 antibody (OR = 1.10, 95% CI 1.05–1.14, $P < 0.001$), Polyomavirus 2 JC VP1 antibody (OR = 1.06, 95% CI 1.02–1.10, P = 0.005), Anti-polyomavirus 2 IgG seropositivity (OR = 1.03, 95% CI 1.01–1.05, P = 0.004), and Anti-human herpes virus 6 IgG seropositivity (OR = 1.02, 95% CI 1.00–1.04, P = 0.034) were robustly associated with an increased risk of coronary heart disease (Figures 2, 3; Supplementary Table S1). However, the association with Anti-Merkel cell polyomavirus IgG seropositivity (IVW: OR = 1.03, 95% CI 1.01–1.05, P = 0.006) exhibited both

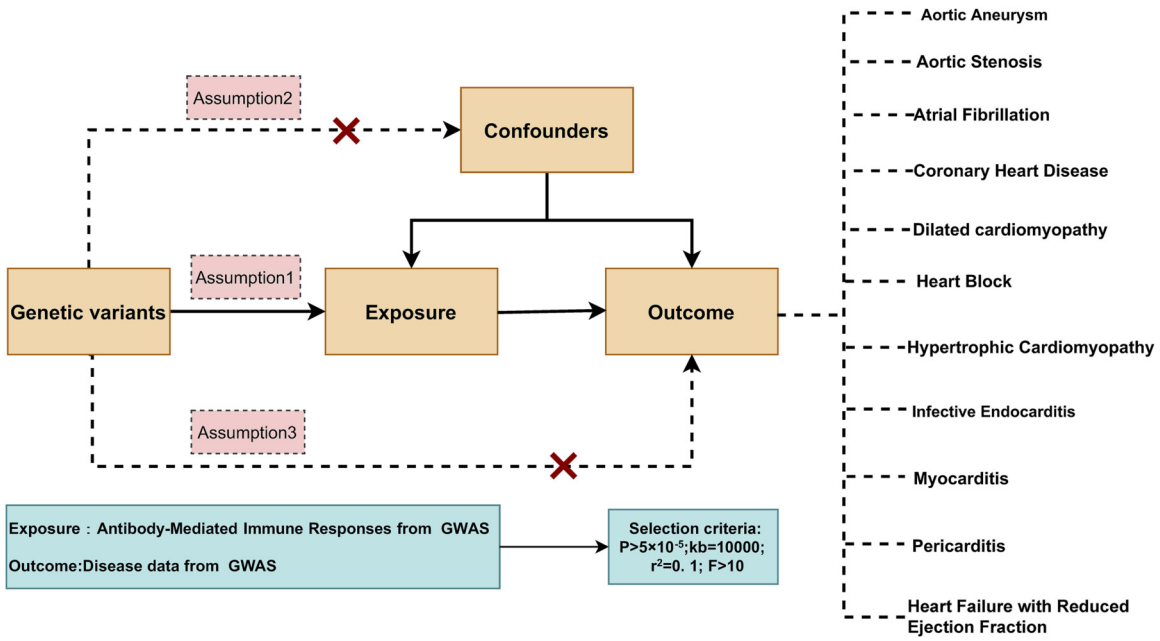

FIGURE 1
Design of the two-sample mendelian randomization analysis.

significant heterogeneity (Q P = 0.022) and evidence of horizontal pleiotropy (MR-Egger intercept P = 0.017), suggesting that this estimate may be biased. The Wald ratio estimates for individual SNPs are presented in Supplementary Table S4.

Relationship between antigen–antibody responses and dilated cardiomyopathy

This study identified four antibody-mediated immune responses with causal associations to dilated cardiomyopathy at the nominal significance level (P < 0.05). All associations showed no evidence of significant heterogeneity or horizontal pleiotropy in sensitivity analyses (Supplementary Tables S2, S3). Specifically, genetically predicted higher levels of BK polyomavirus VP1 antibody (OR = 1.10, 95% CI 1.05–1.14, P < 0.001), Toxoplasma gondii p22 antibody (OR = 1.06, 95% CI 1.02–1.10, P = 0.005), Herpes simplex virus 1 mgG-1 antibody (OR = 1.03, 95% CI 1.01–1.05, P = 0.004), and Anti-varicella zoster virus IgG seropositivity (OR = 1.03, 95% CI 1.01–1.05, P = 0.006) were all associated with an increased risk of dilated cardiomyopathy (Figures 2, 3; Supplementary Table S1). The Wald ratio estimates for individual SNPs are presented in Supplementary Table S4.

Relationship between antigen–antibody responses and hypertrophic cardiomyopathy

This study identified one antibody-mediated immune response with a causal association to hypertrophic cardiomyopathy. The analysis showed no evidence of heterogeneity or horizontal pleiotropy (Supplementary Tables S2, S3). Specifically, genetically predicted Anti-varicella zoster virus IgG seropositivity was associated with an increased risk of hypertrophic cardiomyopathy (OR = 1.16, 95% CI 1.01–1.34, P = 0.032). The Wald ratio estimates for individual SNPs are presented in Supplementary Table S4.

Relationship between antigen–antibody responses and infective endocarditis

This study identified four antibody-mediated immune responses with causal associations to infective endocarditis at the nominal significance level (P < 0.05). All associations showed no evidence of significant heterogeneity or horizontal pleiotropy in sensitivity analyses (Supplementary Tables S2,S3). Specifically, genetically predicted higher levels of Varicella zoster virus glycoproteins E and I antibody (OR = 1.09, 95% CI 1.02–1.17, P = 0.014), Anti-varicella zoster virus IgG seropositivity (OR = 1.05, 95% CI 1.01–1.10, P = 0.014), and Anti-polyomavirus 2 IgG seropositivity (OR = 1.04, 95% CI 1.00–1.08, P = 0.033) were associated with an increased risk of infective endocarditis. Conversely, Anti-Epstein-Barr virus IgG seropositivity was associated with a reduced risk (OR = 0.97, 95% CI 0.94–0.99, P = 0.013). The Wald ratio estimates for individual SNPs are presented in Supplementary Table S4.

Relationship between antigen–antibody responses and myocarditis

This study identified six antibody-mediated immune responses with causal associations to myocarditis at the nominal significance level (P < 0.05). All associations showed no evidence of significant heterogeneity or horizontal pleiotropy in sensitivity analyses (Supplementary Tables S2,S3). Specifically, genetically predicted higher levels of Epstein–Barr virus EBNA-1 antibody (OR = 1.73,

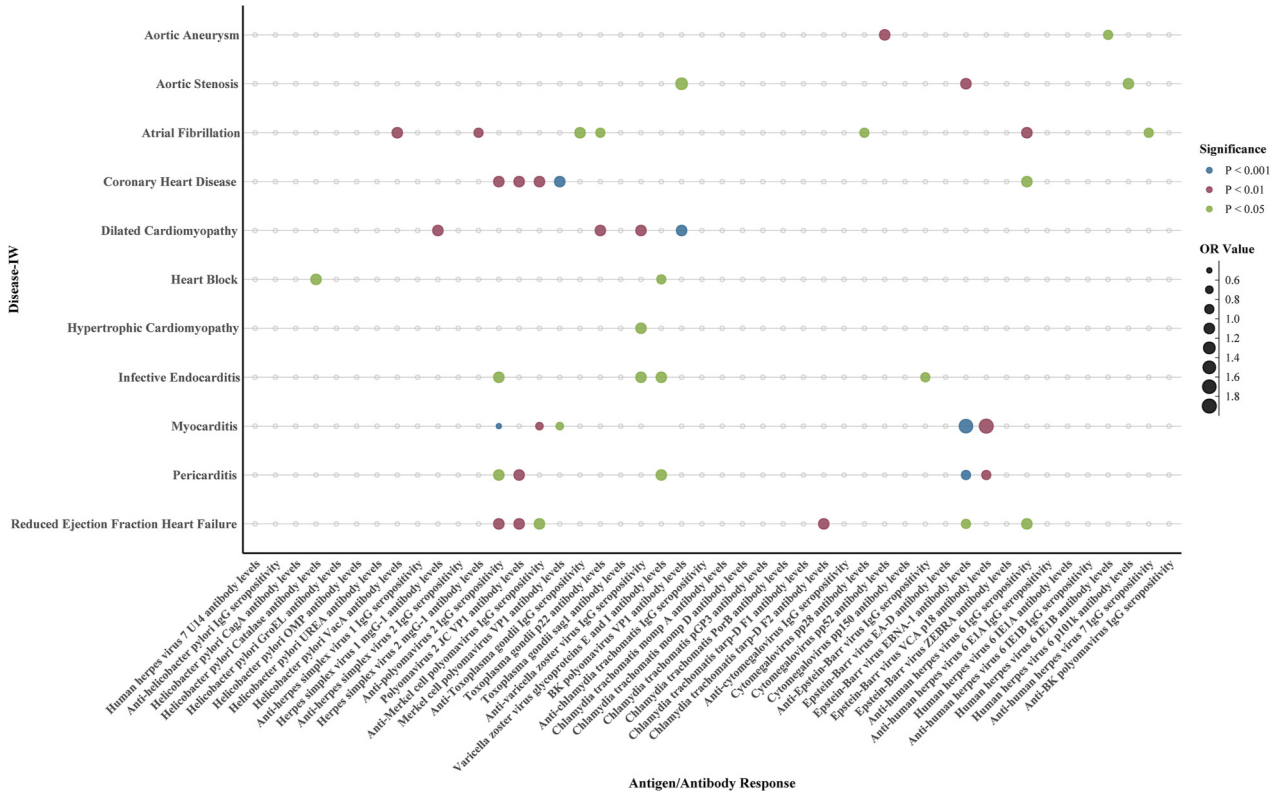

FIGURE 2
Causal estimates from Mendelian randomization analysis of antibody-mediated immune responses on cardiovascular diseases. Each dot represents the inverse-variance weighted (IVW) odds ratio (OR) estimate for the association between a specific antigen/antibody response and a cardiovascular disease. The size of the dot corresponds to the magnitude of the OR, with larger dots indicating stronger effects. Color indicates statistical significance: blue (P < 0.001), red (P < 0.01), and green (P < 0.05). Antibody responses associated with multiple cardiovascular outcomes are underlined in red. IVW: inverse-variance weighted; MR: Mendelian randomization.

95% CI 1.28–2.36, P < 0.001) and Epstein–Barr virus VCA p18 antibody (OR = 1.82, 95% CI 1.20–2.75, P = 0.005) were associated with an increased risk of myocarditis. Conversely, Anti-polyomavirus 2 IgG seropositivity (OR = 0.57, 95% CI 0.45–0.72, P < 0.001), Anti-Merkel cell polyomavirus IgG seropositivity (OR = 0.68, 95% CI 0.54–0.86, P = 0.001), Merkel cell polyomavirus VP1 antibody levels (OR = 0.61, 95% CI 0.40–0.93, P = 0.023), and Varicella zoster virus glycoproteins E and I antibody levels (OR = 0.43, 95% CI 0.29–0.64, P < 0.001) were associated with a reduced risk of myocarditis (Figures 2, 3; Supplementary Table S1). The Wald ratio estimates for individual SNPs are presented in Supplementary Table S4.

Relationship between antigen–antibody responses and pericarditis

This study identified five antibody-mediated immune responses with causal associations to pericarditis at the nominal significance level (P < 0.05). Sensitivity analyses indicated that four of these associations showed no evidence of significant heterogeneity or horizontal pleiotropy (Supplementary Tables S2, S3). Specifically, genetically predicted higher levels of Polyomavirus 2 JC VP1 antibody (OR = 1.10, 95% CI 1.03–1.17, P = 0.006), Anti-polyomavirus 2 IgG seropositivity (OR = 1.02, 95% CI 1.00–1.04, P = 0.034), Varicella zoster virus glycoproteins E and I antibody levels (OR = 1.08, 95% CI 1.00–1.16, P = 0.039), and Epstein–Barr virus VCA p18 antibody levels (OR = 0.91, 95% CI 0.86–0.97, P = 0.002) were robustly associated with pericarditis risk (Figures 2, 3; Supplementary Table S1).

However, the inverse association between Epstein–Barr virus EBNA-1 antibody levels and pericarditis (OR = 0.92, 95% CI 0.88–0.95, P < 0.001) exhibited both significant heterogeneity (Q P = 0.011) and evidence of horizontal pleiotropy (MR-Egger intercept P = 0.012), suggesting that this estimate may be subject to bias. The Wald ratio estimates for individual SNPs are presented in Supplementary Table S4.

Relationship between antigen–antibody responses and heart failure with reduced ejection fraction

This study identified six antibody-mediated immune responses with causal associations to heart failure with reduced ejection fraction at the nominal significance level (P < 0.05). All associations showed no evidence of significant heterogeneity or horizontal pleiotropy in sensitivity analyses (Supplementary Tables S2, S4). Specifically, genetically predicted higher levels of Polyomavirus 2 JC VP1 antibody (OR = 1.04, 95% CI 1.01–1.07, P =

10.3389/ebm.2026.10945

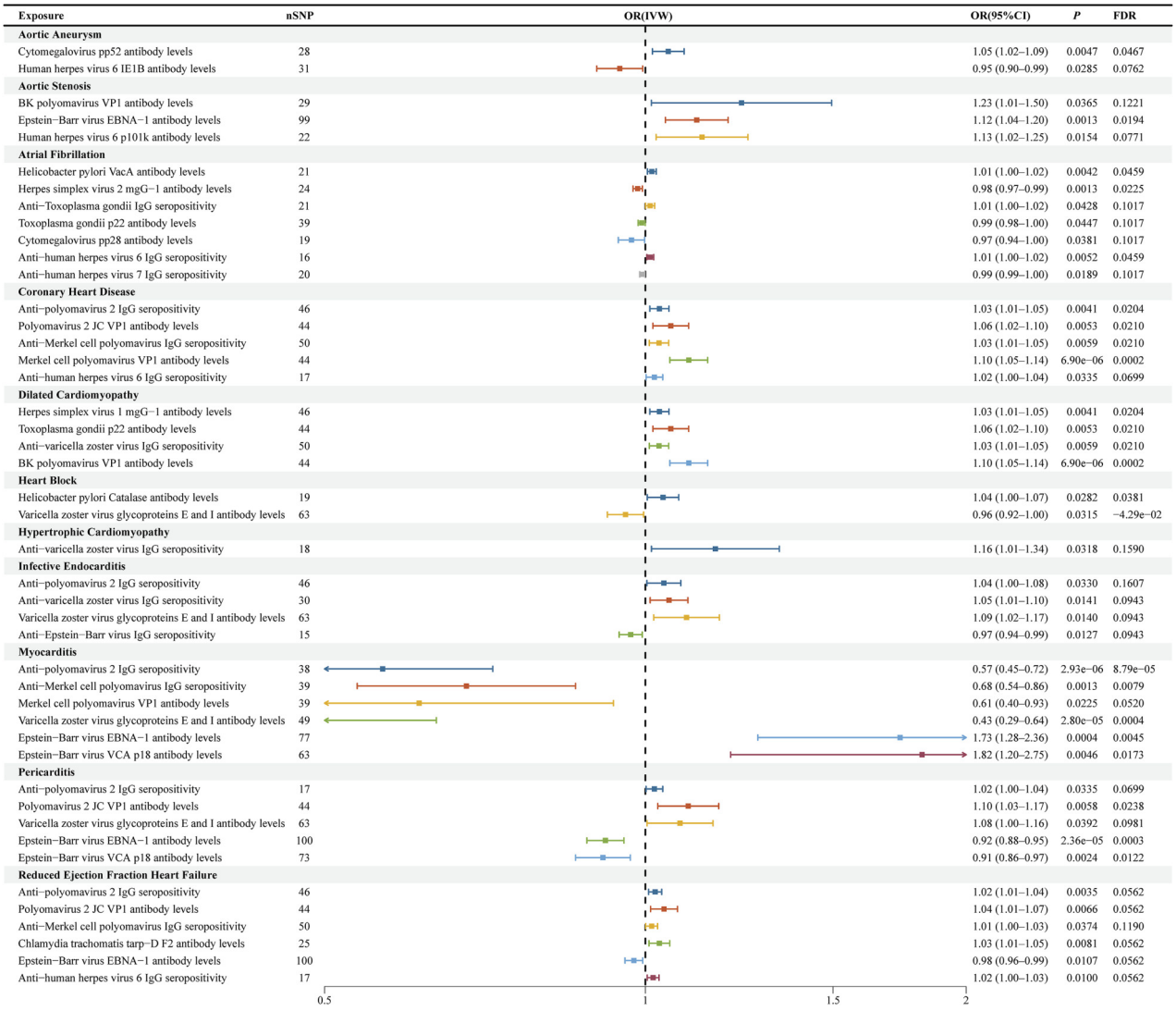

FIGURE 3
Forest plots for causal effects of antibody-mediated immune responses on cardiovascular diseases. The horizontal bars correspond to the estimated odds ratios (ORs) with 95% confidence intervals (CIs) using the inverse-variance weighted (IVW) method. MR: Mendelian randomization; OR: odds ratio; CI: confidence interval.

0.0066), Anti-polyomavirus 2 IgG seropositivity (OR = 1.02, 95% CI 1.01–1.04, P = 0.0035), Chlamydia trachomatis tarp-D F2 antibody (OR = 1.03, 95% CI 1.01–1.05, P = 0.0081), Anti-human herpes virus 6 IgG seropositivity (OR = 1.02, 95% CI 1.00–1.03, P = 0.0100), and Anti-Merkel cell polyomavirus IgG seropositivity (OR = 1.01, 95% CI 1.00–1.03, P = 0.0374) were associated with an increased risk of heart failure with reduced ejection fraction. Conversely, higher levels of Epstein–Barr virus EBNA-1 antibody (OR = 0.98, 95% CI 0.96–0.99, P = 0.0107) were associated with a reduced risk (Figures 2, 3; Supplementary Table S1). The Wald ratio estimates for individual SNPs are presented in Supplementary Table S4.

Relationship between antigen–antibody responses and atrial fibrillation

This study identified seven antibody-mediated immune responses with causal associations to atrial fibrillation at the nominal significance level (P < 0.05). Sensitivity analyses indicated that four of these associations showed no evidence of significant heterogeneity or horizontal pleiotropy (Supplementary Tables S2, S3). Specifically, genetically predicted higher levels of *Helicobacter pylori* VacA antibody (OR = 1.01, 95% CI 1.00–1.02, P = 0.004), Anti-human herpes virus 6 IgG seropositivity (OR = 1.01, 95% CI 1.00–1.02, P = 0.005), Anti-Toxoplasma gondii IgG seropositivity (OR = 1.01, 95% CI 1.00–1.02, P = 0.043), and lower Anti-human herpes virus 7 IgG seropositivity (OR = 0.99, 95% CI 0.99–1.00, P = 0.019) were robustly associated with atrial fibrillation risk (Figures 2, 3; Supplementary Table S1). However, three inverse associations exhibited evidence of both heterogeneity and horizontal pleiotropy: Herpes simplex virus 2 mgG-1 antibody levels (OR = 0.98, 95% CI 0.97–0.99, P = 0.001; Q P = 0.046, Egger P = 0.035), Cytomegalovirus pp28 antibody levels (OR = 0.97, 95% CI 0.94–1.00, P = 0.038; Q P = 0.0002, Egger P = 0.0007), and Toxoplasma gondii p22 antibody levels (OR = 0.99, 95% CI

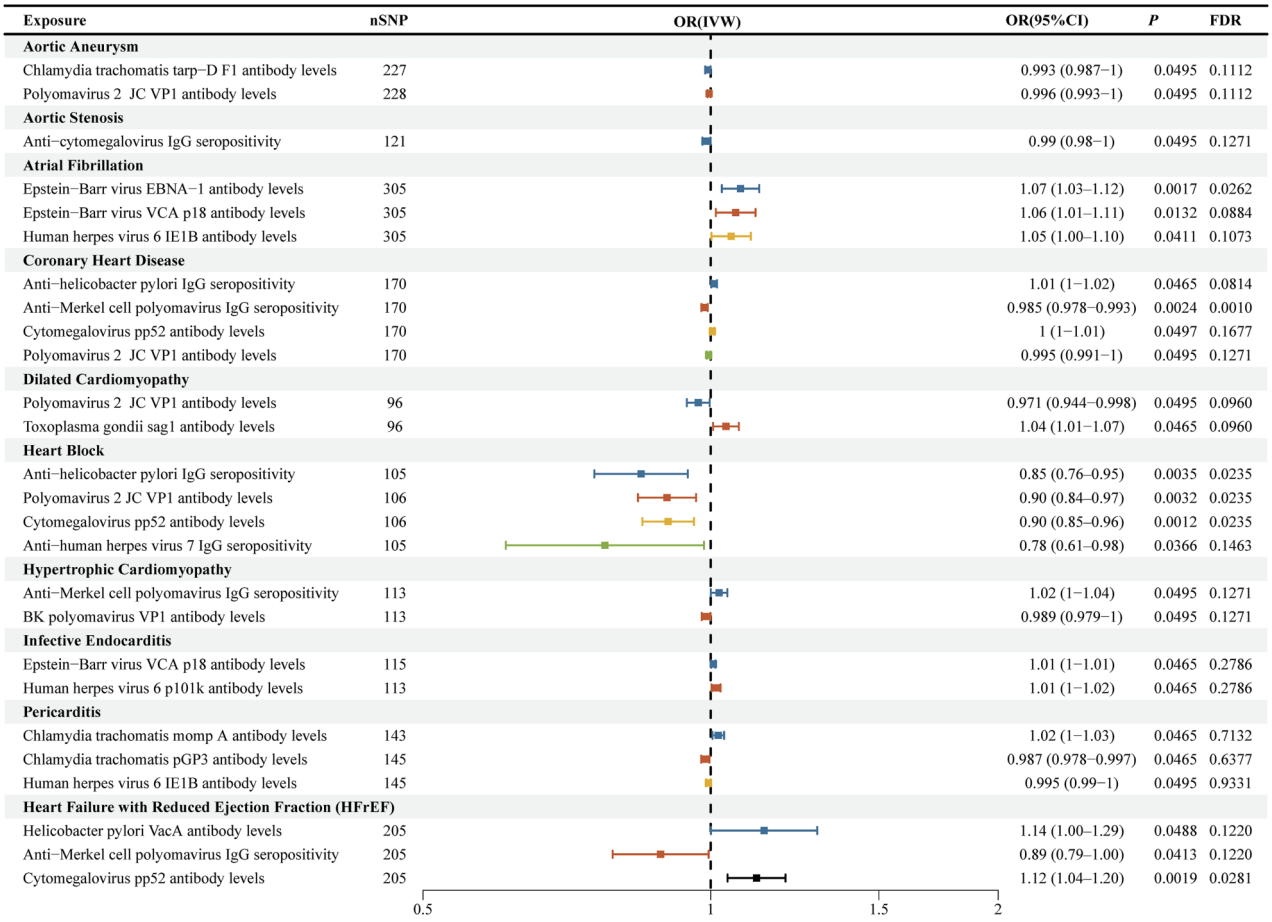

FIGURE 4
Forest plots for reverse Mendelian randomization analysis of cardiovascular diseases on antibody-mediated immune responses. The horizontal bars represent the inverse-variance weighted (IVW) odds ratios (ORs) with 95% confidence intervals (CIs) for the causal effect of each cardiovascular disease on specific antigen/antibody responses. Results are grouped by disease, and significant associations at FDR <0.05 are indicated in bold. IVW: inverse-variance weighted; OR: odds ratio; CI: confidence interval; FDR: false discovery rate.

0.98–1.00, P = 0.045; Q P = 0.017, Egger P = 0.023). These latter estimates may be subject to bias and should be interpreted with caution. The Wald ratio estimates for individual SNPs are presented in Supplementary Table S4.

Relationship between antigen–antibody responses and heart block

This study identified two antibody-mediated immune responses with causal associations to heart block at the nominal significance level (P < 0.05). Both associations showed no evidence of significant heterogeneity or horizontal pleiotropy in sensitivity analyses (Supplementary Tables S2, S3). Specifically, genetically predicted higher levels of *Helicobacter pylori* Catalase antibody were associated with an increased risk of heart block (OR = 1.04, 95% CI 1.00–1.07, P = 0.028). Conversely, higher levels of Varicella zoster virus glycoproteins E and I antibody were associated with a reduced risk of heart block (OR = 0.96, 95% CI 0.92–1.00, P = 0.031) (Figures 2, 3; Supplementary Table S1). The Wald ratio estimates for individual SNPs are presented in Supplementary Table S4.

Relationship between cardiovascular diseases and antigen–antibody responses

Reverse Mendelian randomization analyses revealed several cardiovascular diseases with causal effects on antibody-mediated immune responses at the nominal significance level (P < 0.05). Most of these associations showed no evidence of significant heterogeneity or horizontal pleiotropy in sensitivity analyses (Supplementary Tables S6, S7). Specifically, genetically predicted atrial fibrillation was associated with elevated antibody levels against Epstein–Barr virus EBNA-1 (OR = 1.07, 95% CI: 1.03–1.12; P = 0.0017) and VCA p18 (OR = 1.06, 95% CI: 1.01–1.11; P = 0.013). Atrioventricular block was causally linked to reduced seropositivity to *Helicobacter pylori* (OR = 0.85, 95% CI: 0.76–0.95; P = 0.0035) and lower antibody levels against cytomegalovirus pp52 (OR = 0.90, 95% CI: 0.84–0.97; P = 0.0012) and polyomavirus 2 JC VP1 (OR = 0.90, 95% CI: 0.84–0.97; P = 0.0032). Additionally, HFrEF was associated with increased cytomegalovirus pp52 antibody levels (OR = 1.12, 95% CI: 1.04–1.20; P = 0.0019) and decreased anti–Merkel cell polyomavirus IgG seropositivity (OR = 0.89, 95% CI: 0.79–1.00; P = 0.041). These findings collectively suggest a modest but bidirectional interplay

between cardiac pathology and humoral immune responses (Figure 4; Supplementary Table S5). The Wald ratio estimates for individual SNPs are presented in Supplementary Table S8.

Discussion

The immune response to viral infection depends on key components such as the complement system, the coagulation cascade, and natural antibodies; these elements interact to form a complex network and are tightly regulated to maintain homeostasis and prevent immune dysregulation [19]. Antibody-mediated immune responses refer to antigen-specific antibodies produced by B cells that recognize and bind antigens and eliminate pathogens or toxins via neutralization, opsonization, complement activation, and Fc receptor–mediated cellular effector functions [11, 20, 21]. Antigen-specific immunity that limits viral spread and clears viruses is beneficial to the host; however, in some cases it can cause tissue damage [22]. The mechanisms by which viral infections cause myocardial injury remain debated, with three main hypotheses: immune cell–mediated myocardial destruction, autoimmune myocardial injury driven by circulating autoantibodies, and direct virus-induced cardiomyocyte cytotoxicity [23]. The prevailing view is that myocardial injury is mainly caused by virus-associated immune responses rather than direct viral action on cardiomyocytes [24].

Herpesviruses are widespread in humans, with cytomegalovirus (CMV),Epstein-Barr virus (EBV) and herpes simplex virus (HSV) being particularly common and implicated in various cardiovascular conditions. EBV infection is prevalent worldwide and can persist in the host, often lifelong. Acute EBV infection commonly causes acute cardiovascular injury manifested by myocarditis, pericardial involvement, and heart failure, whereas chronic EBV infection is more often associated with vascular lesions and chronic myocarditis [25, 26]. The mechanisms of EBV-induced cardiovascular injury can be categorized as direct and indirect. Screening of myocardial tissue from adults with idiopathic left ventricular dysfunction detected EBV in approximately 2% of cases [27], but quantitative analyses have not found an association between persistent EBV infection and idiopathic myocarditis [28]. In EBV-associated myocarditis, marked inflammatory infiltrates are observed despite lack of evidence for direct viral invasion of cardiomyocytes, suggesting indirect immune-mediated injury rather than direct cytotoxicity [29], Both EBV and HCMV lack specific receptors to infect cardiomyocytes directly and are frequently detected within inflammatory cells in the heart, further supporting an immune-mediated mechanism of cardiac damage [30]. This indirect, inflammation-driven pattern is also evident more broadly in the cardiovascular system. For example, in individuals carrying the T allele of VEGF rs3025039—which is associated with reduced VEGF expression—high titers of EBV early antigen IgG (EA-IgG) are significantly associated with an increased risk of atherosclerosis (OR = 1.88) [31]. Furthermore, cross-sectional studies have shown that higher burdens of antiviral IgG antibodies, such as EBV EA-IgG, are significantly linked not only to greater atherosclerosis risk but also to elevated levels of systemic inflammatory markers [32]. This suggests that cumulative pathogen-specific antibody responses may promote vascular injury through sustained low-grade systemic inflammation. In patients with acute myocardial infarction (AMI) who are seropositive for anti-EBV antibodies, EBV can trigger acute coronary events via the pro-inflammatory effects of its early protein dUTPase—even in the absence of active viral replication [33]. Similarly, among people with HIV, higher levels of CMV-specific IgG antibodies are significantly associated with atherosclerosis, obstructive coronary artery disease, and increased coronary plaque volume [34]. Another study showed that CMV seropositivity *per se* was associated with a modestly increased risk of secondary cardiovascular events in patients with coronary heart disease, but the risk was significantly amplified in those with diabetes (HR = 2.58), suggesting that CMV antibody positivity serves as an important inflammation-related risk marker in specific high-risk populations, such as individuals with diabetes [35]. This association likely stems from chronic immune activation driven by persistent CMV infection. In younger individuals, higher anti-CMV IgG titers are already linked to a pro-inflammatory state and early remodeling of memory T-cell subsets. In older adults, they primarily drive the expansion of terminally differentiated $CD8^+$ effector memory cells and NK cells, reinforcing low-grade inflammation and adaptive immune skewing [36]. A study at the University of Minnesota reported a markedly higher incidence of CADat 2 years post–heart transplant among CMV-positive immunosuppressed patients (32%) compared with CMV-negative patients (10%) [37]. Serum antibody levels against varicella-zoster virus (VZV) are significantly associated with coronary atherosclerosis, and this association is modulated by host genetic background, specifically HLA-A alleles [38, 39]. In coxsackievirus B (CVB) infection, mice injected with CVB plus non-neutralizing antibodies exhibited viral titers in tissues that were one to two orders of magnitude higher than those in mice injected with virus alone. Concomitantly, these mice also showed more severe histopathological damage, particularly in the heart, suggesting that pre-existing antiviral antibodies may exacerbate cardiovascular disease through cross-reactive immune mechanisms [40]. Collectively, these findings indicate that virus-related antibody levels serve as markers of chronic immune activation and are positively correlated with cardiovascular disease burden, further supporting their potential role in the pathogenesis of atherosclerosis and coronary events. Our Mendelian randomization analysis demonstrates that genetically predicted higher levels of specific antiviral antibodies—rather than viral exposure per se—are differentially associated with increased cardiovascular disease risk. Elevated Epstein-Barr virus EBNA-1–specific IgG levels, a marker of long-term control of latent infection, were causally linked to aortic stenosis and myocarditis. Among beta herpesviruses, increased cytomegalovirus pp52-specific IgG levels were associated with aortic aneurysm, while higher human herpesvirus 6 p101k-specific IgG levels and anti-HHV-6 IgG seropositivity correlated with aortic stenosis and coronary heart disease, respectively. Additionally, greater herpes simplex virus type 1 glycoprotein G-1 (mgG-1)–specific IgG levels were positively associated with dilated cardiomyopathy. These findings further confirm that specific herpesvirus antibody levels are linked to cardiovascular disease risk, supporting their role in disease development and potential use in prevention strategies.

Serological positivity and pathogen detection rates for *Chlamydia* species are often higher in patients with coronary

artery disease (CAD) than in control populations, suggesting a possible association with CAD [41]. In one comparative study that included 159 individuals with coronary artery disease, 71 with valvular heart disease, and 300 controls, seropositivity for *Chlamydia* exceeded 80% in the cohort [42]. *Chlamydia* pneumoniae IgG antibody levels are associated with the progression of aortic valve stenosis (AVS), suggesting that these antibodies may promote AVS development through sustained immune activation [43]. This notion is supported by multiple epidemiological studies showing that C. pneumoniae seropositivity is significantly linked to an increased risk of future cardiovascular events, particularly stroke [44, 45]. Moreover, C. pneumoniae IgG antibodies have been identified as an independent risk factor for coronary heart disease [46]. Mechanistically, persistent exposure to chlamydial antigens is thought to induce endothelial dysfunction and chronic vascular inflammation. Further evidence indicates that, in patients with coronary heart disease, seropositivity for *Chlamydia* LPS-specific IgA is strongly associated with elevated levels of inflammatory and endothelial activation markers, including IFNγ, IL-10, TNFα, sVCAM-1, and sE-selectin [47]. Consistent with this, Nazmi et al. reported that high antibody levels against C. pneumoniae are significantly correlated with systemic pro-inflammatory markers such as IL-6 and CRP, implicating chronic immune activation as a key pathway linking chlamydial immune responses to cardiovascular risk [48]. Beyond inflammation-driven pathways, autoimmune mechanisms may also contribute: for instance, the monoclonal antibody MAb 7B5, raised against chlamydial gG1, cross-reacts with human apolipoprotein B (ApoB), suggesting that molecular mimicry could induce autoantibodies against ApoB/LDL and thereby promote autoimmune responses in atherosclerosis [49]. Molecular mimicry may also contribute: actin and members of the HSP family share high homology with *Chlamydia* antigens (80.6%), suggesting cross-reactivity as a potential mechanism of tissue injury [50]. However, simple epitope similarity alone is insufficient to cause tissue damage; outcomes depend on HLA background, antigen presentation and MHC restriction, immune tolerance, and specific pathogen–host interactions [51]. Our Mendelian randomization analysis also identified a positive association within the *Chlamydia* family: genetically predicted higher levels of *Chlamydia trachomatis* Tarp-D F2–specific IgG antibodies were associated with an increased risk of heart failure with reduced ejection fraction. This finding highlights the need for further investigation into the role of chlamydial antigen-specific immune responses in cardiac outcomes.

In the Kitava population of Papua New Guinea, the high prevalence of *Treponema* infection is closely associated with elevated levels of naturally occurring cardioprotective autoantibodies—specifically IgM antibodies against phosphorylcholine (anti-PC IgM)—which have been linked to the low incidence of cardiovascular disease in this group, suggesting that certain infection-induced antibody responses may confer cardiovascular protection through immunomodulatory mechanisms [52]. This dual role of antiviral immunity is further illustrated in coxsackievirus B3 (CVB3)-induced myocarditis: high-titer neutralizing antibodies effectively block viral entry, suppress replication, and prevent myocardial injury, thereby exerting cardioprotective effects; in contrast, low-titer (sub-neutralizing) antibodies enhance viral uptake into macrophages via Fcγ receptors, promoting viral replication and exacerbating inflammation and tissue damage [53]. Supporting the importance of immune polarization, murine studies show that male mice develop severe myocarditis driven by $V\gamma4^+$ γδ T cell–mediated Th1/IFN-γ inflammatory responses, whereas female mice are protected through a $V\gamma1^+$ γδ T cell–dependent Th2/IL-4 pathway that promotes neutralizing antibody production [54, 55]. Seropositivity to common pathogens in adulthood—including enteroviruses, HSV, and *Chlamydia* pneumoniae—is associated with an increased risk of coronary heart disease (OR = 1.57–1.86), whereas a higher number of childhood infectious diseases (e.g., measles, chickenpox) correlates with reduced risk (OR = 0.86 per additional infection), highlighting the dual role of infections as both pro-inflammatory triggers and inducers of protective immune training [56]. Moreover, human cytomegalovirus (HCMV) can modulate humoral immunity by engaging IgG^+ memory B cells via its glycoprotein gp34, suppressing their proliferation, plasma cell differentiation, and antibody secretion, thereby inducing a state of global B-cell hyperresponsiveness; however, altered gp34 phenotypes can instead promote more effective immune cell activation and restrict viral spread in HCMV-infected fibroblasts [33, 55]. In dilated cardiomyopathy, antibodies against cardiotropic viruses such as coxsackievirus B can cross-react with anti-myolemmal antibodies (AMLA); this molecular mimicry may confer protection by blocking pathogenic autoantibodies from binding to cardiomyocytes or by modulating complement activation, thereby attenuating myocardial injury [57]. The observed associations between certain antiviral antibodies and reduced cardiovascular disease (CVD) risk may not reflect a direct effect of the antibodies on the cardiovascular system. Instead, they likely signify that the host has successfully established a protective immune profile characterized by effective humoral immunity and anti-inflammatory responses. Such an immune profile may minimize virus-induced inflammatory cardiovascular damage while simultaneously modulating immune regulation or enabling cross-protective mechanisms that lower CVD risk. This provides an important immunological perspective for understanding the complex relationship between viral serological markers and CVD. Our Mendelian randomization analysis identified several protective associations between pathogen-specific antibody responses and cardiovascular outcomes. Genetically predicted higher levels of Epstein-Barr virus EBNA-1–specific IgG antibodies were significantly associated with a reduced risk of pericarditis (OR = 0.92, 95% CI: 0.88–0.95; $p = 2.36 \times 10^{-5}$) and heart failure with reduced ejection fraction (OR = 0.98, 95% CI: 0.96–0.99; p = 0.011). Similarly, elevated EBV VCA p18–specific IgG was linked to lower pericarditis risk (OR = 0.91, 95% CI: 0.86–0.97; p = 0.0024).Notably, seropositivity or higher antibody levels against multiple polyomaviruses conferred strong protection against myocarditis.

The characterization of pathogen-specific antigen–antibody interactions in cardiovascular disease opens promising avenues for translational applications. Beyond their role as diagnostic or prognostic biomarkers, these immune responses may inform the development of precision immunotherapies, for example, by harnessing protective antibody profiles to design monoclonal antibodies that mimic natural cardioprotective immunity or

block pathogenic cross-reactivity. Furthermore, conserved microbial antigens capable of eliciting beneficial humoral responses could serve as candidates for therapeutic vaccines aimed at reprogramming maladaptive inflammation toward a more regulated, anti-inflammatory state. In drug discovery, molecular epitopes involved in protective versus pathogenic antibody binding may be leveraged to develop peptide-based inhibitors, small molecules, or tolerogenic platforms that selectively dampen autoimmune reactivity while preserving host defense. Ultimately, deciphering the fine specificity and functional consequences of antigen–antibody interactions could enable a new class of immune-guided interventions in cardiovascular medicine.

This study has several limitations. First, all samples were derived from individuals of European ancestry, and therefore the generalizability of our findings requires validation in cohorts from other ethnicities and geographic regions. Second, despite the corrections applied, the possibility of false-positive findings cannot be fully excluded. Third, our work provides epidemiological and genetic evidence of associations and potential causality but lacks sufficient cellular or animal model experiments to elucidate underlying molecular mechanisms, specific immune cell types involved, and detailed pathological processes.

Conclusion

This study comprehensively evaluated causal relationships between antibody-mediated immune response phenotypes and eleven cardiovascular diseases, and confirmed these relationships were not confounded by other factors. We identified multiple antibody-mediated immune phenotypes that may influence aortic aneurysm, aortic valve stenosis, coronary artery disease, hypertrophic cardiomyopathy, dilated cardiomyopathy, infective endocarditis, myocarditis, pericarditis, atrial fibrillation, heart block, and reduced ejection fraction heart failure. Notably, antibody responses to Epstein–Barr virus (particularly EBNA-1 and VCA p18), cytomegalovirus pp52, and varicella zoster virus were robustly associated with altered risks of several cardiovascular conditions. These findings provide new evidence for the role of infections in cardiovascular disease, suggest novel approaches for screening and identifying high-risk individuals, and highlight the potential of antiviral immunity and inflammation-modulating strategies as targets for prevention and intervention.

Author contributions

YL and JF contributed equally to this work and are co-first authors; YL performed formal analysis and wrote the original draft, while JF also contributed to formal analysis. LW, the corresponding author, provided critical review and editing of the manuscript and supervised the research. All authors contributed to the article and approved the submitted version.

Data availability

The data presented in this study are publicly available in the GWAS Catalog.

Ethics statement

All data used in this study were obtained from publicly available, and did not involve new collections of human participants, identifiable human data, or animal subjects.

Funding

The author(s) declared that financial support was not received for this work and/or its publication.

Conflict of interest

The author(s) declared no potential conflicts of interest with respect to the research, authorship, and/or publication of this article.

Generative AI statement

The author(s) declared that generative AI was used in the creation of this manuscript. Language and logical errors were corrected with assistance from artificial intelligence (GPT-5 mini).

Any alternative text (alt text) provided alongside figures in this article has been generated by Frontiers with the support of artificial intelligence and reasonable efforts have been made to ensure accuracy, including review by the authors wherever possible. If you identify any issues, please contact us.

Supplementary material

The Supplementary Material for this article can be found online at: https://www.ebm-journal.org/articles/10.3389/ebm.2026.10945/full#supplementary-material

References

1. Ebrahimi H, Aryan Z, Saeedi Moghaddam S, Bisignano C, Rezaei S, Pishgar F, et al. Global, regional, and national burden of respiratory tract cancers and associated risk factors from 1990 to 2019: a systematic analysis for the global burden of disease study 2019. *The Lancet Respir Med* (2021) 9(9):1030–49. doi:10.1016/S2213-2600(21)00164-8

2. Danaei G, Ding EL, Mozaffarian D, Taylor B, Rehm J, Murray CJL, et al. The preventable causes of death in the United States: comparative risk assessment of dietary, lifestyle, and metabolic risk factors. *Plos Med* (2009) 6(4):e1000058. doi:10.1371/journal.pmed.1000058

3. Khera AV, Chaffin M, Aragam KG, Haas ME, Roselli C, Choi SH, et al. Genome-wide polygenic scores for common diseases identify individuals with risk equivalent to monogenic mutations. *Nat Genet* (2018) 50(9):1219–24. doi:10.1038/s41588-018-0183-z

4. Kühl U, Pauschinger M, Seeberg B, Lassner D, Noutsias M, Poller W, et al. Viral persistence in the myocardium is associated with progressive cardiac dysfunction. *Circulation* (2005) 112(13):1965–70. doi:10.1161/CIRCULATIONAHA.105.548156

5. Libby P, Ridker PM, Hansson GK, Leducq Transatlantic Network on Atherothrombosis. Inflammation in atherosclerosis. *J Am Coll Cardiol* (2009) 54(23): 2129–38. doi:10.1016/j.jacc.2009.09.009

6. Caforio ALP, Pankuweit S, Arbustini E, Basso C, Gimeno-Blanes J, Felix SB, et al. Current state of knowledge on aetiology, diagnosis, management, and therapy of myocarditis: a position statement of the european society of cardiology working group on myocardial and pericardial diseases. *Eur Heart J* (2013) 34(33):2636–48. doi:10.1093/eurheartj/eht210

7. Cahill TJ, Prendergast BD. Infective endocarditis. *The Lancet* (2016) 387(10021): 882–93. doi:10.1016/S0140-6736(15)00067-7

8. Dale MA, Ruhlman MK, Baxter BT. Inflammatory cell phenotypes in aaas. *Arteriosclerosis, Thromb Vasc Biol* (2015) 35(8):1746–55. doi:10.1161/ATVBAHA.115.305269

9. Lindman BR, Clavel M, Mathieu P, Iung B, Lancellotti P, Otto CM, et al. Calcific aortic stenosis. *Nat Rev Dis Primers* (2016) 2(1):16006. doi:10.1038/nrdp.2016.6

10. Sheng J, Zhang Y, Dong L, Yao J. Causal effects of antibody-mediated immune responses on myocarditis: a two-sample Mendelian randomization study. *Medicine (Baltimore)* (2025) 104(29):e42496. doi:10.1097/MD.0000000000042496

11. Nimmerjahn F, Ravetch JV. Fcγ receptors as regulators of immune responses. *Nat Rev Immunol* (2008) 8(1):34–47. doi:10.1038/nri2206

12. Rose NR. Negative selection, epitope mimicry and autoimmunity. *Curr Opin Immunol* (2017) 49:51–5. doi:10.1016/j.coi.2017.08.014

13. Garrido F. Hla class-i expression and cancer immunotherapy. *Adv Experimental Medicine Biology* (2019) 1151:79–90. doi:10.1007/978-3-030-17864-2_3

14. Massilamany C, Gangaplara A, Reddy J. Intricacies of cardiac damage in coxsackievirus b3 infection: implications for therapy. *Int J Cardiol* (2014) 177(2): 330–9. doi:10.1016/j.ijcard.2014.09.136

15. Rose NR. Viral myocarditis. *Curr Opin Rheumatol* (2016) 28(4):383–9. doi:10.1097/BOR.0000000000000303

16. Butler-Laporte G, Kreuzer D, Nakanishi T, Harroud A, Forgetta V, Richards JB. Genetic determinants of antibody-mediated immune responses to infectious diseases agents: a genome-wide and hla association study. *Open Forum Infect Dis* (2020) 7(11): ofaa450. doi:10.1093/ofid/ofaa450

17. Burgess S, Small DS, Thompson SG. A review of instrumental variable estimators for mendelian randomization. *Stat Methods Med Res* (2017) 26(5):2333–55. doi:10.1177/0962280215597579

18. Choi KW, Chen C, Stein MB, Klimentidis YC, Wang M, Koenen KC, et al. Assessment of bidirectional relationships between physical activity and depression among adults. *Jama Psychiatry* (2019) 76(4):399–408. doi:10.1001/jamapsychiatry.2018.4175

19. Maloney BE, Perera KD, Saunders DRD, Shadipeni N, Fleming SD. Interactions of viruses and the humoral innate immune response. *Clin Immunol* (2020) 212:108351. doi:10.1016/j.clim.2020.108351

20. Hjelm F, Carlsson F, Getahun A, Heyman B. Antibody-mediated regulation of the immune response. *Scand J Immunol* (2006) 64(3):177–84. doi:10.1111/j.1365-3083.2006.01818.x

21. Zhao L, Fu Z. Roles of host immunity in viral myocarditis and dilated cardiomyopathy. *J Immunol Res* (2018) 2018:1–12. doi:10.1155/2018/5301548

22. Esfandiarei M, McManus BM. Molecular biology and pathogenesis of viral myocarditis. *Annu Rev Pathol Mech Dis* (2008) 3(1):127–55. doi:10.1146/annurev.pathmechdis.3.121806.151534

23. Maisch B, Ristić AD, Hufnagel G, Pankuweit S. Pathophysiology of viral myocarditis: the role of humoral immune response. *Cardiovasc Pathol* (2002) 11(2):112–22. doi:10.1016/s1054-8807(01)00113-2

24. Chimenti C, Verardo R, Grande C, Francone M, Frustaci A. Infarct-like myocarditis with coronary vasculitis and aneurysm formation caused by epstein–barr virus infection. *Esc Heart Fail* (2020) 7(3):938–41. doi:10.1002/ehf2.12611

25. Teng L, Shen C, Gu W, Wu J, Lu M, Xu X. Epstein-barr virus infection associated polymyositis and coronary artery dilation. *Bmc Infect Dis* (2022) 22(1):227. doi:10.1186/s12879-022-07221-9

26. Kühl U, Pauschinger M, Noutsias M, Seeberg B, Bock T, Lassner D, et al. High prevalence of viral genomes and multiple viral infections in the myocardium of adults with "idiopathic" left ventricular dysfunction. *Circulation* (2005) 111(7):887–93. doi:10.1161/01.CIR.0000155616.07901.35

27. Moimas S, Zacchigna S, Merlo M, Buiatti A, Anzini M, Dreas L, et al. Idiopathic dilated cardiomyopathy and persistent viral infection: lack of association in a controlled study using a quantitative assay. *Heart Lung Circ* (2012) 21(12):787–93. doi:10.1016/j.hlc.2012.07.013

28. Kindermann I, Kindermann M, Kandolf R, Klingel K, Bültmann B, Müller T, et al. Predictors of outcome in patients with suspected myocarditis. *Circulation* (2008) 118(6): 639–48. doi:10.1161/CIRCULATIONAHA.108.769489

29. Pankuweit S, Klingel K. Viral myocarditis: from experimental models to molecular diagnosis in patients. *Heart Fail Rev* (2013) 18(6):683–702. doi:10.1007/s10741-012-9357-4

30. Shimizu Y, Yamanashi H, Kawashiri S, Noguchi Y, Sasaki N, Nakamichi S, et al. Anti–early antigen epstein-barr virus titer and atherosclerosis in relation to vascular endothelial growth factor (vegf) polymorphism rs3025039 among older japanese individuals. *Environ Health Prev Med* (2025) 30:25–334. doi:10.1265/ehpm.25-00334

31. Fan F, Yang C, Zhu X, Liu Z, Liu H, Li J, et al. Association between infectious burden and cerebral microbleeds: a pilot cross-sectional study. *Ann Clin Transl Neurol* (2021) 8(2):395–405. doi:10.1002/acn3.51285

32. Binkley PF, Cooke GE, Lesinski A, Taylor M, Chen M, Laskowski B, et al. Evidence for the role of epstein barr virus infections in the pathogenesis of acute coronary events. *Plos One* (2013) 8(1):e54008. doi:10.1371/journal.pone.0054008

33. Qerqez AN, Hoffmann K, Lee AG, Pareek S, Hager K, Mishra AK, et al. Selective decoupling of igg1 binding to viral fc receptors restores antibody-mediated nk cell activation against hcmv. *Cell Rep* (2025) 44(12):116593. doi:10.1016/j.celrep.2025.116593

34. Guech-Ongey M, Brenner H, Twardella D, Hahmann H, Rothenbacher D. Role of cytomegalovirus sero-status in the development of secondary cardiovascular events in patients with coronary heart disease under special consideration of diabetes. *Int J Cardiol* (2006) 111(1):98–103. doi:10.1016/j.ijcard.2005.07.028

35. Watanabe M, Davidson L, Smith P, Castellucio PF, Jergovic M, Uhrlaub JL, et al. Anti-cytomegalovirus antibody levels stratify human immune profiles across the lifespan. *Geroscience* (2024) 46(5):4225–42. doi:10.1007/s11357-024-01124-0

36. Koskinen PK, Nieminen MS, Krogerus LA, Lemstr MKB, Mattila SP, H Yry PJ, et al. Cytomegalovirus infection and accelerated cardiac allograft vasculopathy in human cardiac allografts. *The J Heart Lung Transplant* (1993) 12(5):724–9. doi:10.1097/00005344-199309000-00025

37. Fouladseresht H, Ghamar Talepoor A, Farjadian S, Khosropanah S, Doroudchi M. Anti-varicella zoster virus igg and hscrp levels correlate with progression of coronary artery atherosclerosis. *Iranian J Allergy Asthma Immunol* (2019) 18(5):543–53. doi:10.18502/ijaai.v18i5.1924

38. Fouladseresht H, Safa A, Khosropanah S, Doroudchi M. Increased frequency of hla-a*02 in patients with atherosclerosis is associated with vzv seropositivity. *Arch Physiol Biochem* (2021) 127(4):351–8. doi:10.1080/13813455.2019.1640253

39. Girn J, Kavoosi M, Chantler J. Enhancement of coxsackievirus b3 infection by antibody to a different coxsackievirus strain. *J Gen Virol* (2002) 83(2):351–8. doi:10.1099/0022-1317-83-2-351

40. Boman J, Hammerschlag MR. Chlamydia pneumoniae and atherosclerosis: critical assessment of diagnostic methods and relevance to treatment studies. *Clin Microbiol Rev* (2002) 15(1):1–20. doi:10.1128/CMR.15.1.1-20.2002

41. Almeida NCC, Queiroz MAF, Lima SS, Brasil Costa I, Ayin Fossa MA, Vallinoto ACR, et al. Association of chlamydia trachomatis, c. Pneumoniae, and il-6 and il-8 gene alterations with heart diseases. *Front Immunol* (2019) 10:87. doi:10.3389/fimmu.2019.00087

42. Swierszcz J, Jacek DS, Milewicz T, Krzysiek J, Sztefko K, Galicka-Latała D. One-year observation of inflammatory markers in patients with aortic valve stenosis who expressed high or low chlamydia pneumoniae antibody titers. *J Heart Valve Dis* (2012) 21(5):599–607. doi:10.1007/s00395-012-0288-y

43. Fagerberg B, Gnarpe J, Gnarpe H, Agewall S, Wikstrand J. Chlamydia pneumoniae but not cytomegalovirus antibodies are associated with future risk of stroke and cardiovascular disease: a prospective study in middle-aged to elderly men with treated hypertension. *Stroke* (1999) 30(2):299–305. doi:10.1161/01.str.30.2.299

44. Mendall MA, Carrington D, Strachan D, Patel P, Molineaux N, Levi J, et al. Chlamydia pneumoniae: risk factors for seropositivity and association with coronary heart disease. *J Infect* (1995) 30(2):121–8. doi:10.1016/S0163-4453(95)80006-9

45. Prasad A, Zhu J, Halcox JP, Waclawiw MA, Epstein SE, Quyyumi AA. Predisposition to atherosclerosis by infections: role of endothelial dysfunction. *Circulation* (2002) 106(2):184–90. doi:10.1161/01.cir.0000021125.83697.21

46. Schumacher A, Seljeflot I, Lerkerød AB, Sommervoll L, Otterstad JE, Arnesen H. Chlamydia lps and momp seropositivity are associated with different cytokine profiles in patients with coronary heart disease. *Eur J Clin Invest* (2005) 35(7):431–7. doi:10.1111/j.1365-2362.2005.01511.x

47. Nazmi A, Diez-Roux AV, Jenny NS, Tsai MY, Szklo M, Aiello AE. The influence of persistent pathogens on circulating levels of inflammatory markers: a cross-sectional analysis from the multi-ethnic study of atherosclerosis. *Bmc Public Health* (2010) 10(1):706. doi:10.1186/1471-2458-10-706

48. Petyaev IM, Zigangirova NA, Tsibezov VV, Ross A, Bashmakov YK. Monoclonal antibodies against lipopolysaccharide ofchlamydia trachomatis with cross reactivity to human apob. *Hybridoma* (2011) 30(2):131–6. doi:10.1089/hyb.2010.0107

49. Sánchez-Caraballo A, García-Solano V, González-Rangel SK, Grattz-Lamadrid V, Munera-Gomez M. Molecular mimic between cardiovascular diseases and microorganism antigens. *Rev Alerg Mex* (2024) 71(1):61. doi:10.29262/ram.v71i1.1379

50. Rojas M, Restrepo-Jiménez P, Monsalve DM, Pacheco Y, Acosta-Ampudia Y, Ramírez-Santana C, et al. Molecular mimicry and autoimmunity. *J Autoimmun* (2018) 95:100–23. doi:10.1016/j.jaut.2018.10.012

51. Agmon Levin N, Bat Sheva PK, Barzilai O, Ram M, Lindeberg S, Frostegård J, et al. Antitreponemal antibodies leading to autoantibody production and protection from atherosclerosis in kitavans from papua New Guinea. *Ann N Y Acad Sci* (2009) 1173(1): 675–82. doi:10.1111/j.1749-6632.2009.04671.x

52. Kishimoto C, Kurokawa M, Ochiai H. Antibody-mediated immune enhancement in coxsackievirus b3 myocarditis. *J Mol Cell Cardiol* (2002) 34(9):1227–38. doi:10.1006/jmcc.2002.2087

53. Huber S, Sartini D. T cells expressing the vγ1 t-cell receptor enhance virus-neutralizing antibody response during coxsackievirus b3 infection of balb/c mice: differences in male and female mice. *Viral Immunol* (2005) 18(4):730–9. doi:10.1089/vim.2005.18.730

54. Wan F, Yan K, Xu D, Qian Q, Liu H, Li M, et al. Vγ1+γδt, early cardiac infiltrated innate population dominantly producing il-4, protect mice against cvb3 myocarditis by modulating ifnγ+ t response. *Mol Immunol* (2017) 81:16–25. doi:10.1016/j.molimm.2016.11.006

55. Cramer P, Neys SFH, Fiedler M, Lorenzetti R, Reinhard H, Janowska I, et al. A viral glycoprotein targets igg+ memory b cells to mediate humoral immune evasion. *Embo Mol Med* (2026) 18(2):795–823. doi:10.1038/s44321-026-00372-1

56. Pesonen E, Andsberg E, Öhlin H, Puolakkainen M, Rautelin H, Sarna S, et al. Dual role of infections as risk factors for coronary heart disease. *Atherosclerosis* (2007) 192(2): 370–75. doi:10.1016/j.atherosclerosis.2006.05.018

57. Maisch B. Immunologic regulator and effector functions in perimyocarditis, postmyocarditic heart muscle disease and dilated cardiomyopathy. *Basic Res Cardiol* (1986) 81(Suppl. 1):217–41. doi:10.1007/978-3-662-11374-5_21

EBM Experimental Biology and Medicine

TYPE Original Research
PUBLISHED 12 June 2026
DOI 10.3389/ebm.2026.10979

OPEN ACCESS

*CORRESPONDENCE
Theresa Manful Gwira,
tmgwira@ug.edu.gh

RECEIVED 08 January 2026
REVISED 14 April 2026
ACCEPTED 22 May 2026
PUBLISHED 12 June 2026

CITATION
Akazue PI, Quashie NB, Vaughan S, de Koning HP and Gwira TM (2026) Phenotypic profiling of Pathogen Box compounds MMV667494 and MMV028694 in bloodstream-form *Trypanosoma brucei brucei*. *Exp. Biol. Med.* 251:10979. doi: 10.3389/ebm.2026.10979

Phenotypic profiling of Pathogen Box compounds MMV667494 and MMV028694 in bloodstream-form *Trypanosoma brucei brucei*

Pearl Ihuoma Akazue[1,2,3], Neils Ben Quashie[1,4], Sue Vaughan[5], Harry P. de Koning[6] and Theresa Manful Gwira[1,2]*

[1]West African Centre for Cell Biology of Infectious Pathogens, University of Ghana, Accra, Ghana, [2]Department of Biochemistry, Cell and Molecular Biology, University of Ghana, Accra, Ghana, [3]Department of Biochemistry, Faculty of Life Sciences, University of Benin, Benin City, Nigeria, [4]Centre for Tropical Clinical Pharmacology and Therapeutics, University of Ghana Medical School, Accra, Ghana, [5]Department of Biological and Medical Sciences, Oxford Brookes University, Oxford, United Kingdom, [6]School of Infection and Immunity, University of Glasgow, Glasgow, United Kingdom

Abstract

Open-access drug discovery platforms have accelerated hit identification and lead prioritization across multiple diseases and enable systematic repurposing of bioactive compounds beyond their original indications. However, there remains a need for new chemotypes for African trypanosomiasis with improved efficacy and resilience to emerging drug resistance. In this study, we evaluated the antitrypanosomal potential and cellular effects of two Pathogen Box compounds, MMV667494 and MMV028694. The compounds were selected through a resazurin-based *in vitro* phenotypic viability screen that measures metabolic activity as a proxy for parasite viability against bloodstream-form *Trypanosoma brucei brucei*. To explore cellular phenotypes consistent with potential mechanisms of action, we applied cytological profiling using flow cytometry- and microscopy-based assays, including Annexin V/propidium iodide staining, cell-cycle DNA-content analysis, mitochondrial membrane potential (TMRE), and mitochondrial reactive oxygen species (MitoSOX) measurements. Both MMV667494 and MMV028694 (IC_{50} = 0.44 ± 0.05 μM and 0.33 ± 0.03 μM, respectively) displayed sub-micromolar antitrypanosomal potency and preferential toxicity toward trypanosomes over mammalian cells (selectivity indices >10). Growth profiling demonstrated dose-dependent inhibition of parasite proliferation, with evidence of trypanocidal activity at higher concentrations and longer exposure times. Treatment resulted in increased populations of phosphatidylserine-exposed and membrane-compromised cells, which is consistent with apoptosis-like phenotypes in trypanosomes. Although both compounds induced mitochondrial membrane depolarization in treated *T. b. brucei* cells, this effect was observed predominantly in a subpopulation of cells and is therefore unlikely to represent the primary cause of cell death. Increased mitochondrial production of reactive oxygen species and altered cell-cycle progression were also observed, which might indicate disruption of key cellular processes. These findings shows that MMV667494 and MMV028694 are selective antitrypanosomal compounds and their activities are associated with induce apoptosis-like features, cell-cycle disruption, and mitochondrial stress signatures in bloodstream-form *T. b. brucei*. These findings provide phenotypic insights into the activity of the

compounds, warranting further target deconvolution and optimization, although validation in human-infective subspecies and *in vivo* systems will be required.

KEYWORDS

African trypanosomiasis, antitrypanosomal activity, mitochondrial reactive oxygen species, mitochondrial stress, Pathogen Box

Impact statement

New chemotherapeutics for African trypanosomiasis with improved efficacy and resilience to drug resistance are still needed despite recent significant advances in drug discovery for the disease. This study investigated the possible mode of action of two promising Pathogen Box compounds, MMV667494 and MMV028694, using phenotypic profiling. The compounds were identified through a resazurin-based *in vitro* cell viability screen. We show that MMV667494 and MMV028694 are selective antitrypanosomal compounds that induce apoptosis-like phenotypes, cell-cycle disruption, and mitochondrial stress signatures in bloodstream-form *Trypanosoma brucei brucei*. These data provide evidence that these compounds could be repurposed for African trypanosomiasis chemotherapy.

Introduction

African trypanosomiasis is a two-staged parasitic disease, caused by the protozoa of the genus *Trypanosoma*, that affects humans and animals imposing severe public-health and socioeconomic consequences in endemic regions of sub-Saharan Africa [1–3]. Human African trypanosomiasis (HAT), also known as sleeping sickness, is caused by two subspecies of *Trypanosoma brucei*: *T. b. gambiense* and *T. b. rhodesiense*. The early (haemolymphatic) stage is often characterized by nonspecific symptoms such as intermittent fever, which can delay diagnosis, allowing progression to the late (meningoencephalitic) stage, a condition that is invariably fatal if untreated [4]. In parallel, animal African trypanosomiasis (AAT), caused by several *Trypanosoma species*, poses a significant constraint on livestock productivity and food security. Unlike HAT, AAT is not confined to the geographical distribution of the tsetse fly; species such as *T. vivax* and *T. evansi* have adapted to mechanical transmission by other biting flies, while *T. equiperdum* is transmitted sexually among equines [5].

Current chemotherapy for African trypanosomiasis relies on a few repertoires of drugs, many of which are decades old, stage-specific, difficult to administer, or associated with significant toxicity, and continuous use is seriously threatened by rising levels of drug resistance [6, 7]. Although recent advances have led to the introduction of oral agents such as fexinidazole and promising late-stage candidates [8–10], substantial gaps remain. These include the risk of emerging drug resistance, limited therapeutic options for late-stage *T. b. rhodesiense* HAT, inadequate treatments for AAT, and the challenge posed by parasite populations adapted to distinct host tissues and organs [7, 11–18].

Drug discovery efforts aim to identify hit compounds that can be optimized into viable therapeutic candidates, traditionally drawing heavily from natural products, which have historically inspired many successful antiparasitic drugs [19–22]. However, the relative decline in natural-product-based discovery pipelines has been attributed to factors such as complex chemical architectures with high sp^3 character and multiple stereocenters, challenging synthesis and derivatization, batch-to-batch variability, and constraints on scalable production [19, 23].

In contrast, synthetic compound libraries enable rapid, scalable (semi)synthesis and systematic optimization of hits and leads via scaffold-hopping and expansion strategies. Public–private partnerships have further accelerated these efforts by providing open access compound libraries. For instance, the Medicines for Malaria Venture (MMV) provides open-access compound libraries, including the "Pathogen Box" used in this study. The Pathogen Box is a collection of 400 diverse, drug-like molecules (including 26 reference compounds) with documented activity against pathogens that cause neglected tropical diseases. Several Pathogen Box compounds have shown promising activity against parasites beyond their original target indications [24–30]. Importantly, only a subset of these compounds has documented activity against kinetoplastids, highlighting the potential for systematic repurposing of the remaining compounds for antitrypanosomal drug discovery.

In an earlier study, we identified promising antitrypanosomal constituents from herbal preparation that were originally used in the treatment of schistosomiasis rather than African trypanosomiasis, demonstrating the feasibility of repurposing treatments developed for other neglected tropical diseases [31, 32]. Similarly, de Brito et al. reported the antischistosomal activity of diminazene aceturate, one of the standard antitrypanosomal drugs [33], further demonstrating the potential of repurposing efforts in facilitating the discovery and development of new treatments for neglected diseases [34]. In this study, we screened selected compounds from the MMV pathogen box for activity against bloodstream form *T. b. brucei* and performed phenotypic profiling to investigate cellular responses associated with compound exposure. Using cell-based phenotypic assays coupled with flow cytometry and confocal microscopy, we examined the effects of two selected compounds, MMV667494 and MMV028694, on mitochondrial function and cell cycle progression. While this study focuses on *T. b. brucei* as a model organism, the findings provide preliminary insights that may inform future investigations in human-infective subspecies.

Materials and methods

General compound information and compound selection

Stock solutions of individual test compounds in 100% DMSO (10 µL of 10 mM solution per compound) were provided by the Medicines for Malaria Venture (MMV;[1]). The compounds

1 https://www.mmv.org

originated from the MMV Pathogen Box, an open-access compound collection of 400 structurally diverse, drug-like molecules with activity against pathogens responsible for neglected tropical diseases. The pathogen box is distributed across five 96-well plates, each containing 80 compounds.

In this study, two plates (plates A and E) comprising 160 compounds were selected for initial screening based on assay throughput considerations, providing a representative subset for preliminary hit identification. These plates contain compounds spanning multiple chemical classes and disease indications, providing a manageable yet chemically diverse representative subset. Compound handling and dilution were performed according to MMV guidelines.[2] Briefly, 1 mM parent stock solutions were prepared in 100% DMSO from the 10 mM master stocks supplied by MMV, aliquoted into 96-well plates, and stored at −20 °C. Working solutions were freshly prepared by diluting the intermediate stocks into autoclaved distilled water and subsequently into the assay medium to achieve a final compound concentration of 10 μM (1% DMSO). The two compounds selected for downstream mode-of-action studies, MMV667494 and MMV028694, were selected based on their sub-micromolar activity in secondary screening assays (Supplementary Material 1). Fresh supplies of these compounds were subsequently obtained from MMV, and 10 mM stock solutions were prepared in DMSO for all confirmatory and mechanistic experiments.

Ethical approval

Ethical approval and informed content were not required for this study, as all experiments were conducted using established cell lines and did not involve human participants or animal subjects.

Trypanosome cell cultures

Wild-type bloodstream-form *Trypanosoma brucei brucei* GUTat 3.1 cells in logarithmic growth phase were cultured at 37 °C and 5% CO_2 in HMI-9 medium [35], supplemented with 10% fetal bovine serum and 1% penicillin-streptomycin.

In vitro antitrypanosomal screening

Antitrypanosomal activity was assessed using a resazurin-based viability assay adapted from a previously described method [36]. This assay measures metabolic activity as a proxy for parasite viability. Screening was conducted in two phases: (i) a single-concentration primary screen to identify active compounds, and (ii) a dose-response secondary screen to determine IC_{50} values of the compounds. For the primary screen, a single-concentration assay (1 μM) was used to screen all compounds. Compounds were incubated with *T. b. brucei* cells (2×10^4 cells/well) for 24 h, followed by the addition of alamarBlue dye solution (500 μM of resazurin sodium salt in PBS pH 7.3) and further incubation for 24 h. Fluorescence was measured at an excitation wavelength of 530 nm and an emission wavelength of 500 nm using a Varioskan™ multimode plate reader (Thermo Fisher Scientific). Antitrypanosomal activity in this context was defined as a reduction in resazurin fluorescence relative to untreated controls, indicating reduced metabolic activity. The assay was performed in four biological replicates. Untreated cells served as negative controls, while cells treated with 1 μM diminazene aceturate, a standard antitrypanosomal drug, served as positive controls. For secondary screening, selected compounds were subjected to two-fold serial dilution (maximum concentration: 1 μM) to determine the IC_{50} values. The upper concentration limit was capped at 1 μM to prioritize the identification of high-potency compounds with sub-micromolar activity. The assay was carried out as described for the primary screening. IC_{50} values were determined using a non-linear regression (four-parameter logistic model) in GraphPad Prism version 9. The experiments were conducted in three biological replicates, each with three technical replicates.

In vitro mammalian cytotoxicity assay

Mammalian cytotoxicity was assessed using RAW 264.7 murine macrophages and HEK 293 human embryonic kidney cells in a resazurin-based cell viability assay. These cell lines were selected to provide a preliminary assessment of compound toxicity across immune and non-immune mammalian cell types. Cells were seeded at 1.5×10^4 cells/well and incubated for 24 h in Dulbecco's Modified Eagle's Media (DMEM) before compound exposure. After 24-h treatment, alamarBlue dye solution (500 μM of resazurin sodium salt in PBS) was added, and fluorescence was measured after an additional 24 h. As with the antitrypanosomal assay, this assay reflects metabolic activity as a proxy for cell viability. The half-maximal cytotoxic concentration (CC_{50}) values were determined using a non-linear regression (four-parameter logistic model) in GraphPad Prism version 9. The assay was conducted in three biological replicates, each with three technical replicates. Cells treated with phenylarsine oxide (PAO; Sigma-Aldrich) served as the positive control. Selectivity indices ($SI = CC_{50}/IC_{50}$) were calculated.

Growth profiling

To assess effects on parasite proliferation, bloodstream-form *T. b. brucei* cells were treated with compounds at different concentrations ($1 \times IC_{50}$, $2 \times IC_{50}$, and $4 \times IC_{50}$). Cells were seeded at 2×10^5 cells/mL, and viable parasites were counted every 24 h using a haemocytometer over a period of up to 4 days. Cells were subcultured daily to maintain densities at 2×10^5 cells/mL. Cumulative cell numbers were calculated to account for daily dilution during subculturing, and doubling times were obtained directly from non-linear regression analysis (exponential growth model) in GraphPad Prism version 9, using the best-fit parameter output. Statistical comparison between the treated and untreated cells was made using an ordinary one-way ANOVA with Dunnett's multiple comparison test. Diminazene aceturate-treated cells served as positive controls and untreated cells served as the negative control. Experiments were conducted in three biological replicates, each with three technical replicates.

2 https://www.mmv.org/mmv-open/pathogen-box/pathogen-box-supporting-information

Annexin V/propidium iodide apoptosis assay

The mode of *T. b. brucei* cell death following treatment with MMV667494 and MMV028694 was investigated using the Annexin V-FITC apoptosis detection assay (Sigma-Aldrich). The assay was used to identify apoptosis-like phenotypes based on phosphatidylserine exposure and membrane integrity; however, it does not confirm classical apoptosis in *T. b. brucei.* The experiment was carried out following the manufacturer's instructions. Briefly, cells (2×10^5) were treated for 24 h at $1 \times IC_{50}$, $2 \times IC_{50}$, and $4 \times IC_{50}$, except the untreated cells which served as the controls. Propidium iodide was added immediately before acquisition to discriminate membrane-compromised cells. Data were acquired using a BD FACS LSR Fortessa X-20 flow cytometer with BD FACSDiva software version 8. Data analysis was carried out using FlowJo software 10.7.1. Statistical analysis was performed using two-way ANOVA with Dunnett's multiple comparison test in GraphPad Prism version 9. Three independent experiments (biological replicates) were conducted.

Cell cycle analysis

Cell-cycle distribution was assessed using the Guava cell cycle reagent (EMD Millipore, Cat No 4500-0220). Cells were treated for 24 h at $1\times IC_{50}$, $2 \times IC_{50}$, and $4 \times IC_{50}$, and fluorescence acquisition was performed using a BD FACS LSR Fortessa X-20 flow cytometer with BD FACSDiva software version 8. Data were analysed using FlowJo software 10.7.1, and statistical analysis was performed using two-way ANOVA with Dunnett's multiple comparison test in GraphPad Prism version 9. Two independent experiments (biological replicates) were conducted.

Mitochondrial membrane potential (TMRE) assay

Mitochondrial membrane potential ($\Delta\psi m$) was measured using tetramethylrhodamine ethyl ester (TMRE; Thermo Fisher Scientific, T669). This assay provided a population-level assessment of mitochondrial membrane potential. Cells (2×10^5 cells/mL) were treated for 24 h at $1\times IC_{50.}$ Valinomycin (100 nM) and troglitazone (10 μM) were used as depolarization and hyperpolarization controls, respectively [37]. Fluorescence was acquired using a BD FACSCalibur (4-colour) cytometer with CellQuest Pro software. Data were analyzed using FlowJo software 10.7.1, and statistical analysis was performed using two-way ANOVA with Dunnett's multiple comparison test in GraphPad Prism version 9. Two independent experiments (biological replicates) were carried out.

MitoSOX red assay

Mitochondrial reactive oxygen species (ROS) production was quantified using the MitoSOX Red assay as a specific indicator of mitochondrial oxidative stress associated with compound-induced cytotoxicity. Bloodstream-form *T. b. brucei* cells were treated with MMV667494 and MMV028694 at $1 \times IC_{50}$, $2 \times IC_{50}$ and $4 \times IC_{50}$ for 1h and 24 h to distinguish early versus delayed mitochondrial ROS responses. Following treatment, cells were incubated with MitoSOX Red according to the manufacturer's protocol, and fluorescence intensity was measured by flow cytometry using a BD FACS LSR Fortessa X-20 flow cytometer equipped with BD FACSDiva software version 8.0.1. A minimum of 10,000 events per sample were acquired, and debris and doublets were excluded by forward- and side-scatter gating. Mean fluorescence intensity (MFI) values were calculated for each condition and normalized to untreated controls at the corresponding time point. Data analysis was performed using FlowJo software version 10.7.1, The assay was conducted in three biological replicates. Statistical analysis was carried out using repeated measures two-way ANOVA with Dunnett's *post hoc* test. Fluoresence intensity was used as a measure of mitochondrial superoxide levels, indicative of mitochondrial oxidative stress.

Intracellular ROS assay

To determine whether compound-induced cell death was associated with intracellular oxidative stress, intracellular ROS levels were measured using a fluorometric ROS detection kit (Sigma-Aldrich, Cat No MAK145). Live bloodstream-form *T. b. brucei* cells (2×10^4 cells per well) were treated with MMV667494 or MMV028694 at $1 \times IC_{50}$, $2 \times IC_{50}$ and $4 \times IC_{50}$ for 1h and 24 h, respectively. Following treatment, the cells were washed with PBS and incubated with 100 μL of the master reaction mix for 1 h at 37 °C and 5% CO_2, protected from light. Fluorescence was measured using a Varioskan™ multimode plate reader at excitation 520 nm and emission 605 nm. Fluorescence values were background-subtracted and normalized to untreated controls at each time point prior to statistical analysis to account for time-dependent changes in cell density and metabolic activity. The assay was conducted in three biological replicates. Statistical analysis was performed using repeated-measures two-way ANOVA with Dunnett's and Sidak's *post hoc* test.

Fixation of cells and fluorescent staining for microscopy

To assess mitochondrial morphology and kinetoplast–nuclear organization, cells were stained with MitoTracker™ Red CMXRos (Invitrogen, Thermo Fisher Scientific) before fixation. The Mitotracker stain served as a qualitative assessment of mitochondrial morphology. Following compound treatment at $1 \times IC_{50}$, cells were incubated with MitoTracker dye according to the manufacturer's recommendations and subsequently fixed in 4% formaldehyde, as previously described [31, 38]. Fixed cells were mounted onto poly-L-lysine-coated slides (Sigma-Aldrich) and allowed to adhere for 1 h, washed with PBS, and blocked with 100 mM of Tris-HCl in PBS (pH 7.5) for 10 min and washed again with PBS to reduce background fluorescence. Nuclear DNA was counterstained with Hoechst 33342 (Invitrogen, Cat No H3570) before the final PBS wash and mounting with Vectashield antifade mounting medium (Vector laboratories, Cat No H-1000).

Confocal microscopy and image analysis

Fluorescence imaging was performed using a Zeiss Axio Observer Z1 microscope equipped with an LSM 800 confocal unit using a 63× oil-immersion objective (Plan-Apochromat 63x/

TABLE 1 Antitrypanosomal activity and physiochemical properties of selected Pathogen Box compounds following secondary screening.

Compound ID	*T. b. brucei* IC_{50} ± SD (μM)	Disease set (as indicated by MMV)*	Total molecular weight*	Molecular formula*	cLogP*
MMV688889	0.67 ± 0.06	Tuberculosis	349.82	$C_{19}H_{16}N_5Cl$	3.46
MMV688776	1.04 ± 0.07	Kinetoplastids	313.78	$C_{17}H_{16}N_3OCl$	3.90
MMV676603	4.63 ± 0.66	Tuberculosis	431.39	$C_{17}H_{16}N_3O_5F_3S$	1.29
MMV676401	3.85 ± 0.68	Tuberculosis	308.38	$C_{18}H_{20}N_4O$	3.22
MMV688798	0.67 ± 0.08	Kinetoplastids	365.45	$C_{21}H_{19}NO_3S$	3.48
MMV667494	**0.44 ± 0.05**	**Malaria**	**494.03**	**$C_{25}H_{34}N_5OClF_2$**	**4.39**
MMV028694	**0.33 ± 0.03**	**Malaria**	**332.37**	**$C_{18}H_{16}N_6O$**	**2.12**
MMV689243	0.70 ± 0.08	Kinetoplastids	466.42	$C_{23}H_{20}N_4F_6$	4.26
MMV026313	0.50 ± 0.04	Malaria	237.26	$C_{14}H_{11}N_3O$	1.92
MMV688415	2.85 ± 0.91	Kinetoplastids	433.54	$C_{26}H_{31}N_3O_3$	2.71

IC_{50} values (mean ± SD) were determined from three independent biological experiments, each performed in triplicate, using a resazurin-based viability assay in bloodstream-form *Trypanosoma brucei brucei*. Compounds were tested using two-fold serial dilutions with a maximum concentration of 1 μM. *Asterisked information (molecular weight, molecular formula, disease set classification, and cLogP values) was obtained from the MMV Pathogen Box Supplementary Material: https://www.mmv.org/mmv-open/pathogen-box/pathogen-box-supporting-information. IC_{50}: half-maximal inhibitory concentration.

1.4 Oil DIC M27). Image acquisition was carried out using Zen Blue 2.3 software, with fluorescence channels configured using the "smart setup" function for two-colour imaging. Hoechst 33342 and Mitotracker Red CMXRos were excited using the 405 nm (5 mW) and 561 nm (10 mW) laser lines, respectively, with emission collected at 410–546 nm and 590–700 nm. Detector saturation was avoided using the range-indicator function, and Z-stacks were acquired at 1 μm intervals with a pinhole size of 1 Airy unit. Images were acquired in CZI format and exported as TIFF files for analysis in ImageJ (Fiji). Linear adjustments to contrast and brightness were applied uniformly across conditions, and Z-stacks were visualized using maximum-intensity projections. Kinetoplast/nucleus (K/N) counts as well as cell and mitochondrial morphology profiling were carried out manually using cell counts. At least 500 cells per condition were analyzed across biological replicates. Statistical analysis was carried out using one-way ANOVA with Sidak's *post hoc* test.

Results

Identification of two selective antitrypanosomal compounds for mode of action studies

A total of 160 compounds from the MMV Pathogen Box (plates A and E compounds of theathogen box) were subjected to single-concentration *in vitro* antitrypanosomal phenotypic screening against bloodstream-form *T. b. brucei*. The primary screen was designed to be a one-point phenotypic assay to identify compounds that reduced parasite metabolic activity at 1 μM rather than to determine IC_{50} values. After this initial screen, 10 compounds demonstrating activity were identified for secondary screening. Secondary screening was performed using eleven two-fold serial dilutions (maximum concentration 1 μM), allowing the determination of IC_{50} values (Table 1). Two compounds, MMV667494 and MMV028694 (Figure 1), exhibited sub-micromolar potency (IC_{50} < 0.5 μM were prioritized for further analysis based on their potency. Both compounds are classified by MMV as antimalarial hits showed the most promising *in vitro* antitrypanosomal activity among the compounds tested (Table 1). To assess parasite selectivity, mammalian cytotoxicity was evaluated using RAW 264.7 murine macrophages and HEK 293 human kidney cells. Both MMV667494 and MMV028694 showed good selectivity toward *T. b. brucei*, with selectivity indices greater than 10 (calculated using 24 h CC_{50} and IC_{50} values), indicating their preferential toxicity toward trypanosomes relative to mammalian cells (Tables 1, 2; Supplementary Material 2).

MMV667494 and MMV028694 display concentration- and time-dependent trypanocidal activity

The effect of both compounds on the proliferation of *T. b. brucei* cells was assessed by longitudinal growth profiling following treatment with increasing concentrations of MMV667494 (Figures 2A,B) and MMV028694 (Figures 2C,D). At 24 h, both compounds reduced cell numbers across all the tested concentrations (1 × IC_{50}, 2 × IC_{50}, and 4 × IC_{50}), although statistical significance was reached only at higher concentrations - specifically MMV667494 at 2 × IC_{50} ($p = 0.041$), and 4 × IC_{50} ($p = 0.014$) and MMV028694 at 4 × IC_{50} ($p = 0.026$) (Figure 2). At 48 h and 72 h, both compounds produced dose-dependent reductions in parasite numbers, with statistically significant inhibition observed at all concentrations tested ($p \leq 0.0001$) (Figures 2A,C). Notably, a net decline in parasite numbers was observed at 4 × IC_{50} after 72 h, indicating that both MMV667494 and MMV028694 killed a proportion of the trypanosome population under these conditions. At lower concentrations, parasite growth was inhibited without net loss of viable cells, consistent with a predominantly trypanostatic effect

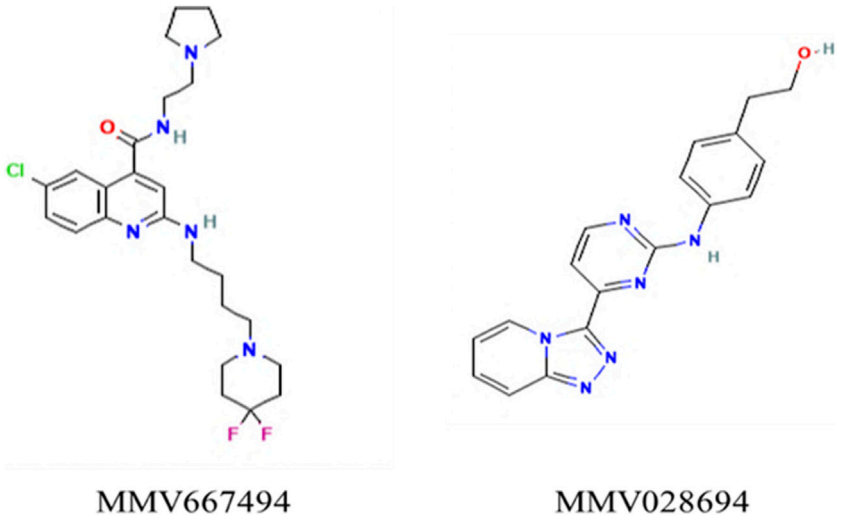

FIGURE 1
Chemical structures for the selected MMV compounds, MMV667494 and MMV028694. MMV667494 is 6-Chloro-2-[4-(4,4-difluoropiperidin-1-yl) butylamino]-N-(2-pyrrolidin-1-ylethyl) quinoline-4-carboxamide, while MMV028694 is 2-[4-[[4-([1,2,4] triazolo [4,3-a]pyridin-3-yl)pyrimidin-2-yl] amino]phenyl]ethanol. Both compounds are categorised as antimalarial compounds in the MMV pathogen box (https://www.mmv.org/mmv-open/pathogen-box/pathogen-box-supporting-information).

TABLE 2 Cytotoxicity and selectivity indices of MMV667494 and MMV028694 in mammalian cell lines.

Compound ID	*T. b. brucei* IC_{50} ± SD (μM)	RAW 264.7 CC_{50} ± SD (μM)	Selectivity index (CC_{50} RAW/IC_{50})	*HEK 293* CC_{50} ± SD (μM)	Selectivity index (CC_{50} HEK/IC_{50})
MMV667494	0.44 ± 0.05	5.50 ± 0.12	12.5	17.31 ± 2.5	39.3
MMV028694	0.33 ± 0.03	4.34 ± 0.38	13.2	8.12 ± 2.15	24.6
Diminazene aceturate	0.25 ± 0.00	7.33 ± 0.20	29.0	28.97 ± 7.37	115.9
Phenylarsine oxide	ND	0.57 ± 0.06	-	0.37 ± 0.03	-

CC_{50} values (mean ± SD) were determined in RAW, 264.7 murine macrophages and HEK, 293 human embryonic kidney cells using a resazurin-based viability assay after 24 h of compound exposure. Selectivity index (SI) was calculated as CC_{50} (mammalian cells) divided by IC_{50} (*T. b. brucei*). All experiments were performed in three independent biological replicates, each with three technical replicates. CC_{50}, half-maximal cytotoxic concentration; SI, selectivity index.

that transitions to trypanocidal activity at higher exposure, like previously reported for a series of adenosine analogues [39]. Consistent with these observations, cell doubling times were significantly prolonged following treatment. At 1 × IC_{50}, doubling times increased to 17.7 h (MMV667494) and 18.7 h (MMV028694), while at 2 × IC_{50}, doubling times further increased to 20.0 h and 27.6 h, respectively, compared with 7.4 h for untreated cells (Figure 2E). These findings confirm that both compounds markedly impair parasite proliferation in a concentration-dependent manner.

MMV667494 and MMV028694 induce apoptotic-like phenotypes in a subset of treated cells

The annexin V-FITC/PI assay was used to investigate whether the observed trypanocidal cell death was associated with apoptosis-like or necrotic phenotypes. Phosphatidylserine is usually found in the inner leaflet of the plasma membrane of healthy cells. Upon initiation of apoptosis, phosphatidylserine is translocated to the extracellular membrane leaflet, making it easily accessible for annexin V-FITC to bind to it. Propidium iodide (PI), a nucleic acid binding dye, is a fluorescent indicator that is excluded from intact cells but enters when the plasma membrane becomes compromised. Annexin V-FITC/propidium iodide (PI) staining therefore allows to distinguish between viable (FITC-/PI-), early apoptotic-like (FITC+/PI-), late apoptotic-like (FITC+/PI+), and necrotic (FITC-/PI+) populations. The term "apoptotic-like" is used because *T. b. brucei* lacks canonical caspases, which are the classical apoptotic cell death signalling machinery, despite displaying hallmark features such as phosphatidylserine externalisation [40]. Treatment with MMV667494 for 24 h resulted in a significant increase in early apoptotic-like cells defined as increased Annexin V fluorescence but unchanged cell permeability measured with PI, at 2 × IC_{50} (10.9%, $p = 0.0004$) and 4 × IC_{50} (12.0%, $p < 0.0001$) compared with untreated controls 0.49%) (Figure 3). Late apoptotic-like cells were also significantly increased at 4 × IC_{50} (15.6%, $p < 0.0001$) with increased fluorescence on both channels, relative to untreated cells (0.52%) (Figures 3D,E). A similar pattern was

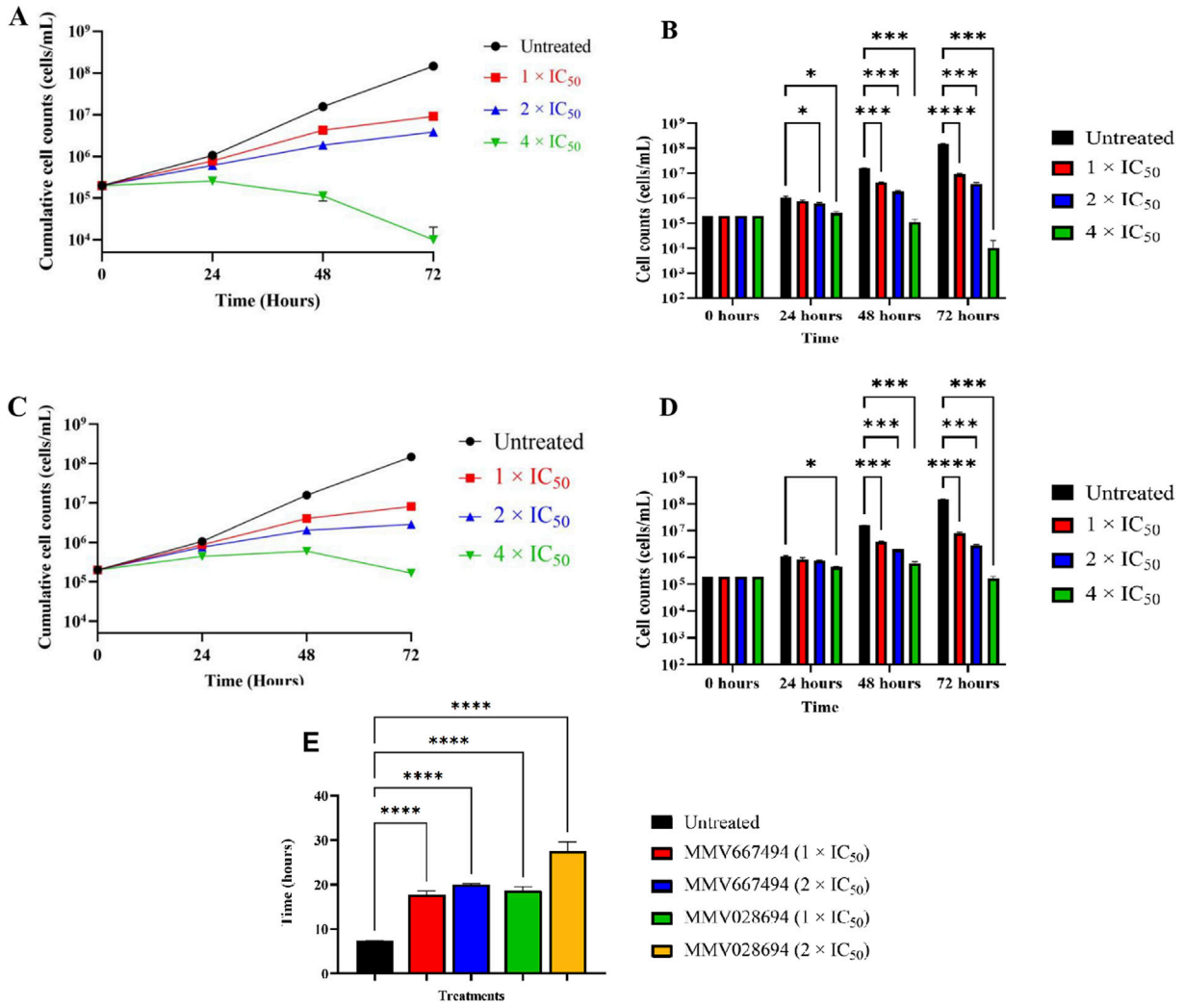

FIGURE 2
Growth inhibition and effects on doubling time of *T. b. brucei* following compound treatment. MMV667494 **(A,B)** and MMV028694 **(C,D)**. **(E)** Effect of compounds on doubling time. Cells were treated at 1 × IC_{50}, 2 × IC_{50} and 4 × IC_{50} for up to 72 h. Untreated cells served as controls. Data are averages of three independent experiments (biological replicates). Error bars show standard deviation. Statistical analysis was performed using ordinary one-way ANOVA with Dunnett's multiple comparison test relative to untreated controls. Untreated cells served as controls. *p ≤ 0.05, ***p ≤ 0.001, ****p ≤ 0.0001. Cells were sub-cultured, as necessary, to maintain cell density below 2 × 10^6 cells/mL.

observed for MMV028694, although significant increases in early apoptotic-like cells were already evident at 1 × IC_{50} (5.3%. p = 0.0193) (Figure 4). Despite these increases, the overall proportion of Annexin V-positive cells remained relatively modest indicating that apoptosis-like features were restricted to a subset of the population at the time points examined.

Mitochondrial membrane depolarization occurs in a subpopulation of treated cells

The mitochondrial membrane potential (ΔΨm) of *T. b. brucei* cells treated with MMV667494 and MMV028694 was determined by flow cytometry in TMRE-stained live cells exposed to a concentration of 1 × IC_{50} of the compounds for 24 h (Figures 5A–F). Both MMV667494 and MMV028694 treatments resulted in a statistically significant reduction in mean ΔΨm (p = 0.029 and p = 0.001 respectively). However, analysis of fluorescence distributions revealed that depolarization was confined to a distinct subpopulation of cells, while the majority retained mitochondrial membrane potential. This is evident from the observed low-fluorescence peak in treated samples (Figures 5D,E), suggesting that mitochondrial depolarization is associated with cells undergoing death or severe stress rather than a uniform effect across the population. Consistent with this interpretation, confocal microscopy of MitoTracker-stained cells showed largely preserved mitochondrial morphology in most treated cells, particularly following MMV667494 exposure (Figure 5F; Supplementary Figure S1). Control treatments behaved as expected: troglitazone induced mitochondrial hyperpolarization, while valinomycin caused complete depolarization (both p < 0.0001) (Figures 5A–C), in agreement with previous reports [37, 41].

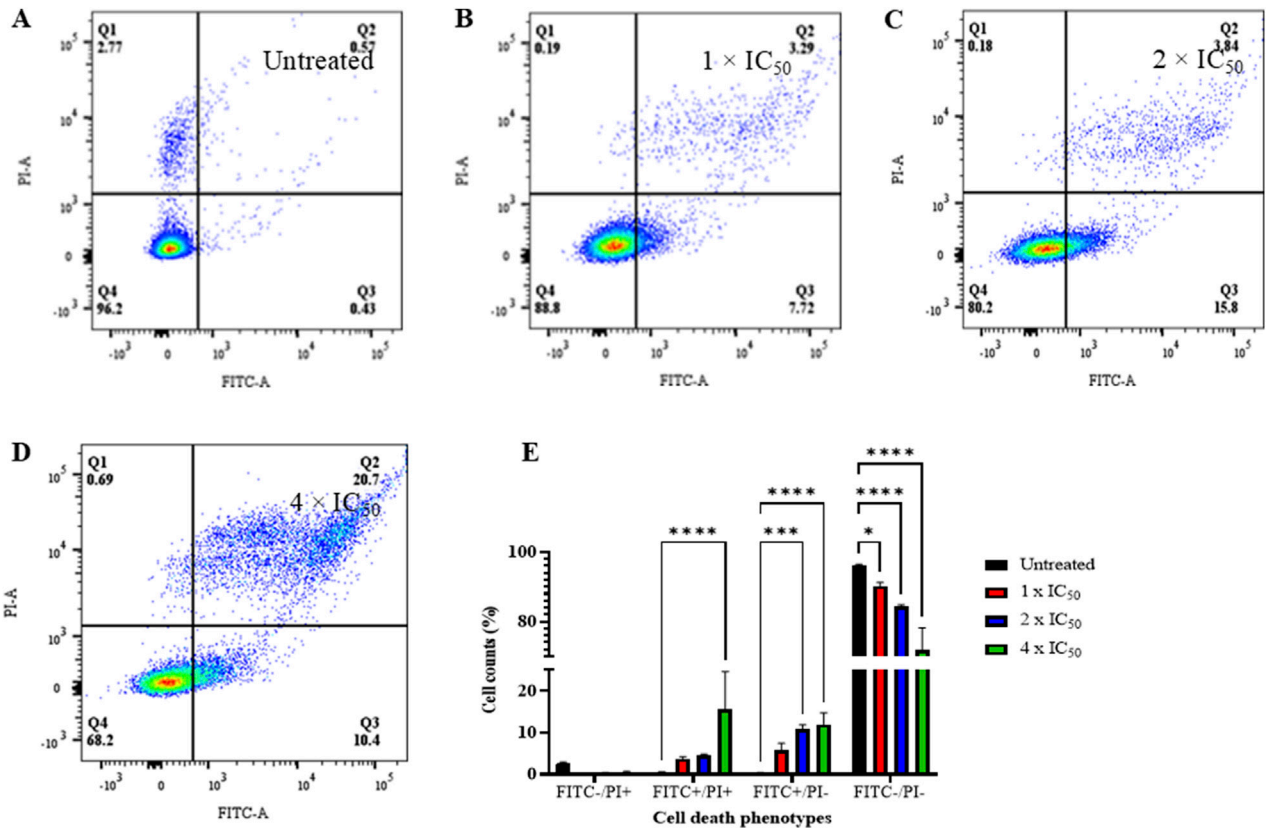

FIGURE 3
Annexin V/PI analysis of MMV667494-induced cell death in *T. b. brucei*. Representative pseudocolour two-parameter density plots showing Annexin V-FITC (x-axis) versus PI (y-axis) staining for **(A)** Untreated *T. b. brucei* cells, **(B)** MMV667494-treated (1 × IC_{50}), **(C)** MMV667494-treated (2 × IC_{50}), and **(D)** MMV667494-treated (4 × IC_{50}) *T. b. brucei* cells. Trypanosomes (except the controls) were treated for 24 h. Quadrant interpretation: Viable cells are FITC-, PI- (lower left quadrant), early apoptotic-like cells are FITC+, PI- (lower right quadrant), and late apoptotic-like/necrotic cells are FITC+, PI+ (upper right quadrant). The FITC-, PI+ population (upper left quadrant) was classified as necrotic cells. **(E)** Shows the proportion of cells exhibiting different cell death phenotypes. Data represents SD from three independent experiments (biological replicates). Statistical analysis was performed using two-way ANOVA with Dunnett's multiple comparison test relative to untreated and heat-treated controls. *p ≤ 0.05, ***p ≤ 0.001, ****p ≤ 0.0001. Note: The term apoptosis-like reflects phosphatidylserine externalization in trypanosomes, which lack canonical caspase-dependent apoptotic pathways.

MMV667494 and MMV028694 increased mitochondrial ROS levels in a time-dependent manner

The effect of MMV667494 and MMV028694 on mitochondrial levels of reactive oxygen species was determined using the MitoSOX red assay at 1 h and 24 h of treatment (Figure 6). MMV667494 did not significantly alter mitochondrial ROS levels at 1 h, whereas MMV028694 caused a significant increase only at 4 × IC_{50} ($p < 0.0001$) but not at lower concentrations (Figure 6A). After 24 h, both compounds significantly increased mitochondrial ROS levels at all concentrations tested, relative to untreated controls (Figure 6A). Time-course analysis revealed a significant increase ($p < 0.0001$) in mitochondrial ROS between 1 h and 24 h for MMV667494 at all concentrations (Figures 6A,B). For MMV028694, significant increases between time points were observed at 1 × IC_{50} and 2 × IC_{50} ($p < 0.0001$ for both), but not at 4 × IC_{50} ($p = 0.76$), likely reflecting advanced cell damage or loss of viable mitochondria at higher exposure (Figure 6B). Overall, the magnitude of ROS increases was modest, and the delayed onset suggests that mitochondrial oxidative stress is more likely a downstream consequence of compound-induced cellular effects rather than the primary cause of cell death.

Intracellular ROS levels remain largely unchanged following treatment with MMV667494 and MMV028694

The intracellular levels of ROS in MMV667494-treated, MMV028694-treated and untreated cells were determined using a fluorescence-based commercially available kit as earlier described. The results obtained showed that neither MMV667494 nor MMV028694 significantly altered intracellular ROS levels at 1 h or 24 h across all tested concentrations, except for a just-significantly modest decrease observed at 1 h for MMV028694 at 4 × IC_{50} ($p = 0.029$) (Supplementary Material 4). As this effect was not sustained at 24 h, it is unlikely to be biologically meaningful. A similar increase in intracellular ROS was observed over time in both treated and untreated cultures, consistent with increased cell density and prolonged culture, leading to media changes, rather

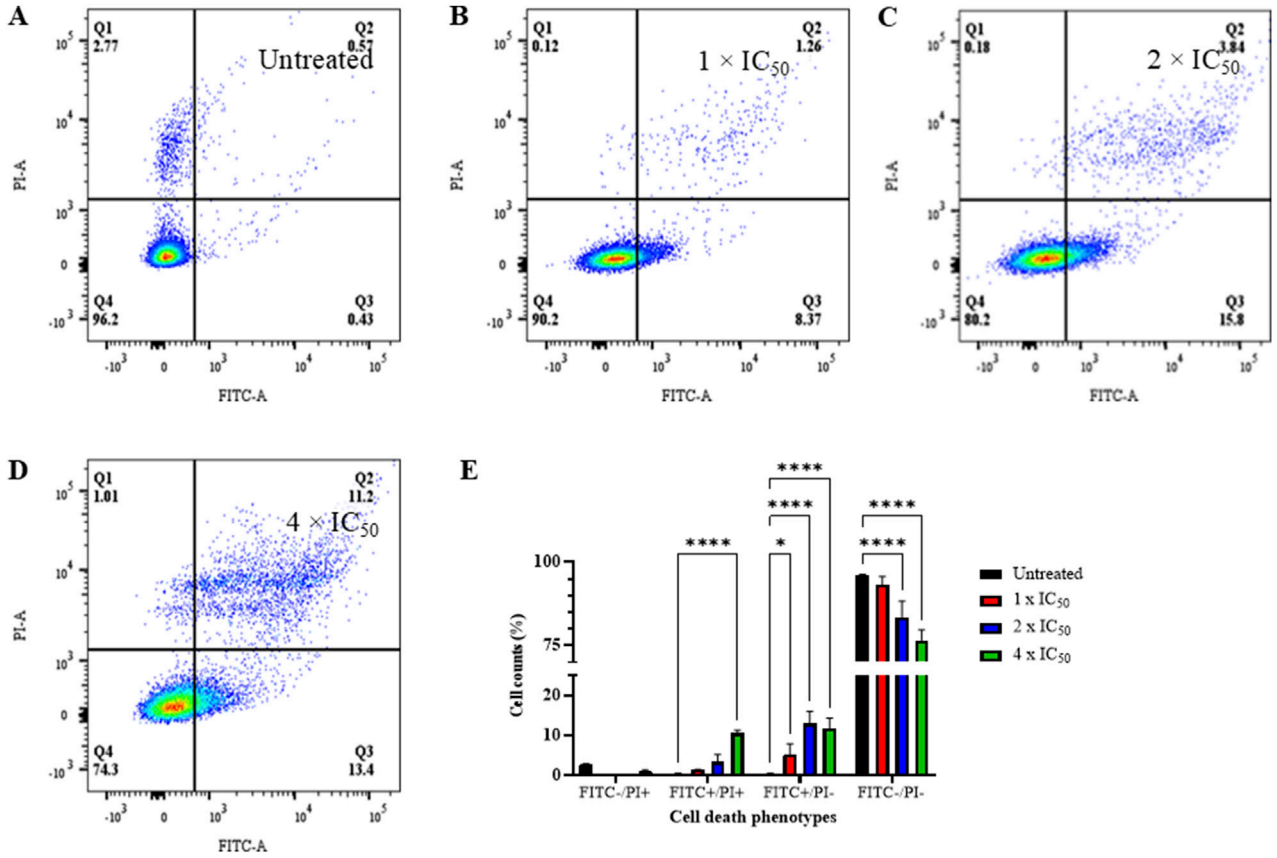

FIGURE 4
Annexin V/PI analysis of MMV028694-induced cell death in *T. b. brucei*. Representative pseudocolour two-parameter density plots showing Annexin V-FITC (x-axis) versus PI (y-axis) staining for **(A)** Untreated T. b. brucei cells, **(B)** 1 × IC_{50}, **(C)** 2 × IC_{50}, and **(D)** 4 × IC_{50}. Trypanosomes (except the controls) were treated for 24 h. Quadrant interpretation: Viable cells are FITC-, PI- (lower left quadrant), early apoptotic-like cells are FITC+, PI- (lower right quadrant), and late apoptotic-like/necrotic cells are FITC+, PI+ (upper right quadrant). The FITC-, PI+ population (upper left quadrant) was classified as necrotic cells. **(E)** Shows the proportion of cells exhibiting different cell death phenotypes. Data represents SD from three independent experiments (biological replicates). Statistical analysis was performed using two-way ANOVA with Dunnett's multiple comparison test relative to untreated and heat-treated controls. *p ≤ 0.05 and ****p ≤ 0.0001. Note: The term apoptosis-like reflects phosphatidylserine externalization in trypanosomes, which lack canonical caspase-dependent apoptotic pathways.

than compound-specific effects. These findings suggest that intracellular oxidative stress is not the primary mechanism underlying MMV667494- or MMV028694-induced parasite death.

MMV667494 and MMV028694 disrupt cell-cycle progression without inducing widespread morphological abnormalities

Cell cycle effects were analyzed using DNA-content flow cytometry (Figure 7) and confocal microscopy (Supplementary Material 3, 5). Following MMV667494 treatment, a significant reduction in G1-phase cells was observed at 4 × IC_{50} ($p < 0.0001$), accompanied by a concomitant increase in S-phase cells (Figure 7A). G2-phase cells were significantly reduced at all concentrations tested, while cells with sub-G1 DNA content (<G1) increased in a dose-dependent manner, consistent with DNA fragmentation or aberrant division. Similarly, MMV028694 treatment resulted in the accumulation of <G1 cells and depletion of G2-phase cells i.e., with a completely replicated diploid set of chromosomes, at all concentrations (Figure 7B). A modest reduction in G1-phase cells was also observed, reaching statistical significance at 2 × IC_{50} ($p = 0.0326$). These profiles are consistent with disrupted cell cycle progression and accumulation of cells with abnormal DNA content. Overall, both compounds produced cell-cycle profiles consistent with slowed S-phase progression and impaired cell division, in agreement with the observed growth defects. The observations suggest that the compounds exerts a direct or indirect inhibitory action on DNA synthesis, likely not only prolonging S-phase but causing incomplete replicate of daughter chromosomes, leading to the highly significant drop in cells with fully replicated nuclei and associated increase in cells that contain less DNA than the normal diploid set of chromosomes (<G1 DNA content) after cell division, which would not be viable.

Confocal microscopy was used to validate the results obtained from the flow cytometry-based cell cycle progression assay. The confocal microscopy corroborated these findings at 1 × IC_{50} and 24 h of exposure. Both compounds increased the proportion of

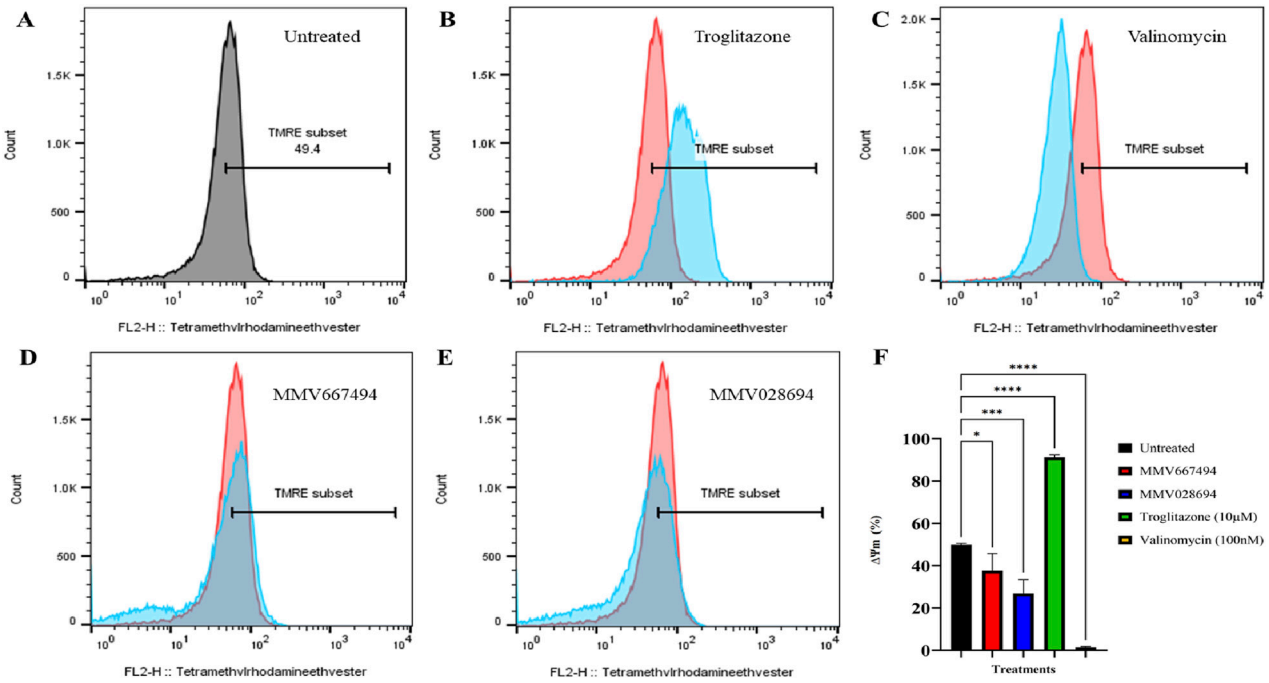

FIGURE 5
Effects of MMV667494 and MMV028694 on mitochondrial membrane potential in *T. b. brucei*. Representative histogram plots for trypanosomes stained with tetramethylrhodamine ethyl ester (TMRE). Histograms in red show untreated cells while the histograms in blue show respective treatment: **(A)** untreated, **(B)** troglitazone-treated (10 μM), **(C)** valinomycin-treated (100 nM), **(D)** MMV667494 (1 × IC_{50}), and **(E)** MMV028694 (1 × IC_{50}). Cells were treated for 24 h before assay **(F)** Shows the quantification of mean TMRE fluorescence intensity. Data represents mean ± SD from three independent biological replicates. Statistical analysis was performed using two-way ANOVA with Dunnett's multiple comparison test relative to untreated and heat-treated controls. Valinomycin-treated cells served as the negative control (mitochondrial membrane depolarization) while troglitazone-treated cells served as the positive control (mitochondrial membrane hyperpolarization). Statistical analysis was performed using two-way ANOVA with Dunnett's multiple comparison test, *p ≤ 0.05, ***p ≤ 0.001, ****p ≤ 0.0001. Note: depolarization was observed primarily in a subpopulation of cells, indicating heterogeneous mitochondrial responses rather than a uniform effect across population.

0K1N cells (~6% vs. 1.9% in controls) and 2K1N cells, while 1K2N and other aberrant K/N configurations remained rare (Supplementary Material 5A). MMV028694 uniquely increased the proportion of 1K0N cells, and rare events such as cojoined nuclei and cytokinesis failure (<1%) were observed (Supplementary Material 5B). Gross morphological distortions were limited to a very small fraction of treated cells and were not widespread (Supplementary Material 5C), indicating that cell death and growth inhibition primarily result from functional disruption of cell-cycle progression rather than widespread structural damage. Together, the most prominent changes in the N/K configuration therefore concerned the lack of an intact (visible) nucleus or kinetoplast at the point of cell division or thereafter. This is consistent with an impact of the treatments on DNA synthesis both of kinetoplast and nuclear DNA.

Discussion

In this study, we aimed to identify antitrypanosomal hit compounds from a diverse synthetic library and to provide insights into their potential cellular effects using a cytology-based profiling approach. The compound set used - MMV's Pathogen Box -comprises 400 drug-like molecules spanning multiple chemical classes, assembled based on known activity against pathogens responsible for neglected tropical diseases. Although the collection has supported repurposing efforts across diverse parasite systems, only a minority of Pathogen Box compounds were originally annotated with anti-kinetoplastid activity, leaving substantial space for systematic cross-pathogen exploration and repositioning.

Using a single-concentration phenotypic screening strategy followed by IC_{50} confirmation, we identified two compounds - MMV667494 and MMV028694 - with the most promising sub-micromolar activity against bloodstream-form *T. b. brucei* and selected them for further investigation. Both MMV667494 (a quinoline compound) and MMV028694 (a benzotriazole compound) were categorized by MMV as antimalarial hits, yet quinoline- and benzotriazole-related scaffolds have previously been associated with anti-trypanosomatid activity [42–46]. Prior studies have also reported antitrypanosomal activity for MMV028694 [42] and MMV667494 [29], though the IC_{50} values differ from those measured here - an expected outcome given that phenotypic potency estimates can vary across laboratories due to differences in parasite strains, media composition, incubation time, cell density, and growth rate [47, 48]. The present study extends these findings by providing a detailed phenotypic characterization of

10.3389/ebm.2026.10979

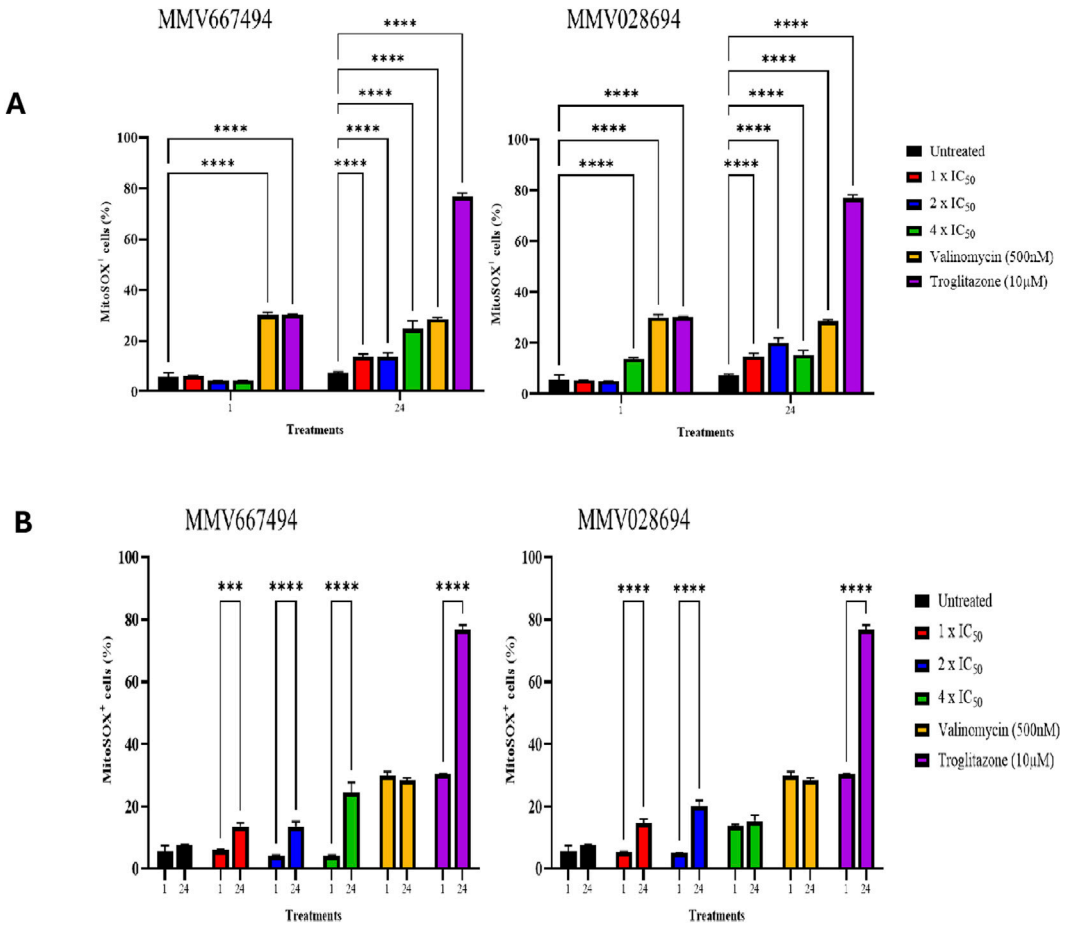

FIGURE 6
Effect of MMV667494 and MMV028694 on mitochondrial reactive oxygen species (mROS) levels in *T. b. brucei*. Mitochondrial superoxide levels were assessed using MitoSOX Red following 1-h and 24-h treatments. **(A)** mROS levels after 1 h of exposure and **(B)** mROS levels after 24 h of exposure. Cells were treated at 1 × IC_{50}, 2 × IC_{50} and 4 × IC_{50}. Data represents the mean mitochondrial superoxide levels for MMV667494-treated and MMV028694-treated trypanosomes stained with MitoSOX dye for three biological replicates. Statistical analysis was performed using repeated-measures two-way ANOVA with Dunnett's multiple comparison test. Error bars indicate standard deviation. Untreated, valinomycin-treated and troglitazone-treated cells served as controls. ***p ≤ 0.001 and ****p ≤ 0.0001. Note: Increases in mROS were modest and time-dependent, suggesting association with downstream cellular stress rather than a primary mechanism of action.

compound-induced cellular effects rather than assigning definitive molecular targets.

Published insights into possible targets for these scaffolds largely come from structural analogues characterized in malaria systems [29]. For MMV667494, quinoline-4-carboxamide analogues have been linked to inhibition of protein synthesis, particularly via interference with *Plasmodium* eEF2-dependent translation elongation [49–51]. Similarly, analogues related to MMV028694 have been associated with inhibition of c-Jun N-terminal kinase (JNK)-related signaling in *P. falciparum* [29]. While these data provide useful hypotheses, direct target equivalence cannot be assumed across parasites, particularly between apicomplexans and kinetoplastids. Therefore, the present study should be interpreted within the context of phenotypic evidence of compound-induced cellular perturbations occurring after treatment with MMV667494 and MMV028694, rather than definitive mechanistic targets.

Both MMV667494 and MMV028694 showed selective toxicity toward *T. b. brucei* relative to the mammalian cell lines tested, supporting their potential utility as starting points for lead optimization. Growth profiling revealed a pattern in which lower exposures primarily reduced proliferation rate. In contrast, higher exposure (4 × IC_{50} over 72 h) produced a net decline in parasite numbers, consistent with cidal activity under the conditions tested. Such transitions from trypanostatic-like growth suppression to trypanocidal outcomes at higher exposure are not uncommon [39] and may well reflect two separate mechanisms of action or, alternatively, inhibition of the same mechanism to a greater and more lethal extent. The markedly increased doubling time during the growth-inhibited phase indicates that even when parasites were not rapidly eliminated, cell-cycle progression and/or completion of cytokinesis was impaired.

The observed parasite death phenotype was apoptosis-like, supported by the increased proportion of Annexin V–positive cells (early and late apoptotic-like populations). In kinetoplastids,

10.3389/ebm.2026.10979

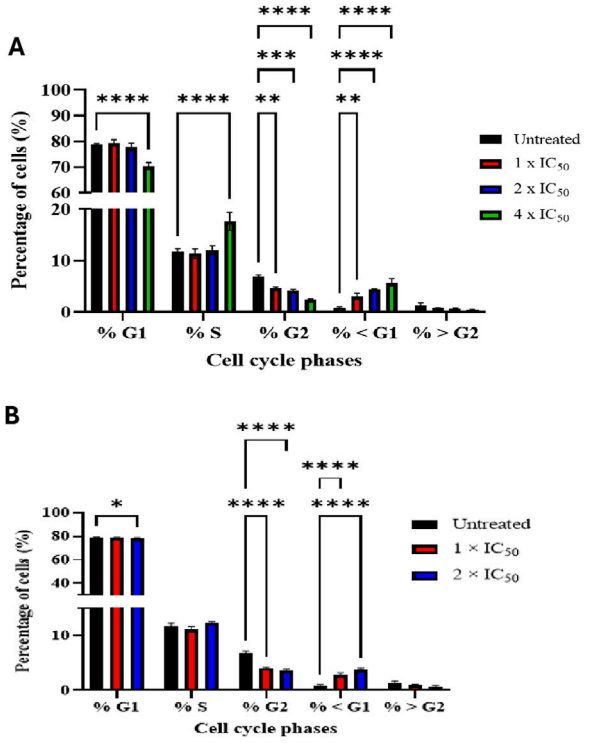

FIGURE 7
Effect of MMV667494 and MMV028694 on cell cycle progression in *T. b. brucei*. Cell cycle distribution was determined by flow cytometry following Hoechst staining for **(A)** MMV667494-treated cells and **(B)** MMV028694-treated cells. Untreated cells served as controls. Data represents mean ± SD from three biological replicates. Statistical analysis was performed using repeated-measures two-way ANOVA with Dunnett's multiple comparison test relative to untreated controls. **p ≤ 0.01, ***p ≤ 0.001, ****p ≤ 0.0001. Note: Increased sub-G1 populations and altered G2/S distributions are consistent with disrupted cell cycle progression rather than a defined cell cycle arrest point.

the term "apoptosis-like" is widely used because these organisms can display apoptosis-associated markers, including phosphatidylserine exposure, despite lacking canonical caspase machinery [40]. A notable feature of our dataset is the alignment between apoptotic-like populations and mitochondrial readouts. At 24 h and 1 × IC_{50}, only a minority of cells showed marked mitochondrial membrane depolarization (TMRE-low), and this minority corresponded conceptually to the subset showing apoptotic-like features. Therefore, given the absence of canonical apoptotic machinery in trypanosomes, these findings should be interpreted cautiously. The pattern observed argues against an interpretation in which ΔΨm collapse is an early, uniform primary event. Instead, mitochondrial depolarization appears enriched in dying cells, consistent with a downstream hallmark of apoptosis-like death rather than a direct universal target effect.

Similarly, both compounds increased mitochondrial ROS (mROS) most clearly at 24 h, whereas global intracellular ROS did not increase in a compound-dependent manner. This distinction suggests that mitochondrial oxidative stress accompanies compound exposure and loss of viability but does not manifest as broad cytosolic oxidative stress and may not be the sole driver of parasite death. The timing also supports a model in which mROS elevation is either downstream of progressive cellular dysfunction, or part of an amplifying death cascade rather than the initiating process.

The most consistent and informative phenotype across assays was cell-cycle disruption, observed in DNA-content profiles and supported by microscopy-based K/N scoring. Both compounds increased sub-G1-like populations and reduced progression into normal G2/M distributions, consistent with impaired completion of a productive division cycle. Errors in the faithful replication of either nuclear or mitochondrial DNA, including the formation of dyskinetoplastic cells or cells with multiple nuclei, are a known trigger for apoptosis [52, 53]. The dataset shows that only a minority of cells displayed irregular kinetoplast/nucleus ratios or other cell cycle aberration–all consistent with the slow effect of the drug on *in vitro* cell growth. However, in choosing the moderate concentration and early exposure time, we believe we have captured the initial cellular events rather than only the late, indirect effects derived from the primary action of the drug on its target.

Overall, this study identified two promising antitrypanosomal compounds, MMV667494 and MMV028694, and characterized their effects on parasite growth and cellular physiology. Rather than defining a single molecular target, our findings indicate that both compounds induce a combination of growth and cell cycle inhibition, and apoptosis-like phenotypes, with mitochondrial perturbations occurring in a subset of affected cells. While MMV667494 and MMV028694 demonstrate promising *in vitro* activity and selectivity, several factors must be considered in evaluating their potential as drug discovery starting points. Both compounds originate from the Pathogen Box, a library curated for favourable drug-like properties, including physicochemical features compatible with oral bioavailability; however, further optimization and detailed pharmacokinetic and ADME profiling will be required to assess their suitability as lead compounds. In addition, the potential for resistance development remains an important consideration, and future studies should evaluate resistance selection and cross-resistance profiles. Importantly, the present study was conducted using *T. b. brucei* as a model organism, and validation against human-infective subspecies (*T. b. gambiense* and *T. b. rhodesiense*) will be necessary. Finally, *in vivo* efficacy, pharmacokinetics, and toxicity studies will be required to determine whether the observed *in vitro* activity translates into therapeutic potential.

Author contributions

PA, NQ, SV, HK, and TG: Conceived and designed the experiments. PA: Performed the experiments. PA, NQ, HK, and TG: Analysed the data. PA, NQ, SV, HK and TG: Wrote the paper. All authors contributed to the article and approved the submitted version.

Data availability

The original contributions presented in the study are included in the article/Supplementary Material, further inquiries can be directed to the corresponding author.

Funding

The author(s) declared that financial support was received for this work and/or its publication. This study was supported by a WACCBIP-Wellcome Trust PhD Fellowship (DEL-15-007: Awandare) and a Tertiary Education Fund of Nigeria (TETFUND) scholarship awarded to PA, and an Academy of Medical Sciences' Global Challenges Research Fund (GCRF) grant that was awarded to TG and SV.

Acknowledgements

We are immensely grateful to Medicine for Malaria Ventures (MMV) for providing the compounds (MMV667494 and MMV028694) used for this study. We are also grateful to John Tetteh (Noguchi Memorial Institute of Medical Research), Henrietta Mensah-Brown (West African Centre for Cell Biology of Infectious Pathogens, University of Ghana) for technical guidance with flow cytometry; Geoff Lambright for technical guidance with confocal microscopy and to Jack Sunter (Oxford Brookes University) for technical guidance and useful discussions.

Conflict of interest

The author(s) declared no potential conflicts of interest with respect to the research, authorship, and/or publication of this article.

Generative AI statement

The author(s) declared that generative AI was not used in the creation of this manuscript.

Any alternative text (alt text) provided alongside figures in this article has been generated by Frontiers with the support of artificial intelligence and reasonable efforts have been made to ensure accuracy, including review by the authors wherever possible. If you identify any issues, please contact us.

Supplementary material

The Supplementary Material for this article can be found online at: https://www.ebm-journal.org/articles/10.3389/ebm.2026.10979/full#supplementary-material

References

1. Brun R, Don R, Jacobs RT, Wang MZ, Barrett MP. Development of novel drugs for human African trypanosomiasis. *Future Microbiol* (2011) 6(6):677–91. doi:10.2217/fmb.11.44

2. Giordani F, Morrison LJ, Rowan TG, Hp DEK, Barrett MP. The animal trypanosomiases and their chemotherapy: a review. *Parasitology* (2016) 143(14):1862–89. doi:10.1017/S0031182016001268

3. Morrison LJ, MacLeod A. African trypanosomiasis. *Parasite Immunol* (2011) 33(8):421–2. doi:10.1111/j.1365-3024.2011.01302.x

4. Brun R, Blum J, Chappuis F, Burri C. Human African trypanosomiasis. *Lancet.* (2010) 375(9709):148–59. doi:10.1016/S0140-6736(09)60829-1

5. Ungogo MA, de Koning HP. Drug resistance in animal trypanosomiases: epidemiology, mechanisms and control strategies. *Int J Parasitol Drugs Drug Resist* (2024) 25:100533. doi:10.1016/j.ijpddr.2024.100533

6. de Koning HP. The drugs of sleeping sickness: their mechanisms of action and resistance, and a brief history. *Trop Med Infect Dis* (2020) 5(1). doi:10.3390/tropicalmed5010014

7. Dickie EA, Giordani F, Gould MK, Maser P, Burri C, Mottram JC, et al. New drugs for human African trypanosomiasis: a twenty first century success story. *Trop Med Infect Dis* (2020) 5(1). doi:10.3390/tropicalmed5010029

8. Ebiloma GU, Alhejeli A, de Koning HP. Interventions for neglected diseases caused by kinetoplastid parasites: a one health approach to drug discovery, development, and deployment. *Pharmaceuticals (Basel)* (2025) 18(9):1415. doi:10.3390/ph18091415

9. Lindner AK, Lejon V, Barrett MP, Blumberg L, Bukachi SA, Chancey RJ, et al. New WHO guidelines for treating *rhodesiense* human African trypanosomiasis: expanded indications for fexinidazole and pentamidine. *Lancet Infect Dis* (2025) 25(2):e77–e85. doi:10.1016/S1473-3099(24)00581-4

10. Tarral A, Hovsepian L, Duvauchelle T, Donazzolo Y, Latreille M, Felices M, et al. Determination of the optimal single dose treatment for acoziborole, a novel drug for the treatment of human African trypanosomiasis: first-in-human study. *Clin Pharmacokinet* (2023) 62(3):481–91. doi:10.1007/s40262-023-01216-8

11. Kaiser M, Bray MA, Cal M, Bourdin Trunz B, Torreele E, Brun R. Antitrypanosomal activity of fexinidazole, a new oral nitroimidazole drug candidate for treatment of sleeping sickness. *Antimicrob Agents Chemother* (2011) 55(12):5602–8. doi:10.1128/AAC.00246-11

12. Maser P, Wittlin S, Rottmann M, Wenzler T, Kaiser M, Brun R. Antiparasitic agents: new drugs on the horizon. *Curr Opin Pharmacol* (2012) 12(5):562–6. doi:10.1016/j.coph.2012.05.001

13. Paine MF, Wang MZ, Generaux CN, Boykin DW, Wilson WD, De Koning HP, et al. Diamidines for human African trypanosomiasis. *Curr Opin Investig Drugs* (2010) 11(8):876–83.

14. Silva Pereira S, Trindade S, De Niz M, Figueiredo LM. Tissue tropism in parasitic diseases. *Open Biol* (2019) 9(5):190036. doi:10.1098/rsob.190036

15. Sokolova AY, Wyllie S, Patterson S, Oza SL, Read KD, Fairlamb AH. Cross-resistance to nitro drugs and implications for treatment of human African trypanosomiasis. *Antimicrob Agents Chemother* (2010) 54(7):2893–900. doi:10.1128/AAC.00332-10

16. Thuita JK, Karanja SM, Wenzler T, Mdachi RE, Ngotho JM, Kagira JM, et al. Efficacy of the diamidine DB75 and its prodrug DB289, against murine models of human African trypanosomiasis. *Acta Trop* (2008) 108(1):6–10. doi:10.1016/j.actatropica.2008.07.006

17. Trindade S, Rijo-Ferreira F, Carvalho T, Pinto-Neves D, Guegan F, Aresta-Branco F, et al. *Trypanosoma brucei* parasites occupy and functionally adapt to the adipose tissue in mice. *Cell Host Microbe* (2016) 19(6):837–48. doi:10.1016/j.chom.2016.05.002

18. Wyllie S, Foth BJ, Kelner A, Sokolova AY, Berriman M, Fairlamb AH. Nitroheterocyclic drug resistance mechanisms in *Trypanosoma brucei*. *J Antimicrob Chemother* (2016) 71(3):625–34. doi:10.1093/jac/dkv376

19. Davison EK, Brimble MA. Natural product derived privileged scaffolds in drug discovery. *Curr Opin Chem Biol* (2019) 52:1–8. doi:10.1016/j.cbpa.2018.12.007

20. Ebiloma GU, Ichoron N, Siheri W, Watson DG, Igoli JO, De Koning HP. The strong anti-kinetoplastid properties of bee propolis: composition and identification of the active agents and their biochemical targets. *Molecules* (2020) 25(21). doi:10.3390/molecules25215155

21. Newman DJ, Cragg GM. Natural products as sources of new drugs from 1981 to 2014. *J Nat Prod* (2016) 79(3):629–61. doi:10.1021/acs.jnatprod.5b01055

22. Newman DJ, Cragg GM. Natural products as sources of new drugs over the nearly four decades from 01/1981 to 09/2019. *J Nat Prod* (2020) 83(3):770–803. doi:10.1021/acs.jnatprod.9b01285

23. Laraia L, Robke L, Waldmann H. Bioactive compound collections: from design to target identification. *Chem* (2018) 4(4):705–30. doi:10.1016/j.chempr.2018.01.012

24. Canever MF, Miletti LC. Screening and identification of pathogen Box(R) compounds with anti-*trypanosoma* evansi activity. *Acta Trop* (2020) 206:105421. doi:10.1016/j.actatropica.2020.105421

25. Kaiser M, Maes L, Tadoori LP, Spangenberg T, Ioset JR. Repurposing of the open access malaria box for kinetoplastid diseases identifies novel active scaffolds against trypanosomatids. *J Biomol Screen* (2015) 20(5):634–45. doi:10.1177/1087057115569155

26. Kipandula W, Young SA, MacNeill SA, Smith TK. Screening of the MMV and GSK open access chemical boxes using a viability assay developed against the kinetoplastid *Crithidia fasciculata*. *Mol Biochem Parasitol* (2018) 222:61–9. doi:10.1016/j.molbiopara.2018.05.001

27. Muller J, Aguado A, Laleu B, Balmer V, Ritler D, Hemphill A. *In vitro* screening of the open source pathogen box identifies novel compounds with profound activities against Neospora caninum. *Int J Parasitol* (2017) 47(12):801–9. doi:10.1016/j.ijpara.2017.06.002

28. Nugraha AB, Tuvshintulga B, Guswanto A, Tayebwa DS, Rizk MA, Gantuya S, et al. Screening the medicines for malaria venture pathogen box against piroplasm parasites. *Int J Parasitol Drugs Drug Resist* (2019) 10:84–90. doi:10.1016/j.ijpddr.2019.06.004

29. Veale CGL. Unpacking the pathogen Box-An open source tool for fighting neglected tropical disease. *ChemMedChem* (2019) 14(4):386–453. doi:10.1002/cmdc.201800755

30. Veale CGL, Hoppe HC. Screening of the pathogen box reveals new starting points for anti-trypanosomal drug discovery. *Medchemcomm* (2018) 9(12):2037–44. doi:10.1039/c8md00319j

31. Akazue PI, Quashie NB, Osei-Safo D, Vaughan S, de Koning HP, Gwira TM. Cytological profiling of trypanocidal principles from Aloe barbadensis and *Taraxacum officinale*. *Phytomed Plus* (2025) 5(2):None. doi:10.1016/j.phyplu.2025.100793

32. Twumasi EB, Akazue PI, Kyeremeh K, Gwira TM, Keiser J, Cho-Ngwa F, et al. Antischistosomal, antionchocercal and antitrypanosomal potentials of some Ghanaian traditional medicines and their constituents. *PLoS Negl Trop Dis* (2020) 14(12):e0008919. doi:10.1371/journal.pntd.0008919

33. de Brito MG, Mengarda AC, Oliveira GL, Cirino ME, Silva TC, de Oliveira RN, et al. Therapeutic effect of diminazene aceturate on parasitic blood fluke *Schistosoma mansoni* infection. *Antimicrob Agents Chemother* (2020) 64(11). doi:10.1128/AAC.01372-20

34. Bharti H, Singal A, Saini M, Cheema PS, Raza M, Kundu S, et al. Repurposing the Pathogen Box compounds for identification of potent anti-malarials against blood stages of *Plasmodium falciparum* with PfUCHL3 inhibitory activity. *Sci Rep* (2022) 12(1):918. doi:10.1038/s41598-021-04619-4

35. Hirumi H, Hirumi K. Axenic culture of African trypanosome bloodstream forms. *Parasitol Today* (1994) 10(2):80–4. doi:10.1016/0169-4758(94)90402-2

36. Raz B, Iten M, Grether-Buhler Y, Kaminsky R, Brun R. The Alamar Blue assay to determine drug sensitivity of African trypanosomes (T.b. rhodesiense and T.b. gambiense) *in vitro*. *Acta Trop* (1997) 68(2):139–47. doi:10.1016/s0001-706x(97)00079-x

37. Denninger V, Figarella K, Schonfeld C, Brems S, Busold C, Lang F, et al. Troglitazone induces differentiation in *Trypanosoma brucei*. *Exp Cell Res* (2007) 313(9):1805–19. doi:10.1016/j.yexcr.2007.03.003

38. Dean S, Sunter J. Light microscopy in trypanosomes: use of fluorescent proteins and tags. *Methods Mol Biol* (2020) 2116:367–83. doi:10.1007/978-1-0716-0294-2_23

39. Rodenko B, van der Burg AM, Wanner MJ, Kaiser M, Brun R, Gould M, et al. 2,N6-disubstituted adenosine analogs with antitrypanosomal and antimalarial activities. *Antimicrob Agents Chemother* (2007) 51(11):3796–802. doi:10.1128/AAC.00425-07

40. Kaczanowski S, Sajid M, Reece SE. Evolution of apoptosis-like programmed cell death in unicellular protozoan parasites. *Parasit Vectors* (2011) 4:44. doi:10.1186/1756-3305-4-44

41. Ibrahim HM, Al-Salabi MI, El Sabbagh N, Quashie NB, Alkhaldi AA, Escale R, et al. Symmetrical choline-derived dications display strong anti-kinetoplastid activity. *J Antimicrob Chemother* (2011) 66(1):111–25. doi:10.1093/jac/dkq401

42. Duffy S, Sykes ML, Jones AJ, Shelper TB, Simpson M, Lang R, et al. Screening the medicines for malaria venture pathogen box across multiple pathogens reclassifies starting points for open-source drug discovery. *Antimicrob Agents Chemother* (2017) 61(9). doi:10.1128/AAC.00379-17

43. Jagu E, Pomel S, Diez-Martinez A, Ramiandrasoa F, Krauth-Siegel RL, Pethe S, et al. Synthesis and *in vitro* antikinetoplastid activity of polyamine-hydroxybenzotriazole conjugates. *Bioorg Med Chem* (2017) 25(1):84–90. doi:10.1016/j.bmc.2016.10.013

44. Nefertiti ASG, Batista MM, Da Silva PB, Batista DGJ, Da Silva CF, Peres RB, et al. *In vitro* and *in vivo* studies of the trypanocidal effect of novel quinolines. *Antimicrob Agents Chemother* (2018) 62(2). doi:10.1128/AAC.01936-17

45. Samant BS, Nyangari N. A novel microwave synthesis of quinoline-3-carboxylic acid derivatives for treatment against human African trypanosomiasis. *Mol Divers* (2012) 16(4):685–95. doi:10.1007/s11030-012-9401-2

46. Ugwu DI, Okoro UC, Mishra NK. Synthesis, characterization and *in vitro* antitrypanosomal activities of new carboxamides bearing quinoline moiety. *PLoS One* (2018) 13(1):e0191234. doi:10.1371/journal.pone.0191234

47. Errington TM, Iorns E, Gunn W, Tan FE, Lomax J, Nosek BA. An open investigation of the reproducibility of cancer biology research. *Elife* (2014) 3. doi:10.7554/eLife.04333

48. Hafner M, Niepel M, Chung M, Sorger PK. Growth rate inhibition metrics correct for confounders in measuring sensitivity to cancer drugs. *Nat Methods* (2016) 13(6):521–7. doi:10.1038/nmeth.3853

49. Baragana B, Hallyburton I, Lee MC, Norcross NR, Grimaldi R, Otto TD, et al. A novel multiple-stage antimalarial agent that inhibits protein synthesis. *Nature* (2015) 522(7556):315–20. doi:10.1038/nature14451

50. Baragana B, Norcross NR, Wilson C, Porzelle A, Hallyburton I, Grimaldi R, et al. Discovery of a Quinoline-4-carboxamide derivative with a novel mechanism of action, multistage antimalarial activity, and potent *in vivo* efficacy. *J Med Chem* (2016) 59(21):9672–85. doi:10.1021/acs.jmedchem.6b00723

51. Hallyburton I, Grimaldi R, Woodland A, Baragana B, Luksch T, Spinks D, et al. Screening a protein kinase inhibitor library against *Plasmodium falciparum*. *Malar J* (2017) 16(1):446. doi:10.1186/s12936-017-2085-4

52. Mignotte B, Vayssiere JL. Mitochondria and apoptosis. *Eur J Biochem* (1998) 252(1):1–15. doi:10.1046/j.1432-1327.1998.2520001.x

53. Rong Z, Tu P, Xu P, Sun Y, Yu F, Tu N, et al. The mitochondrial response to DNA damage. *Front Cell Dev Biol* (2021) 9:669379. doi:10.3389/fcell.2021.669379

EBM Experimental Biology and Medicine

TYPE Original Research
PUBLISHED 13 May 2026
DOI 10.3389/ebm.2026.10987

OPEN ACCESS

*CORRESPONDENCE
Hui Dong,
huidong@hebmu.edu.cn
Yaling Liu,
yalingliu@hebmu.edu.cn

RECEIVED 15 January 2026
REVISED 31 March 2026
ACCEPTED 22 April 2026
PUBLISHED 13 May 2026

CITATION
Yang X, Yang J, Li R, Dong H and Liu Y (2026) Peripheral immune cells and glycation indices as potential diagnostic biomarkers in amyotrophic lateral sclerosis.
Exp. Biol. Med. 251:10987.
doi: 10.3389/ebm.2026.10987

Peripheral immune cells and glycation indices as potential diagnostic biomarkers in amyotrophic lateral sclerosis

Xue Yang[1,2,3], Jing Yang[2,4,5], Rui Li[2,4,5], Hui Dong[2,4,5]* and Yaling Liu[2,4,5]*

[1]Department of Neurology, Hebei Medical University, Shijiazhuang, Hebei, China, [2]Department of Neurology, The Second Hospital of Hebei Medical University, Shijiazhuang, China, [3]Department of Neurology, Affiliated Hospital of Hebei Engineering University, Handan, China, [4]Key Laboratory of Clinical Neurology, Ministry of Education, Hebei Medical University, Shijiazhuang, China, [5]Neurological Laboratory of Hebei Province, Shijiazhuang, China

Abstract

The diagnosis of amyotrophic lateral sclerosis (ALS) mainly relies on clinical symptoms and the exclusion of other diseases, with a lack of specific biomarkers, leading to delayed diagnosis and a high rate of misdiagnosis. This study aims to explore the utility of peripheral immune cells and glycosylation indices as potential diagnostic biomarkers for ALS to enhance the accuracy and efficiency of early ALS diagnosis. This retrospective study included 54 ALS patients diagnosed in our hospital from June 2023 to October 2024, along with 54 healthy controls. Blood samples and laboratory data, including levels of peripheral immune cells and glycosylation indices, were collected from both groups. Through logistic regression, random forest models, receiver operating characteristic (ROC) curve analysis, and SHAP interpretability analysis, the predictive abilities and clinical significance of each candidate indicator were screened and evaluated. Notable disparities were detected in age, leukocyte count, monocyte levels, glycated haemoglobin A1c (HbA1c), and haemoglobin glycation index (HGI) between the control and ALS groups (all $P < 0.05$). Logistic regression analysis revealed that age (OR = 1.114) and monocyte (OR = 3.174) were risk factors for ALS, while leukocyte (OR = 0.533) and HbA1c (OR = 0.069) were protective factors. The random forest algorithm, ranked by decreasing importance, showed that leukocyte, HGI, monocyte, and HbA1c level all influenced ALS. Using these indicators to predict ALS resulted in a false-positive rate of 18% and a false-negative rate of 6%. ROC curve analysis indicated that the combined use of leukocyte, monocyte, HbA1c level, and HGI provided the highest diagnostic value for ALS (AUC = 0.774), which was higher than that of any individual indicator (all $P < 0.05$). SHAP analysis visualization demonstrated that increased monocyte and decreased leukocyte, HGI, and HbA1c level were all associated with an increased risk of ALS onset, ranked in descending order of feature importance as monocyte, leukocyte, HGI, and HbA1c. Peripheral blood white blood cells, monocytes, HbA1c, and HGI can serve as potential diagnostic biomarkers for ALS. Combined detection can improve the diagnostic accuracy of ALS, facilitating early diagnosis and

intervention, and ultimately improving patient prognosis. Further validation in cohorts including disease controls is required to confirm specificity.

KEYWORDS
amyotrophic lateral sclerosis, biomarkers, glycated haemoglobin A1c, glycosylation index, leukocyte

Impact statement

The diagnosis of ALS is notoriously delayed due to the lack of specific biomarkers, often relying on clinical exclusion. This study demonstrates that readily available peripheral blood markers (leukocyte and monocyte counts, HbA1c, and HGI) hold significant diagnostic value. The combined use of these indicators, reflecting both inflammatory and metabolic pathways implicated in ALS, provides a practical and minimally invasive approach to improve diagnostic accuracy. This biomarker panel could facilitate earlier identification of ALS in clinical practice, enabling timely intervention and potentially improving patient management and prognosis.

Introduction

Amyotrophic lateral sclerosis (ALS) is a progressive neurodegenerative disease characterized by the degeneration of both upper and lower motor neurons in the brain and spinal cord [1]. Current estimates indicate an annual incidence rate of approximately 2 per 100,000 people and a prevalence of 6–9 per 100,000 [2]. In China, the annual incidence and prevalence rates are approximately (1.33–2.01) per 100,000 people and (2.31–3.58) per 100,000 people, respectively [3]. ALS typically strikes between the ages of 60 and 79 and is invariably fatal [4]. ALS is characterized by progressive muscle weakness and atrophy of the trunk, limbs, pharyngeal muscles, and respiratory muscles, with high disability and mortality rates [5]. Despite continuous in-depth research on ALS in recent years, its exact etiology and pathogenesis remain incompletely understood, and there is currently a lack of effective treatment methods [6]. The diagnosis of ALS primarily relies on clinical manifestations, electrophysiological examinations (such as electromyography), and imaging examinations. However, these methods have certain limitations [7]. The non-specificity of clinical manifestations and their similarity to other neuromuscular diseases make the diagnosis of ALS often challenging, resulting in high rates of diagnostic delay and misdiagnosis [8]. Although electrophysiological and imaging examinations are helpful for diagnosis, they do not provide specific biomarkers for the early identification of ALS [9]. Therefore, the search for biomarkers with high specificity and sensitivity is of great significance for the early diagnosis and disease monitoring of ALS.

The pathogenesis of ALS remains unclear, with neuroinflammation being recognized as a significant contributor to disease progression, in which the peripheral immune system plays a crucial role [10]. Subsets of innate immune cells, including monocytes/macrophages, natural killer cells, mast cells, dendritic cells, and neutrophils, are all implicated in the pathogenesis of ALS [11]. Previous studies have demonstrated that ALS patients with a higher neutrophil-to-lymphocyte ratio have a shorter survival time, and monocytes are associated with inflammatory responses [12]. Clinical indicators of glucose metabolism are significantly correlated with ALS progression. Research shows that ALS patients exhibit altered serum IgG glycosylation, characterized by high sialylation and low core fucosylation. A specific glycan, A2BG2, enhances antibody-dependent cellular cytotoxicity by increasing IgG's affinity for CD16 on effector cells, suggesting its potential role as a biomarker in neuronal damage [13]. Furthermore, a prospective cohort study suggested that a diet higher in glycemic index and load may slow ALS progression [14]. Therefore, peripheral immune cell counts and glycosylation indices may serve as potential diagnostic biomarkers for ALS.

It is noteworthy that when analyzing the combined diagnostic value of multiple indicators, traditional statistical methods are often constrained by the assumption of linear relationships, making it difficult to capture the complex interactions among indicators. Moreover, they have stringent requirements for data distribution and are prone to model misspecification bias when handling non-linear, high-dimensional data commonly encountered in clinical settings. In contrast, machine learning prediction models demonstrate greater flexibility and adaptability. Random forest, as an ensemble learning method, effectively captures non-linear associations and interaction effects among variables by constructing multiple decision trees and integrating their predictive results. It does not require pre-specified data distribution forms, making it better suited to the complex characteristics of clinical data [15]. Additionally, through Bootstrap resampling and random feature selection, random forest reduces the risk of overfitting to a certain extent and enhances model stability in scenarios with limited sample sizes. However, its generalization ability still needs to be evaluated through cross-validation and external validation [16]. Further integration with SHAP interpretability analysis enables the quantification of the contribution of each candidate indicator to the prediction results at the model level and visually displays the direction and strength of its association with the risk of ALS onset. This not only facilitates the screening of potential key biomarkers but also enhances the transparency of the model's predictive logic, making it easier for clinical researchers to understand and validate. It provides support for the clinical translation and application of the model.

This study aims to explore the potential of peripheral immune cells and glycosylation indices as potential diagnostic biomarkers for ALS through retrospective analysis. To screen valuable biomarkers for ALS diagnosis, this study included 54 confirmed ALS patients and 54 healthy controls. It analyzed peripheral immune cell counts and glycosylation index levels and comprehensively evaluated the predictive ability and clinical significance of each indicator by integrating logistic regression, random forest models, receiver operating characteristic (ROC) curves, and SHAP interpretability analysis. The objective of this study is to provide new ideas and

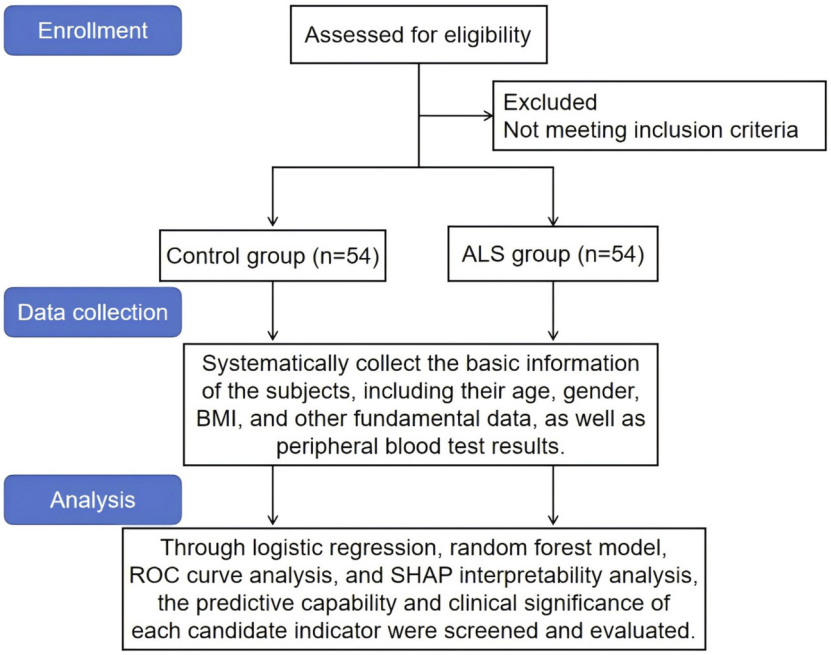

FIGURE 1
Research flowchart.

methods for the early diagnosis of ALS, improve the diagnostic accuracy and early identification ability of ALS, thereby improving patient prognosis.

Materials and methods

Study subjects

This study was a retrospective clinical controlled study. A total of 54 ALS patients diagnosed in our hospital from June 2023 to October 2024, along with 54 healthy controls, were included. Blood samples and laboratory data, including peripheral immune cell counts and glycosylation index levels, were collected from subjects in both groups. To screen valuable biomarkers for ALS diagnosis, this study comprehensively evaluated the predictive ability and clinical significance of each candidate indicator by integrating logistic regression, random forest models, ROC curves, and SHAP interpretability analysis. The detailed research process is shown in Figure 1.

Inclusion criteria

ALS Group: (1) All patients were diagnosed according to the revised El Escorial criteria (Airlie House criteria), which remain the gold standard for ALS diagnosis [17]. Diagnosis was confirmed through a combination of clinical neurological examination, electromyography (EMG), neuroimaging (MRI of the cervical spine and brain), and comprehensive laboratory tests to exclude ALS-mimicking conditions. Genetic testing was not routinely performed in this cohort; thus, patients were not classified as familial or sporadic. (2) Aged 18 years or older; (3) Newly diagnosed cases; (4) Having complete and accessible peripheral blood test data; (5) Not having received riluzole or edaravone treatment; (6) Not having used corticosteroids or anti-inflammatory drugs.

Healthy Control Group: (1) Healthy individuals with gender matching to the ALS patient group and assessed as having no neurological diseases; (2) Aged 18 years or older; (3) Having complete and accessible peripheral blood test data.

Exclusion criteria

(1) Coexisting with other neurological diseases, such as Parkinson's disease or multiple sclerosis; (2) Coexisting with severe metabolic diseases, such as diabetes or thyroid dysfunction; (3) Having used immunomodulatory drugs or glucocorticoids within the past 3 months; (4) Having severe infectious diseases, such as active tuberculosis or HIV infection; (5) Having severe liver or kidney dysfunction.

Sample size calculation

Sample-size estimation was performed using Rosner's method [18] and G*Power software. Based on a two-sample t-test comparing biomarker levels between groups, with an effect size (Cohen's d) of 0.8, two-tailed $\alpha = 0.05$, and power = 0.95, a minimum of 42 subjects per group was required. A total of 54 participants per group were ultimately enrolled, exceeding this requirement.

Data collection

The collected data included basic demographic details such as age, gender of the participants, along with peripheral blood test

TABLE 1 Baseline data of the study participants.

Variables	Control group (n = 54)	ALS group (n = 54)	$t/\chi^2/Z$	*P*
Age [year, M (Q1, Q3)]	56.50 (46.00, 64.00)	63.00 (57.75, 68.25)	−3.232	0.001
Male [n (%)]	34 (62.96%)	36 (66.67%)	0.162	0.687
Hypertension [n (%)]	27 (50.00%)	27 (50.00%)	0.000	1.000
Leukocyte ($\times10^9$/L, mean ± SD)	5.86 ± 1.51	5.31 ± 1.14	−2.165	0.033
Neutrophil [$\times10^9$/L, M (Q1, Q3)]	3.37 (2.78, 4.00)	3.10 (2.41, 3.80)	−1.782	0.075
Eosinophil [$\times10^9$/L, M (Q1, Q3)]	0.12 (0.07, 0.18)	0.11 (0.07, 0.19)	−0.348	0.728
Basophil [$\times10^9$/L, M (Q1, Q3)]	0.03 (0.02, 0.05)	0.03 (0.02, 0.04)	−1.391	0.164
Monocyte ($\times10^9$/L, mean ± SD)	0.36 ± 0.07	0.39 ± 0.08	2.114	0.037
Lymphocyte ($\times10^9$/L, mean ± SD)	1.78 ± 0.55	1.68 ± 0.49	−1.028	0.306
HbA1c [%, M (Q1, Q3)]	5.80 (5.60, 6.10)	5.60 (5.38, 6.00)	−2.873	0.004
FPG [mmol/L, M (Q1, Q3)]	4.94 (4.72, 5.51)	5.05 (4.54, 5.35)	−0.578	0.563
HGI (mean ± SD)	−1.24 ± 0.34	−1.44 ± 0.47	−2.516	0.014

ALS, Amyotrophic lateral sclerosis; HbA1c, glycated haemoglobin A1c; FPG, fasting plasma glucose; HGI, haemoglobin glycation index. The same below.

results. Age is defined as the participant's age at the time of blood sample collection. Blood Collection Procedure: Participants were instructed to fast overnight for 8 h. Between 6:00 and 7:00 AM, venous blood samples were collected from the elbow using sterile K2EDTA anticoagulant blood collection tubes (Hebei Xinle Medical Apparatus & Instruments Co., Ltd.). Subsequently, the blood samples were analyzed in the laboratory using an automated hematology analyzer (Unicel DxH800 Coulter Cellular Analysis System; Beckman Coulter, Inc.). The analyzed parameters included white blood cells, neutrophils, eosinophils, basophils, monocytes, lymphocytes, glycated haemoglobin A1c (HbA1c), fasting plasma glucose (FPG), and the haemoglobin glycation index (HGI). HGI is an indicator used to evaluate inter-individual differences in HbA1c levels, reflecting variations in the degree of hemoglobin glycation at a given blood glucose level. HGI is calculated by subtracting the predicted HbA1c value, derived from the average blood glucose (AG) level, from the laboratory-measured HbA1c value, using the formula: HGI = observed HbA1c – predicted HbA1c.

Statistical analysis

Statistical analyses were performed using SPSS 25.0 and R 4.4.0. Continuous variables were tested for normality using the Shapiro-Wilk test. Variables following a normal distribution are reported as mean ± standard deviation (SD) and compared using the t-test; non-normally distributed variables are reported as median (M) with interquartile ranges (Q1, Q3) and compared using the Mann-Whitney U test. Categorical data are expressed as n (%) and evaluated with χ^2 test. Spearman correlation analysis was used to evaluate the potential impact of age on biomarker levels. Logistic regression identified ALS-associated factors, and ROC curves assessed predictor performance. The AUC and its 95% confidence interval were calculated using the DeLong method. Random-forest and SHAP analyses supplemented these findings. The random forest model was built with 500 trees, and the number of variables randomly sampled at each split was set to the square root of the total number of predictors. Given the exploratory nature of this study and the testing of multiple biomarkers, we did not apply a correction for multiple comparisons to avoid an increased risk of type II errors and to prioritize the identification of potential signals for hypothesis generation. However, we acknowledge this as a methodological limitation, and the findings should be interpreted with caution. Significance was set at $P < 0.05$.

TABLE 2 Spearman correlation analysis.

Age	Leukocyte	Monocyte	HbA1c	HGI
r	−0.003	0.234	0.327	0.263
P	0.972	0.015	0.001	0.006

Results

Comparison of clinical data between the two groups

Table 1 compares the basic demographic information and peripheral blood test data of the participants in the two groups. The results revealed significant differences between the two groups in terms of age ($Z = -3.232$, $P = 0.001$), leukocyte ($t = -2.165$, $P = 0.033$), monocyte ($t = 2.114$, $P = 0.037$), HbA1c level ($t = -2.873$, $P = 0.004$), and HGI ($t = -2.516$, $P = 0.014$).

Spearman correlation analysis

To assess the potential influence of age on biomarker levels, Spearman correlation analysis was performed. As summarized in Table 2, age showed statistically significant positive correlations with monocyte count ($r = 0.234$, $P = 0.015$), HbA1c level ($r = 0.327$, $P = 0.001$), and HGI ($r = 0.263$, $P = 0.006$). In contrast, no significant

TABLE 3 Logistic regression exploration of ALS-related influences.

Variables	β	SE	Wald	*P*	OR (95% CI)
Age	0.108	0.029	13.495	<0.001	1.114 (1.052–1.180)
Leukocyte	−0.630	0.249	6.412	0.011	0.533 (0.327–0.867)
Monocyte	1.155	0.409	7.974	0.005	3.174 (1.424–7.076)
HbA1c	−2.675	1.070	6.252	0.012	0.069 (0.008–0.561)
HGI	−0.287	1.058	0.073	0.786	0.751 (0.094–5.974)

OR, odds ratio; CI: Confidence Interval. The same below.

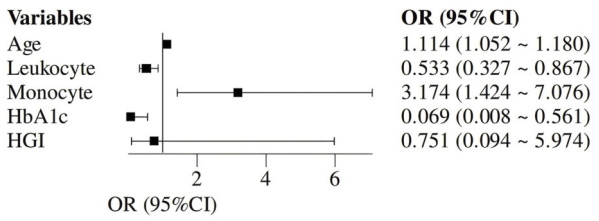

FIGURE 2
Distribution of OR Values and 1 in the Logistic regression analysis of factors influencing ALS.

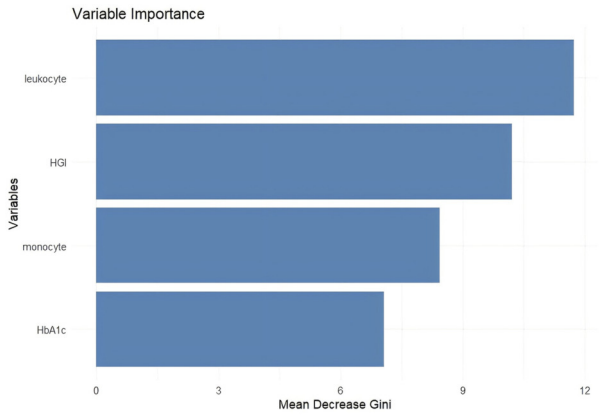

FIGURE 3
Significance ranking of factors influencing ALS in the random forest prediction model. Note: The random forest model was trained using peripheral blood and glycation biomarkers (leukocyte, monocyte, HbA1c, and HGI) as predictors. Variable importance was assessed using the mean decrease in accuracy (MDA), which quantifies the reduction in model accuracy when each variable is permuted. Higher MDA values indicate greater predictive importance. The x-axis shows the mean decrease in accuracy, and the y-axis lists the predictor variables in descending order of importance. Leukocyte count ranked highest, followed by HGI, monocyte, and HbA1c level.

correlation was observed between age and leukocyte count (r = −0.003, P = 0.972). These findings indicate that older age is associated with higher levels of monocytes, HbA1c, and HGI in the study population. However, leukocyte count appears to be independent of age in this cohort.

Logistic regression exploration of ALS-related influences

Logistic regression analysis was conducted with age, leukocyte, monocyte, HbA1c, and HGI as independent variables, and ALS diagnosis as the dependent variable. The results demonstrated that age (OR = 1.114, 95% CI: 1.052–1.180, P < 0.001), leukocyte (OR = 0.533, 95% CI: 0.327–0.867, P = 0.011), monocyte (OR = 3.174, 95% CI: 1.424–7.076, P = 0.005), and HbA1c level (OR = 0.069, 95% CI: 0.008–0.561, P = 0.012) were significant factors influencing ALS. However, the logistic regression model included both HbA1c and HGI, which are mathematically related, potentially leading to multicollinearity and unstable estimates; the extremely low odds ratio for HbA1c with a wide confidence interval (0.008–0.561) suggests this finding should be interpreted with caution. See Table 3 and Figure 2.

Construction of a random forest model

The random forest algorithm was employed to rank the factors in Table 2 based on their controllability. The random forest model was trained using the full dataset, and predictive performance was evaluated using out-of-bag (OOB) predictions to minimize overfitting. Age was not included in the random forest model to focus the analysis on the diagnostic potential of the peripheral blood and glycation biomarkers. The results indicated that, in descending order of importance, leukocyte count, HGI, monocyte, and HbA1c level all had an impact on ALS (Figure 3). When using these indicators to predict ALS, the false-positive rate was 18%, and the false-negative rate was 6% (Figure 4).

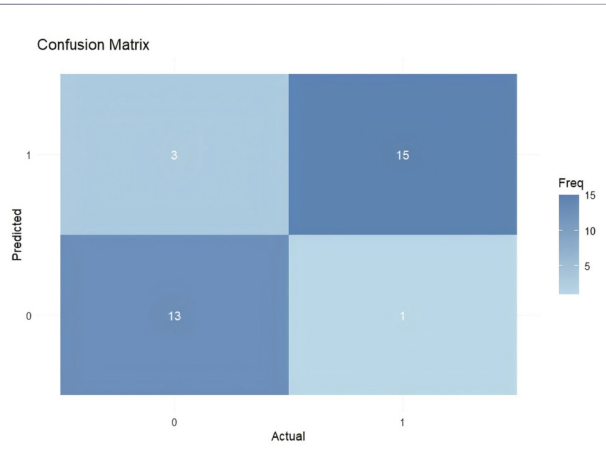

FIGURE 4
Confusion matrix of prediction accuracy in the random forest prediction model for ALS. Note: Predictions were generated using out-of-bag (OOB) samples to reduce overfitting. The matrix displays the number of correctly and incorrectly classified cases based on the random forest model. The x-axis represents the predicted classification (0: healthy control, 1: ALS), and the y-axis represents the actual classification (0: healthy control, 1: ALS). The color intensity corresponds to the frequency count, as indicated by the color bar.

TABLE 4 ROC curve analysis of the prediction model for factors influencing ALS.

Indicator	AUC	95% CI	Sensitivity	Specificity	Best cut-off value	*Z*	*P*
Leukocyte	0.602	0.504–0.695	48.15	72.22	≤5.15	1.865	0.062
Monocyte	0.592	0.493–0.686	61.11	62.96	>0.37	1.678	0.093
HbA1c	0.660	0.562–0.748	55.56	74.07	≤5.60	3.033	0.002
HGI	0.619	0.521–0.711	38.89	88.89	≤-1.58	2.168	0.030
Joint application	0.774	0.683–0.849	79.63	70.37		6.018	<0.001

The "joint application" refers to a combined logistic regression model incorporating leukocyte, monocyte, HbA1c, and HGI as predictors.

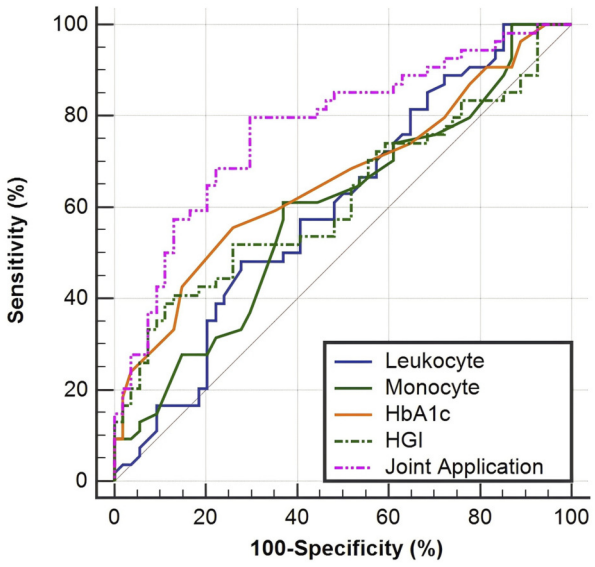

FIGURE 5
ROC curve of the prediction model for factors influencing ALS.

Construction of the ROC model

This study evaluated the predictive efficacy of four individual indicators—leukocytes, monocytes, HbA1c, and HGI—as well as their joint application for ALS through ROC curve analysis. As shown in Table 4 and Figure 5, among the individual indicators, HbA1c demonstrated an AUC of 0.660 (95% CI: 0.562–0.748), and HGI showed an AUC of 0.619 (95% CI: 0.521–0.711) ($P < 0.05$). The joint application of these indicators exhibited the highest diagnostic value, with an AUC of 0.774 (95% CI: 0.683–0.849), a sensitivity of 79.63%, and a specificity of 70.37%. Table 5 shows, via pairwise comparisons, that the joint application AUC significantly exceeded that of every single indicator (all $P < 0.05$), indicating that combining multiple indicators can significantly enhance the differential diagnostic capability for ALS.

Construction of the SHAP model

The SHAP analysis method was employed to visually interpret the selected variables and illustrate their contributions to the model's identification results. Figure 6 displays the four feature variables included in the model: monocyte, leukocyte count, HGI, and HbA1c. A dot plot shows each variable's contribution to the prediction, with yellow and purple dots indicating high- and low-risk values, respectively.

The analysis reveals that an elevation in monocyte, along with reductions in leukocyte count, HGI, and HbA1c levels, is associated with an increased risk of ALS onset. The bar chart ranks risk factors by their mean absolute SHAP values. The horizontal axis represents the SHAP values, where positive values enhance the probability of identification, whereas negative values decrease it. The vertical axis reflects the relative importance of each feature in the predictive model, with variables positioned higher being more important and those lower being less important. The results show that, in descending order of importance, the variables are: monocyte, leukocyte count, HGI, and HbA1c.

Discussion

Evidence indicates that patients typically wait 12–18 months from first symptoms to a confirmed ALS diagnosis [19]. Diagnostic delays often result in patients missing the optimal window for early intervention, further exacerbating irreversible motor function

TABLE 5 Pairwise comparison of ROC curves.

Comparison	Difference between areas	95% CI	*Z*	*P*
Leukocyte~joint application	0.171	0.054–0.289	2.864	0.004
Monocyte~joint application	0.181	0.069–0.294	3.159	0.002
HbA1c~joint application	0.114	0.019–0.209	2.345	0.019
HGI~joint application	0.155	0.045–0.264	2.769	0.006

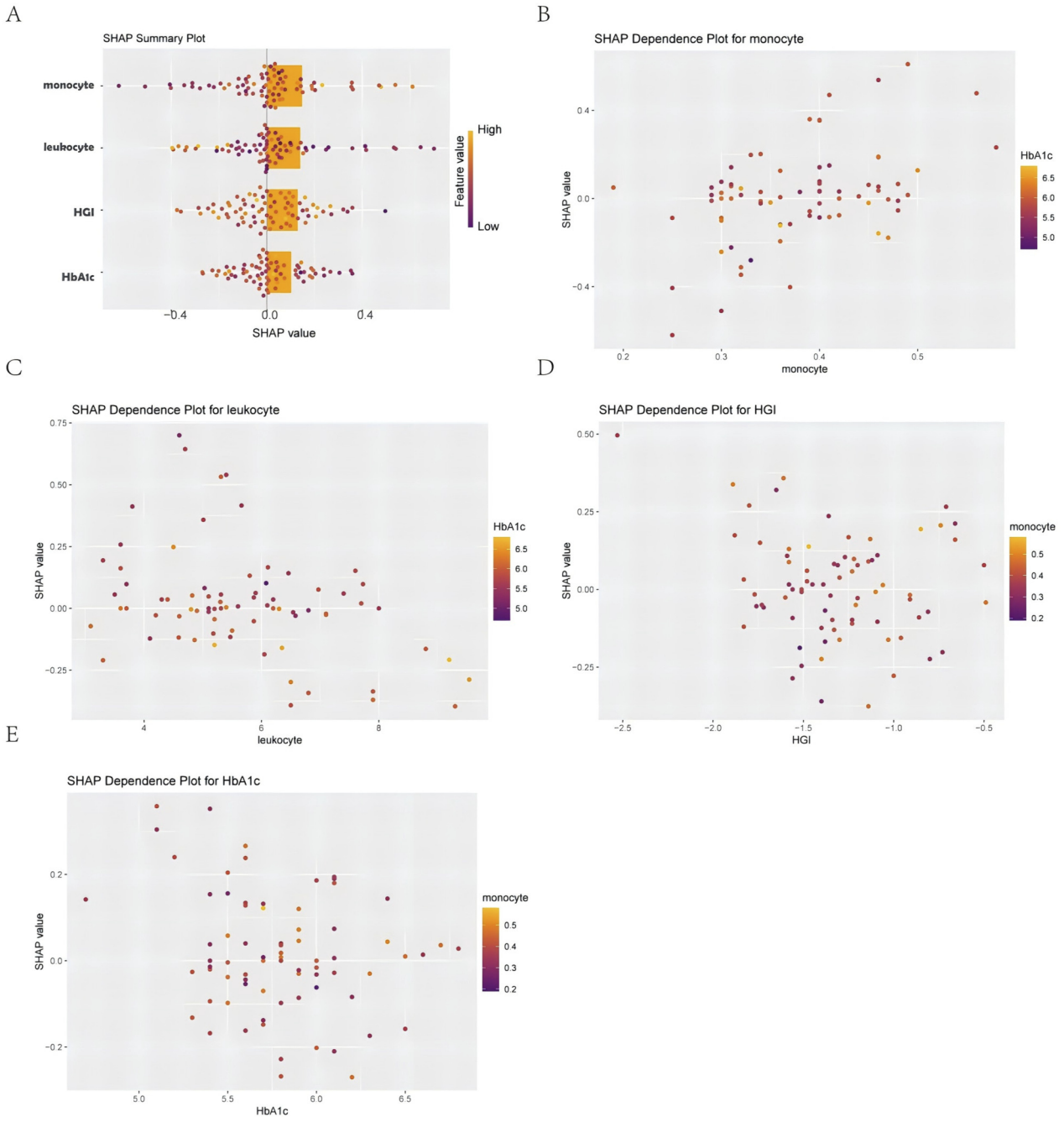

FIGURE 6
(A) SHAP summary plot for monocyte, leukocyte, HGI, and HbA1c. **(B)** SHAP dependence plot for monocyte. **(C)** SHAP dependence plot for leukocyte. **(D)** SHAP dependence plot for HGI. **(E)** SHAP dependence plot for HbA1c.

impairment and significantly reducing both quality of life and survival duration. Therefore, identifying potential diagnostic biomarkers with high specificity and sensitivity, as well as establishing an efficient early diagnostic system, has emerged as one of the core research priorities in the field of ALS. This study focused on peripheral immune cells and glycosylation indices, systematically exploring their diagnostic value in ALS through multidimensional statistical analyses and model validations.

Initially, baseline data comparisons revealed significant statistical differences between the ALS and control group in terms of age, leukocyte count, monocyte, HbA1c level, and HGI. Regarding age, logistic regression analysis demonstrated that age was a risk factor for ALS (OR = 1.114, $P < 0.001$), indicating that for each additional year of age, the risk of developing ALS increased by approximately 11.4%. This finding aligns with the conclusions of most previous epidemiological studies, which have shown a clear upward trend in ALS incidence with advancing age, peaking

particularly in the 50–70 age group [20–22]. The potential underlying reasons include the gradual decline of neuroprotective mechanisms, elevated oxidative stress levels, disrupted protein homeostasis, and reduced repair capacity of nerve cells with aging, all of which increase the vulnerability of neurons to damage and thereby raise the risk of neurodegenerative diseases [23]. These results also suggest that in clinical practice, when older people present with unexplained muscle weakness, atrophy, or other symptoms, a high index of suspicion for ALS is warranted, and of proceeding with targeted testing to confirm it.

This study found a significantly higher monocyte in the ALS group compared to healthy controls, and logistic regression revealed it as a risk factor for the disease. While previous research has implicated neuroinflammation in ALS pathogenesis [24], our findings are limited to demonstrating a statistical association between elevated peripheral monocyte counts and ALS. The biological mechanisms underlying this association remain to be elucidated and cannot be directly inferred from the current data. In contrast to monocytes, we observed that leukocytes were notably diminished in ALS patients relative to healthy individuals and were identified as a protective factor. We acknowledge that this finding differs from some previous studies, some of which have reported normal or elevated leukocyte counts in ALS patients [25, 26]. Rather than speculating on the reasons for these discrepancies, we emphasize that they may be attributable to differences in sample size, disease stage, clinical heterogeneity, or population characteristics across studies. In the present cohort, no significant differences were observed in neutrophil or lymphocyte counts between the two groups, suggesting that the NLR—a well-established prognostic marker in ALS—also did not differ. This observation further indicates that the lower total leukocyte count in our ALS group was not driven by meaningful shifts in these key immune subsets. Taken together, these findings highlight the need for future studies with larger, well-phenotyped cohorts and standardized protocols to clarify the role of peripheral immune cell profiles in ALS.

ALS is not only a neurodegenerative disease but also accompanied by significant systemic metabolic disturbances, among which glucose metabolic disorders represent a crucial manifestation. Both HbA1c levels and the HGI were significantly lower in the ALS group, but only HbA1c was identified as a protective factor for ALS via logistic regression. However, the random forest prediction model identified HGI as the second most important predictor of ALS, second only to leukocyte count. This discrepancy in assessing the importance of HGI may stem from differences in the underlying assumptions of the two models: unlike logistic regression, which assumes linearity, random forest captures nonlinear relationships and complex interactions among variables. We hypothesize that HbA1c and HGI may jointly participate in ALS pathogenesis through linear and nonlinear mechanisms, respectively. The association between decreased levels of HbA1c and HGI and an increased risk of ALS onset resonates with recent research on the metabolic mechanisms of ALS, suggesting that glucose metabolic disturbances may contribute to the pathological processes of ALS through multiple pathways.

A nationwide Danish study found a protective association between type 2 diabetes and ALS [27]. This was supported by a large case-control study, which found a significant inverse correlation specifically for non-insulin-dependent diabetes implying a potential ALS-protective effect [28]. Furthermore, multiple studies have confirmed that elevated blood glucose levels may delay the onset of ALS in diabetic patients [29–32]. Our findings corroborate those earlier observations, as HbA1c and HGI demonstrated significant predictive value in the models, indicating that decreased levels of these indicators might signal a higher chance of ALS occurrence. This could be because ALS patients often exhibit a hypermetabolic state, and hyperglycemia or diabetes may, to some extent, alleviate the neuronal energy crisis by providing more abundant energy substrates, thereby delaying disease onset [33]. Additionally, under hyperglycemic conditions, cells may activate the Nrf2 pathway, a key transcription factor regulating antioxidant stress responses. Activation of Nrf2 can reduce oxidative stress damage, which is an important mechanism underlying ALS pathogenesis [34]. It is important to note that not all forms of hyperglycemia are protective; for instance, the autoimmune form is instead linked to a higher ALS risk, suggesting that the presence of insulin may be a critical factor. Furthermore, although hyperglycemia may delay the onset of ALS, diabetic patients may experience faster disease progression and poorer prognosis after ALS diagnosis [35].

ROC curve analysis is a crucial method for evaluating the diagnostic performance of biomarkers. In this study, ROC curve analyses of both individual and combined indicators were conducted to clarify the diagnostic value of each indicator. Among the individual indicators, HbA1c demonstrated the highest diagnostic efficacy, followed by HGI, while the diagnostic efficacy of leukocyte count and monocyte was relatively low. Given that a single biomarker often struggles to comprehensively reflect the pathological processes of complex diseases, combining multiple indicators with distinct biological significances typically enhances diagnostic accuracy. The findings of this study corroborate this notion, as the combined diagnosis using four indicators—leukocytes, monocytes, HbA1c, and HGI—achieved an AUC of 0.774, with 79.63% sensitivity and 70.37% specificity. The combined detection integrates information on both immune inflammation and metabolic disturbances, providing a more comprehensive reflection of the pathological state of ALS and thereby improving diagnostic accuracy. The indicators involved in the combined detection are all peripheral blood tests, which offer advantages such as convenient sampling, minimal invasiveness, and low detection costs, facilitating their clinical application, particularly in primary hospitals and large-scale screening programs, and providing a feasible technical solution for the early diagnosis of ALS.

To comprehensively evaluate the impact of each candidate indicator on ALS diagnosis, this study also employed the random forest model and SHAP interpretability analysis, reinforcing the credibility of the outcomes. The random forest algorithm, through ensemble learning of multiple decision trees, effectively handles interactions among variables and assesses the importance of each indicator. The results showed that, in descending order of importance, leukocyte count, HGI, monocyte, and HbA1c level all influenced ALS diagnosis, which was largely consistent with the findings from logistic regression analysis and ROC curve analysis,

further confirming the significant role of these indicators in ALS diagnosis. Meanwhile, the random forest model exhibited good predictive performance with low false-positive and false-negative rates, indicating its strong potential for clinical application as an auxiliary diagnostic tool for ALS. SHAP analysis, as an interpretability method based on game theory, gauges each variable's effect on the model's predictive performance and visually displays the relationship between each indicator and disease risk through charts. The SHAP analysis results in this study revealed that elevated monocyte and decreased leukocyte count, HGI, and HbA1c level were all associated with ALS onset, with the feature importance ranked in descending order as monocyte, leukocyte count, HGI, and HbA1c. This visual interpretation not only aids clinicians in better understanding the diagnostic significance of each indicator but also provides clear directions for subsequent mechanistic research.

For high-risk populations, such as those with a family history of ALS or unexplained muscle weakness, preliminary screening can be conducted through combined peripheral blood testing. If the model indicates a high risk, further examinations such as electromyography and cranial MRI can be performed, which can significantly reduce the misdiagnosis rate and shorten the diagnostic time. Additionally, dynamic monitoring of indicators such as monocytes and HbA1c during treatment can indirectly assess inflammatory and metabolic states. A decrease in monocyte may suggest effective anti-inflammatory treatment, while an increase in HbA1c may reflect improved energy metabolism, providing references for individualized treatment. Although this study has yielded valuable results, it still has some limitations. First, while logistic regression identified HbA1c as a potential protective factor, the extremely low odds ratio and wide confidence interval indicate considerable instability in this estimate. Moreover, HbA1c and the HGI are mathematically related, and their simultaneous inclusion in the same regression model may introduce multicollinearity, making it difficult to reliably disentangle their individual effects. Therefore, this finding should be interpreted with caution and considered exploratory, requiring validation in larger, independent cohorts. Second, the study's relatively small sample size and single-center, retrospective design increase the risk of model overfitting. Although the random forest model utilized out-of-bag error for internal validation, the logistic regression model did not undergo any internal validation procedures, such as cross-validation, bootstrapping, or optimism correction. Consequently, the reliability and generalizability of our findings, particularly those from the logistic regression model, remain unproven and require external validation in larger, independent cohorts, such as the UK Biobank. Third, this study did not include patients with other neuromuscular diseases as controls. Therefore, we cannot conclude that the observed biomarker profile is specific to ALS. Future studies should incorporate disease control groups to evaluate the specificity of these biomarkers for distinguishing ALS from ALS-mimic conditions. Fourth, critical clinical parameters that are essential for a comprehensive understanding of ALS, such as site of onset, disease duration, genetic status, and progression rate, were not systematically collected in this retrospective cohort. Consequently, we were unable to explore the relationship between the candidate biomarkers and these key clinical characteristics, including their potential to reflect disease severity rather than merely serving as diagnostic indicators. This represents an important gap that should be addressed in future prospective studies. Lastly, this study did not explore the dynamic change patterns of the indicators. If their temporal sequences of change could be clarified, the value for early diagnosis could be further enhanced. Therefore, future research should conduct multi-center prospective cohort studies, expand the sample size, and include patients with underlying comorbidities to validate the stability and specificity of the combined model. Convenient diagnostic tools based on combined indicators can also be developed and clinically translated in primary hospitals to truly achieve early diagnosis and intervention for ALS. It is important to note that, given the above-mentioned limitations—particularly the retrospective design, single-center recruitment, lack of external validation, and absence of disease control groups—our findings should be considered exploratory. The proposed clinical application of the combined detection model requires further validation before it can be implemented in routine practice.

In summary, this study provides preliminary evidence that peripheral blood leukocytes, monocytes, HbA1c, and HGI may serve as potential diagnostic biomarkers for ALS. Combined detection of these indicators demonstrated improved diagnostic accuracy in this cohort. However, given the exploratory nature of the findings and the limitations of the study design, these results should be interpreted with caution. Further validation in larger, independent cohorts—including disease control groups—is required to confirm the specificity and robustness of these biomarkers before they can be considered for clinical application.

Author contributions

XY: Developed and planned the study, performed experiments, and interpreted results. Edited and refined the manuscript with a focus on critical intellectual contributions. JY and RL: Participated in collecting, assessing, and interpreting the date. Made significant contributions to data interpretation and manuscript preparation. YL and HD: Provided substantial intellectual input during the drafting and revision of the manuscript. All authors contributed to the article and approved the submitted version.

Data availability

The original contributions presented in the study are included in the article/supplementary material, further inquiries can be directed to the corresponding authors.

Ethics statement

This study was approved by the Ethics Committee of the Second Hospital of Hebei Medical University (Approval No.: 2024-R644). The study involved 108 human participants, from whom blood samples were collected and analyzed. All procedures were conducted in accordance with the ethical standards of the institutional research committee and with the 1964 Helsinki Declaration and its later amendments.

Funding

The author(s) declared that financial support was not received for this work and/or its publication.

Conflict of interest

The author(s) declared no potential conflicts of interest with respect to the research, authorship, and/or publication of this article.

Generative AI statement

The author(s) declared that generative AI was not used in the creation of this manuscript.

Any alternative text (alt text) provided alongside figures in this article has been generated by Frontiers with the support of artificial intelligence and reasonable efforts have been made to ensure accuracy, including review by the authors wherever possible. If you identify any issues, please contact us.

References

1. Ilieva H, Vullaganti M, Kwan J. Advances in molecular pathology, diagnosis, and treatment of amyotrophic lateral sclerosis. *BMJ (Clinical Research Ed)* (2023) 383: e075037. doi:10.1136/bmj-2023-075037

2. Mead RJ, Shan N, Reiser HJ, Marshall F, Shaw PJ. Amyotrophic lateral sclerosis: a neurodegenerative disorder poised for successful therapeutic translation. *Nat Reviews Drug Discovery* (2023) 22(3):185–212. doi:10.1038/s41573-022-00612-2

3. Xu L, Chen L, Wang S, Feng J, Liu L, Liu G, et al. Incidence and prevalence of amyotrophic lateral sclerosis in urban China: a national population-based study. *J Neurology, Neurosurgery, Psychiatry* (2020) 91(5):520–5. doi:10.1136/jnnp-2019-322317

4. Rizea RE, Corlatescu AD, Costin HP, Dumitru A, Ciurea AV. Understanding amyotrophic lateral sclerosis: pathophysiology, diagnosis, and therapeutic advances. *Int Journal Molecular Sciences* (2024) 25(18):9966. doi:10.3390/ijms25189966

5. Van Es MA. Amyotrophic lateral sclerosis; clinical features, differential diagnosis and pathology. *Int Review Neurobiology* (2024) 176:1–47. doi:10.1016/bs.irn.2024.04.011

6. Mercadante S, Al-Husinat L. Palliative care in amyotrophic lateral sclerosis. *J Pain Symptom Management* (2023) 66(4):e485–e499. doi:10.1016/j.jpainsymman.2023.06.029

7. Izenberg A. Amyotrophic lateral sclerosis and other motor neuron diseases. *Continuum (Minneapolis, Minn)* (2023) 29(5):1538–63. doi:10.1212/con.0000000000001345

8. Thomson CG, Hutchinson PR, Stern PJ. Misdiagnosis in amyotrophic lateral sclerosis. *The J Hand Surgery* (2023) 48(8):822–6. doi:10.1016/j.jhsa.2023.03.023

9. Norris SP, Likanje MN, Andrews JA. Amyotrophic lateral sclerosis: update on clinical management. *Curr Opinion Neurology* (2020) 33(5):641–8. doi:10.1097/wco.0000000000000864

10. De Marchi F, Munitic I, Amedei A, Berry JD, Feldman EL, Aronica E, et al. Interplay between immunity and amyotrophic lateral sclerosis: clinical impact. *Neurosci Biobehavioral Reviews* (2021) 127:958–78. doi:10.1016/j.neubiorev.2021.06.027

11. Mimic S, Aru B, Pehlivanoğlu C, Sleiman H, Andjus PR, Yanıkkaya Demirel G. Immunology of amyotrophic lateral sclerosis - role of the innate and adaptive immunity. *Front Neuroscience* (2023) 17:1277399. doi:10.3389/fnins.2023.1277399

12. Choi SJ, Hong YH, Kim SM, Shin JY, Suh YJ, Sung JJ. High neutrophil-to-lymphocyte ratio predicts short survival duration in amyotrophic lateral sclerosis. *Scientific Reports* (2020) 10(1):428. doi:10.1038/s41598-019-57366-y

13. Zhang W, Chen T, Zhao H, Ren S. Glycosylation in aging and neurodegenerative diseases. *Acta Biochim Biophys Sinica* (2024) 56(8):1208–20. doi:10.3724/abbs.2024136

14. Lee I, Mitsumoto H, Lee S, Kasarskis E, Rosenbaum M, Factor-Litvak P, et al. Higher glycemic index and glycemic load diet is associated with slower disease progression in amyotrophic lateral sclerosis. *Ann Neurology* (2024) 95(2):217–29. doi:10.1002/ana.26825

15. Hu J, Szymczak S. A review on longitudinal data analysis with random forest. *Brief Bioinformatics* (2023) 24(2):bbad002. doi:10.1093/bib/bbad002

16. Founta K, Dafou D, Kanata E, Sklaviadis T, Zanos TP, Gounaris A, et al. Gene targeting in amyotrophic lateral sclerosis using causality-based feature selection and machine learning. *Mol Medicine (Cambridge, Mass)* (2023) 29(1):12. doi:10.1186/s10020-023-00603-y

17. Vidovic M, Müschen LH, Brakemeier S, Machetanz G, Naumann M, Castro-Gomez S. Current state and future directions in the diagnosis of amyotrophic lateral sclerosis. *Cells* (2023) 12(5):736. doi:10.3390/cells12050736

18. Kim N, Fischer AH, Dyring-Andersen B, Rosner B, Okoye GA. Research techniques made simple: choosing appropriate statistical methods for clinical research. *The J Investigative Dermatology* (2017) 137(10):e173–e178. doi:10.1016/j.jid.2017.08.007

19. Segura T, Medrano IH, Collazo S, Maté C, Sguera C, Del Rio-Bermudez C, et al. Symptoms timeline and outcomes in amyotrophic lateral sclerosis using artificial intelligence. *Scientific Reports* (2023) 13(1):702. doi:10.1038/s41598-023-27863-2

20. Marin B, Fontana A, Arcuti S, Copetti M, Boumédiene F, Couratier P, et al. Age-specific ALS incidence: a dose-response meta-analysis. *Eur Journal Epidemiology* (2018) 33(7):621–34. doi:10.1007/s10654-018-0392-x

21. Longinetti E, Fang F. Epidemiology of amyotrophic lateral sclerosis: an update of recent literature. *Curr Opinion Neurology* (2019) 32(5):771–6. doi:10.1097/wco.0000000000000730

22. Vasta R, Moglia C, Manera U, Canosa A, Grassano M, Palumbo F, et al. What is amyotrophic lateral sclerosis prevalence? *Amyotroph Lateral Sclerosis and Frontotemporal Degeneration* (2022) 23(3-4):203–8. doi:10.1080/21678421.2021.1936557

23. Li C, Wei Q, Hou Y, Lin J, Ou R, Zhang L, et al. Genome-wide analyses identify NEAT1 as genetic modifier of age at onset of amyotrophic lateral sclerosis. *Mol Neurodegeneration* (2023) 18(1):77. doi:10.1186/s13024-023-00669-6

24. Calma AD, Pavey N, Menon P, Vucic S. Neuroinflammation in amyotrophic lateral sclerosis: pathogenic insights and therapeutic implications. *Curr Opinion Neurology* (2024) 37(5):585–92. doi:10.1097/wco.0000000000001279

25. Yang J, Liu T, Zhang L, Li X, Du FP, Liu Q, et al. Eosinophils at diagnosis are elevated in amyotrophic lateral sclerosis. *Front Neurology* (2023) 14:1289467. doi:10.3389/fneur.2023.1289467

26. Murdock BJ, Zhou T, Kashlan SR, Little RJ, Goutman SA, Feldman EL. Correlation of peripheral immunity with rapid amyotrophic lateral sclerosis progression. *JAMA Neurology* (2017) 74(12):1446–54. doi:10.1001/jamaneurol.2017.2255

27. Kioumourtzoglou MA, Rotem RS, Seals RM, Gredal O, Hansen J, Weisskopf MG. Diabetes mellitus, obesity, and diagnosis of amyotrophic lateral sclerosis: a population-based study. *JAMA Neurology* (2015) 72(8):905–11. doi:10.1001/jamaneurol.2015.0910

28. Mariosa D, Kamel F, Bellocco R, Ye W, Fang F. Association between diabetes and amyotrophic lateral sclerosis in Sweden. *Eur Journal Neurology* (2015) 22(11):1436–42. doi:10.1111/ene.12632

29. Mariosa D, Kamel F, Bellocco R, Ronnevi LO, Almqvist C, Larsson H, et al. Antidiabetics, statins and the risk of amyotrophic lateral sclerosis. *Eur Journal Neurology* (2020) 27(6):1010–6. doi:10.1111/ene.14190

30. Jawaid A, Schulz PE. Pre-morbid type 2 diabetes mellitus as a prognostic factor in amyotrophic lateral sclerosis. *Muscle and Nerve* (2015) 52(4):690–1. doi:10.1002/mus.24758

31. Schumacher J, Peter RS, Nagel G, Rothenbacher D, Rosenbohm A, Ludolph AC, et al. Statins, diabetes mellitus and prognosis of amyotrophic lateral sclerosis: data from 501 patients of a population-based registry in southwest Germany. *Eur Journal Neurology* (2020) 27(8):1405–14. doi:10.1111/ene.14300

32. Hollinger SK, Okosun IS, Mitchell CS. Antecedent disease and amyotrophic lateral sclerosis: what is protecting whom? *Front Neurology* (2016) 7:47. doi:10.3389/fneur.2016.00047

33. Martinelli I, Gianferrari G, Santarelli R, Zucchi E, Simonini C, Fini N, et al. Exploring the role of diabetes in ALS: a population-based cohort study. *Life (Basel, Switzerland)* (2025) 15(6):936. doi:10.3390/life15060936

34. Zhao J, Liu L, Li X, Zhang L, Lv J, Guo X, et al. Neuroprotective effects of an Nrf2 agonist on high glucose-induced damage in HT22 cells. *Biol Research* (2019) 52(1):53. doi:10.1186/s40659-019-0258-z

35. Wei QQ, Chen Y, Cao B, Ou RW, Zhang L, Hou Y, et al. Blood hemoglobin A1c levels and amyotrophic lateral sclerosis survival. *Mol Neurodegeneration* (2017) 12(1):69. doi:10.1186/s13024-017-0211-y

EBM Experimental Biology and Medicine

TYPE Review
PUBLISHED 01 May 2026
DOI 10.3389/ebm.2026.10997

OPEN ACCESS

*CORRESPONDENCE
Longlong Liu,
lllbzshq@163.com

RECEIVED 20 January 2026
REVISED 06 March 2026
ACCEPTED 20 April 2026
PUBLISHED 01 May 2026

CITATION
Wu Y, Zhang C, Peng Y and Liu L (2026) Ferroptosis and futile recanalization after mechanical thrombectomy in acute ischemic stroke: mechanisms, risk factors, predictive models and therapeutic interventions.
Exp. Biol. Med. 251:10997.
doi: 10.3389/ebm.2026.10997

Ferroptosis and futile recanalization after mechanical thrombectomy in acute ischemic stroke: mechanisms, risk factors, predictive models and therapeutic interventions

Yuexin Wu, Cuiying Zhang, Yangyang Peng and Longlong Liu*

Emergency Department, Binzhou People's Hospital, Binzhou, Shandong, China

Abstract

Acute ischemic stroke (AIS) remains a leading cause of mortality and long-term disability worldwide. Endovascular mechanical thrombectomy (EVT) has revolutionized stroke treatment by enabling rapid recanalization of occluded cerebral vessels. However, a significant proportion of patients experience futile recanalization, where successful vessel reopening fails to translate into favorable functional outcomes. Emerging evidence highlights ferroptosis, a regulated form of cell death driven by iron-dependent lipid peroxidation, as a critical mechanism contributing to neuronal damage in ischemic stroke, particularly during reperfusion injury. This comprehensive review examines the intricate relationship between ferroptosis and futile recanalization following mechanical thrombectomy. We systematically explore the molecular mechanisms underlying ferroptosis in the context of cerebral ischemia-reperfusion injury, including iron metabolism dysregulation, lipid peroxidation cascades, glutathione depletion, and mitochondrial dysfunction. Multiple factors contribute to futile recanalization, including patient demographics (age, comorbidities), stroke characteristics (severity, infarct volume, collateral status), procedural variables (time to treatment, recanalization quality), and post-procedural complications (hemorrhagic transformation, reperfusion injury). We review current predictive models, including nomograms and machine learning algorithms, that integrate clinical, radiological, and biomarker data to stratify patient risk. Importantly, we discuss potential therapeutic interventions targeting ferroptosis pathways, such as iron chelators, lipophilic antioxidants, and ferroptosis-specific inhibitors. The integration of ferroptosis biomarkers into predictive models may enhance risk stratification and guide personalized treatment strategies. Future research should focus on validating ferroptosis-targeted therapies in clinical trials, developing real-time monitoring techniques, and establishing standardized protocols for neuroprotective interventions during mechanical thrombectomy. A deeper understanding of ferroptosis mechanisms and their contribution to futile recanalization may pave the way for novel therapeutic approaches to improve stroke outcomes.

KEYWORDS
acute ischemic stroke, ferroptosis, futile recanalization, iron metabolism, mechanical thrombectomy

Impact statement

We are pleased to submit our review manuscript entitled "Ferroptosis and Futile Recanalization after Mechanical Thrombectomy in Acute Ischemic Stroke: Mechanisms, Risk Factors, Predictive Models and Therapeutic Interventions" for your consideration. This comprehensive review explores the critical role of ferroptosis—a regulated, iron-dependent cell death pathway—in contributing to poor functional outcomes (futile recanalization) following successful endovascular thrombectomy. We systematically synthesize current evidence on molecular mechanisms, clinical predictors, emerging prognostic models, and promising therapeutic strategies targeting ferroptosis. By integrating preclinical insights with clinical observations, this work aims to advance the understanding of reperfusion injury and highlight novel neuroprotective approaches to improve stroke outcomes. We believe this review will be of significant interest to your readers and contribute to ongoing translational research in stroke neurology.

Introduction

Acute ischemic stroke (AIS) represents one of the most devastating neurological emergencies, ranking as the second leading cause of death and the third leading cause of disability-adjusted life years worldwide [1–3]. The abrupt interruption of cerebral blood flow triggers a complex pathophysiological cascade, including excitotoxicity, oxidative stress, inflammation, and cell death, ultimately resulting in neuronal injury and functional impairment [4]. Despite significant advances in acute stroke management, including intravenous thrombolysis and endovascular mechanical thrombectomy (EVT), a substantial proportion of patients continue to experience poor functional outcomes [5].

The introduction of EVT has revolutionized the treatment paradigm for patients with large vessel occlusion (LVO) stroke. Multiple landmark randomized controlled trials, including MR CLEAN, EXTEND-IA, ESCAPE, SWIFT PRIME, and REVASCAT, have demonstrated the superiority of EVT over medical therapy alone, with significant improvements in functional independence and reduced mortality [6, 7]. Subsequent trials such as DAWN and DEFUSE-3 further expanded the therapeutic window, showing benefits in carefully selected patients up to 24 h from symptom onset [8, 9]. Despite these remarkable advances in recanalization rates, achieving successful angiographic recanalization (modified Treatment in Cerebral Ischemia [mTICI] score 2b-3) does not guarantee favorable functional outcomes [10, 11].

This phenomenon, termed "futile recanalization," occurs when successful vessel recanalization fails to translate into meaningful clinical improvement, typically defined as a modified Rankin Scale (mRS) score of 3–6 at 90 days despite achieving mTICI 2b-3 reperfusion [12, 13]. The incidence of futile recanalization ranges from 30% to 68% across different studies, representing a significant clinical challenge and highlighting the complexity of ischemic stroke pathophysiology beyond vessel occlusion [14, 15]. Understanding the mechanisms underlying futile recanalization is crucial for developing strategies to optimize treatment outcomes and identify patients who are most likely to benefit from aggressive revascularization therapy.

Recent advances in cell death research have unveiled ferroptosis as a novel and distinct form of regulated cell death that plays a critical role in ischemic stroke pathophysiology [16–18]. Unlike apoptosis, necrosis, or autophagy, ferroptosis is characterized by iron-dependent accumulation of lipid peroxides, resulting from the failure of cellular antioxidant defenses [19]. This form of cell death was first described by Dixon et al. in 2012 and has since emerged as a significant contributor to neuronal injury in various neurological disorders, including stroke, traumatic brain injury, and neurodegenerative diseases [7].

The relevance of ferroptosis to stroke becomes particularly evident in the context of ischemia-reperfusion injury. While prompt restoration of blood flow through mechanical thrombectomy is essential to salvage ischemic tissue, reperfusion paradoxically triggers additional injury mechanisms, including oxidative stress, calcium overload, mitochondrial dysfunction, and inflammatory responses [20]. Ferroptosis appears to be a key mediator of reperfusion injury, as the restoration of blood flow delivers oxygen and iron to ischemic tissue, creating conditions conducive to lipid peroxidation and ferroptotic cell death [21]. This dual-edged nature of reperfusion may partially explain the phenomenon of futile recanalization, where successful vessel reopening fails to prevent ongoing neuronal damage.

Multiple lines of evidence support the involvement of ferroptosis in acute ischemic stroke. Experimental studies have demonstrated increased markers of ferroptosis, including elevated iron levels, lipid peroxidation products (such as malondialdehyde and 4-hydroxynonenal), and depleted glutathione, in ischemic brain tissue [22]. Furthermore, pharmacological inhibition of ferroptosis using specific inhibitors like ferrostatin-1 and liproxstatin-1 has shown neuroprotective effects in preclinical stroke models, reducing infarct volume and improving functional outcomes [22]. Genetic manipulations targeting key ferroptosis regulators, such as glutathione peroxidase 4 (GPX4) and ferroptosis suppressor protein 1 (FSP1), have similarly demonstrated the causal role of ferroptosis in stroke pathophysiology [23].

The molecular mechanisms governing ferroptosis involve a complex interplay of iron metabolism, lipid peroxidation, and antioxidant defense systems. Iron homeostasis is tightly regulated under physiological conditions through coordinated expression of iron import proteins (transferrin receptor 1), storage proteins (ferritin), and export proteins (ferroportin) [24]. However, cerebral ischemia and subsequent reperfusion disrupt this delicate balance, leading to increased intracellular labile iron pools that catalyze the Fenton reaction, generating highly reactive hydroxyl radicals [20]. These radicals initiate lipid peroxidation of polyunsaturated fatty acids (PUFAs) in cellular membranes, particularly phosphatidylethanolamines containing arachidonic acid or adrenic acid [25, 26]. The accumulation of lipid peroxides ultimately leads to membrane damage and ferroptotic cell death.

Cellular antioxidant defense mechanisms, particularly the GPX4-glutathione axis and the FSP1-CoQ10 system, serve as critical barriers against ferroptosis [27]. GPX4, a selenoprotein,

reduces lipid hydroperoxides to lipid alcohols using glutathione (GSH) as a cofactor, thereby preventing the propagation of lipid peroxidation [28]. System xc^-, a cystine/glutamate antiporter composed of SLC7A11 and SLC3A2 subunits, imports cystine for GSH synthesis, representing another key component of the anti-ferroptotic defense [29, 30]. During ischemic stroke, depletion of GSH, inactivation of GPX4, or dysfunction of system xc^- sensitizes neurons to ferroptotic cell death [31, 32]. Understanding these molecular mechanisms provides a foundation for developing targeted therapeutic interventions to prevent ferroptosis-mediated injury in stroke patients undergoing mechanical thrombectomy.

This comprehensive review aims to elucidate the role of ferroptosis in futile recanalization following mechanical thrombectomy for acute ischemic stroke. We systematically examine the molecular mechanisms of ferroptosis in the context of cerebral ischemia-reperfusion injury, explore clinical and radiological factors associated with futile recanalization, review current predictive models, and discuss potential therapeutic interventions targeting ferroptosis pathways. By integrating basic science discoveries with clinical observations, we hope to provide a framework for future research and therapeutic development aimed at optimizing outcomes after mechanical thrombectomy through ferroptosis-targeted neuroprotection.

Molecular mechanisms of ferroptosis in cerebral ischemia

Iron metabolism and dysregulation in ischemic stroke

Iron is an essential cofactor for numerous biological processes, including oxygen transport, DNA synthesis, and mitochondrial respiration. However, its redox-active nature makes iron a double-edged sword, as excessive free iron can catalyze the formation of reactive oxygen species (ROS) through Fenton chemistry [30]. In the brain, iron homeostasis is particularly critical, as neurons are highly vulnerable to oxidative damage due to their high metabolic rate, abundant polyunsaturated fatty acids, and relatively limited antioxidant capacity [33].

Under physiological conditions, iron levels in the brain are tightly regulated through the coordinated action of multiple proteins. Transferrin receptor 1 (TfR1) mediates cellular iron uptake by binding iron-loaded transferrin, which is subsequently internalized via clathrin-mediated endocytosis [34]. Once inside the cell, iron is released from transferrin in the acidic endosomal environment and reduced from Fe^{3+} to Fe^{2+} by the ferrireductase STEAP3. The Fe^{2+} is then transported into the cytosol by divalent metal transporter 1 (DMT1), where it enters the labile iron pool (LIP) - a redox-active pool of chelatable iron that serves as the source for iron incorporation into various cellular processes [29].

Excess intracellular iron is stored in ferritin, a multi-subunit protein complex composed of heavy (FTH1) and light (FTL) chains that can sequester up to 4,500 iron atoms in a non-toxic ferric form [28]. Ferroportin (FPN), the sole known mammalian iron exporter, mediates cellular iron efflux and is regulated by hepcidin, a systemic iron regulatory hormone [33]. This intricate regulatory network maintains iron homeostasis and prevents iron-mediated toxicity under normal conditions.

Cerebral ischemia profoundly disrupts iron homeostasis through multiple mechanisms. During ischemia, the breakdown of the blood-brain barrier allows extravasation of iron-containing proteins, including hemoglobin and transferrin, into the brain parenchyma [34]. Simultaneously, hemorrhagic transformation, a common complication following ischemic stroke, particularly after reperfusion therapy, introduces large amounts of hemoglobin-derived iron into brain tissue [29]. Red blood cell lysis releases hemoglobin, which is subsequently broken down by heme oxygenase-1 (HO-1), liberating free iron [30]. Interestingly, the role of heme oxygenase-1 (HO-1) in ischemic stroke appears to be dual and highly context-dependent. Under physiological or mildly stressed conditions, HO-1 is generally regarded as cytoprotective, largely due to its antioxidant, anti-inflammatory, and heme-detoxifying effects. However, during acute ischemia–reperfusion (I/R) injury, excessive or dysregulated HO-1 induction may paradoxically facilitate ferroptosis by increasing intracellular iron availability as a consequence of heme degradation. The resulting surge in free ferrous iron expands the labile iron pool and accelerates Fenton chemistry, thereby amplifying lipid peroxidation and aggravating neuronal injury [31]. Thus, while moderate HO-1 activity may confer endogenous protection, uncontrolled activation in the reperfusion phase has the potential to exacerbate ferroptosis-mediated neuronal damage, which may in turn contribute to futile recanalization despite successful vessel reopening [32].

Reperfusion following mechanical thrombectomy creates conditions particularly conducive to ferroptosis. The sudden restoration of oxygen supply in the presence of elevated iron levels creates an ideal environment for Fenton chemistry: $Fe^{2+} + H_2O_2 \rightarrow Fe^{3+} + OH^- + \bullet OH$. The hydroxyl radical (•OH) generated is among the most reactive oxygen species, capable of initiating lipid peroxidation cascades that culminate in ferroptotic cell death. Moreover, ischemia-reperfusion injury triggers inflammatory responses that further exacerbate iron dysregulation. Activated microglia and infiltrating macrophages release pro-inflammatory cytokines that upregulate TfR1 expression and downregulate ferroportin, promoting cellular iron accumulation [29].

Recent studies have identified ferritinophagy, the selective autophagic degradation of ferritin, as a key mechanism driving ferroptosis in ischemic stroke [30]. Nuclear receptor coactivator 4 (NCOA4) acts as a cargo receptor for ferritinophagy, binding to ferritin heavy chain and delivering it to lysosomes for degradation [35]. While ferritinophagy serves an important physiological role in mobilizing iron stores under iron-deficient conditions, excessive ferritinophagy during ischemia-reperfusion injury liberates large amounts of iron from ferritin, expanding the labile iron pool and promoting ferroptosis. Genetic or pharmacological inhibition of NCOA4 has been shown to attenuate ferroptosis and reduce ischemic brain injury in experimental models (Figure 1) [36].

Lipid peroxidation and membrane damage

Lipid peroxidation represents the biochemical hallmark of ferroptosis and is initiated by the oxidation of polyunsaturated fatty acids (PUFAs) in cellular membranes. Unlike other forms of

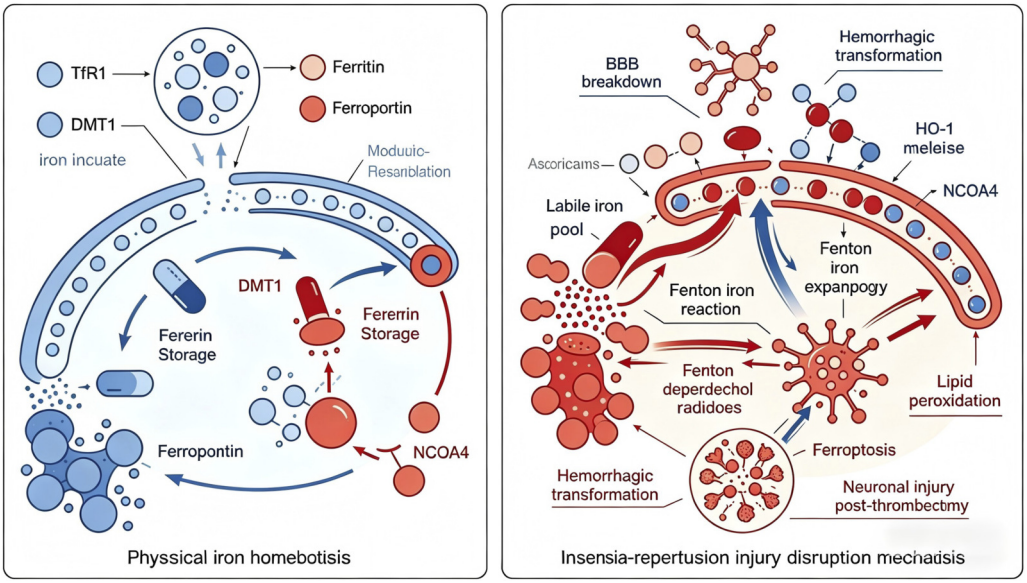

FIGURE 1
Iron Metabolism Dysregulation and Ferroptosis in Cerebral Ischemia-Reperfusion Injury. Left panel: Under physiological conditions, neuronal iron homeostasis is maintained through coordinated TfR1-mediated uptake, DMT1 transport, ferritin storage, and ferroportin export. Right panel: Ischemia-reperfusion injury disrupts iron homeostasis via multiple mechanisms including blood-brain barrier breakdown, hemorrhagic transformation, HO-1-mediated iron release, and NCOA4-driven ferritinophagy, leading to labile iron pool expansion. Excess free iron (Fe^{2+}) reacts with reperfusion oxygen via Fenton chemistry, generating hydroxyl radicals that initiate lipid peroxidation and trigger ferroptosis, contributing to neuronal injury and futile recanalization following mechanical thrombectomy.

cell death that may involve lipid peroxidation as a secondary event, ferroptosis is defined by the overwhelming accumulation of lipid peroxides to levels that exceed cellular repair capacity. The process is highly specific, targeting phospholipids containing PUFA tails, particularly those esterified to arachidonic acid (AA, 20:4) or adrenic acid (AdA, 22:4) [37].

The lipid peroxidation cascade begins with the abstraction of a bis-allylic hydrogen atom from PUFAs by reactive oxygen species, particularly hydroxyl radicals generated through Fenton chemistry. This produces a carbon-centered lipid radical (L•), which rapidly reacts with molecular oxygen to form a lipid peroxyl radical (LOO•). The lipid peroxyl radical can then abstract a hydrogen atom from an adjacent PUFA, generating a lipid hydroperoxide (LOOH) and propagating a chain reaction that amplifies oxidative damage [37]. This autocatalytic nature of lipid peroxidation explains why even small amounts of initial oxidative stress can trigger extensive membrane damage.

Recent lipidomics studies have revealed that ferroptosis selectively targets specific phospholipid species. Acyl-CoA synthetase long-chain family member 4 (ACSL4) plays a crucial role in determining ferroptosis sensitivity by preferentially incorporating AA and AdA into phospholipids. Lysophosphatidylcholine acyltransferase 3 (LPCAT3) further esterifies these PUFAs specifically into phosphatidylethanolamine (PE), generating PE-AA and PE-AdA species that are highly susceptible to peroxidation [38]. Cells lacking ACSL4 or LPCAT3 show remarkable resistance to ferroptosis, even in the presence of canonical ferroptosis inducers, highlighting the critical importance of PUFA-containing phospholipids in the ferroptotic process [39].

In the context of ischemic stroke and reperfusion, multiple factors converge to promote lipid peroxidation. First, ischemia depletes cellular ATP, impairing energy-dependent antioxidant systems and phospholipid repair mechanisms [35]. Second, reperfusion generates a burst of reactive oxygen species through multiple sources, including mitochondrial electron transport chain dysfunction, NADPH oxidase activation, and xanthine oxidase-mediated superoxide production [36]. Third, the inflammatory response following stroke upregulates lipoxygenases (LOXs), particularly 15-LOX, which directly catalyze the peroxidation of PUFA-containing phospholipids [38]. 15-LOX has been specifically implicated in ferroptotic cell death, and its inhibition provides neuroprotection in experimental stroke models [39].

The accumulation of lipid hydroperoxides causes catastrophic membrane damage through several mechanisms. Lipid peroxidation disrupts membrane fluidity and integrity, leading to loss of ion gradients, impaired function of membrane-bound proteins, and ultimately cell lysis [38]. Additionally, lipid peroxidation products, such as malondialdehyde (MDA) and 4-hydroxynonenal (4-HNE), are highly reactive aldehydes that can modify proteins and DNA, amplifying cellular dysfunction [40]. These lipid-derived aldehydes serve as biomarkers of oxidative stress and ferroptosis, with elevated levels detected in both experimental stroke models and human stroke patients (Figure 2).

Glutathione peroxidase 4 and antioxidant defense systems

Glutathione peroxidase 4 (GPX4) represents the central guardian against ferroptosis, functioning as the only enzyme

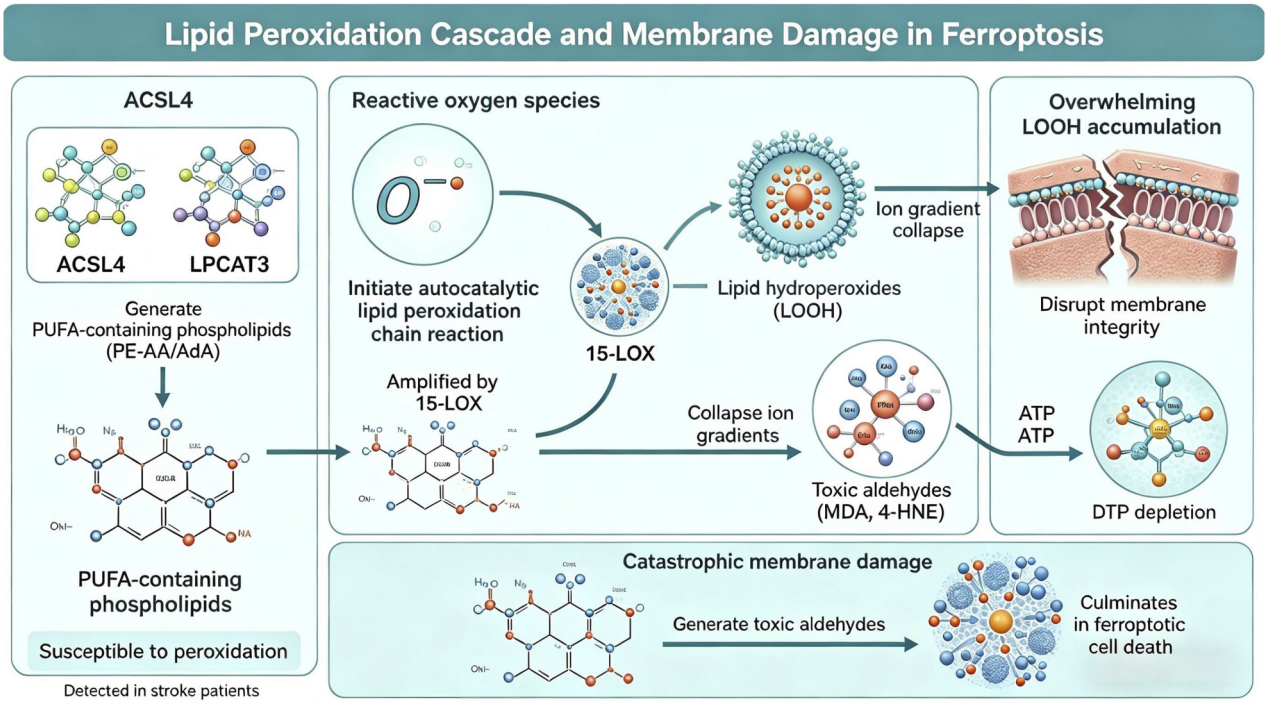

FIGURE 2
Lipid Peroxidation Cascade and Membrane Damage in Ferroptosis. ACSL4 and LPCAT3 generate PUFA-containing phospholipids (PE-AA/AdA) susceptible to peroxidation. Reactive oxygen species initiate an autocatalytic lipid peroxidation chain reaction, amplified by 15-LOX, producing lipid hydroperoxides (LOOH). Overwhelming LOOH accumulation disrupts membrane integrity, collapses ion gradients, generates toxic aldehydes (MDA, 4-HNE), and depletes ATP, culminating in catastrophic membrane damage and ferroptotic cell death detected in stroke patients.

capable of directly reducing lipid hydroperoxides within biological membranes [39]. Unlike other members of the glutathione peroxidase family that primarily reduce hydrogen peroxide and other small molecular oxidants, GPX4's unique ability to access and reduce phospholipid hydroperoxides makes it indispensable for preventing ferroptosis [35]. The critical importance of GPX4 is underscored by the fact that complete genetic deletion of GPX4 is embryonically lethal in mice, while conditional deletion in specific tissues leads to spontaneous ferroptosis [36].

GPX4 functions through a catalytic mechanism that requires reduced glutathione (GSH) as a cofactor and selenium in the form of selenocysteine at its active site [37]. The enzyme reduces lipid hydroperoxides (LOOH) to their corresponding alcohols (LOH), while oxidizing GSH to glutathione disulfide (GSSG). The GSSG is then reduced back to GSH by glutathione reductase using NADPH, completing the antioxidant cycle [38]. Therefore, the efficacy of GPX4 in preventing ferroptosis depends not only on adequate GPX4 expression and activity but also on sufficient availability of GSH, the proper functioning of glutathione reductase, and adequate NADPH supply [39].

During cerebral ischemia and reperfusion, multiple factors conspire to impair GPX4 function and cellular antioxidant capacity. First, ischemia-induced energy depletion reduces NADPH levels, limiting the regeneration of GSH from GSSG. Second, oxidative stress during reperfusion can directly oxidize and inactivate GPX4, rendering it unable to reduce lipid peroxides [41]. Third, selenium deficiency, whether due to dietary insufficiency or increased utilization during oxidative stress, can compromise GPX4 activity, as selenocysteine incorporation is essential for its catalytic function [42].

The synthesis of glutathione, a tripeptide composed of glutamate, cysteine, and glycine, is rate-limited by cysteine availability. System xc^-, a sodium-independent cystine/glutamate antiporter located on the plasma membrane, plays a crucial role in providing cysteine for GSH synthesis. This transporter imports cystine (the oxidized form of cysteine) from the extracellular space in exchange for intracellular glutamate. Once inside the cell, cystine is rapidly reduced to cysteine, which is then incorporated into GSH by the sequential action of glutamate-cysteine ligase (GCL) and glutathione synthetase (GS) [43].

System xc^- comprises two subunits: SLC7A11 (also known as xCT), the light chain responsible for substrate transport, and SLC3A2 (also known as 4F2hc or CD98), a heavy chain chaperone protein required for proper trafficking and stabilization of SLC7A11 at the plasma membrane [44]. Inhibition of system xc^-, whether through genetic deletion, pharmacological blockade (e.g., by erastin or sulfasalazine), or downregulation in pathological conditions, leads to cysteine depletion, GSH exhaustion, and ultimately ferroptosis [45].

In ischemic stroke, system xc^- activity may be compromised through multiple mechanisms. Glutamate excitotoxicity, a well-established consequence of cerebral ischemia, results in massive accumulation of extracellular glutamate, which can inhibit system xc^- by reducing the driving force for cystine import. Additionally, inflammatory mediators released during ischemia-reperfusion injury can regulate SLC7A11 expression. For instance, interferon-

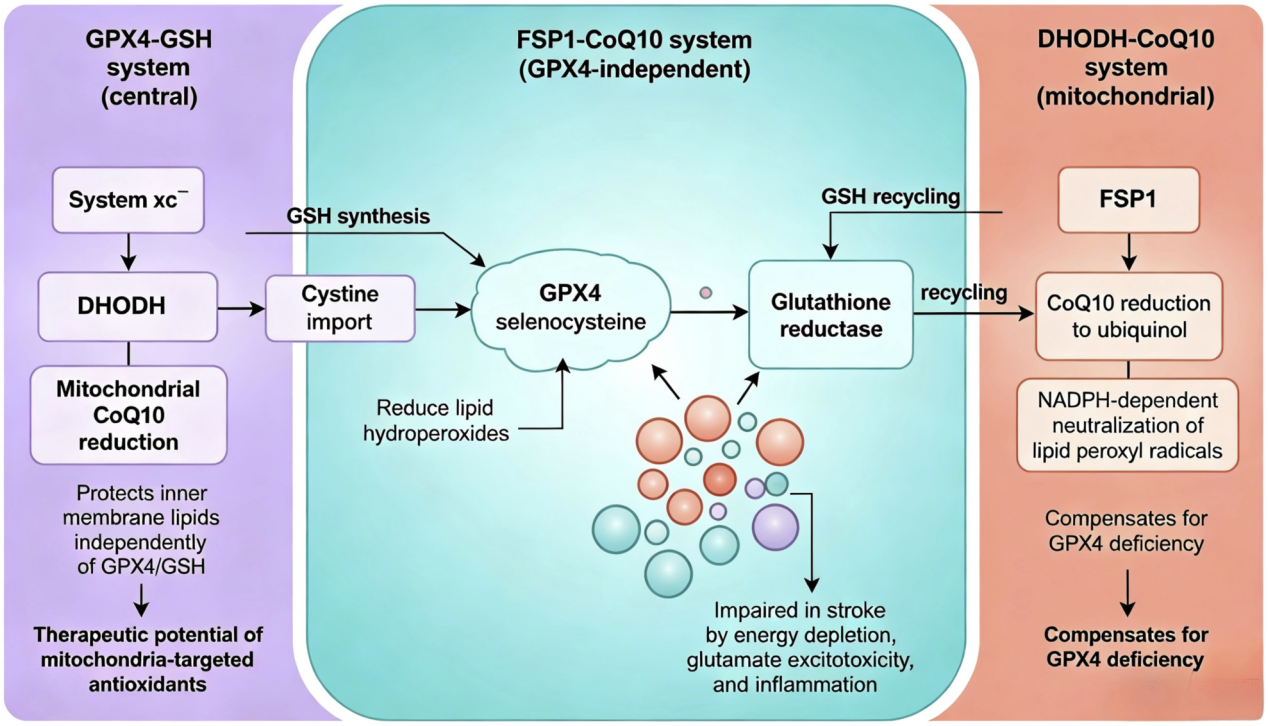

FIGURE 3
Three Complementary Antioxidant Pathways Against Ferroptosis. GPX4-GSH system (central): System xc⁻ imports cystine for GSH synthesis, which GPX4 uses with selenocysteine to reduce lipid hydroperoxides, recycled by glutathione reductase; impaired in stroke by energy depletion, glutamate excitotoxicity, and inflammation. FSP1-CoQ10 system (GPX4-independent): FSP1 reduces CoQ10 to ubiquinol using NADPH, directly neutralizing lipid peroxyl radicals and compensating for GPX4 deficiency. DHODH-CoQ10 system (mitochondrial): DHODH reduces mitochondrial CoQ10, protecting inner membrane lipids independently of GPX4/GSH, highlighting therapeutic potential of mitochondria-targeted antioxidants.

gamma (IFN-γ) has been shown to downregulate SLC7A11 through JAK-STAT1 signaling, potentially sensitizing cells to ferroptosis [46]. Conversely, activation of the Nrf2 (nuclear factor erythroid 2-related factor 2) pathway, a master regulator of antioxidant responses, can upregulate SLC7A11 expression, enhancing cellular resistance to ferroptosis [47].

Beyond the GPX4-GSH axis, recent research has identified additional anti-ferroptotic pathways that provide redundancy in cellular defense mechanisms. The FSP1 (ferroptosis suppressor protein 1)-CoQ10 (coenzyme Q10) system represents a parallel pathway that operates independently of GSH [48]. FSP1, also known as AIFM2, functions as an oxidoreductase that reduces CoQ10 to its active antioxidant form, ubiquinol, using NADPH as a cofactor. Ubiquinol can then directly reduce lipid peroxyl radicals, thereby inhibiting the propagation of lipid peroxidation [49]. Importantly, FSP1 can compensate for GPX4 deficiency, and cells expressing high levels of FSP1 show resistance to GPX4 inhibition [50].

More recently, the DHODH (dihydroorotate dehydrogenase)-CoQ10 system has been identified as another GPX4-independent ferroptosis suppression mechanism [51]. DHODH, a mitochondrial enzyme involved in pyrimidine biosynthesis, can reduce CoQ10 within the mitochondrial inner membrane, protecting mitochondrial lipids from peroxidation [46]. This discovery highlights the importance of mitochondrial integrity in ferroptosis regulation and suggests that mitochondria-targeted antioxidants may offer therapeutic benefits in preventing ferroptosis-mediated injury during ischemic stroke (Figure 3).

Ferroptosis in cerebral ischemia-reperfusion injury and futile recanalization

Temporal dynamics of ferroptosis following reperfusion

The temporal profile of ferroptosis following cerebral ischemia-reperfusion injury reveals a complex biphasic pattern that begins during ischemia but dramatically accelerates upon reperfusion [47]. During the acute ischemic phase, energy depletion and glutamate excitotoxicity initiate early cellular stress, but the full manifestation of ferroptosis requires the oxygen and iron availability that comes with reperfusion [48]. This paradoxical nature of reperfusion injury, where restoration of blood flow exacerbates tissue damage, has long been recognized, but the specific role of ferroptosis in this process has only recently been elucidated [49].

Experimental studies using middle cerebral artery occlusion (MCAO) models in rodents have demonstrated that markers of ferroptosis, including elevated lipid peroxidation products and

depleted GSH, begin to rise within hours of reperfusion [51]. The expression of ferroptosis-related genes shows dynamic changes, with downregulation of GPX4 and SLC7A11 and upregulation of ACSL4 and transferrin receptor observed in the peri-infarct region during the first 24–72 h post-reperfusion. Importantly, the timing of ferroptosis coincides with the critical period when clinical decisions regarding mechanical thrombectomy are made, suggesting that peri-procedural interventions targeting ferroptosis may be particularly effective [47].

The spatial distribution of ferroptosis in post-ischemic brain tissue provides additional insights into its role in futile recanalization. While the infarct core undergoes rapid necrotic death during ischemia, the penumbra—the potentially salvageable tissue surrounding the core—appears particularly vulnerable to ferroptotic cell death following reperfusion [52]. This observation is crucial for understanding futile recanalization, as successful vessel reopening aims to salvage the penumbra, but ferroptosis-mediated injury in this region may prevent functional recovery despite restored blood flow [49].

Furthermore, the delayed nature of ferroptosis creates a therapeutic window that extends beyond the hyperacute phase of stroke treatment. While mechanical thrombectomy primarily addresses the acute vessel occlusion, ferroptosis continues to contribute to neuronal damage for days after reperfusion, potentially explaining why some patients deteriorate despite successful early recanalization [51]. This extended time course suggests that anti-ferroptotic therapies could be administered not only during the thrombectomy procedure but also in the post-procedural period, offering multiple opportunities for intervention [46].

The temporal relationship between ferroptosis activation and therapeutic intervention represents a critical consideration for clinical translation. Based on experimental evidence from MCAO models, ferroptosis markers begin rising within 2–4 h post-reperfusion and peak at 24–72 h, suggesting multiple intervention opportunities [53]. Three potential timing strategies emerge: (1) prophylactic administration immediately before or during thrombectomy to preemptively block ferroptosis pathways; (2) concurrent administration during the procedure to target the acute reperfusion phase; and (3) post-procedural administration within 24 h to address the delayed ferroptotic injury phase [54]. The extended time course of ferroptosis, unlike the rapid necrotic core formation, provides a clinically feasible window that extends beyond the hyperacute thrombectomy period, making this approach practically implementable in real-world settings.

Ferroptosis as a mechanistic link to futile recanalization

The phenomenon of futile recanalization, where successful angiographic vessel reopening fails to translate into favorable functional outcomes, represents one of the most frustrating challenges in acute stroke management [47]. While multiple factors contribute to futile recanalization—including advanced age, high baseline NIHSS, large infarct core, poor collaterals, and hemorrhagic transformation—the underlying cellular and molecular mechanisms remain incompletely understood. Emerging evidence suggests that ferroptosis may serve as a critical mechanistic link connecting successful recanalization to poor outcomes [52].

Several lines of evidence support the role of ferroptosis in futile recanalization. First, biomarker studies in stroke patients have shown that elevated levels of ferroptosis markers, including serum iron, ferritin, lipid peroxidation products (MDA, 4-HNE), and reduced GSH/GSSG ratio, correlate with poor functional outcomes despite successful reperfusion [55]. Patients with higher baseline serum ferritin levels, reflecting increased iron stores, show significantly higher rates of futile recanalization after mechanical thrombectomy, independent of other risk factors. Similarly, genetic polymorphisms affecting iron metabolism and antioxidant capacity have been associated with variable responses to reperfusion therapy [56].

Second, advanced neuroimaging studies have revealed patterns consistent with ferroptosis-mediated injury in patients with futile recanalization. Susceptibility-weighted imaging (SWI) and quantitative susceptibility mapping (QSM), which are sensitive to iron deposition, show increased signal in the peri-infarct region of patients with poor outcomes after thrombectomy [57]. These imaging findings correlate with histological evidence of iron accumulation and ferroptotic cell death in animal models, suggesting a translational link between preclinical and clinical observations [58].

Third, the timing of reperfusion influences the extent of ferroptosis-mediated injury and correlates with clinical outcomes. Patients who achieve earlier reperfusion generally have better outcomes, potentially because earlier restoration of blood flow limits the accumulation of iron and oxidative damage in the ischemic tissue. Conversely, delayed reperfusion allows for greater iron accumulation and more extensive oxidative stress, creating conditions more conducive to ferroptosis upon blood flow restoration [52]. This temporal relationship may partially explain the time-dependent benefit of mechanical thrombectomy and the phenomenon of futile recanalization in late-presenting patients [55].

Hemorrhagic transformation, a major complication following reperfusion therapy and a strong predictor of futile recanalization, provides another link to ferroptosis [56]. The extravasation of red blood cells into brain parenchyma introduces massive amounts of hemoglobin-derived iron, dramatically expanding the labile iron pool and triggering ferroptosis in peri-hematoma regions [57]. Indeed, experimental studies have shown that ferroptosis is a major mechanism of secondary brain injury following intracerebral hemorrhage, and ferroptosis inhibitors reduce perihematomal edema and improve functional outcomes. Similarly, in patients experiencing hemorrhagic transformation after thrombectomy, ferroptosis likely contributes to ongoing neuronal damage, explaining the particularly poor prognosis associated with this complication [55].

Microvascular dysfunction following reperfusion, often referred to as the “no-reflow” phenomenon, represents another aspect of futile recanalization that may involve ferroptosis [56]. Despite successful recanalization of the proximal vessel, microvascular obstruction can prevent adequate tissue perfusion. Ferroptosis of endothelial cells and pericytes in the microcirculation may contribute to this phenomenon, as lipid peroxidation damages

vascular cells and promotes microvascular thrombosis. Furthermore, ferroptosis-induced release of damage-associated molecular patterns (DAMPs) from dying cells can trigger inflammatory responses that exacerbate microvascular injury [52]. These damage-associated molecular patterns (DAMPs) engage innate immune signaling pathways via pattern-recognition receptors, particularly Toll-like receptors, thereby driving microglial activation and the recruitment of peripheral immune cells into the ischemic brain. The resulting neuroinflammatory response leads to the release of pro-inflammatory cytokines such as interleukin-1β (IL-1β), tumor necrosis factor-α (TNF-α), and interleukin-6 (IL-6), which further enhance oxidative stress and perturb iron homeostasis [59]. These cytokines can upregulate transferrin receptor expression and promote hepcidin-induced ferroportin degradation, thereby reducing iron efflux and promoting intracellular iron accumulation. In parallel, inflammatory signaling pathways compromise antioxidant defense systems, notably the GPX4–glutathione axis, which facilitates unchecked lipid peroxidation and increases cellular vulnerability to ferroptosis [60]. Consequently, inflammation and ferroptosis may form a self-perpetuating pathological cycle that aggravates neuronal and microvascular injury after reperfusion, potentially contributing to futile recanalization despite successful vessel reopening.

Patient heterogeneity significantly influences ferroptosis susceptibility and treatment responses. Age-related iron accumulation and declining antioxidant defenses make elderly patients more vulnerable to ferroptotic injury [61]. Comorbidities such as diabetes mellitus induce chronic oxidative stress and may pre-sensitize tissues to ferroptosis, while chronic kidney disease alters systemic iron homeostasis. Genetic polymorphisms in ferroptosis-related genes (GPX4, SLC7A11, iron metabolism proteins) create variable baseline susceptibilities across individuals. Differences in stroke etiology—cardioembolic versus atherosclerotic versus small vessel occlusion—may influence the extent of ferroptotic injury and response to inhibitors [62, 63]. This heterogeneity necessitates personalized approaches that account for individual patient biology, comorbidities, and stroke characteristics when developing ferroptosis-targeted interventions.

Clinical and radiological factors associated with futile recanalization

While ferroptosis represents a key molecular mechanism underlying futile recanalization, clinical outcomes following mechanical thrombectomy are influenced by a complex interplay of patient-specific, stroke-specific, and procedural factors [55]. Understanding these factors is essential for identifying high-risk patients and developing comprehensive strategies to prevent futile recanalization. Multiple studies have investigated predictors of poor outcomes despite successful reperfusion, revealing several consistent themes across demographic, clinical, radiological, and procedural domains.

Sex differences in ferroptosis susceptibility and stroke outcomes

Sexual dimorphism in iron metabolism and oxidative stress responses represents an important but underappreciated factor influencing ferroptosis susceptibility and stroke outcomes. Premenopausal women demonstrate lower serum ferritin levels and greater iron regulatory protein activity compared to age-matched men, potentially providing inherent protection against ferroptosis-mediated injury. Estrogen's antioxidant properties, including upregulation of GPX4 expression and enhancement of glutathione synthesis, may explain the well-documented sex differences in stroke outcomes among younger patients [64].

However, this protection diminishes after menopause, with postmenopausal women showing increased iron accumulation and oxidative vulnerability comparable to men. Sex chromosomes independently influence ferroptosis pathways, with X-linked genes encoding several iron metabolism proteins (including G6PD and ALAS2) potentially conferring different baseline susceptibilities [65]. Importantly, most preclinical ferroptosis studies have used male animals exclusively, representing a critical gap in translational validity.

Future clinical trials of ferroptosis inhibitors should prospectively examine sex-specific effects and consider hormone status as a key biological variable. Treatment algorithms may need to account for menopausal status, endogenous hormone levels, and sex-specific biomarker thresholds to optimize therapeutic efficacy across all patient populations [66].

Advanced age consistently emerges as one of the strongest independent predictors of futile recanalization, with patients over 80 years showing significantly higher rates of poor outcomes despite successful vessel reopening [58]. The biological basis for this age-related vulnerability likely involves multiple factors, including reduced vascular compliance, decreased cerebrovascular reserve, higher prevalence of comorbidities, and age-related decline in antioxidant defenses. Importantly, aging is associated with increased brain iron accumulation and reduced GPX4 expression, potentially predisposing elderly patients to more severe ferroptosis-mediated injury following reperfusion.

Baseline stroke severity, quantified by the National Institutes of Health Stroke Scale (NIHSS) score, represents another critical determinant of outcomes after thrombectomy. Higher NIHSS scores, reflecting more extensive neurological deficits at presentation, correlate strongly with futile recanalization [57]. This relationship is intuitive, as severe baseline deficits typically indicate larger ischemic territories and more profound tissue injury. However, the molecular mechanisms linking stroke severity to ferroptosis susceptibility remain to be fully elucidated. It is plausible that more severe ischemia creates conditions more conducive to ferroptosis, including greater iron accumulation, more extensive depletion of antioxidant reserves, and more severe mitochondrial dysfunction [58].

Neuroimaging parameters, particularly those reflecting the extent of irreversibly injured tissue and the quality of collateral circulation, are powerful predictors of thrombectomy outcomes. The Alberta Stroke Program Early CT Score (ASPECTS), which quantifies early ischemic changes on non-contrast CT or DWI MRI, inversely correlates with functional outcomes—lower ASPECTS indicates more extensive early infarction and higher risk of futile recanalization [67]. Advanced perfusion imaging techniques, including CT perfusion (CTP) and MRI perfusion, provide additional prognostic information by distinguishing the ischemic core (irreversibly injured tissue) from the penumbra (at-risk but

potentially salvageable tissue) [68]. Patients with large core volumes (typically defined as >70 mL) show substantially higher rates of futile recanalization, even with successful reperfusion [69].

Collateral circulation status plays a pivotal role in determining tissue fate during ischemia and outcomes following reperfusion. Good collaterals maintain some blood flow to the ischemic territory, limiting the extent of core infarction and preserving penumbral tissue that can be salvaged with timely reperfusion [70]. Conversely, poor collaterals allow rapid infarct expansion and tissue damage, reducing the opportunity for meaningful recovery despite successful thrombectomy. Collateral grading systems, such as the American Society of Interventional and Therapeutic Neuroradiology/Society of Interventional Radiology (ASITN/SIR) scale and the Miteff scale, have been developed to standardize collateral assessment and predict outcomes [71].

The time from symptom onset to reperfusion remains a fundamental determinant of outcomes, embodying the principle of "time is brain." Each minute of delay results in the loss of approximately 1.9 million neurons, emphasizing the critical importance of rapid treatment [72]. However, the relationship between time and outcomes is not simply linear. Recent trials have demonstrated that carefully selected patients can benefit from thrombectomy even in extended time windows (up to 24 h), challenging traditional time-based paradigms and shifting focus toward tissue-based selection criteria [73]. Nevertheless, even in these extended windows, faster treatment times within the eligible period correlate with better outcomes, and delayed reperfusion increases the risk of futile recanalization [67].

Procedural factors, including the quality of recanalization achieved and the number of device passes required, influence outcomes. The modified Thrombolysis in Cerebral Infarction (mTICI) scale grades recanalization success, with mTICI 3 (complete reperfusion) associated with better outcomes compared to mTICI 2b (partial reperfusion of >50% but <100% of territory) [68]. However, even among patients achieving mTICI 2b-3, substantial heterogeneity in functional outcomes exists, underscoring the multifactorial nature of futile recanalization [69]. The number of thrombectomy passes required to achieve recanalization also matters, with first-pass complete reperfusion associated with superior outcomes compared to multiple-pass reperfusion, likely due to reduced endothelial injury and shorter procedure times [70].

Beyond traditional 90-day mRS outcomes, ferroptosis may specifically impact cognitive domains through injury to hippocampal regions that are particularly vulnerable due to high iron content and metabolic activity [74]. These regions are critical for memory consolidation and executive function. Emerging evidence links ferroptosis to post-stroke cognitive impairment and dementia risk, which profoundly affects quality of life independent of motor recovery. Post-stroke depression, affecting up to 30–40% of stroke survivors, involves oxidative stress and inflammation closely linked to ferroptosis pathways. Preventing futile recanalization through ferroptosis inhibition could reduce severe disability (mRS 4-5) that creates substantial caregiver burden and healthcare utilization [75].

Ferroptosis may limit neuroplasticity during the recovery phase, as ongoing ferroptotic injury could impair synaptic reorganization and functional compensation. Future clinical trials should incorporate comprehensive neuropsychological testing, quality-of-life assessments (such as Stroke-Specific Quality of Life scale), and caregiver burden measures alongside traditional functional outcomes. Meaningful recovery encompasses cognitive, emotional, and social dimensions beyond physical independence, aligning mechanistic insights with outcomes that truly matter to patients and families [32].

Predictive models for futile recanalization

The development of predictive models to identify patients at high risk for futile recanalization represents a critical area of investigation, offering the potential to refine patient selection, guide treatment decisions, and stratify patients in clinical trials. These models integrate multiple variables across clinical, radiological, and laboratory domains to generate individualized risk estimates [71]. The past decade has witnessed substantial progress in this field, with the emergence of traditional statistical models (primarily nomograms) and more recently, machine learning-based approaches that can capture complex, non-linear relationships between predictor variables [76].

Several nomogram-based models have been developed and validated for predicting futile recanalization. These models typically incorporate readily available variables such as age, baseline NIHSS score, ASPECTS, glucose levels, atrial fibrillation status, time to treatment, and recanalization grade [72]. The SPAN-100 index, calculated as stroke severity (NIHSS) × age, has been widely used as a simple screening tool, with values ≥ 100 identifying patients at higher risk for poor outcomes despite successful recanalization [73]. However, while simple scoring systems offer ease of use, they may not capture the full complexity of factors influencing outcomes and generally show moderate discriminative performance with area under the curve (AUC) values of 0.65–0.75 [77].

More sophisticated nomograms have been constructed using multivariable logistic regression, incorporating additional parameters such as collateral status, white blood cell count, blood pressure variability, and comorbidities [67]. These comprehensive models show improved predictive accuracy compared to simpler scoring systems, with AUC values reaching 0.75–0.85 in derivation cohorts. However, external validation in independent cohorts often reveals reduced performance, highlighting challenges in model generalizability across different populations and practice settings [68].

Rigorous validation strategies are essential for clinical translation of predictive models. Internal validation approaches including k-fold cross-validation (typically 5- or 10-fold) and bootstrap resampling techniques (commonly 500–1,000 iterations) help assess model stability and reduce overfitting risk [53]. However, internal validation alone is insufficient for establishing clinical utility. External validation, testing models in independent cohorts from different institutions or geographic regions, represents the gold standard for assessing generalizability. Most published futile recanalization models show 10–15% decreases in AUC when tested externally, declining from

0.75 to 0.85 in derivation cohorts to 0.65–0.75 in validation cohorts [64].

This performance degradation reflects several factors: (1) differences in patient populations (geographic, demographic, and stroke severity variations); (2) heterogeneity in imaging protocols and interpretation; (3) variability in thrombectomy techniques and operator experience; and (4) differences in post-procedural care pathways. The reduced generalizability highlights critical challenges for clinical implementation. Models developed in comprehensive stroke centers with advanced imaging capabilities may not perform well in community hospitals with limited resources [77]. Prospective, multicenter validation studies are essential before widespread clinical adoption. Collaborative international registries could facilitate more robust external validation by providing large, diverse patient cohorts that better represent real-world practice heterogeneity.

The advent of machine learning has opened new avenues for predictive modeling in stroke. Machine learning algorithms, including random forests, gradient boosting machines, support vector machines, and neural networks, can automatically learn complex patterns from data without requiring explicit specification of variable relationships [78]. These approaches have shown promising results in predicting futile recanalization, with some studies reporting AUC values exceeding 0.85 [79]. Feature importance analyses from these models have identified novel predictors and confirmed the significance of established factors, providing insights into the multifaceted nature of futile recanalization.

Recent studies have begun incorporating ferroptosis-related biomarkers into predictive models, offering the potential for improved risk stratification. Serum ferritin, lipid peroxidation products, and genetic polymorphisms in ferroptosis-related genes (such as GPX4 and SLC7A11) have shown associations with outcomes after thrombectomy [79]. Machine learning models incorporating these biomarkers alongside traditional clinical and radiological variables demonstrate enhanced predictive performance, suggesting that ferroptosis markers provide complementary prognostic information. However, most of these biomarker-enriched models remain in early validation stages and require larger, prospective studies to confirm their clinical utility [80].

Despite these advances, several challenges remain in translating predictive models into routine clinical practice. First, many models lack external validation in diverse populations and healthcare settings, limiting confidence in their generalizability. Second, the optimal threshold for defining "futile recanalization" varies across studies, with some using mRS 3–6 and others using mRS 4–6, complicating comparisons and meta-analyses [81]. Third, most models focus on 90-day functional outcomes, but earlier prediction of outcomes could inform acute management decisions, such as intensity of monitoring or timing of rehabilitation.

Future directions in predictive modeling include the integration of multimodal data, including advanced neuroimaging features (e.g., texture analysis, deep learning-based image interpretation), multi-omic biomarkers (genomics, proteomics, metabolomics), and real-time procedural parameters [82]. Dynamic prediction models that update risk estimates during the course of treatment, incorporating procedural outcomes and early post-procedural data, may offer more nuanced guidance for individualized care. Additionally, the development of explainable AI models that provide transparent reasoning for predictions will be essential for clinical acceptance and implementation [79].

Therapeutic interventions targeting ferroptosis and futile recanalization

The recognition of ferroptosis as a critical mechanism in cerebral ischemia-reperfusion injury and futile recanalization has spurred intense interest in developing therapeutic strategies to inhibit this cell death pathway. Potential interventions span multiple levels, from modulating iron metabolism and enhancing antioxidant defenses to directly inhibiting lipid peroxidation and promoting membrane repair. While most anti-ferroptotic therapies remain in preclinical stages, some have shown sufficient promise to warrant clinical investigation [82].

Iron chelation therapy

Iron chelation represents one of the most direct approaches to preventing ferroptosis by reducing the availability of catalytically active iron. Deferoxamine (DFO), an FDA-approved iron chelator used for treating iron overload conditions, has shown neuroprotective effects in experimental stroke models. DFO chelates free iron, preventing its participation in Fenton chemistry and subsequent lipid peroxidation. In rodent MCAO models, DFO administration reduced infarct volume, improved functional outcomes, and decreased markers of ferroptosis when given during or shortly after reperfusion [80].

Small clinical studies have explored DFO in intracerebral hemorrhage patients, where iron-mediated injury is prominent, showing safety and potential efficacy signals. However, DFO has limitations, including poor blood-brain barrier penetration, short half-life requiring continuous infusion, and potential side effects with high-dose or prolonged use. Newer iron chelators with improved pharmacokinetic properties, such as deferiprone and deferasirox, have shown promise in preclinical studies and may offer advantages for clinical translation [83].

Alternative strategies to modulate iron metabolism include targeting specific components of the iron regulatory pathway. Inhibition of ferritinophagy, either through NCOA4 knockdown or lysosomal inhibition, has demonstrated neuroprotective effects by preventing the liberation of iron from ferritin stores [80]. Upregulation of ferroportin expression or prevention of hepcidin-mediated ferroportin degradation could enhance cellular iron export, reducing intracellular iron accumulation. These more targeted approaches may offer advantages over broad iron chelation by preserving essential iron-dependent processes while specifically blocking pathological iron accumulation [82].

Several ferroptosis-targeting compounds have advanced beyond preclinical stages, providing important translational insights. Deferoxamine has been tested in the i-DEF trial (NCT00777140), a completed phase II study in intracerebral hemorrhage patients that demonstrated safety but mixed efficacy signals. Ongoing investigations are exploring deferoxamine in ischemic stroke populations, though optimal dosing and timing remain uncertain

[53]. N-acetylcysteine (NAC), which replenishes glutathione stores, has been evaluated in recent phase II trials in acute ischemic stroke, demonstrating safety with high-dose intravenous administration (up to 70 mg/kg loading dose followed by 20 mg/kg/hour infusion), though definitive efficacy trials are still needed [63].

Regarding selenium supplementation, observational studies show associations between selenium status and stroke outcomes, but large-scale randomized controlled trials specifically testing selenium in acute stroke are lacking. Novel ferroptosis inhibitors are entering clinical development, including liproxstatin-1 analogs being optimized for improved pharmacokinetics and blood-brain barrier penetration [84]. These compounds show promising preclinical neuroprotective effects, but extensive safety testing is required before human trials. The translation requires addressing challenges including optimal timing relative to reperfusion, identification of biomarkers for patient selection, and development of combination strategies that target multiple ferroptosis pathways simultaneously [54].

Lipophilic antioxidants and ferroptosis inhibitors

Lipophilic radical-trapping antioxidants (RTAs) directly inhibit ferroptosis by intercepting lipid peroxyl radicals and breaking the chain reaction of lipid peroxidation. Ferrostatin-1 (Fer-1), the prototypical ferroptosis inhibitor discovered during the initial characterization of ferroptosis, has shown robust neuroprotective effects in numerous experimental stroke models. Fer-1 functions by directly reducing lipid peroxyl radicals in membranes, preventing the propagation of lipid peroxidation. Importantly, Fer-1 provides protection even when administered hours after ischemia onset, highlighting a therapeutic window that extends well beyond the acute reperfusion phase [80].

Liproxstatin-1 (Lip-1), a more potent analog of Fer-1 with improved pharmacokinetic properties, demonstrates enhanced efficacy in preventing ferroptosis-mediated neuronal death. Lip-1 exhibits better blood-brain barrier penetration and longer half-life compared to Fer-1, making it more suitable for clinical development. In MCAO models with reperfusion, Lip-1 treatment significantly reduced infarct volume, preserved penumbral tissue, and improved neurobehavioral outcomes [85].

Vitamin E (α-tocopherol), a lipid-soluble antioxidant that has been used safely in humans for decades, functions as a chain-breaking antioxidant by donating hydrogen atoms to lipid peroxyl radicals. While vitamin E has shown mixed results in clinical stroke trials when used alone, its combination with other antioxidants or ferroptosis inhibitors may offer synergistic neuroprotection. Tocotrienols, unsaturated forms of vitamin E with enhanced antioxidant activity, have demonstrated superior neuroprotective effects in experimental models and warrant further investigation [86].

CoQ10 and its reduced form, ubiquinol, serve dual roles as mitochondrial electron transport chain components and lipophilic antioxidants capable of preventing lipid peroxidation [73]. Given the newly discovered FSP1-CoQ10 and DHODH-CoQ10 anti-ferroptotic pathways, therapeutic strategies to enhance CoQ10 availability may offer particular promise. CoQ10 supplementation has shown safety in numerous clinical studies, though its efficacy in acute stroke requires rigorous evaluation [85].

Enhancing GPX4 activity and glutathione availability

Strategies to enhance GPX4 expression and activity represent logical approaches to preventing ferroptosis, given GPX4's central role as the primary defense against lipid peroxidation. Selenium supplementation can enhance GPX4 activity by ensuring adequate incorporation of selenocysteine into the enzyme's catalytic site. Clinical studies have shown associations between selenium status and stroke outcomes, with selenium deficiency linked to increased stroke severity and poorer recovery. However, optimal dosing and timing of selenium supplementation in acute stroke remain to be established, and excessive selenium can be toxic [86].

Increasing GSH availability represents another avenue for enhancing GPX4-dependent ferroptosis resistance. N-acetylcysteine (NAC), a precursor to cysteine and GSH, has been widely used as an antioxidant and mucolytic agent with an excellent safety profile [87]. NAC can replenish cellular GSH stores, supporting GPX4 activity and enhancing overall antioxidant capacity. Clinical trials of NAC in acute stroke have shown mixed results, potentially due to suboptimal dosing or timing, but the compound's safety and theoretical rationale support continued investigation [86].

Modulation of system xc^- activity presents a more nuanced challenge. While inhibition of system xc^- induces ferroptosis in experimental settings, enhancing its activity may protect against ferroptosis by promoting cystine uptake and GSH synthesis. However, system xc^- upregulation could potentially exacerbate glutamate excitotoxicity, a competing mechanism of ischemic injury. This complex interplay highlights the need for careful optimization of therapeutic strategies targeting system xc^- in stroke [87].

Activation of the Nrf2 pathway, which transcriptionally upregulates multiple antioxidant genes including SLC7A11, GPX4, and glutamate-cysteine ligase, offers a coordinated approach to enhancing cellular anti-ferroptotic defenses [86]. Several Nrf2 activators, including dimethyl fumarate (DMF) and sulforaphane, have shown neuroprotective effects in experimental stroke models. DMF is already FDA-approved for multiple sclerosis treatment, potentially facilitating its repurposing for stroke neuroprotection [87].

Future perspectives and clinical translation

The integration of ferroptosis biology into our understanding of ischemic stroke pathophysiology and futile recanalization represents a paradigm shift with significant implications for future research and clinical practice [86]. Moving forward, several key priorities emerge that could accelerate the translation of ferroptosis-targeted therapies from bench to bedside and ultimately improve outcomes for stroke patients undergoing mechanical thrombectomy [88].

Implementation challenges and health economics considerations

The proposed integration of ferroptosis biomarkers, advanced multimodal neuroimaging, and machine learning-based predictive models requires substantial infrastructure investment that may be prohibitive in many healthcare settings. Low-resource settings might initially focus on simple, readily available markers such as serum ferritin and basic iron panels, while reserving sophisticated multimodal approaches for well-resourced comprehensive stroke centers. Preventing futile recanalization could substantially reduce long-term healthcare costs associated with severe disability, potentially offsetting upfront diagnostic and therapeutic expenses. However, formal cost-effectiveness analyses are currently lacking and represent a critical research priority [53].

Global health equity concerns are paramount, as low- and middle-income countries bearing the highest stroke burden often lack access even to basic thrombectomy services, let alone advanced ferroptosis-targeted interventions. International collaborations should focus on developing affordable, point-of-care ferroptosis biomarker assays and simplified risk stratification tools that can be implemented in resource-limited settings [75]. This approach grounds our translational framework in practical healthcare delivery realities and acknowledges the economic constraints that will ultimately determine clinical adoption of ferroptosis-targeted strategies.

Translational challenges and the validity gap in ferroptosis research

Most preclinical ferroptosis studies employ young (8–12 week old), genetically uniform rodents subjected to standardized temporary MCAO, which poorly represents the elderly, heterogeneous stroke population with multiple comorbidities [89]. Specific translational concerns include: (1) aging-related changes, noting that elderly patients demonstrate baseline iron accumulation, reduced GPX4 expression, impaired autophagy, and chronic oxidative stress that fundamentally alter ferroptosis susceptibility; (2) comorbidity effects, with diabetes causing chronic hyperglycemia and oxidative stress that may pre-sensitize neurons, while chronic kidney disease alters systemic iron handling; (3) pre-existing white matter disease and cerebral small vessel disease that modify tissue vulnerability; (4) polypharmacy effects, as commonly used medications (statins, antihypertensives, anticoagulants) may interact with ferroptosis pathways unpredictably [74].

Development of aged animal models with relevant comorbidities (diabetic, hypertensive strains) and incorporation of chronic treatment paradigms are essential for more clinically relevant translational research. Early-phase clinical trials should specifically recruit patients representative of real-world stroke populations rather than highly selected cohorts, and translational studies should systematically examine how aging and comorbidities modify responses to ferroptosis inhibition [62]. This critical self-reflection acknowledges fundamental limitations in the current evidence base and provides a roadmap for more clinically relevant research.

First, the development and validation of clinically applicable ferroptosis biomarkers is essential for identifying patients at highest risk and monitoring treatment responses. While experimental studies have identified numerous ferroptosis markers in brain tissue, translating these findings to accessible biomarkers in blood or cerebrospinal fluid remains challenging. Potential candidates include circulating levels of lipid peroxidation products (MDA, 4-HNE), iron metabolism markers (ferritin, transferrin saturation, hepcidin), and emerging omics-based signatures (ferroptosis-related gene expression panels, metabolomic profiles) [90]. Prospective studies correlating these biomarkers with clinical outcomes in well-characterized patient cohorts are needed to establish their prognostic value.

Second, advanced neuroimaging techniques capable of detecting ferroptosis *in vivo* would enable real-time assessment of ferroptotic injury and guide therapeutic interventions. Quantitative susceptibility mapping (QSM) shows promise for detecting iron accumulation in the brain and has already been applied in stroke patients [91]. The development of PET or SPECT tracers specific for ferroptosis markers, such as lipid peroxidation products or ferroptosis-related proteins, could provide dynamic imaging of ferroptotic cell death. Integration of these imaging biomarkers into predictive models may substantially improve risk stratification and treatment selection [92].

Third, rigorous clinical trials of ferroptosis inhibitors in acute ischemic stroke are urgently needed. Several candidates with favorable safety profiles in other indications (e.g., DFO, NAC, vitamin E, selenium, CoQ10) could be rapidly moved into phase II trials. Novel compounds with superior pharmacokinetic properties and greater specificity for ferroptosis pathways are in preclinical development and should be prioritized for clinical translation [93]. Trial design considerations include optimal timing of intervention (during thrombectomy, immediately post-procedure, or in the subsequent hours to days), dosing regimens, and selection of appropriate patient populations most likely to benefit [94].

Fourth, combination therapeutic strategies that target multiple aspects of reperfusion injury, including ferroptosis, excitotoxicity, inflammation, and oxidative stress, may offer synergistic neuroprotection [94]. Historical neuroprotection trials have largely focused on single mechanisms, potentially explaining their failure to demonstrate clinical benefit. A precision medicine approach that matches specific neuroprotective strategies to individual patient biology and injury patterns, informed by biomarkers and predictive models, may finally succeed where previous one-size-fits-all approaches have failed [95].

Finally, the investigation of ferroptosis extends beyond the acute reperfusion period, with potential relevance to stroke recovery and long-term neuroplasticity. Chronic neuroinflammation and oxidative stress persist for weeks to months after stroke, potentially contributing to ongoing neuronal loss and limiting recovery. Whether ferroptosis continues to play a role in this chronic phase and whether sustained ferroptosis inhibition could enhance recovery remains to be determined [90]. Additionally, understanding how ferroptosis and its inhibition influence neuroplasticity, neurogenesis, and functional reorganization could inform rehabilitation strategies and optimize long-term outcomes [91].

Discussion

Overall interpretation of the evidence

Futile recanalization following mechanical thrombectomy for acute ischemic stroke represents a critical challenge that limits the effectiveness of an otherwise revolutionary treatment. The emergence of ferroptosis as a key mechanism underlying reperfusion injury and poor outcomes provides new insights into this phenomenon and offers novel therapeutic targets. Ferroptosis, characterized by iron-dependent lipid peroxidation, is driven by disruption of iron homeostasis, accumulation of oxidized phospholipids, and failure of antioxidant defense systems, particularly the GPX4-GSH axis. Multiple lines of evidence from experimental and clinical studies support the involvement of ferroptosis in ischemic stroke, especially in the context of reperfusion injury following mechanical thrombectomy.

Clinical implications

A comprehensive understanding of futile recanalization requires integration of ferroptosis mechanisms with established clinical, radiological, and procedural factors. Patient characteristics (age, comorbidities), stroke features (severity, infarct size, collateral status), timing of treatment, and quality of reperfusion all interact to determine outcomes. Predictive models incorporating these multiple dimensions, potentially enhanced by ferroptosis biomarkers, offer promise for improved risk stratification and personalized treatment strategies. Therapeutic interventions targeting ferroptosis, including iron chelation, lipophilic antioxidants, and strategies to enhance GPX4 activity, have shown efficacy in preclinical models and warrant clinical investigation.

Future directions

Moving forward, the field requires continued collaboration between basic scientists, clinical researchers, and industry partners to translate ferroptosis biology into actionable clinical applications. The development of validated biomarkers, advanced imaging techniques, and targeted therapies specifically designed for the unique pathophysiology of ischemic stroke with reperfusion will be essential. With the growing recognition that successful recanalization is necessary but not sufficient for good outcomes, addressing the molecular mechanisms of reperfusion injury, particularly ferroptosis, may finally bridge the gap between technical success and meaningful functional recovery.

Conclusion

By combining optimal revascularization techniques with targeted strategies aimed at preventing or attenuating ferroptosis-mediated neuronal injury and its downstream pathological consequences, it may be possible to reduce the incidence of futile recanalization and maximize the benefit of mechanical thrombectomy for stroke patients.

Author contributions

YW drafted the manuscript. CZ and YP contributed to literature collection, manuscript writing, and revision. LL conceived and supervised the work and critically revised the manuscript. All authors contributed to the article and approved the submitted version.

Funding

The author(s) declared that financial support was not received for this work and/or its publication.

Conflict of interest

The author(s) declared no potential conflicts of interest with respect to the research, authorship, and/or publication of this article.

Generative AI statement

The author(s) declared that generative AI was not used in the creation of this manuscript.

Any alternative text (alt text) provided alongside figures in this article has been generated by Frontiers with the support of artificial intelligence and reasonable efforts have been made to ensure accuracy, including review by the authors wherever possible. If you identify any issues, please contact us.

References

1. Global, regional, and national burden of stroke and its risk factors, 1990-2019: a systematic analysis for the global burden of disease study 2019. *Lancet Neurol* (2021) 20: 795–820. doi:10.1016/s1474-4422(21)00252-0

2. Campbell BCV, De Silva DA, Macleod MR, Coutts SB, Schwamm LH, Davis SM, et al. Ischaemic stroke. *Nat Rev Dis Primers* (2019) 5:70. doi:10.1038/s41572-019-0118-8

3. Virani SS, Alonso A, Benjamin EJ, Bittencourt MS, Callaway CW, Carson AP, et al. Heart disease and stroke Statistics-2020 update: a report from the American heart association. *Circulation* (2020) 141:e139–e596. doi:10.1161/cir.0000000000000757

4. Dirnagl U, Iadecola C, Moskowitz MA. Pathobiology of ischaemic stroke: an integrated view. *Trends Neurosci* (1999) 22:391–7. doi:10.1016/s0166-2236(99)01401-0

5. Powers WJ, Rabinstein AA, Ackerson T, Adeoye OM, Bambakidis NC, Becker K, et al. Guidelines for the early management of patients with acute ischemic stroke: 2019 update to the 2018 guidelines for the early management of acute ischemic stroke: a guideline for healthcare professionals from the American heart association/american stroke association. *Stroke* (2019) 50:e344–e418. doi:10.1161/str.0000000000000211

6. Goyal M, Menon BK, van Zwam WH, Dippel DW, Mitchell PJ, Demchuk AM, et al. Endovascular thrombectomy after large-vessel ischaemic stroke: a meta-analysis of individual patient data from five randomised trials. *Lancet* (2016) 387:1723–31. doi:10.1016/s0140-6736(16)00163-x

7. Berkhemer OA, Fransen PS, Beumer D, van den Berg LA, Lingsma HF, Yoo AJ, et al. A randomized trial of intraarterial treatment for acute ischemic stroke. *N Engl J Med* (2015) 372:11–20. doi:10.1056/NEJMoa1411587

8. Campbell BC, Mitchell PJ, Kleinig TJ, Dewey HM, Churilov L, Yassi N, et al. Endovascular therapy for ischemic stroke with perfusion-imaging selection. *N Engl J Med* (2015) 372:1009–18. doi:10.1056/NEJMoa1414792

9. Goyal M, Demchuk AM, Menon BK, Eesa M, Rempel JL, Thornton J, et al. Randomized assessment of rapid endovascular treatment of ischemic stroke. *N Engl J Med* (2015) 372:1019–30. doi:10.1056/NEJMoa1414905

10. Saver JL, Goyal M, Bonafe A, Diener HC, Levy EI, Pereira VM, et al. Stent-retriever thrombectomy after intravenous t-PA vs. t-PA alone in stroke. *N Engl J Med* (2015) 372: 2285–95. doi:10.1056/NEJMoa1415061

11. Jovin TG, Chamorro A, Cobo E, de Miquel MA, Molina CA, Rovira A, et al. Thrombectomy within 8 hours after symptom onset in ischemic stroke. *N Engl J Med* (2015) 372:2296–306. doi:10.1056/NEJMoa1503780

12. Nogueira RG, Jadhav AP, Haussen DC, Bonafe A, Budzik RF, Bhuva P, et al. Thrombectomy 6 to 24 hours after stroke with a mismatch between deficit and infarct. *N Engl J Med* (2018) 378:11–21. doi:10.1056/NEJMoa1706442

13. Albers GW, Marks MP, Kemp S, Christensen S, Tsai JP, Ortega-Gutierrez S, et al. Thrombectomy for stroke at 6 to 16 hours with selection by perfusion imaging. *N Engl J Med* (2018) 378:708–18. doi:10.1056/NEJMoa1713973

14. Zaidat OO, Yoo AJ, Khatri P, Tomsick TA, von Kummer R, Saver JL, et al. Recommendations on angiographic revascularization grading standards for acute ischemic stroke: a consensus statement. *Stroke* (2013) 44:2650–63. doi:10.1161/strokeaha.113.001972

15. Hussein HM, Georgiadis AL, Vazquez G, Miley JT, Memon MZ, Mohammad YM, et al. Occurrence and predictors of futile recanalization following endovascular treatment among patients with acute ischemic stroke: a multicenter study. *AJNR Am J Neuroradiol* (2010) 31:454–8. doi:10.3174/ajnr.A2006

16. Kim H, Kim J-T, Choi K-H, Yoon W, Baek BH, Kim SK, et al. Futile recanalization after endovascular treatment in acute ischemic stroke with large ischemic core. *BMC Neurol* (2024) 24:395. doi:10.1186/s12883-024-03912-9

17. Kaesmacher J, Dobrocky T, Heldner MR, Bellwald S, Mosimann PJ, Mordasini P, et al. Systematic review and meta-analysis on outcome differences among patients with TICI2b *versus* TICI3 reperfusions: success revisited. *J Neurol Neurosurg Psychiatry* (2018) 89:910–7. doi:10.1136/jnnp-2017-317602

18. van Horn N, Kniep H, Leischner H, McDonough R, Deb-Chatterji M, Broocks G, et al. Predictors of poor clinical outcome despite complete reperfusion in acute ischemic stroke patients. *J Neurointerv Surg* (2021) 13:14–8. doi:10.1136/neurintsurg-2020-015889

19. Leng X, Lan L, Liu L, Leung TW, Wong KS. Good collateral circulation predicts favorable outcomes in intravenous thrombolysis: a systematic review and meta-analysis. *Eur J Neurol* (2016) 23:1738–49. doi:10.1111/ene.13111

20. Stockwell BR, Friedmann Angeli JP, Bayir H, Bush AI, Conrad M, Dixon SJ, et al. Ferroptosis: a regulated cell death nexus linking metabolism, redox biology, and disease. *Cell* (2017) 171:273–85. doi:10.1016/j.cell.2017.09.021

21. Jiang X, Stockwell BR, Conrad M. Ferroptosis: mechanisms, biology and role in disease. *Nat Rev Mol Cell Biol* (2021) 22:266–82. doi:10.1038/s41580-020-00324-8

22. Dixon SJ, Lemberg KM, Lamprecht MR, Skouta R, Zaitsev EM, Gleason CE, et al. Ferroptosis: an iron-dependent form of nonapoptotic cell death. *Cell* (2012) 149: 1060–72. doi:10.1016/j.cell.2012.03.042

23. Iadecola C, Anrather J. The immunology of stroke: from mechanisms to translation. *Nat Med* (2011) 17:796–808. doi:10.1038/nm.2399

24. Kalogeris T, Baines CP, Krenz M, Korthuis RJ. Cell biology of ischemia/reperfusion injury. *Int Rev Cell Mol Biol* (2012) 298:229–317. doi:10.1016/b978-0-12-394309-5.00006-7

25. Li J, Cao F, Yin HL, Huang ZJ, Lin ZT, Mao N, et al. Ferroptosis: past, present and future. *Cell Death Dis* (2020) 11:88. doi:10.1038/s41419-020-2298-2

26. Tang D, Chen X, Kang R, Kroemer G. Ferroptosis: molecular mechanisms and health implications. *Cell Res* (2021) 31:107–25. doi:10.1038/s41422-020-00441-1

27. Chen X, Li J, Kang R, Klionsky DJ, Tang D. Ferroptosis: machinery and regulation. *Autophagy* (2021) 17:2054–81. doi:10.1080/15548627.2020.1810918

28. Li Q, Han X, Lan X, Gao Y, Wan J, Durham F, et al. Inhibition of neuronal ferroptosis protects hemorrhagic brain. *JCI Insight* (2017) 2:e90777. doi:10.1172/jci.insight.90777

29. Linkermann A, Skouta R, Himmerkus N, Mulay SR, Dewitz C, De Zen F, et al. Synchronized renal tubular cell death involves ferroptosis. *Proc Natl Acad Sci U S A* (2014) 111:16836–41. doi:10.1073/pnas.1415518111

30. Guiney SJ, Adlard PA, Bush AI, Finkelstein DI, Ayton S. Ferroptosis and cell death mechanisms in parkinson's disease. *Neurochem Int* (2017) 104:34–48. doi:10.1016/j.neuint.2017.01.004

31. Zhou L, Han S, Guo J, Qiu T, Zhou J, Shen L. Ferroptosis-A new dawn in the treatment of organ ischemia-reperfusion injury. *Cells* (2022) 11:3653. doi:10.3390/cells11223653

32. Long Z, Zhu Y, Zhao H, Liao S, Liu C. Ferroptosis in ischemic stroke: mechanisms, pathological implications, and therapeutic strategies. *Front Neurosci* (2025) 19:1623485. doi:10.3389/fnins.2025.1623485

33. Tuo QZ, Lei P, Jackman KA, Li XL, Xiong H, Li XL, et al. Tau-mediated iron export prevents ferroptotic damage after ischemic stroke. *Mol Psychiatry* (2017) 22:1520–30. doi:10.1038/mp.2017.171

34. Zille M, Karuppagounder SS, Chen Y, Gough PJ, Bertin J, Finger J, et al. Neuronal death after hemorrhagic stroke *in vitro* and *in vivo* shares features of ferroptosis and necroptosis. *Stroke* (2017) 48:1033–43. doi:10.1161/strokeaha.116.015609

35. Yang WS, SriRamaratnam R, Welsch ME, Shimada K, Skouta R, Viswanathan VS, et al. Regulation of ferroptotic cancer cell death by GPX4. *Cell* (2014) 156:317–31. doi:10.1016/j.cell.2013.12.010

36. Doll S, Proneth B, Tyurina YY, Panzilius E, Kobayashi S, Ingold I, et al. ACSL4 dictates ferroptosis sensitivity by shaping cellular lipid composition. *Nat Chem Biol* (2017) 13:91–8. doi:10.1038/nchembio.2239

37. Wenzel SE, Tyurina YY, Zhao J, St Croix CM, Dar HH, Mao G, et al. PEBP1 wardens ferroptosis by enabling lipoxygenase generation of lipid death signals. *Cell* (2017) 171: 628–41.e26. doi:10.1016/j.cell.2017.09.044

38. Shah R, Shchepinov MS, Pratt DA. Resolving the role of lipoxygenases in the initiation and execution of ferroptosis. *ACS Cent Sci* (2018) 4:387–96. doi:10.1021/acscentsci.7b00589

39. Skouta R, Dixon SJ, Wang J, Dunn DE, Orman M, Shimada K, et al. Ferrostatins inhibit oxidative lipid damage and cell death in diverse disease models. *J Am Chem Soc* (2014) 136:4551–6. doi:10.1021/ja411006a

40. Kagan VE, Mao G, Qu F, Angeli JP, Doll S, Croix CS, et al. Oxidized arachidonic and adrenic PEs navigate cells to ferroptosis. *Nat Chem Biol* (2017) 13:81–90. doi:10.1038/nchembio.2238

41. Friedmann AJP, Schneider M, Proneth B, Tyurina YY, Tyurin VA, Hammond VJ, et al. Inactivation of the ferroptosis regulator Gpx4 triggers acute renal failure in mice. *Nat Cell Biol* (2014) 16:1180–91. doi:10.1038/ncb3064

42. Bersuker K, Hendricks JM, Li Z, Magtanong L, Ford B, Tang PH, et al. The CoQ oxidoreductase FSP1 acts parallel to GPX4 to inhibit ferroptosis. *Nature* (2019) 575: 688–92. doi:10.1038/s41586-019-1705-2

43. Doll S, Freitas FP, Shah R, Aldrovandi M, da Silva MC, Ingold I, et al. FSP1 is a glutathione-independent ferroptosis suppressor. *Nature* (2019) 575:693–8. doi:10.1038/s41586-019-1707-0

44. Kraft VAN, Bezjian CT, Pfeiffer S, Ringelstetter L, Müller C, Zandkarimi F, et al. GTP cyclohydrolase 1/Tetrahydrobiopterin counteract ferroptosis through lipid remodeling. *ACS Cent Sci* (2020) 6:41–53. doi:10.1021/acscentsci.9b01063

45. Soula M, Weber RA, Zilka O, Alwaseem H, La K, Yen F, et al. Metabolic determinants of cancer cell sensitivity to canonical ferroptosis inducers. *Nat Chem Biol* (2020) 16:1351–60. doi:10.1038/s41589-020-0613-y

46. Chen L, Hambright WS, Na R, Ran Q. Ablation of the ferroptosis inhibitor glutathione peroxidase 4 in neurons results in rapid motor neuron degeneration and paralysis. *J Biol Chem* (2015) 290:28097–106. doi:10.1074/jbc.M115.680090

47. Forcina GC, Dixon SJ. GPX4 at the crossroads of lipid homeostasis and ferroptosis. *Proteomics* (2019) 19:e1800311. doi:10.1002/pmic.201800311

48. Ursini F, Maiorino M. Lipid peroxidation and ferroptosis: the role of GSH and GPx4. *Free Radic Biol Med* (2020) 152:175–85. doi:10.1016/j.freeradbiomed.2020.02.027

49. Yant LJ, Ran Q, Rao L, Van Remmen H, Shibatani T, Belter JG, et al. The selenoprotein GPX4 is essential for mouse development and protects from radiation and oxidative damage insults. *Free Radic Biol Med* (2003) 34:496–502. doi:10.1016/s0891-5849(02)01360-6

50. Imai H, Matsuoka M, Kumagai T, Sakamoto T, Koumura T. Lipid peroxidation-dependent cell death regulated by GPx4 and ferroptosis. *Curr Top Microbiol Immunol* (2017) 403:143–70. doi:10.1007/82_2016_508

51. Brigelius-Flohé R, Maiorino M. Glutathione peroxidases. *Biochim Biophys Acta* (2013) 1830:3289–303. doi:10.1016/j.bbagen.2012.11.020

52. Shimada K, Skouta R, Kaplan A, Yang WS, Hayano M, Dixon SJ, et al. Global survey of cell death mechanisms reveals metabolic regulation of ferroptosis. *Nat Chem Biol* (2016) 12:497–503. doi:10.1038/nchembio.2079

53. Yeh SJ, Chen CH, Lin YH, Tsai LK, Lee CW, Sun Y, et al. Ferroptosis biomarkers predict the outcomes of patients with acute ischemic stroke undergoing endovascular thrombectomy. *Sci Rep* (2025) 15:39510. doi:10.1038/s41598-025-23289-0

54. Bao S, Liu C, Wang QW, Zhang C, Zhao H. Temporal dynamics of ferroptosis markers and neuroprotective intervention in cerebral ischemia-reperfusion injury: insights for therapeutic strategy development. *Iran J Basic Med Sci* (2025) 28: 1699–705. doi:10.22038/ijbms.2025.82625.17865

55. Dixon SJ, Winter GE, Musavi LS, Lee ED, Snijder B, Rebsamen M, et al. Human haploid cell genetics reveals roles for lipid metabolism genes in nonapoptotic cell death. *ACS Chem Biol* (2015) 10:1604–9. doi:10.1021/acschembio.5b00245

56. Yuan H, Li X, Zhang X, Kang R, Tang D. Identification of ACSL4 as a biomarker and contributor of ferroptosis. *Biochem Biophys Res Commun* (2016) 478:1338–43. doi:10.1016/j.bbrc.2016.08.124

57. Zou Y, Li H, Graham ET, Deik AA, Eaton JK, Wang W, et al. Cytochrome P450 oxidoreductase contributes to phospholipid peroxidation in ferroptosis. *Nat Chem Biol* (2020) 16:302–9. doi:10.1038/s41589-020-0472-6

58. Yan B, Ai Y, Sun Q, Ma Y, Cao Y, Wang J, et al. Membrane damage during ferroptosis is caused by oxidation of phospholipids catalyzed by the oxidoreductases POR and CYB5R1. *Mol Cell* (2021) 81:355–69.e10. doi:10.1016/j.molcel.2020.11.024

59. Shimamura M, Nakagami H, Katsuya T, Morishita R. Current status and prospects for development of therapy targeting post-ischemic inflammation in ischemic stroke. *Vasc Fail* (2023) 7:1–5. doi:10.30548/vascfail.7.1_1

60. Cherayil BJ. Pathophysiology of iron homeostasis during inflammatory states. *J Pediatr* (2015) 167:S15–9. doi:10.1016/j.jpeds.2015.07.015

61. Wu C, Xu Z, Wang Q, Zhu S, Tang C. Decoding ferroptosis in ischemic stroke: key genes and the therapeutic potential of acupuncture. *Front Aging Neurosci* (2025) 17: 1506276. doi:10.3389/fnagi.2025.1506276

62. Tuo QZ, Lei P. Ferroptosis in ischemic stroke: animal models and mechanisms. *Zool Res* (2024) 45:1235–48. doi:10.24272/j.issn.2095-8137.2024.239

63. Liu C, Wang G, Han W, Tian Q, Li M. Ferroptosis: a potential therapeutic target for stroke. *Neural Regen Res* (2024) 19:988–97. doi:10.4103/1673-5374.385284

64. Shah EG, Bhojwani M, Chang K, Dongarwar D, Gonzales NR, Jones E, et al. Sex differences in etiologies, risk factors, and outcomes among young adult patients with acute ischemic stroke. *J Stroke Cerebrovasc Dis* (2025) 34:108380. doi:10.1016/j.jstrokecerebrovasdis.2025.108380

65. Ide S, Ide K, Abe K, Kobayashi Y, Kitai H, McKey J, et al. Sex differences in resilience to ferroptosis underlie sexual dimorphism in kidney injury and repair. *Cell Rep* (2022) 41:111610. doi:10.1016/j.celrep.2022.111610

66. Ugidos IF, Pistono C, Korhonen P, Gómez-Budia M, Sitnikova V, Klecki P, et al. Sex differences in poststroke inflammation: a focus on microglia across the lifespan. *Stroke* (2022) 53:1500–9. doi:10.1161/strokeaha.122.039138

67. Gao M, Monian P, Pan Q, Zhang W, Xiang J, Jiang X. Ferroptosis is an autophagic cell death process. *Cell Res* (2016) 26:1021–32. doi:10.1038/cr.2016.95

68. Hou W, Xie Y, Song X, Sun X, Lotze MT, Zeh HJ, 3rd, et al. Autophagy promotes ferroptosis by degradation of ferritin. *Autophagy* (2016) 12:1425–8. doi:10.1080/15548627.2016.1187366

69. Yang M, Chen P, Liu J, Zhu S, Kroemer G, Klionsky DJ, et al. Clockophagy is a novel selective autophagy process favoring ferroptosis. *Sci Adv* (2019) 5:eaaw2238. doi:10.1126/sciadv.aaw2238

70. Sun X, Ou Z, Chen R, Niu X, Chen D, Kang R, et al. Activation of the p62-Keap1-NRF2 pathway protects against ferroptosis in hepatocellular carcinoma cells. *Hepatology* (2016) 63:173–84. doi:10.1002/hep.28251

71. Kerins MJ, Ooi A. The roles of NRF2 in modulating cellular iron homeostasis. *Antioxid Redox Signal* (2018) 29:1756–73. doi:10.1089/ars.2017.7176

72. Mancias JD, Wang X, Gygi SP, Harper JW, Kimmelman AC. Quantitative proteomics identifies NCOA4 as the cargo receptor mediating ferritinophagy. *Nature* (2014) 509:105–9. doi:10.1038/nature13148

73. Gao M, Monian P, Quadri N, Ramasamy R, Jiang X. Glutaminolysis and transferrin regulate ferroptosis. *Mol Cell* (2015) 59:298–308. doi:10.1016/j.molcel.2015.06.011

74. Bu ZQ, Yu HY, Wang J, He X, Cui YR, Feng JC, et al. Emerging role of ferroptosis in the pathogenesis of ischemic stroke: a new therapeutic target? *ASN Neuro* (2021) 13: 17590914211037505. doi:10.1177/17590914211037505

75. Song C, Liu Z, Tang J, Huang Y. Ferroptosis in cerebral ischemia/reperfusion injury: Mechanistic drivers and therapeutic frontiers. *Neuropsychiatr Dis Treat* (2026) 22: 580170. doi:10.2147/ndt.S580170

76. Dodson M, Castro-Portuguez R, Zhang DD. NRF2 plays a critical role in mitigating lipid peroxidation and ferroptosis. *Redox Biol* (2019) 23:101107. doi:10.1016/j.redox.2019.101107

77. Carcel C, Sandset EC, Ali M, Allende Echanez MI, Mosconi MG, de Souza AC, et al. Addressing sex and gender differences in stroke risk and management: a scientific statement from the world stroke organization. *Int J Stroke* (2026) 21:303–23. doi:10.1177/17474930251393009

78. Brown CW, Amante JJ, Chhoy P, Elaimy AL, Liu H, Zhu LJ, et al. Prominin2 drives ferroptosis resistance by stimulating iron export. *Dev Cell* (2019) 51:575–86.e4. doi:10.1016/j.devcel.2019.10.007

79. Seiler A, Schneider M, Förster H, Roth S, Wirth EK, Culmsee C, et al. Glutathione peroxidase 4 senses and translates oxidative stress into 12/15-lipoxygenase dependent- and AIF-mediated cell death. *Cell Metab* (2008) 8:237–48. doi:10.1016/j.cmet.2008.07.005

80. Ayala A, Muñoz MF, Argüelles S. Lipid peroxidation: production, metabolism, and signaling mechanisms of malondialdehyde and 4-hydroxy-2-nonenal. *Oxid Med Cell Longev* (2014) 2014:360438. doi:10.1155/2014/360438

81. Zhong H, Yin H. Role of lipid peroxidation derived 4-hydroxynonenal (4-HNE) in cancer: focusing on mitochondria. *Redox Biol* (2015) 4:193–9. doi:10.1016/j.redox.2014.12.011

82. Esterbauer H, Schaur RJ, Zollner H. Chemistry and biochemistry of 4-hydroxynonenal, malonaldehyde and related aldehydes. *Free Radic Biol Med* (1991) 11:81–128. doi:10.1016/0891-5849(91)90192-6

83. Yang WS, Kim KJ, Gaschler MM, Patel M, Shchepinov MS, Stockwell BR. Peroxidation of polyunsaturated fatty acids by lipoxygenases drives ferroptosis. *Proc Natl Acad Sci U S A* (2016) 113:E4966–75. doi:10.1073/pnas.1603244113

84. Cao Y, Li Y, He C, Yan F, Li JR, Xu HZ, et al. Selective ferroptosis inhibitor Liproxstatin-1 attenuates neurological deficits and neuroinflammation after subarachnoid hemorrhage. *Neurosci Bull* (2021) 37:535–49. doi:10.1007/s12264-020-00620-5

85. Meister A, Anderson ME. Glutathione. *Annu Rev Biochem* (1983) 52:711–60. doi:10.1146/annurev.bi.52.070183.003431

86. Lu SC. Glutathione synthesis. *Biochim Biophys Acta* (2013) 1830:3143–53. doi:10.1016/j.bbagen.2012.09.008

87. Conrad M, Sato H. The oxidative stress-inducible cystine/glutamate antiporter, system x (c) (-): cystine supplier and beyond. *Amino Acids* (2012) 42:231–46. doi:10.1007/s00726-011-0867-5

88. Cao JY, Dixon SJ. Mechanisms of ferroptosis. *Cell Mol Life Sci* (2016) 73:2195–209. doi:10.1007/s00018-016-2194-1

89. Lee J, Hyun DH. The interplay between intracellular iron homeostasis and neuroinflammation in neurodegenerative diseases. *Antioxidants (Basel)* (2023) 12: 918. doi:10.3390/antiox12040918

90. Viswanathan VS, Ryan MJ, Dhruv HD, Gill S, Eichhoff OM, Seashore-Ludlow B, et al. Dependency of a therapy-resistant state of cancer cells on a lipid peroxidase pathway. *Nature* (2017) 547:453–7. doi:10.1038/nature23007

91. Hassannia B, Vandenabeele P, Vanden Berghe T. Targeting ferroptosis to iron out cancer. *Cancer Cell* (2019) 35:830–49. doi:10.1016/j.ccell.2019.04.002

92. Anthonymuthu TS, Kenny EM, Bayır H. Therapies targeting lipid peroxidation in traumatic brain injury. *Brain Res* (2016) 1640:57–76. doi:10.1016/j.brainres.2016.02.006

93. Magtanong L, Ko PJ, To M, Cao JY, Forcina GC, Tarangelo A, et al. Exogenous monounsaturated Fatty acids promote a ferroptosis-resistant cell state. *Cell Chem Biol* (2019) 26:420–32.e9. doi:10.1016/j.chembiol.2018.11.016

94. Zilka O, Shah R, Li B, Friedmann Angeli JP, Griesser M, Conrad M, et al. On the mechanism of cytoprotection by Ferrostatin-1 and Liproxstatin-1 and the role of lipid peroxidation in ferroptotic cell death. *ACS Cent Sci* (2017) 3:232–43. doi:10.1021/acscentsci.7b00028

95. Ingold I, Berndt C, Schmitt S, Doll S, Poschmann G, Buday K, et al. Selenium utilization by GPX4 is required to prevent hydroperoxide-induced ferroptosis. *Cell* (2018) 172:409–22.e21. doi:10.1016/j.cell.2017.11.048

EBM Experimental Biology and Medicine

TYPE Review
PUBLISHED 12 June 2026
DOI 10.3389/ebm.2026.10941

OPEN ACCESS

*CORRESPONDENCE
Li Jiang,
lhljiangli@nbu.edu.cn

†These authors have contributed equally to this work

RECEIVED 21 December 2025
REVISED 25 April 2026
ACCEPTED 03 June 2026
PUBLISHED 12 June 2026

CITATION
Wang Y, Ben T, Fang J, Li Z, Ding J, Xu L, Lin K and Jiang L (2026) Nicotinamide adenine dinucleotide phosphate oxidase 4 in lung disease: a review of its biology and therapeutic potential.
Exp. Biol. Med. 251:10941.
doi: 10.3389/ebm.2026.10941

Nicotinamide adenine dinucleotide phosphate oxidase 4 in lung disease: a review of its biology and therapeutic potential

Yilin Wang[1†], Tianru Ben[2†], Jianjiang Fang[3], Zengpan Li[3], Jinhua Ding[4], Liyan Xu[5], Kai Lin[6] and Li Jiang[3*]

[1]The Fourth Clinical College of China Medical University, Shenyang, China, [2]The First Clinical College of China Medical University, Shenyang, China, [3]Department of Emergency, The Affiliated Lihuili Hospital of Ningbo University, Ningbo, China, [4]Department of Breast Surgery, The Affiliated Lihuili Hospital of Ningbo University, Ningbo, China, [5]Department of General Practice, The Affiliated Lihuili Hospital of Ningbo University, Ningbo, China, [6]Department of Geriatrics, The Affiliated Lihuili Hospital of Ningbo University, Ningbo, China

Abstract

Nicotinamide adenine dinucleotide phosphate oxidase 4 (NOX4) is a constitutively active enzyme that primarily produces hydrogen peroxide, a reactive oxygen species (ROS) with diverse cellular functions. While initially recognized for its role in oxidative stress, emerging evidence suggests that NOX4 plays a pivotal role in the pathogenesis of various lung diseases. This review delineates the structure characteristics of NOX4, emphasizing how its domain organization underlies a distinctive mode of molecular regulation. It further discusses current knowledge on the biological functions of NOX4-derived oxygen species, including their roles in modulating inflammation, cell death pathways, oxygen sensing, nuclear signaling, and metabolic reprogramming. Through these interconnected processes, NOX4 is positioned as a central mediator linking redox imbalance to cellular dysfunction. In addition, the contribution of NOX4 to the pathogenesis of major lung diseases, including idiopathic pulmonary fibrosis (IPF), chronic obstructive pulmonary disease (COPD), asthma, acute lung injury/acute respiratory distress syndrome (ALI/ARDS), and pulmonary hypertension are critically evaluated. Emerging therapeutic strategies targeting NOX4 are also discussed, together with key challenges associated with clinical translation, including isoform specificity, off-target effects, and tissue-selective delivery. Overall, this review provides an integrated framework for understanding NOX4 biology across multiple levels and highlights its potential as a therapeutic target in lung disease.

KEYWORDS
acute lung injury, chronic obstructive pulmonary disease, idiopathic pulmonary fibrosis, nicotinamide adenine dinucleotide phosphate oxidase, pulmonary hypertension

Impact statement

Lung diseases driven by oxidative stress remain a major cause of morbidity and mortality, yet therapies targeting reactive oxygen species have largely failed due to a lack of specificity. This review is important because it focuses on NOX4, a distinct and constitutively active source of oxidants that plays a central role in lung injury, inflammation, fibrosis, and vascular remodeling. By integrating structural biology,

regulatory mechanisms, and disease-specific functions, this work advances the field by explaining why NOX4 acts not merely as a damage-inducing enzyme but as a context-dependent signaling hub. The review brings together emerging evidence on nuclear NOX4, metabolic reprogramming, and regulated protein turnover—areas that have not previously been synthesized in a lung-focused framework. This integrated perspective reframes NOX4 as a tractable, disease-modifying therapeutic target and provides a clear rationale for selective NOX4 inhibition in chronic and acute lung diseases.

Introduction

Reactive oxygen species (ROS) are a double-edged sword in biological systems. At low concentrations, they act as crucial signaling molecules involved in various physiological processes, including cell proliferation [1–3], differentiation [4, 5], and immune responses [6–8]. However, excessive ROS production, termed oxidative stress, contributes to cellular damage and is implicated in the pathogenesis of numerous diseases [9]. NADPH oxidases (NOXs) are a family of enzymes specifically dedicated to generating ROS, with seven isoforms (NOX1-5 and DUOX1-2) identified in mammals. Among these, NOX4 stands out due to its unique characteristic of being constitutively active and primarily producing hydrogen peroxide (H_2O_2) rather than superoxide [10]. The lung, being constantly exposed to environmental oxidants and inflammatory stimuli, is particularly vulnerable to oxidative stress [11]. Consequently, NOX enzymes, including NOX4, are highly expressed in various lung cell types, such as epithelial cells [12, 13], fibroblasts [14, 15], endothelial cells [16–18], and smooth muscle cells [19, 20]. The intricate and often conflicting roles of NOX4 in lung health and disease have garnered significant research interest, paving the way for potential therapeutic interventions. This review aims to consolidate the current knowledge regarding NOX4's multifaceted involvement in lung diseases, providing a comprehensive overview of its pathogenic mechanisms and therapeutic implications. To better understand how NOX4 exerts these diverse biological effects, it is essential to first examine its unique structural features, which distinguish it from other NOX isoforms and underline its constitutive activity.

Molecular structure of NOX family and specific features of NOX4

The NADPH oxidase (NOX) family are membrane-bound enzymes that share a conserved core architecture but differ significantly in their regulatory domains and activation mechanisms. As illustrated in Table 1, all NOX isoforms possess transmembrane domains with six α-helices and two heme-binding sites, and a cytosolic dehydrogenase domain that binds flavin adenine dinucleotide (FAD) and nicotinamide adenine dinucleotide phosphate (NADPH) for electron transfer [21, 22]. However, their regulatory domains vary: NOX1, NOX2, and NOX3 require cytosolic subunits like p47phox and p67phox for activation [23]; NOX5 contains EF-hand calcium-binding domains, making it calcium-sensitive [24, 25]. In contrast, NOX4 lacks these regulatory domains, making it constitutively active—it does not require cytosolic activators or calcium for ROS production [26, 27]. These structural differences underpin the functional diversity of NOX isoforms in physiological and pathological contexts. In the following sections, we will focus primarily on NOX4 and compare its structure features with those of NOX1-3, which are more loosely

TABLE 1 NOX4 domains and residue localization.

Region	Residue range	Description
N-terminal tail	1–65	Cytosolic; may influence localization and transcriptional regulation
Transmembrane Helix I	66–85	First membrane anchor; part of the conserved catalytic core
Extracellular Loop 1	86–105	Short loop; may modulate ROS accessibility or isoform-specific interactions
Transmembrane Helix II	106–125	Anchors the protein; contributes to electron flow
Intracellular Loop 1	126–145	Connects helices; may interact with cytosolic partners or stabilize structure
Transmembrane Helix III	146–165	Conserved helix; part of the redox center
Extracellular Loop 2	166–185	Larger loop; potential role in ROS diffusion or extracellular signaling
Transmembrane Helix IV	186–205	Anchors the protein; contributes to FAD positioning
Intracellular Loop 2	206–225	May stabilize FAD/NADPH binding domains
Transmembrane Helix V	226–245	Final membrane anchor; links to extracellular loop 3
Extracellular Loop 3	246–265	Often glycosylated; may regulate extracellular ROS release.
Transmembrane Helix VI	266–285	Final helix; connects to cytosolic catalytic domains
FAD-binding domain	286–400	Essential for electron transfer; highly conserved across NOX isoforms
NADPH-binding domain	401–560	Drives ROS production; includes Rossmann fold-like motifs
C-terminal tail	561–578	Cytosolic; may regulate activity or interact with scaffolding proteins

related to it than NOX5 or DUOX1/2. As shown in Figure 1, NOX1–3 share ~91%–93% identity with NOX4 overall, their pairwise identity is much lower (~33%–35%), reflecting notable divergence in non-conserved regions. This divergence is most pronounced in the N- and C-terminal regions, which may contribute to isoform-specific regulatory mechanisms or differences in subcellular localization. By contrast, the preservation of transmembrane helices and FAD/NADPH-binding sites indicates that the structural framework required for catalytic activity is maintained across isoforms. These observations suggest that the NOX family combines a conserved enzymatic core with variable terminal regions that confer functional diversification. NOX4 contains highly conserved sequences and domains that are essential for its unique structure, constitutive activity, and function as a generator of hydrogen peroxide. These conserved regions, shaped by evolution, distinguish NOX4 from other members of the NOX family and are crucial for its biological roles.

Transmembrane domains

The transmembrane domains are conservative among NOX family. All NOX family members possess six transmembrane helices that span the cellular membrane. Similarly, NOX4 transmembrane domains span from amino acid 100 to 300. These helices are crucial for anchoring the enzyme within internal membranes, such as the endoplasmic reticulum (ER) and nuclear membrane. Within the helices, two heme groups, which are essential for electron transfer, are buried in helices 3 and 5. These hemes serve as a critical bridge in the electron transport chain from the FAD cofactor [28, 29].

Loops connecting the transmembrane helices

Between the six transmembrane helices, five extracellular and intercellular loops are formed, labeled A through E. These loops, along with the N- and C-termini, are crucial for the enzyme's function, stability, and unique product specificity. The orientation of the loops alternates between the intracellular (cytosolic) and extracellular (luminal) sides of the membrane. Loops A, C, and E are extracellular, while loops B and D are intracellular. Loop A, connecting transmembrane helices 1 and 2, is on the extracellular or luminal side of the membrane. Its role is not as extensively studied as the other loops, but it is believed to be important for the overall structural integrity and correct folding of the NOX4 enzyme. As an extracellular loop, it's involved in shaping the environment on the side where oxygen is reduced. Loop B is located between transmembrane helices 2 and 3. In human NOX4, this region contains a conserved polybasic sequence. The B-loop is a critically important as its function is to serve as a key interface between the transmembrane domain and the dehydrogenase (DH) domain of the protein [30, 31]. While other NOX isoforms use this loop to interact with cytosolic regulatory subunits like p47phox, NOX4 does not. Instead, its B-loop binds directly to the C-terminal DH domain, which contains the binding sites for FAD and NADPH [3, 31–33]. This internal binding is a key reason for NOX4's constitutive activity, as it provides a stable connection that keeps the enzyme in an "on" conformation without needing external signals [10]. Loop C extracellularly connects transmembrane helices 3 and 4. Like loop A, it is involved in maintaining the overall protein structure and ensuring the correct orientation of the transmembrane helices [34]. It plays a role in the formation of the channel through which electrons are transferred, and oxygen is reduced, but its specific function is less defined compared to the E-loop. Loop D is located between transmembrane helices 4 and 5 and is on the cytosolic side of the membrane. It's crucial for the interaction with p22phox [35]. Mutational analysis of NOX4 has revealed that the D-loop is critical for the proper heterodimerization of the NOX4-p22phox complex, which is necessary for NOX4 stability and activity [36]. Mutations in this loop can abolish the functional interaction with p22phox [36]. Loop E is the final extracellular loop, connecting transmembrane helices 5 and 6. In NOX4, it is significantly longer than the E-loop in other NOX isoforms. It is the key determinant of why NOX4 produces H_2O_2 as its primary product [37], unlike other NOX enzymes that mainly produce superoxide. A highly conserved histidine residue in this loop is thought to be strategically positioned to act as a proton donor. This unique structural feature allows the E-loop to promote the rapid dismutation of the newly formed superoxide radical to hydrogen peroxide before the ROS product leaves the enzyme, effectively "trapping" and converting it. This makes the E-loop central to NOX4's characteristic signaling properties.

DH domain

Located at the C-terminus and facing the cytosol, the DH domain is the catalytic core of NOX4. This domain contains binding sites for both FAD and NADPH [31–33]. The DH domain is intrinsically activated in NOX4, meaning it doesn't require additional cytosolic regulatory subunits (unlike other NOX isoforms such as NOX1-3 that need proteins like p47 and p67 for activation). This inherent activity allows NOX4 to constitutively transfer electrons from NADPH to FAD.

Also part of the DH domain, a region from 401 to 560 amino acids is responsible for binding NADPH [31, 33], the electron donor for the enzyme. Electrons from NADPH are transferred to the FAD, initiating the electron transport chain that ultimately leads to oxygen reduction and H_2O_2 production. Once bound, NADPH transfers two electrons to the FAD cofactor, which is bound to a β-barrel fold within FAD-binding subdomain ranging from amino acids of 286–400. The electrons are then passed from FAD to a heme group in the transmembrane domain of the enzyme [31]. This transfer is facilitated by the interaction between the DH domain and the B-loop, a polybasic region connecting transmembrane helices. This interaction helps bring the FAD and heme groups into close proximity, enabling electron transfer [30]. While the structural organization of NOX4 explains its intrinsic enzymatic activity, its biological impact is primarily determined by tight regulation of its expression and stability under physiological and pathological conditions.

Molecular regulation of NOX4

The molecular regulation of NOX4 is a complex process that primarily occurs at the level of its expression and protein stability, rather than through a rapid, on-demand activation like other

10.3389/ebm.2026.10941

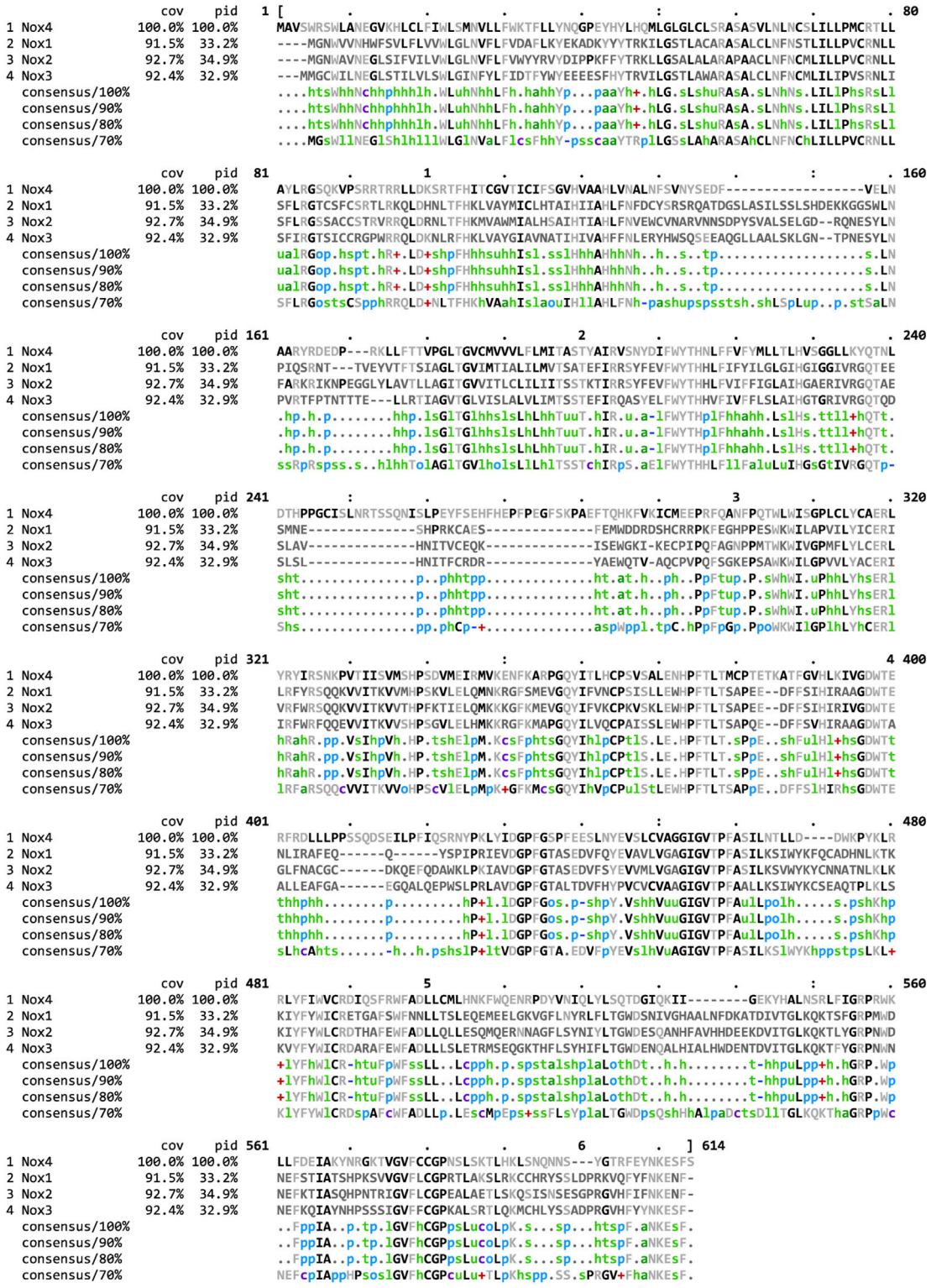

FIGURE 1
NOX family proteins alignment. The alignment of NOX1–NOX4 proteins reveals a high degree of conservation across transmembrane regions and key functional motifs, particularly within the NADPH oxidase core domains. NOX4, serving as the reference sequence, shows 100% identity and coverage, while Nox1, Nox2, and Nox3 exhibit ~91%–93% identity but only ~33%–35% pairwise identity, indicating substantial divergence in non-conserved regions. The transmembrane helices and FAD/NADPH-binding motifs are notably preserved, suggesting functional constraints across the family. However, the N-terminal and C-terminal regions display marked variability, likely reflecting isoform-specific regulatory roles or subcellular targeting. Consensus sequences at varying identity thresholds (70%–100%) highlight conserved residues critical for enzymatic activity and membrane integration, while gaps and substitutions pinpoint regions of evolutionary flexibility. This alignment underscores both the structural integrity and functional diversification within the NOX family.

NADPH oxidases. This constitutive activity makes its regulation distinct and crucial for controlling its cellular effects.

Regulation by transforming growth factor-β (TGF-β)

TGF-β signaling is a potent inducer of NOX4 expression [38–42]. This is a key mechanism in the pathogenesis of fibrotic diseases, as increased NOX4 expression drives the pro-fibrotic signaling cascade. When the cytokine TGF-β1 binds to its receptors, it triggers a phosphorylation cascade that activates Smad2 and Smad3 [38, 43, 44]. These proteins then form a complex with the common mediator Smad4 and translocate into the nucleus. In the nucleus, the Smad complex binds to specific DNA sequences called Smad Binding Elements (SBEs), located within the promoter of the NOX4 gene [45–48]. This binding initiates the recruitment of co-activators and the transcriptional machinery, leading to a robust increase in NOX4 gene transcription. This creates a powerful positive feedback loop, as NOX4-derived ROS, in turn, can activate latent TGF-β1, further amplifying the fibrotic response.

Regulation by hypoxia

Under hypoxia, the transcriptional regulation of NOX4 is primarily controlled by Hypoxia-Inducible Factor 1 (HIF-1) [49, 50]. During hypoxia, the HIF-1α subunit is stabilized and translocated to the nucleus, where it heterodimerizes with HIF-1β [51]. This complex then binds to specific hypoxia-responsive elements (HREs) in the promoter regions of target genes [52, 53]. The NOX4 promoter contains HREs, allowing HIF-1α to directly bind and drive its transcription [20, 49]. This HIF-1-mediated upregulation of NOX4 in hypoxia can contribute to various pathologies, including pulmonary hypertension (PH) [20]. The expression of NOX4 is also regulated by common transcription factors like AP-1 and Sp1, which can respond to a variety of upstream signals, including growth factors and stress [54]. AP-1, a dimer composed of Fos and Jun proteins, and Sp1 are known to bind to consensus sequences within the NOX4 promoter [46]. Their binding can either synergize with or act independently of other transcription factors to modulate NOX4 expression. The coordinated action of these and other transcription factors allows for a precise and nuanced control of NOX4 levels in response to diverse cellular signals.

Epigenetic regulation

NOX4 expression can also be regulated by epigenetic mechanism. This regulation primarily occurs through DNA methylation, histone modifications, and non-coding RNAs, which collectively modulate the accessibility of the NOX4 gene to the transcriptional machinery. Hypermethylation of the NOX4 promoter is generally associated with gene silencing or a decrease in NOX4 expression [55, 56]. The addition of methyl groups physically obstructs the binding of transcription factors, preventing the initiation of transcription. Conversely, promoter hypomethylation can lead to the "un-silencing" of the gene, resulting in its upregulation. The acetylation of histones, mediated by histone acetyltransferases (HATs), generally loosens chromatin structure, making the promoter region of the NOX4 gene more accessible and thereby promoting its transcription [57]. Interestingly, histone deacetylases (HDACs) remove these acetyl groups, leading to a condensed chromatin state, also increase NOX4 expression [58–60]. This discrepancy adds complexity to the regulation of NOX4. The use of HDAC inhibitors, for example, has been shown to reduce NOX4 expression in some contexts [59, 61]. Similar to DNA methylation, the methylation of histones can have both activating and repressive effects on gene expression, depending on the specific histone residue and the number of methyl groups. For example, trimethylation of histone H3 at lysine 4 (H3K4me3) is often associated with active transcription [62–65], while trimethylation at lysine 27 (H3K27me3) is linked to gene silencing [66]. These marks likely influence NOX4 expression, though the precise patterns are still under investigation. MicroRNAs are small, non-coding RNAs that regulate gene expression post-transcriptionally by binding to specific messenger RNA (mRNA) molecules, leading to their degradation or translational repression. This mechanism is also a key player in the epigenetic control of NOX4. A number of miRNAs have been identified that directly target the NOX4 mRNA. For instance, miR-9-5p has been shown to suppress NOX4 expression by binding to its 3′-untranslated region, leading to mRNA degradation [67]. The dysregulation of this and other NOX4-targeting miRNAs can contribute to a variety of pathological conditions [68–70], including fibrosis [67, 71], by altering the delicate balance of NOX4 levels. The ability of miRNAs to fine-tune NOX4 expression provides a sophisticated layer of negative regulation that complements its other control mechanisms.

Regulation by ubiquitination

NOX4 protein levels can also be regulated by ubiquitination and subsequent proteasomal degradation. The ubiquitination of NOX4 is a multi-step enzymatic cascade catalyzed by a trio of enzymes. E1 (ubiquitin-activating enzyme), E2 (ubiquitin-conjugating enzyme), and E3 (ubiquitin ligase). The E3 ubiquitin ligase is the most important component, as it provides the specificity by recognizing the target protein and catalyzing the transfer of ubiquitin. For NOX4, specific E3 ligases recognize key motifs on the protein, leading to the formation of polyubiquitin chains, which serve as a signal for degradation by the 26S proteasome. The specificity of NOX4 ubiquitination is largely determined by a few well-characterized E3 ubiquitin ligases and their associated adaptor proteins. Hic-5 is a major negative regulator of NOX4 that acts as an adaptor protein. In response to oxidative stress (often generated by NOX4 itself), Hic-5 undergoes a conformational change that allows it to bind directly to NOX4. Hic-5 then recruits a specific E3 ubiquitin ligase, leading to the polyubiquitination and subsequent degradation of NOX4 [72]. This forms an elegant and rapid negative feedback loop, preventing excessive ROS production and helping to restore redox balance. CHIP is a well-known E3 ubiquitin ligase involved in protein quality control. It partners with molecular chaperones like Hsp70 to recognize misfolded or damaged proteins. Studies have shown that CHIP can bind to and ubiquitinate NOX4, targeting it for proteasomal degradation [73]. This function ensures that improperly folded or

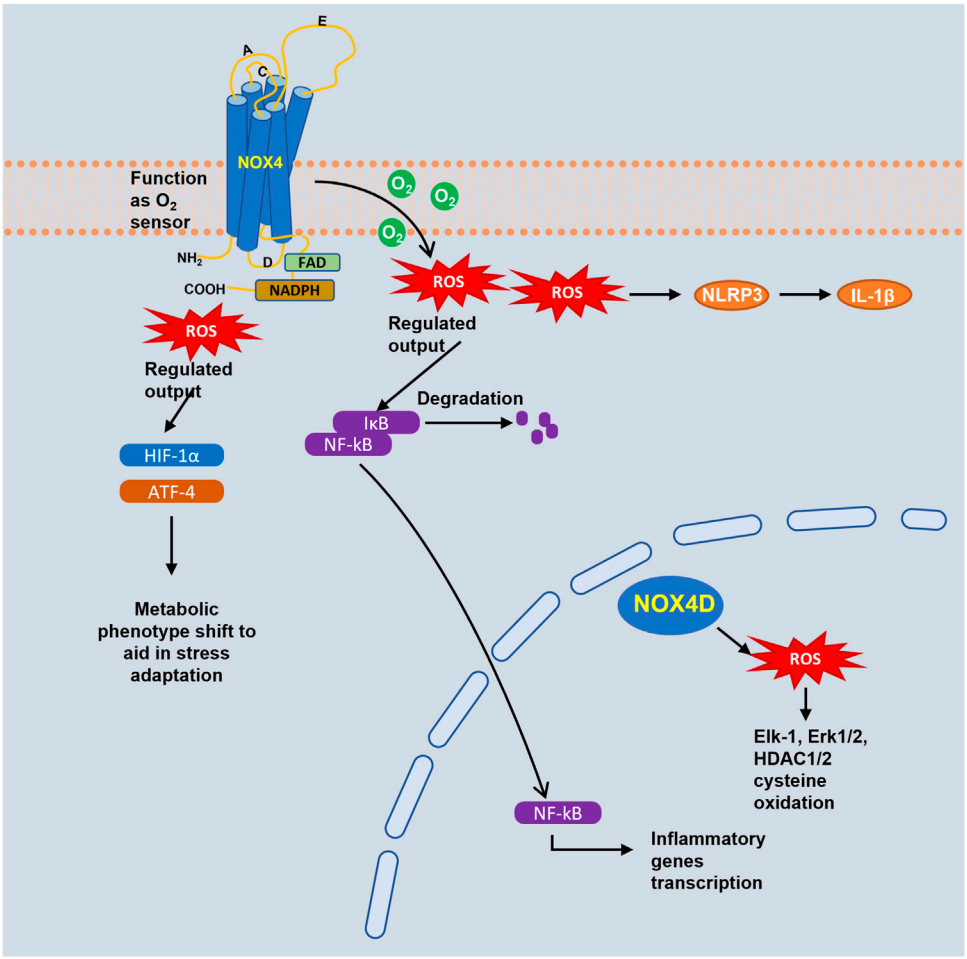

FIGURE 2
NOX4 signaling and its role in cellular stress and inflammation. The diagram illustrates the function of NADPH oxidase 4 (NOX4) as an oxygen sensor, producing reactive oxygen species (ROS) upon activation. NOX4, through the NADPH binding site and FAD domain, generates ROS that regulate various cellular outputs. These include activation of transcription factors such as HIF-1α and ATF-4, which drive a metabolic phenotype shift to aid in stress adaptation. ROS also lead to the degradation of IκB, resulting in NF-κB activation and the transcription of inflammatory genes. Additionally, ROS regulate the NLRP3 inflammasome and the release of interleukin-1β (IL-1β), further promoting inflammatory responses. ROS-induced modifications of proteins, such as cysteine oxidation of Elk-1, Erk1/2, and HDAC1/2, also contribute to inflammation-related gene transcription.

aggregated NOX4 is removed from the cell, maintaining a healthy pool of functional enzyme.

The expanding biological roles of NOX4

The diverse and often contradictory functions of NOX4—from promoting cell survival to inducing cell death—are a testament to the context-dependent nature of its signaling. This intricate regulation is primarily mediated by the ability of H_2O_2 to reversibly oxidize specific cysteine residues on target proteins, thereby modulating their activity.

The role in inflammation and cell death pathways

NOX4 is a key orchestrator of the inflammatory response, particularly through its influence on the NFκB pathway, as seen in LPS-mediated activation [74]. As shown in Figure 2, in its inactive state, the NFκB transcription factor is sequestered in the cytoplasm by its inhibitor, IκB. NOX4-derived ROS facilitates the phosphorylation and subsequent degradation of IκB, thereby promoting NFκB to translocate to the nucleus [75, 76]. In the nucleus, NFκB drives the transcription of a vast array of pro-inflammatory genes, including those encoding cytokines like IL-8 and TNF-α. This molecular link positions NOX4 as an important amplifier of both acute and chronic inflammatory conditions. Furthermore, NOX4 has been shown to regulate pyroptosis [77–79], a highly inflammatory form of programmed cell death, by promoting a redox environment for NLRP3 inflammasome activation [78, 80, 81]. Under certain circumstances NOX4-derived ROS can contribute to NLRP3 inflammasome formation, leading to the cleavage and release of pro-inflammatory cytokines like IL-1β and IL-18. This novel function positions NOX4 as a central mediator of inflammation and cell death in the context of various inflammatory diseases. Recent studies have established a direct link between NOX4 and non-apoptotic forms of cell death,

specifically ferroptosis [82–84]. Ferroptosis is a form of iron-dependent cell death characterized by the accumulation of lipid peroxides. While NOX4 is not considered a primary trigger of ferroptotic cell death, its constitutive production of H_2O_2 contributes to ferroptosis by depleting the antioxidant glutathione (GSH) [82, 83], thereby tipping the balance toward oxidative damage and lipid peroxidation. In this context, NOX4 acts to sensitize cells to ferroptotic stimuli and amplify oxidative damage rather than directly executing the ferroptotic program. Beyond its role in inflammatory signaling and cell death, NOX4 also functions as a sensor of environmental cues, particularly oxygen availability.

NOX4 as an oxygen sensor

In addition to its roles in inflammation and cell death, NOX4 functions as a molecular oxygen sensor, linking oxygen tension to cellular signaling [10, 85]. NOX4 functions as a biochemical oxygen rheostat, translating oxygen levels into redox signals via H_2O_2 production. This makes it a critical player in both normal physiological and pathophysiological conditions like fibrosis, NOX4 has a much higher Michealis constant for oxygen compared to NOX2 (18% vs. 2%–3%) [10], meaning it operates efficiently across a wide physiological range of oxygen tensions. This property allows it to act as a graded sensor, adjusting hydrogen peroxide output in proportion to oxygen availability. This oxygen-sensing capability enables NOX4 to regulate processes like hypoxia response [86], angiogenesis [87–89], cellular differentiation [76, 90–94], especially in tissues like the kidney, vasculature, and heart. NOX4-derived ROS influences the activity of key ion channels, such as the KCNK3/TASK-1 potassium channel [95]. In vascular smooth muscle cells, NOX4's regulation of these channels is critical for controlling pulmonary vascular tone and can contribute to conditions like PH [95]. Furthermore, NOX4-derived ROS can influence the stability and transcriptional activity of HIF-1α, the master regulator of the hypoxic response, thereby regulating a cell's metabolic and genetic adaptation to low oxygen [96, 97]. In addition to cytoplasmic and mitochondrial signaling, emerging evidence highlights a distinct role for NOX4 within the nucleus.

The nuclear function of NOX4

While NOX4 is widely recognized for its roles in the ER and mitochondria, a unique and critical function of the enzyme is its presence and activity within the nucleus and nuclear membrane. A pivotal discovery was the identification of a 28-kDa splice variant of NOX4, termed NOX4D, which lacks transmembrane domains and localizes to the nucleus and nucleolus [98, 99]. This variant was found in vascular smooth muscle cells [98] and other cell types [99, 100], where it actively generates ROS and influences nuclear signaling pathways. Here, NOX4 operates as a direct regulator of the nuclear microenvironment by H_2O_2 in close proximity to the cell's genetic material. This targeted ROS production serves as a potent signaling mechanism that directly influences both transcriptional and epigenetic processes. On a molecular level, the H_2O_2 can reversibly oxidize key redox-sensitive cysteine residues on nuclear proteins, including transcription factors such as Elk-1 and ERK1/2, thereby modulating their ability to bind to DNA and regulate gene expression. This allows NOX4 to act as a direct molecular switch, controlling genes related to cell proliferation, differentiation, and stress responses as shown in Figure 2.

Furthermore, nuclear NOX4's activity can influence chromatin remodeling by affecting the function of enzymes like histone deacetylases (HDACs), providing an additional layer of epigenetic regulation that can alter DNA accessibility and long-term gene expression patterns. This mechanism is particularly relevant in conditions like cellular senescence [101, 102] and chronic inflammation. For instance, in lung fibroblasts, high levels of NOX4 are associated with an increase in the active histone mark H4K16Ac [103] and a decrease in the repressive mark H4K20Me3 [57], which supports an active transcriptional state of the NOX4 gene itself [57, 103]. NOX4 can also influence histone methylation. For example, in the context of inflammation, NOX4-derived nuclear ROS can oxidize and inhibit the activity of HDAC1/2, a class of enzymes that can interact with and regulate histone marks [104]. This "chromatin remodeling" can lead to altered gene expression of pro-inflammatory cytokines, driving the inflammatory response.

This localized production of ROS in the nucleus also carries a dual risk: while it is vital for signaling, an excessive or dysregulated amount can lead to oxidative DNA damage and genomic instability. Overexpression of NOX4D induces γ-H2A phosphorylation [105, 106], a marker of DNA-double strand breaks, linking NOX4 to genomic instability. This effect is dependent on the integrity of the NDAPH-binding domain, as a single amino acid substitution abolishes ROS production and downstream signaling. These spatially distinct functions of NOX4 are further complemented by its ability to regulate cellular metabolism.

Metabolic reprogramming

NOX4 has been newly identified as a regulator of cellular metabolism, going beyond its previously known effects on mitochondria. It is now understood to modulate pathways such as fatty acid oxidation and glucose metabolism [107–112]. By altering the redox state of key metabolic enzymes, NOX4 influences a cell's metabolic preferences, contributing to metabolic reprogramming. This role is particularly significant in cancer [113] and diabetes [110, 114], where metabolic shifts are central to disease progression. NOX4-derived H_2O_2 can activate or inhibit redox-sensitive transcription factors. For instance, in some cancers, NOX4 deficiency leads to the upregulation of MYC and Nrf2 [113, 115, 116], which are master regulators of cell proliferation and metabolic homeostasis. This promotes a more aggressive, glycolytic phenotype. Conversely, in other contexts, NOX4-generated ROS activate pro-survival pathways like HIF-1 alpha [97, 117] and ATF4 (activating transcription factor 4) [118–120], which aid in stress adaptation (Figure 2). Meanwhile, NOX4 can directly alter how cells use different fuel sources. In the heart, NOX4-mediated signaling shifts metabolism away from glucose oxidation and towards fatty acid oxidation [108]. This is mediated through the hexosamine biosynthetic pathway (HBP), which enhances protein O-GlcNAcylation that helps the heart adapt to stress and maintain its energetic status.

TABLE 2 The role of NOX4 in pulmonary disease.

Disease	NOX4-involved mechanisms of pulmonary disease
IPF	1. NOX4-mediated fibroblast differentiation into myofibroblasts via ROS-dependent activation of Smad2/3 signaling [15, 103, 128–130] 2. NOX4-induced TGF-β1 expression [131, 132] 3. NOX4-mediated early epithelial cell death in response to injury [12, 133] 4. NOX4 promoting myofibroblast differentiation, deposition of ECM [134]
COPD	1. NOX4 expression is upregulated in ASM and PASMCs by TGF-β, TNF-α [134, 138, 139] 2. NOX4-derived ROS promote collagen I deposition and α-SMA expression [134, 139] 3. NOX4 drives vascular wall thickening and smooth muscle proliferation in distal pulmonary arteries [138] 4. NOX4 activates NF-κB, promoting pro-inflammatory cytokines expression [141, 142] 5. NOX4/Nrf2 imbalance exacerbate mitochondrial damage and mitophagy [143]
Asthma	1. Airway smooth muscle cells proliferation, hypertrophy [149], and hypersensitivity [19] 2. Elevated NOX4 in cilial epithelial cells reduces cilial beat frequency [150] 3. NOX4 upregulation is involved in mitochondrial damage–induced apoptosis in bronchial epithelial cells [69] 4. In fibroblasts, PI3K-dependent TRPV4 activation mediates NOX4 upregulation, which is required for TGF- β1–induced lung fibroblast differentiation through MRTF-A and PAI-1 [151]
ALI	1. Upregulated NOX4 in alveolar macrophages, endothelia cells and epithelial cells [13, 17, 155] 2. NOX4-derived H_2O_2 activates NF-κB pathway [74, 156] 3. NOX4 contributes directly to alveolar epithelial can endothelial cells apoptosis [12, 13, 17, 104, 157] 4. NOX4 impairs phagocytic function of macrophages, preventing effective cleaning apoptotic cells and repairing [76, 158]
PAH	1. Marked overexpression of NOX4 in remodeled pulmonary arteries [20, 166] 2. Increased NOX4 activates PDGFR-β/Akt pathway leading to activated growth and survival pathways in PASMCs [167, 168] 3. NOX4 compromises endothelial cell integrity, promotes apoptosis by reducing NO bioavailability [169, 170] 4. NOX4-derived H_2O_2 impairs angiogenesis and promotes vascular remodeling [172]

Collectively, these diverse biological functions position NOX4 as a central regulator of redox-dependent signaling. Dysfunction of these processes can lead to persistent inflammation, aberrant cell death, and pathological tissue remodeling. In the lung, such alterations are closely linked to the development and progression of multiple respiratory diseases.

The pathophysiological role of NOX4 in lung diseases

Chronic respiratory diseases represent a significant global health burden, driving intensive research efforts to uncover the precise cellular and molecular mechanisms behind their progression. ROS play a dual role in lung biology, acting as crucial signaling molecules in healthy tissue while contributing to cellular damage and remodeling during disease pathogenesis. NOX4 has emerged as a central, yet complex, player in the progression of chronic respiratory illnesses. Understanding the dysregulated expression and function of NOX4 is critical, as growing evidence links its activity to the underlying pathology of devastating conditions such as Idiopathic Pulmonary Fibrosis (IPF) and Chronic Obstructive Pulmonary Disease (COPD) (see Table 2). Through modulation of redox-sensitive signaling pathways, NOX4 influences diverse aspects of lung cells, including airway epithelial cells, smooth muscle cells, fibroblasts, and endothelial cells (See Figure 3). These cells represent substantial mechanistic overlap of lung disease. The following sections examine the role of NOX4 in the pathophysiology of chronic and acute lung diseases.

NOX4 in IPF

IPF is a chronic, progressive, and often fatal lung disease characterized by the excessive accumulation of extracellular matrix (ECM) components, leading to irreversible scarring and loss of lung function [121]. While the exact etiology of IPF remains elusive, mounting evidence points to a critical role for oxidative stress in its pathogenesis [122, 123]. The lung's continuous exposure to environmental insults and its high oxygen tension makes it particularly vulnerable to oxidative stress [124]. The initial injury to the delicate alveolar epithelium is a hallmark event, which triggers a cascade of events. The damaged epithelial cells release pro-fibrotic mediators, attracting and activating fibroblasts [125–127]. This leads to the overproduction and deposition of ECM components, such as collagen and fibronectin. Among the molecular drivers of IPF, NOX4 has emerged as a central regulator of fibrogenic signaling. NOX4-derived ROS play a pivotal role at every stage of this cascade, acting not as mere byproducts of cellular activity but as crucial signaling molecules that drive the disease forward. The first major study implicating NOX4 in IPF demonstrated that NOX4 expression is significantly upregulated in pulmonary fibroblasts from IPF patients, especially in response to TGF-β1 [15]. This study showed that NOX4 mediates fibroblast differentiation into myofibroblasts via ROS-dependent activation of Smad2/

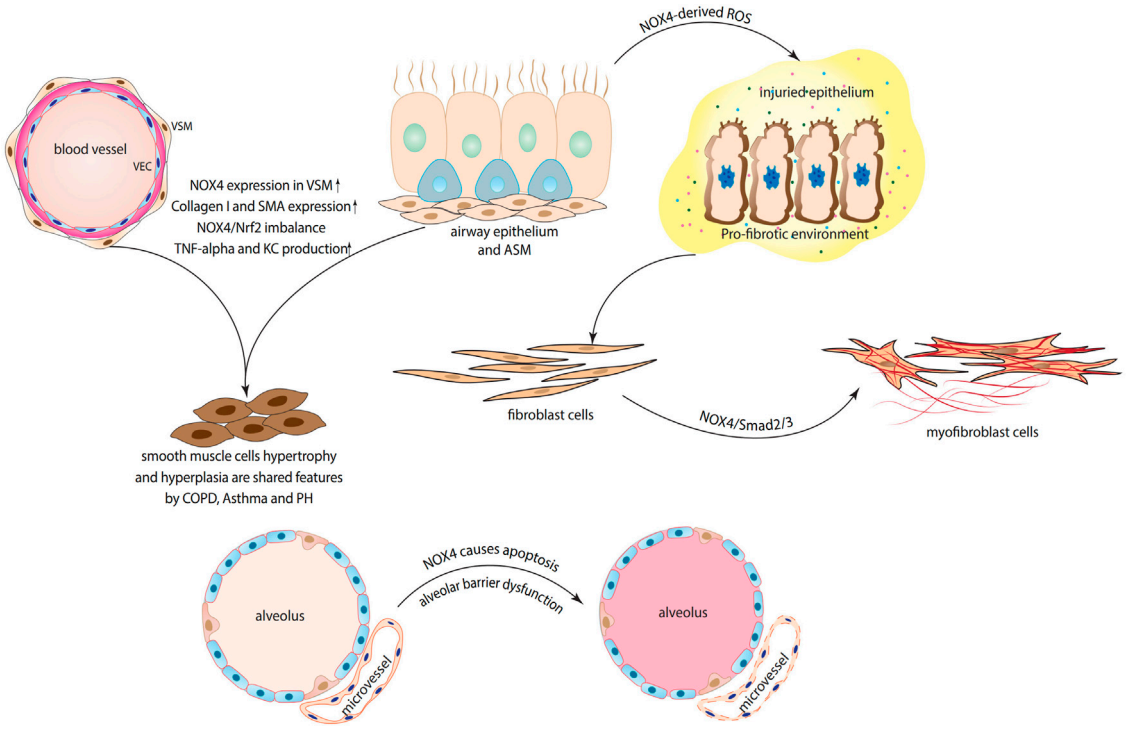

FIGURE 3
NOX4 contributes to the pathogenesis of multiple lung disorder by targeting a broad spectrum of structural and resident cells within the lung. NOX4 ability to drive oxidative stress, cellular injury and inflammatory signaling is central to disease initiation and progression. Key cellular targets of NOX4 include airway epithelial cells, airway and vascular smooth muscle cells, fibroblasts, and endothelial cells, where it modulates redox-sensitive pathways and influence cell survival, differentiation, and function. In chronic lung disease such as IPF, COPD, asthma, and PH, NOX4-dependent mechanisms show substantial overlap. These include enhanced proliferation, hyperplasia, and hypertrophy of airway and vascular smooth muscle cells, contributing to airway narrowing and increased vascular resistance. In parallel, NOX4 promotes fibroblast activation, differentiation into myofibroblasts, and excessive extracellular matrix deposition, which are hallmark features of fibrotic remodeling in IPF. Notably, similar fibroblast activation pathways are also implicated in airway remodeling in asthma, highlighting shared pathogenic mechanisms across these conditions. In contrast, ARDS is mechanically distinct from these chronic disorders. ARDS is characterized by acute and widespread injury to the alveolar epithelium and pulmonary microvascular endothelium. In this setting, NOX4 directly contributes to epithelial and endothelial cell damage, leading to increased permeability and breakdown of the alveolar barrier. This disruption results in protein-rich fluid leakage into the alveolar space.

3 signaling. These findings established NOX4 as a critical mediator of fibrogenic transformation. Further validation came from studies showing that NOX4 is also upregulated in fibroblastic foci, the pathological hallmark of IPF(128), and that its inhibition can reverse fibrotic phenotypes *in vitro* and *in vivo* [103, 128–130]. There are several mechanisms underlying NOX4 contribution to IPF. NOX4 enhances TGF-β1-induced expression of profibrotic genes, including α-smooth muscle actin (α-SMA) and collagen [131, 132]. NOX4 has been implicated in epithelial cell death, particularly in response to injury [12, 133], which is considered an early and crucial step in the development of lung fibrosis [125, 126]. This epithelial damage can then trigger fibroblast activation and subsequent ECM deposition. By promoting myofibroblast differentiation, NOX4 directly contributes to the overproduction and deposition of ECM components like collagen and fibronectin, driving the fibrotic process [134].

Therapeutic potentials: Recent efforts have led to the development of highly selective NOX4 inhibitors, which demonstrate efficacy in reversing fibrosis in aged mouse models [135]. These compounds inhibit ROS production, myofibroblast differentiation, and collagen synthesis. Metformin, an AMPK activator, has been shown to suppress NOX4 expression and attenuate lung fibrosis in bleomycin-induced models [128]. This highlights the potential of metabolic modulators in targeting NOX4-mediated pathways. Studies have explored the role of NOX4 in aging-related fibrosis, showing that its sustained upregulation in aged lungs contributes to persistent fibrotic remodeling [136]. Epigenetic regulation of NOX4 may offer new therapeutic angles. Emerging strategies aim to combine NOX4 inhibitors with Nrf2 activators to simultaneously suppress oxidant production and boost antioxidant defenses [135]. Preclinical models have demonstrated proof-of-concept for NOX4-targeted therapies, and clinical trials are anticipated to evaluate safety and efficacy in IPF patients.

While NOX4-driven fibrotic remodeling has been most extensively characterized in IPF, several of these pathogenic mechanisms are also shared with COPD. Both diseases are marked by persistent oxidative stress, chronic inflammation, and aberrant tissue remodeling. These overlapping pathological features suggest that NOX4 may function as a common upstream regulator linking redox imbalance to both fibrotic and inflammatory process across distinct pulmonary disease contexts. In this regard, emerging evidence supports a similar role for NOX4 in the pathogenesis of COPD.

NOX4 in COPD

COPD, primarily caused by cigarette smoke exposure, is characterized by chronic inflammation, airflow limitation, and progressive lung damage [137]. Oxidative stress is a major contributor to COPD pathophysiology. Among the enzymatic sources of ROS, NOX4 has gained attention due to its constitutive activity and ability to generate H_2O_2, contributing to redox imbalance and tissue injury [138]. Multiple studies have demonstrated that NOX4 expression is significantly upregulated in the lungs of COPD patients, particularly in airway smooth muscle (ASM) and pulmonary artery smooth muscle cells (PASMCs) [134, 138, 139]. This upregulation correlates with disease severity, airway remodeling, and PH, a common complication of advanced COPD [138]. *In vivo* and *in vitro* studies confirm that NOX4 expression is inducible by pro-inflammatory cytokines such as TGF-β1 and TNF-α, both of which are elevated in COPD [134, 140]. NOX4-derived ROS promote collagen I deposition and α-SMA expression in bronchial smooth muscle cells, contributing to ASM hypertrophy and hyperplasia [134, 139]. This remodeling is mediated through noncanonical TGF-β signaling, involving p38 MAPK and Akt pathways, which are activated in response to cigarette smoke and inflammatory stimuli [134]. In COPD patients with PH, NOX4 expression is elevated in distal pulmonary arteries, where it drives vascular wall thickening and smooth muscle proliferation [138]. This remodeling is associated with reduced pulmonary function and right ventricular hypertrophy, as shown by cardiac MRI studies [138]. NOX4 contributes to oxidative stress by generating ROS that damage lipids, proteins, and DNA. In COPD lungs, this is evidenced by increased malondialdehyde and decreased superoxide dismutase levels [138]. NOX4 also modulates the NF-κB pathway, promoting the expression of pro-inflammatory cytokines such as TNF-α and KC [141, 142]. Recent studies show that NOX4/Nrf2 imbalance exacerbates mitochondrial damage and mitophagy, particularly in response to environmental pollutants like PM2.5, increasing susceptibility to acute exacerbations of COPD (AECOPD) [143].

Therapeutical potentials: The traditional use of broad-spectrum antioxidants in COPD has yielded limited success [144], highlighting the need for more specific therapies. Targeting NOX4 offers a rational approach because it strikes at a key upstream driver of multiple pathologies. Instead of simply scavenging ROS, a NOX4 inhibitor can prevent its production at the source, thereby simultaneously blocking inflammation, cell death, and remodeling. The most advanced and well-studied specific inhibitor is setanaxib (GKT137831) [145]. This small-molecule compound acts as a dual inhibitor of both NOX4 and NOX1. Its mechanism involves blocking the transfer of electrons at the catalytic site of the enzyme, thereby suppressing the generation of ROS. Setanaxib has been investigated in clinical trials for other fibrotic diseases like primary biliary cholangitis and liver stiffness (ClinicalTrials.gov ID: NCT05014672, phase II), diabetic kidney disease (ClinicalTrias.gov ID: NCT02010242, phase II) and IPF (ClinicalTrias.gov ID: NCT03865927, phase II), and these trials have provided valuable data on its safety and pharmacokinetics. However, large-scale, dedicated clinical trials to definitively prove its efficacy in a broad COPD population have yet to be completed. The potential for NOX4 inhibition to be a disease-modifying therapy for COPD, rather than just a symptomatic treatment, remains a subject of intense research.

NOX4 in asthma

Asthma and chronic obstructive pulmonary disease (COPD) have traditionally been viewed as distinct airway disorders; however, accumulating evidence indicates that they share several common pathological features, particularly in chronic and severe disease states [146, 147]. Both conditions are characterized by persistent airway inflammation, oxidative stress, and structural remodeling, which collectively contribute to airflow limitation [147]. A central shared mechanism is oxidative stress, driven by both environmental exposures (e.g., allergens, pollutants, cigarette smoke) and endogenous sources such as NADPH oxidases.

Asthma has long been associated with elevated oxidative stress [148]; however, the involvement of NOX4 in asthma was not recognized until 2007, when it was first shown to mediate TGF-β1–induced airway smooth muscle cells proliferation and hypertrophy [149]. Subsequent genome-wide microarray analyses revealed increased NOX4 expression in airway smooth muscle cells from patients with asthma, which was further validated by PCR and protein assays [19]. Functionally, airway smooth muscle cells isolated from asthmatic individuals exhibits enhanced agonist-induced contraction, a response that is attenuated by NOX4 knockdown as well as by pharmacological inhibitors such as diphenyleneiodonium and apocynin, indicating a critical role for NOX4 in airway smooth muscle hyperresponsiveness.

Later studies confirmed that elevated NOX4 expression in asthma is not restricted to airway smooth muscle cells but is also present in other airway cell types. A hallmark of asthma, particularly neutrophilic asthma, is impaired mucociliary clearance. In this context, NOX4 protein levels are significantly higher in airway epithelial cells from patients with neutrophilic asthma compared with those from non-neutrophilic asthma patients and healthy controls. Importantly, these patients exhibit reduced ciliary beat frequency, a key indicator of ciliary function, which can be restored by setanaxib [150].

More recent clinical observations demonstrate a significant correlation between TLR4 and NOX4 mRNA expression in patients with inflammatory asthma, further supporting a role for NOX4 in disease-associated inflammation. In addition, mechanistic studies using IL-13–treated BEAS-2B cells show that NOX4 upregulation is associated with mitochondrial damage–induced apoptosis and decreased levels of miR-182-5p, a microRNA that negatively regulates NOX4 expression by targeting the 3′ untranslated region of its mRNA [69].

Beyond epithelial and smooth muscle dysfunction, NOX4 also plays a central role in airway remodeling through regulation of fibroblast activation. Asthma-associated remodeling is characterized by persistent myofibroblast differentiation driven by TGF-β1, mechanical stress, and oxidative signaling. Recent study has identified the mechanosensitive ion channel TRPV4 as a critical upstream regulator that integrates these signals via a TRPV4–NOX4 axis [151]. Activation of TRPV4 promotes NOX4 expression and ROS generation, which are required for TGF-β1–induced lung fibroblast differentiation through myocardin-related transcription factor-A (MRTF-A) and

plasminogen activator inhibitor-1 (PAI-1). Mechanistically, both TRPV4 and NOX4 are activated downstream of PI3K signaling, and coordinated input from TRPV4 and Rac is necessary for NOX4 upregulation. Importantly, inhibition or genetic deletion of TRPV4 suppresses NOX4 expression and ROS production, thereby attenuating fibroblast activation and allergen-induced airway remodeling *in vivo*. Consistent with these findings, fibroblasts derived from asthmatic patients exhibit higher NOX4 expression compared to those from non-asthmatic controls.

NOX4 in acute lung injury (ALI)

ALI and ARDS are life-threatening conditions characterized by severe inflammation, increased vascular permeability, and impaired gas exchange [152]. Oxidative stress is a key mediator of lung damage in these conditions [153, 154]. In the context of ALI/ARDS, NOX4 is significantly upregulated in key cell types within the lung, including alveolar macrophages [155], endothelial cells [17] and epithelial cells [13]. Its activity contributes to the disease through several interconnected molecular mechanisms. NOX4-derived H_2O_2 acts as a potent pro-inflammatory signal. It triggers the activation of crucial signaling pathways, most notably the NF-κB pathway [74, 156]. By promoting the degradation of the inhibitory IκB protein, NOX4 allows NF-κB to translocate to the nucleus and drive the transcription of numerous pro-inflammatory genes [74]. This results in the massive production of inflammatory cytokines like IL-8 and TNF-alpha which recruit and activate more immune cells, creating a destructive feedback loop that sustains the inflammatory response. A hallmark of ALI/ARDS is the extensive damage and death of the alveolar-capillary barrier's cellular components. NOX4 contributes directly to the apoptosis of both alveolar epithelial and endothelial cells [12, 13, 17, 157]. This widespread cell death compromises the integrity of the lung barrier, leading to the leakage of protein-rich fluid into the alveoli, a phenomenon known as alveolar flooding. This fluid accumulation is a primary cause of the severe hypoxemia and respiratory failure seen in patients. In addition to causing injury, NOX4 can also hinder the body's natural processes of resolution and repair. It can impair the phagocytic function of macrophages [76, 158], preventing them from effectively clearing apoptotic cells and cellular debris from the airspaces. This failure to clear dead cells sustains inflammation and prevents the lung from properly repairing its damaged tissue, contributing to the poor prognosis of the disease.

NOX4 in PH

PH is a severe, debilitating disease defined by a sustained elevation in pulmonary arterial pressure, leading inevitably to right ventricular failure [159]. The underlying structural pathology involves progressive, irreversible pulmonary arterial smooth muscle cell (PASMC) proliferation [160], endothelial dysfunction [161, 162], and excessive vascular remodeling [163–165]. This destructive cascade is highly dependent on chronic, dysregulated oxidative stress, making NOX4 a critical enzymatic hub driving the disease. The hallmark of PH is the muscularization and thickening of the pulmonary arterial wall. NOX4 is markedly overexpressed in the remodeled pulmonary arteries of both human PH patients and in various preclinical animal models [20, 166]. The H_2O_2 generated by NOX4 serves as a potent signaling molecule that initiates growth and survival pathways in PASMCs. Specifically, in models of PH induced by chronic intermittent hypoxia (CIH)—relevant to conditions like obstructive sleep apnea—increased NOX4 expression has been directly correlated with the pathological activation of the platelet-derived growth factor receptor beta (PDGFR-beta) and its downstream signaling cascade, including the PI3K/Akt kinase [167, 168]. This sustained activation accelerates PASMC proliferation and migration, driving the shift from a contractile to a synthetic phenotype and ultimately increasing vascular resistance.

The vascular endothelium is highly vulnerable to NOX4-induced stress. Pathological increases in NOX4 activity compromise endothelial cell integrity, promoting apoptosis and leading to a loss of barrier function and impaired vasodilation, primarily due to reduced nitric oxide (NO) bioavailability [169, 170]. Furthermore, NOX4 dysregulation is not limited to adult PH. While some neonatal models of PH induced by chronic hypoxia in piglets show unchanged NOX4 expression [171], other models, such as those for persistent pulmonary hypertension of the newborn (PPHN) in lambs, clearly demonstrate increased NOX4 and its critical regulatory subunit p22 expression [172]. This elevation is linked to NOX4-derived H_2O_2 mediated signaling that impairs angiogenesis (new blood vessel formation) and promotes vascular remodeling via NF-κB activation and subsequent cyclin D1 upregulation, suggesting its involvement in congenital and developmental forms of the disease.

The consistent identification of NOX4 as a pathological effector positions it as a highly attractive therapeutic target for PH. Specific small-molecule inhibitors of NOX4, such as setanaxib, have been rigorously tested in preclinical PH models [173]. These studies consistently demonstrate that NOX4 inhibition can significantly attenuate PASMC proliferation, reduce overall vascular remodeling, and decrease measured pulmonary arterial pressure. Crucially, this pathogenic role is further underscored by findings that established pharmacological agents known to reverse PH, such as Rosiglitazone, achieve their therapeutic effects, in part, by suppressing both NOX4 expression and the resulting superoxide production in the lung vasculature [174]. Thus, targeting NOX4 offers a promising, disease-modifying strategy to counteract the fundamental drivers of oxidative stress and remodeling in PH.

Discussion

The conceptual transition of NOX4 from a general marker of oxidative stress to a discrete, targetable mediator of lung pathology represents an important shift in our understanding of redox biology in pulmonary disease. As highlighted in this review, NOX4 is not merely a passive source of reactive oxygen species, but rather a context-dependent regulator that integrates environmental and cytokine-driven signals into sustained cellular responses. In particular, its role in promoting myofibroblast activation, (epithelial–mesenchymal transition) EMT, and persistent tissue remodeling underscores its contribution to both inflammatory injury and fibrosis. Among the pulmonary diseases discussed, IPF

and COPD appear to be the most promising candidates for NOX4-targeted interventions, given the consistent upregulation of NOX4 observed in human tissues and their strong association with fibrotic and airway remodeling processes. In contrast, the role of NOX4 in diseases with more heterogeneous inflammatory profiles, such as asthma and ARDS, remains less clearly defined.

Considering the failure of non-specific antioxidant approaches, there is the need for a more targeted and mechanistically informed strategy for NOX4 modulation. A central challenge lies in defining the therapeutic "redox window," whereby pathological H_2O_2 production is selectively suppressed without disrupting physiological signaling required for normal cellular function. To address these challenges, several priorities should be emphasized. First, setanaxib is NOX1 and NOX4 inhibitor, it is needed to improve specificity and minimizing interference with NOX2-dependent host defense mechanisms. Second, integrative therapeutic approaches, including the combination of NOX4 inhibitors with established anti-fibrotic agents (e.g., nintedanib or pirfenidone) or modulators of antioxidant pathways such as Nrf2 activators, may provide synergistic benefits by simultaneously limiting oxidant production and enhancing endogenous defense systems. Third, the cell type-specific roles of NOX4 in different lung compartments need to be completely defined and the relationship between NOX4 expression or activity and disease endotypes, progression, and therapeutic response needs to be established. Finally, the long-term consequences of sustained NOX4 inhibition, especially with respect to physiological redox signaling, host defense, and tissue homeostasis, require careful evaluation in human studies. Addressing these gaps will be essential for translating mechanistic insights into safe and effective disease-modifying therapies.

Author contributions

YW and TB collected literatures and drafted the original manuscript. JF, ZL, JD, LX, and KL collected and analyzed literatures. LJ contributed to the conception and design of the review, and finalized the manuscript. All authors contributed to the article and approved the submitted version.

Funding

The author(s) declared that financial support was received for this work and/or its publication. This work was supported by Zhejiang Provincial Medical, and Health Science and Technology Program Foundations to LJ (No. 2022KY1078, 2025KY1305).

Conflict of interest

The author(s) declared no potential conflicts of interest with respect to the research, authorship, and/or publication of this article.

Generative AI statement

The author(s) declared that generative AI was not used in the creation of this manuscript.

Any alternative text (alt text) provided alongside figures in this article has been generated by Frontiers with the support of artificial intelligence and reasonable efforts have been made to ensure accuracy, including review by the authors wherever possible. If you identify any issues, please contact us.

References

1. Chibaya L, Karim B, Zhang H, Jones SN. Mdm2 phosphorylation by akt regulates the p53 response to oxidative stress to promote cell proliferation and tumorigenesis. *Proc Natl Acad Sci U S A* (2021) 118(4):e2003193118. doi:10.1073/pnas.2003193118

2. Farrell L, Puig-Barbe A, Haque MI, Amcheslavsky A, Yu M, Bergmann A, et al. Actin remodeling mediates ROS production and JNK activation to drive apoptosis-induced proliferation. *PLoS Genet* (2022) 18(12):e1010533. doi:10.1371/journal.pgen.1010533

3. Janbandhu V, Tallapragada V, Patrick R, Li Y, Abeygunawardena D, Humphreys DT, et al. Hif-1a suppresses ROS-induced proliferation of cardiac fibroblasts following myocardial infarction. *Cell Stem Cell* (2022) 29(2):281–97 e12. doi:10.1016/j.stem.2021.10.009

4. Agidigbi TS, Kim C. Reactive oxygen species in osteoclast differentiation and possible pharmaceutical targets of ROS-mediated osteoclast diseases. *Int J Mol Sci* (2019) 20(14):3576. doi:10.3390/ijms20143576

5. Laha D, Sarkar J, Maity J, Pramanik A, Howlader MSI, Barthels D, et al. Polyphenolic compounds inhibit osteoclast differentiation while reducing autophagy through limiting ROS and the mitochondrial membrane potential. *Biomolecules* (2022) 12(9):1220. doi:10.3390/biom12091220

6. Banerjee S, Ghosh S, Mandal A, Ghosh N, Sil PC. ROS-associated immune response and metabolism: a mechanistic approach with implication of various diseases. *Arch Toxicol* (2020) 94(7):2293–317. doi:10.1007/s00204-020-02801-7

7. Liu S, Huang B, Cao J, Wang Y, Xiao H, Zhu Y, et al. ROS fine-tunes the function and fate of immune cells. *Int Immunopharmacol* (2023) 119:110069. doi:10.1016/j.intimp.2023.110069

8. Zhao Y, Liu B, Xu L, Yu S, Fu J, Wang J, et al. ROS-induced mtDNA release: the emerging messenger for communication between neurons and innate immune cells during neurodegenerative disorder progression. *Antioxidants (Basel)* (2021) 10(12):1917. doi:10.3390/antiox10121917

9. Lindsay RT, Rhodes CJ. Reactive oxygen species (ROS) in metabolic disease-don't shoot the metabolic messenger. *Int J Mol Sci* (2025) 26(6):2622. doi:10.3390/ijms26062622

10. Nisimoto Y, Diebold BA, Cosentino-Gomes D, Lambeth JD. Nox4: a hydrogen peroxide-generating oxygen sensor. *Biochemistry* (2014) 53(31):5111–20. doi:10.1021/bi500331y

11. Rogers LK, Cismowski MJ. Oxidative stress in the lung - the essential paradox. *Curr Opin Toxicol* (2018) 7:37–43. doi:10.1016/j.cotox.2017.09.001

12. Carnesecchi S, Deffert C, Donati Y, Basset O, Hinz B, Preynat-Seauve O, et al. A key role for NOX4 in epithelial cell death during development of lung fibrosis. *Antioxid Redox Signal* (2011) 15(3):607–19. doi:10.1089/ars.2010.3829

13. Harijith A, Basa P, Ha A, Thomas J, Jafri A, Fu P, et al. NOX4 mediates epithelial cell death in hyperoxic acute lung injury through mitochondrial reactive oxygen species. *Front Pharmacol* (2022) 13:880878. doi:10.3389/fphar.2022.880878

14. Amara N, Goven D, Prost F, Muloway R, Crestani B, Boczkowski J. NOX4/NADPH oxidase expression is increased in pulmonary fibroblasts from patients with idiopathic pulmonary fibrosis and mediates TGFbeta1-induced fibroblast differentiation into myofibroblasts. *Thorax* (2010) 65(8):733–8. doi:10.1136/thx.2009.113456

15. Hecker L, Vittal R, Jones T, Jagirdar R, Luckhardt TR, Horowitz JC, et al. NADPH oxidase-4 mediates myofibroblast activation and fibrogenic responses to lung injury. *Nat Med* (2009) 15(9):1077–81. doi:10.1038/nm.2005

16. Pendyala S, Gorshkova IA, Usatyuk PV, He D, Pennathur A, Lambeth JD, et al. Role of Nox4 and Nox2 in hyperoxia-induced reactive oxygen species generation and migration of human lung endothelial cells. *Antioxid Redox Signal* (2009) 11(4):747–64. doi:10.1089/ars.2008.2203

17. Fu P, Mohan V, Mansoor S, Tiruppathi C, Sadikot RT, Natarajan V. Role of nicotinamide adenine dinucleotide phosphate-reduced oxidase proteins in pseudomonas aeruginosa-induced lung inflammation and permeability. *Am J Respir Cell Mol Biol* (2013) 48(4):477–88. doi:10.1165/rcmb.2012-0242OC

18. Konior A, Schramm A, Czesnikiewicz-Guzik M, Guzik TJ. NADPH oxidases in vascular pathology. *Antioxid Redox Signal* (2014) 20(17):2794–814. doi:10.1089/ars.2013.5607

19. Sutcliffe A, Hollins F, Gomez E, Saunders R, Doe C, Cooke M, et al. Increased nicotinamide adenine dinucleotide phosphate oxidase 4 expression mediates intrinsic airway smooth muscle hypercontractility in asthma. *Am J Respir Crit Care Med* (2012) 185(3):267–74. doi:10.1164/rccm.201107-1281OC

20. Lu X, Murphy TC, Nanes MS, Hart CM. PPARgamma regulates hypoxia-induced Nox4 expression in human pulmonary artery smooth muscle cells through NF-kappaB. *Am J Physiol Lung Cell Mol Physiol* (2010) 299(4):L559–66. doi:10.1152/ajplung.00090.2010

21. Brandes RP, Weissmann N, Schroder K. Nox family NADPH oxidases: molecular mechanisms of activation. *Free Radic Biol Med* (2014) 76:208–26. doi:10.1016/j.freeradbiomed.2014.07.046

22. Matsumoto J, Higuchi M, Shimada M, Yamamoto Y, Kamio Y. Molecular cloning and sequence analysis of the gene encoding the H2O-forming NADH oxidase from Streptococcus mutans. *Biosci Biotechnol Biochem* (1996) 60(1):39–43. doi:10.1271/bbb.60.39

23. Kawahara T, Quinn MT, Lambeth JD. Molecular evolution of the reactive oxygen-generating NADPH oxidase (Nox/Duox) family of enzymes. *BMC Evol Biol* (2007) 7:109. doi:10.1186/1471-2148-7-109

24. Banfi B, Tirone F, Durussel I, Knisz J, Moskwa P, Molnar GZ, et al. Mechanism of Ca2+ activation of the NADPH oxidase 5 (NOX5). *J Biol Chem* (2004) 279(18):18583–91. doi:10.1074/jbc.M310268200

25. Jagnandan D, Church JE, Banfi B, Stuehr DJ, Marrero MB, Fulton DJ. Novel mechanism of activation of NADPH oxidase 5. calcium sensitization *via* phosphorylation. *J Biol Chem* (2007) 282(9):6494–507. doi:10.1074/jbc.M608966200

26. Ago T, Kuroda J, Pain J, Fu C, Li H, Sadoshima J. Upregulation of Nox4 by hypertrophic stimuli promotes apoptosis and mitochondrial dysfunction in cardiac myocytes. *Circ Res* (2010) 106(7):1253–64. doi:10.1161/CIRCRESAHA.109.213116

27. Martyn KD, Frederick LM, von Loehneysen K, Dinauer MC, Knaus UG. Functional analysis of Nox4 reveals unique characteristics compared to other NADPH oxidases. *Cell Signal* (2006) 18(1):69–82. doi:10.1016/j.cellsig.2005.03.023

28. Vermot A, Petit-Hartlein I, Smith SME, Fieschi F. NADPH oxidases (NOX): an overview from discovery, molecular mechanisms to physiology and pathology. *Antioxidants (Basel).* (2021) 10(6):890. doi:10.3390/antiox10060890

29. Wu X, Henin J, Baciou L, Baaden M, Cailliez F, de la Lande A. Mechanistic insights on heme-to-heme transmembrane electron transfer within NADPH oxydases from atomistic simulations. *Front Chem* (2021) 9:650651. doi:10.3389/fchem.2021.650651

30. Jackson HM, Kawahara T, Nisimoto Y, Smith SM, Lambeth JD. Nox4 B-loop creates an interface between the transmembrane and dehydrogenase domains. *J Biol Chem* (2010) 285(14):10281–90. doi:10.1074/jbc.M109.084939

31. Magnani F, Nenci S, Millana Fananas E, Ceccon M, Romero E, Fraaije MW, et al. Crystal structures and atomic model of NADPH oxidase. *Proc Natl Acad Sci U S A* (2017) 114(26):6764–9. doi:10.1073/pnas.1702293114

32. Ogboo BC, Grabovyy UV, Maini A, Scouten S, van der Vliet A, Mattevi A, et al. Architecture of the NADPH oxidase family of enzymes. *Redox Biol* (2022) 52:102298. doi:10.1016/j.redox.2022.102298

33. Petit-Hartlein I, Vermot A, Thepaut M, Humm AS, Dupeux F, Dupuy J, et al. X-ray structure and enzymatic study of a bacterial NADPH oxidase highlight the activation mechanism of eukaryotic NOX. *Elife* (2024) 13:RP93759. doi:10.7554/eLife.93759

34. O'Neill S, Mathis M, Kovacic L, Zhang S, Reinhardt J, Scholz D, et al. Quantitative interaction analysis permits molecular insights into functional NOX4 NADPH oxidase heterodimer assembly. *J Biol Chem* (2018) 293(23):8750–60. doi:10.1074/jbc.RA117.001045

35. von Lohneysen K, Noack D, Wood MR, Friedman JS, Knaus UG. Structural insights into Nox4 and Nox2: motifs involved in function and cellular localization. *Mol Cell Biol* (2010) 30(4):961–75. doi:10.1128/MCB.01393-09

36. von Lohneysen K, Noack D, Jesaitis AJ, Dinauer MC, Knaus UG. Mutational analysis reveals distinct features of the Nox4-p22 phox complex. *J Biol Chem* (2008) 283(50):35273–82. doi:10.1074/jbc.M804200200

37. Takac I, Schroder K, Zhang L, Lardy B, Anilkumar N, Lambeth JD, et al. The E-loop is involved in hydrogen peroxide formation by the NADPH oxidase Nox4. *J Biol Chem* (2011) 286(15):13304–13. doi:10.1074/jbc.M110.192138

38. Sturrock A, Cahill B, Norman K, Huecksteadt TP, Hill K, Sanders K, et al. Transforming growth factor-beta1 induces Nox4 NAD(P)H oxidase and reactive oxygen species-dependent proliferation in human pulmonary artery smooth muscle cells. *Am J Physiol Lung Cell Mol Physiol* (2006) 290(4):L661–L73. doi:10.1152/ajplung.00269.2005

39. Carmona-Cuenca I, Roncero C, Sancho P, Caja L, Fausto N, Fernandez M, et al. Upregulation of the NADPH oxidase NOX4 by TGF-beta in hepatocytes is required for its pro-apoptotic activity. *J Hepatol* (2008) 49(6):965–76. doi:10.1016/j.jhep.2008.07.021

40. Yan F, Wang Y, Wu X, Peshavariya HM, Dusting GJ, Zhang M, et al. Nox4 and redox signaling mediate TGF-beta-induced endothelial cell apoptosis and phenotypic switch. *Cell Death Dis* (2014) 5(1):e1010. doi:10.1038/cddis.2013.551

41. Cucoranu I, Clempus R, Dikalova A, Phelan PJ, Ariyan S, Dikalov S, et al. NAD(P)H oxidase 4 mediates transforming growth factor-beta1-induced differentiation of cardiac fibroblasts into myofibroblasts. *Circ Res* (2005) 97(9):900–7. doi:10.1161/01.RES.0000187457.24338.3D

42. Michaeloudes C, Sukkar MB, Khorasani NM, Bhavsar PK, Chung KF. TGF-beta regulates Nox4, MnSOD and catalase expression, and IL-6 release in airway smooth muscle cells. *Am J Physiol Lung Cell Mol Physiol* (2011) 300(2):L295–304. doi:10.1152/ajplung.00134.2010

43. Boudreau HE, Casterline BW, Rada B, Korzeniowska A, Leto TL. Nox4 involvement in TGF-beta and SMAD3-driven induction of the epithelial-to-mesenchymal transition and migration of breast epithelial cells. *Free Radic Biol Med* (2012) 53(7):1489–99. doi:10.1016/j.freeradbiomed.2012.06.016

44. Parvani JG, Taylor MA, Schiemann WP. Noncanonical TGF-beta signaling during mammary tumorigenesis. *J Mammary Gland Biol Neoplasia* (2011) 16(2):127–46. doi:10.1007/s10911-011-9207-3

45. Zhou B, Mu J, Gong Y, Lu C, Zhao Y, He T, et al. Brd4 inhibition attenuates unilateral ureteral obstruction-induced fibrosis by blocking TGF-beta-mediated Nox4 expression. *Redox Biol* (2017) 11:390–402. doi:10.1016/j.redox.2016.12.031

46. Bai G, Hock TD, Logsdon N, Zhou Y, Thannickal VJ. A far-upstream AP-1/Smad binding box regulates human NOX4 promoter activation by transforming growth factor-beta. *Gene* (2014) 540(1):62–7. doi:10.1016/j.gene.2014.02.026

47. Boudreau HE, Ma WF, Korzeniowska A, Park JJ, Bhagwat MA, Leto TL. Histone modifications affect differential regulation of TGFbeta-induced NADPH oxidase 4 (NOX4) by wild-type and mutant p53. *Oncotarget* (2017) 8(27):44379–97. doi:10.18632/oncotarget.17892

48. Ijaz T, Jamaluddin M, Zhao Y, Zhang Y, Jay J, Finnerty CC, et al. Coordinate activities of BRD4 and CDK9 in the transcriptional elongation complex are required for TGFbeta-induced Nox4 expression and myofibroblast transdifferentiation. *Cell Death Dis* (2017) 8(2):e2606. doi:10.1038/cddis.2016.434

49. Diebold I, Petry A, Hess J, Gorlach A. The NADPH oxidase subunit NOX4 is a new target gene of the hypoxia-inducible factor-1. *Mol Biol Cell* (2010) 21(12):2087–96. doi:10.1091/mbc.e09-12-1003

50. Hsieh CH, Wu CP, Lee HT, Liang JA, Yu CY, Lin YJ. NADPH oxidase subunit 4 mediates cycling hypoxia-promoted radiation resistance in glioblastoma multiforme. *Free Radic Biol Med* (2012) 53(4):649–58. doi:10.1016/j.freeradbiomed.2012.06.009

51. Jaakkola P, Mole DR, Tian YM, Wilson MI, Gielbert J, Gaskell SJ, et al. Targeting of HIF-alpha to the von Hippel-Lindau ubiquitylation complex by O2-regulated prolyl hydroxylation. *Science* (2001) 292(5516):468–72. doi:10.1126/science.1059796

52. Dengler VL, Galbraith M, Espinosa JM. Transcriptional regulation by hypoxia inducible factors. *Crit Rev Biochem Mol Biol* (2014) 49(1):1–15. doi:10.3109/10409238.2013.838205

53. Liu W, Shen SM, Zhao XY, Chen GQ. Targeted genes and interacting proteins of hypoxia inducible factor-1. *Int J Biochem Mol Biol* (2012) 3(2):165–78.

54. Patel DN, Bailey SR, Gresham JK, Schuchman DB, Shelhamer JH, Goldstein BJ, et al. TLR4-NOX4-AP-1 signaling mediates lipopolysaccharide-induced CXCR6 expression in human aortic smooth muscle cells. *Biochem Biophys Res Commun* (2006) 347(4):1113–20. doi:10.1016/j.bbrc.2006.07.015

55. Li X, Ma TK, Wang P, Shi H, Hai S, Qin Y, et al. HOXD10 attenuates renal fibrosis by inhibiting NOX4-induced ferroptosis. *Cell Death Dis* (2024) 15(6):398. doi:10.1038/s41419-024-06780-w

56. Degasper C, Brunner A, Sampson N, Tsibulak I, Wieser V, Welponer H, et al. NADPH oxidase 4 expression in the normal endometrium and in endometrial cancer. *Tumour Biol* (2019) 41(2):1010428319830002. doi:10.1177/1010428319830002

57. Sanders YY, Liu H, Liu G, Thannickal VJ. Epigenetic mechanisms regulate NADPH oxidase-4 expression in cellular senescence. *Free Radic Biol Med* (2015) 79:197–205. doi:10.1016/j.freeradbiomed.2014.12.008

58. Chen F, Li X, Aquadro E, Haigh S, Zhou J, Stepp DW, et al. Inhibition of histone deacetylase reduces transcription of NADPH oxidases and ROS production and ameliorates pulmonary arterial hypertension. *Free Radic Biol Med* (2016) 99:167–78. doi:10.1016/j.freeradbiomed.2016.08.003

59. Hakami NY, Dusting GJ, Peshavariya HM. Trichostatin A, a histone deacetylase inhibitor suppresses NADPH oxidase 4-Derived redox signalling and angiogenesis. *J Cell Mol Med* (2016) 20(10):1932–44. doi:10.1111/jcmm.12885

60. Chen Y, Lu Y, Xu S, Liu M, Chen W, Zhang Y, et al. HDAC1 expression is positively correlated with NADPH oxidase 4-mediated oxidative stress in a mouse model of traumatic brain injury. *J Neurophysiol* (2022) 127(5):1438–44. doi:10.1152/jn.00049.2022

61. Manea SA, Vlad ML, Fenyo IM, Lazar AG, Raicu M, Muresian H, et al. Pharmacological inhibition of histone deacetylase reduces NADPH oxidase expression, oxidative stress and the progression of atherosclerotic lesions in hypercholesterolemic apolipoprotein E-deficient mice; potential implications for human atherosclerosis. *Redox Biol* (2020) 28:101338. doi:10.1016/j.redox.2019.101338

62. Howe FS, Fischl H, Murray SC, Mellor J. Is H3K4me3 instructive for transcription activation? *Bioessays* (2017) 39(1):1–12. doi:10.1002/bies.201600095

63. Binenbaum J, Adamkova V, Fryer H, Xu L, Gorringe N, Wlodzimierz P, et al. CRISPR targeting of H3K4me3 activates gene expression and unlocks centromere-proximal crossover recombination in arabidopsis. *Nat Commun* (2025) 16(1):9587. doi:10.1038/s41467-025-65167-3

64. Yu H, Zhang Y, Liao Z, Walters BW, Lesch BJ. H3K4me3 amplifies transcription at intergenic active regulatory elements. *Genes Dev* (2025) 39:1290–8. doi:10.1101/gad.352841.125

65. Huang X, Gao X, Li W, Jiang S, Li R, Hong H, et al. Stable H3K4me3 is associated with transcription initiation during early embryo development. *Bioinformatics* (2019) 35(20):3931–6. doi:10.1093/bioinformatics/btz173

66. Cai Y, Zhang Y, Loh YP, Tng JQ, Lim MC, Cao Z, et al. H3K27me3-rich genomic regions can function as silencers to repress gene expression *via* chromatin interactions. *Nat Commun* (2021) 12(1):719. doi:10.1038/s41467-021-20940-y

67. Fierro-Fernandez M, Busnadiego O, Sandoval P, Espinosa-Diez C, Blanco-Ruiz E, Rodriguez M, et al. miR-9-5p suppresses pro-fibrogenic transformation of fibroblasts and prevents organ fibrosis by targeting NOX4 and TGFBR2. *EMBO Rep* (2015) 16(10):1358–77. doi:10.15252/embr.201540750

68. Li W, Sheng Y, Wang J, Wu S, Han C. MicroRNA-9a-5p-NOX4 inhibits intestinal inflammatory injury by regulating the M1 polarization of intestinal macrophages. *J Biochem Mol Toxicol* (2023) 37(2):e23245. doi:10.1002/jbt.23245

69. Wang Z, Song Y, Jiang J, Piao Y, Li L, Bai Q, et al. MicroRNA-182-5p attenuates asthmatic airway inflammation by targeting NOX4. *Front Immunol* (2022) 13:853848. doi:10.3389/fimmu.2022.853848

70. Xiao L, Gu Y, Ren G, Chen L, Liu L, Wang X, et al. miRNA-146a mimic inhibits NOX4/P38 signalling to ameliorate mouse myocardial ischaemia reperfusion (I/R) injury. *Oxid Med Cell Longev* (2021) 2021:6366254. doi:10.1155/2021/6366254

71. Woo SJ, Kim Y, Jung H, Lee JJ, Hong JY. MicroRNA 148a suppresses tuberculous fibrosis by targeting NOX4 and POLDIP2. *Int J Mol Sci* (2022) 23(6):2999. doi:10.3390/ijms23062999

72. Desai LP, Zhou Y, Estrada AV, Ding Q, Cheng G, Collawn JF, et al. Negative regulation of NADPH oxidase 4 by hydrogen peroxide-inducible clone 5 (Hic-5) protein. *J Biol Chem* (2014) 289(26):18270–8. doi:10.1074/jbc.M114.562249

73. Gil Lorenzo AF, Costantino VV, Appiolaza ML, Cacciamani V, Benardon ME, Bocanegra V, et al. Heat shock protein 70 and CHIP promote Nox4 ubiquitination and degradation within the losartan antioxidative effect in proximal tubule cells. *Cell Physiol Biochem* (2015) 36(6):2183–97. doi:10.1159/000430184

74. Park HS, Jung HY, Park EY, Kim J, Lee WJ, Bae YS. Cutting edge: direct interaction of TLR4 with NAD(P)H oxidase 4 isozyme is essential for lipopolysaccharide-induced production of reactive oxygen species and activation of NF-kappa B. *J Immunol* (2004) 173(6):3589–93. doi:10.4049/jimmunol.173.6.3589

75. Maloney E, Sweet IR, Hockenbery DM, Pham M, Rizzo NO, Tateya S, et al. Activation of NF-kappaB by palmitate in endothelial cells: a key role for NADPH oxidase-derived superoxide in response to TLR4 activation. *Arterioscler Thromb Vasc Biol* (2009) 29(9):1370–5. doi:10.1161/ATVBAHA.109.188813

76. Helfinger V, Palfi K, Weigert A, Schroder K. The NADPH oxidase Nox4 controls macrophage polarization in an NFkappaB-Dependent manner. *Oxid Med Cell Longev* (2019) 2019:3264858. doi:10.1155/2019/3264858

77. Ding BY, Xie CN, Xie JY, Gao ZW, Fei XW, Hong EH, et al. Knockdown of NADPH oxidase 4 reduces mitochondrial oxidative stress and neuronal pyroptosis following intracerebral hemorrhage. *Neural Regen Res* (2023) 18(8):1734–42. doi:10.4103/1673-5374.360249

78. Liu C, Wu J, Li Z, Huang X, Xie X, Huang Y. Cinobufotalin inhibits proliferation, migration and invasion in hepatocellular carcinoma by triggering NOX4/NLRP3/GSDMD-dependent pyroptosis. *Front Oncol* (2024) 14:1438306. doi:10.3389/fonc.2024.1438306

79. Gu C, Draga D, Zhou C, Su T, Zou C, Gu Q, et al. miR-590-3p inhibits pyroptosis in diabetic retinopathy by targeting NLRP1 and inactivating the NOX4 signaling pathway. *Invest Ophthalmol Vis Sci* (2019) 60(13):4215–23. doi:10.1167/iovs.19-27825

80. Liu G, Liu Q, Yan B, Zhu Z, Xu Y. USP7 inhibition alleviates H(2)O(2)-Induced injury in chondrocytes *via* inhibiting NOX4/NLRP3 pathway. *Front Pharmacol* (2020) 11:617270. doi:10.3389/fphar.2020.617270

81. Zeng H, Zou P, Chen Y, Zhang P, Shao L. NOX4 aggravates doxorubicin-induced cardiomyocyte pyroptosis by increasing reactive oxygen species content and activating the NLRP3 inflammasome. *Cardiovasc Diagn Ther* (2024) 14(1):84–100. doi:10.21037/cdt-23-142

82. Park MW, Cha HW, Kim J, Kim JH, Yang H, Yoon S, et al. NOX4 promotes ferroptosis of astrocytes by oxidative stress-induced lipid peroxidation *via* the impairment of mitochondrial metabolism in Alzheimer's diseases. *Redox Biol* (2021) 41:101947. doi:10.1016/j.redox.2021.101947

83. Maimaiti Y, Su T, Zhang Z, Ma L, Zhang Y, Xu H. NOX4-mediated astrocyte ferroptosis in Alzheimer's disease. *Cell Biosci* (2024) 14(1):88. doi:10.1186/s13578-024-01266-w

84. Lin Z, Ying C, Si X, Xue N, Liu Y, Zheng R, et al. NOX4 exacerbates Parkinson's disease pathology by promoting neuronal ferroptosis and neuroinflammation. *Neural Regen Res* (2025) 20(7):2038–52. doi:10.4103/NRR.NRR-D-23-01265

85. Lee YM, Kim BJ, Chun YS, So I, Choi H, Kim MS, et al. NOX4 as an oxygen sensor to regulate TASK-1 activity. *Cell Signal* (2006) 18(4):499–507. doi:10.1016/j.cellsig.2005.05.025

86. Ahmad M, Kelly MR, Zhao X, Kandhi S, Wolin MS. Roles for Nox4 in the contractile response of bovine pulmonary arteries to hypoxia. *Am J Physiol Heart Circ Physiol* (2010) 298(6):H1879–88. doi:10.1152/ajpheart.01228.2009

87. Jiang H, Li F, Cai L, Chen Q. Role of the TSPO-NOX4 axis in angiogenesis in glioblastoma. *Front Pharmacol* (2022) 13:1001588. doi:10.3389/fphar.2022.1001588

88. Roshan MS, Pourheydar B, Daneshfar S, Chodari L. Decreased cardiac NOX4 and SIRT-1 protein levels contribute to decreased angiogenesis in the heart of diabetic rats: rescue effects of IGF-1 and exercise. *Adv Pharm Bull* (2023) 13(1):202–9. doi:10.34172/apb.2023.039

89. Tang X, Wang JJ, Wang J, Abboud HE, Chen Y, Zhang SX. Endothelium-specific deletion of Nox4 delays retinal vascular development and mitigates pathological angiogenesis. *Angiogenesis* (2021) 24(2):363–77. doi:10.1007/s10456-020-09757-3

90. Kim J, Kim J, Lim HJ, Lee S, Bae YS, Kim J. Nox4-IGF2 axis promotes differentiation of embryoid body cells into derivatives of the three embryonic germ layers. *Stem Cell Rev Rep* (2022) 18(3):1181–92. doi:10.1007/s12015-021-10303-x

91. Schader T, Lowe O, Reschke C, Malacarne P, Hahner F, Muller N, et al. Oxidation of HDAC4 by Nox4-derived H(2)O(2) maintains tube formation by endothelial cells. *Redox Biol* (2020) 36:101669. doi:10.1016/j.redox.2020.101669

92. Hahner F, Moll F, Warwick T, Hebchen DM, Buchmann GK, Epah J, et al. Nox4 promotes endothelial differentiation through chromatin remodeling. *Redox Biol* (2022) 55:102381. doi:10.1016/j.redox.2022.102381

93. Li J, Stouffs M, Serrander L, Banfi B, Bettiol E, Charnay Y, et al. The NADPH oxidase NOX4 drives cardiac differentiation: role in regulating cardiac transcription factors and MAP kinase activation. *Mol Biol Cell* (2006) 17(9):3978–88. doi:10.1091/mbc.e05-06-0532

94. Brault J, Vigne B, Meunier M, Beaumel S, Mollin M, Park S, et al. NOX4 is the main NADPH oxidase involved in the early stages of hematopoietic differentiation from human induced pluripotent stem cells. *Free Radic Biol Med* (2020) 146:107–18. doi:10.1016/j.freeradbiomed.2019.10.005

95. Mittal M, Gu XQ, Pak O, Pamenter ME, Haag D, Fuchs DB, et al. Hypoxia induces kv channel current inhibition by increased NADPH oxidase-derived reactive oxygen species. *Free Radic Biol Med* (2012) 52(6):1033–42. doi:10.1016/j.freeradbiomed.2011.12.004

96. Eyrich NW, Potts CR, Robinson MH, Maximov V, Kenney AM. Reactive oxygen species signaling promotes hypoxia-inducible factor 1alpha stabilization in sonic hedgehog-driven cerebellar progenitor cell proliferation. *Mol Cell Biol* (2019) 39(8):e00268-18. doi:10.1128/MCB.00268-18

97. Meng D, Mei A, Liu J, Kang X, Shi X, Qian R, et al. NADPH oxidase 4 mediates insulin-stimulated HIF-1alpha and VEGF expression, and angiogenesis *in vitro*. *PLoS One* (2012) 7(10):e48393. doi:10.1371/journal.pone.0048393

98. Anilkumar N, San Jose G, Sawyer I, Santos CX, Sand C, Brewer AC, et al. A 28-kDa splice variant of NADPH oxidase-4 is nuclear-localized and involved in redox signaling in vascular cells. *Arterioscler Thromb Vasc Biol* (2013) 33(4):e104–12. doi:10.1161/ATVBAHA.112.300956

99. Moloney JN, Jayavelu AK, Stanicka J, Roche SL, O'Brien RL, Scholl S, et al. Nuclear membrane-localised NOX4D generates pro-survival ROS in FLT3-ITD-expressing AML. *Oncotarget* (2017) 8(62):105440–57. doi:10.18632/oncotarget.22241

100. Varga ZV, Pipicz M, Baan JA, Baranyai T, Koncsos G, Leszek P, et al. Alternative splicing of NOX4 in the failing human heart. *Front Physiol* (2017) 8:935. doi:10.3389/fphys.2017.00935

101. Matsushima S, Kuroda J, Ago T, Zhai P, Park JY, Xie LH, et al. Increased oxidative stress in the nucleus caused by Nox4 mediates oxidation of HDAC4 and cardiac hypertrophy. *Circ Res* (2013) 112(4):651–63. doi:10.1161/CIRCRESAHA.112.279760

102. Przybylska D, Janiszewska D, Gozdzik A, Bielak-Zmijewska A, Sunderland P, Sikora E, et al. NOX4 downregulation leads to senescence of human vascular smooth muscle cells. *Oncotarget* (2016) 7(41):66429–43. doi:10.18632/oncotarget.12079

103. Sanders YY, Lyv X, Zhou QJ, Xiang Z, Stanford D, Bodduluri S, et al. Brd4-p300 inhibition downregulates Nox4 and accelerates lung fibrosis resolution in aged mice. *JCI Insight* (2020) 5(14):e137127. doi:10.1172/jci.insight.137127

104. Fu P, Ramchandran R, Sudhadevi T, Kumar PPK, Krishnan Y, Liu Y, et al. NOX4 mediates pseudomonas aeruginosa-Induced nuclear reactive oxygen species generation and chromatin remodeling in lung epithelium. *Antioxidants (Basel)* (2021) 10(3):477. doi:10.3390/antiox10030477

105. Helfinger V, Freiherr von Gall F, Henke N, Kunze MM, Schmid T, Rezende F, et al. Genetic deletion of Nox4 enhances cancerogen-induced formation of solid tumors. *Proc Natl Acad Sci U S A*. (2021) 118(11):e2020152118. doi:10.1073/pnas.2020152118

106. Stanicka J, Russell EG, Woolley JF, Cotter TG. NADPH oxidase-generated hydrogen peroxide induces DNA damage in mutant FLT3-expressing leukemia cells. *J Biol Chem* (2015) 290(15):9348–61. doi:10.1074/jbc.M113.510495

107. Zeng C, Wu Q, Wang J, Yao B, Ma L, Yang Z, et al. NOX4 supports glycolysis and promotes glutamine metabolism in non-small cell lung cancer cells. *Free Radic Biol Med* (2016) 101:236–48. doi:10.1016/j.freeradbiomed.2016.10.500

108. Nabeebaccus AA, Zoccarato A, Hafstad AD, Santos CX, Aasum E, Brewer AC, et al. Nox4 reprograms cardiac substrate metabolism *via* protein O-GlcNAcylation to enhance stress adaptation. *JCI Insight* (2017) 2(24):e96184. doi:10.1172/jci.insight.96184

109. Bond JM, Dzubanova M, Addington AK, Najt CP, Gilbert ER, Tencerova M, et al. Sex-specific metabolic responses to high-fat diet in mice with NOX4 deficiency. *Redox Biol* (2025) 85:103698. doi:10.1016/j.redox.2025.103698

110. Xirouchaki CE, Jia Y, McGrath MJ, Greatorex S, Tran M, Merry TL, et al. Skeletal muscle NOX4 is required for adaptive responses that prevent insulin resistance. *Sci Adv* (2021) 7(51):eabl4988. doi:10.1126/sciadv.abl4988

111. Specht KS, Kant S, Addington AK, McMillan RP, Hulver MW, Learnard H, et al. Nox4 mediates skeletal muscle metabolic responses to exercise. *Mol Metab* (2021) 45:101160. doi:10.1016/j.molmet.2020.101160

112. Dzubanova M, Bond JM, Craige SM, Tencerova M. NOX4-reactive oxygen species axis: critical regulators of bone health and metabolism. *Front Cell Dev Biol* (2024) 12:1432668. doi:10.3389/fcell.2024.1432668

113. Penuelas-Haro I, Espinosa-Sotelo R, Crosas-Molist E, Herranz-Iturbide M, Caballero-Diaz D, Alay A, et al. The NADPH oxidase NOX4 regulates redox and metabolic homeostasis preventing HCC progression. *Hepatology* (2023) 78(2):416–33. doi:10.1002/hep.32702

114. Sedeek M, Callera G, Montezano A, Gutsol A, Heitz F, Szyndralewiez C, et al. Critical role of Nox4-based NADPH oxidase in glucose-induced oxidative stress in the kidney: implications in type 2 diabetic nephropathy. *Am J Physiol Renal Physiol* (2010) 299(6):F1348–58. doi:10.1152/ajprenal.00028.2010

115. Xiong Y, Weng Y, Zhu S, Qin J, Feng J, Jing X, et al. NOX4 modulates breast cancer progression through cancer cell metabolic reprogramming and CD8(+) T cell antitumor activity. *Front Immunol* (2025) 16:1534936. doi:10.3389/fimmu.2025.1534936

116. Herranz-Iturbide M, Lopez-Luque J, Gonzalez-Sanchez E, Caballero-Diaz D, Crosas-Molist E, Martin-Mur B, et al. NADPH oxidase 4 (Nox4) deletion accelerates liver regeneration in mice. *Redox Biol* (2021) 40:101841. doi:10.1016/j.redox.2020.101841

117. Bonello S, Zahringer C, BelAiba RS, Djordjevic T, Hess J, Michiels C, et al. Reactive oxygen species activate the HIF-1alpha promoter *via* a functional NFkappaB site. *Arterioscler Thromb Vasc Biol* (2007) 27(4):755–61. doi:10.1161/01.ATV.0000258979.92828.bc

118. Sciarretta S, Volpe M, Sadoshima J. NOX4 regulates autophagy during energy deprivation. *Autophagy* (2014) 10(4):699–701. doi:10.4161/auto.27955

119. Sun J, Chen W, Li S, Yang S, Zhang Y, Hu X, et al. Nox4 promotes RANKL-induced autophagy and osteoclastogenesis *via* activating ROS/PERK/eIF-2alpha/ATF4 pathway. *Front Pharmacol* (2021) 12:751845. doi:10.3389/fphar.2021.751845

120. Sciarretta S, Zhai P, Shao D, Zablocki D, Nagarajan N, Terada LS, et al. Activation of NADPH oxidase 4 in the endoplasmic reticulum promotes cardiomyocyte autophagy and survival during energy stress through the protein kinase RNA-activated-like endoplasmic reticulum kinase/eukaryotic initiation factor 2alpha/activating transcription factor 4 pathway. *Circ Res* (2013) 113(11):1253–64. doi:10.1161/CIRCRESAHA.113.301787

121. Noble PW, Barkauskas CE, Jiang D. Pulmonary fibrosis: patterns and perpetrators. *J Clin Invest* (2012) 122(8):2756–62. doi:10.1172/JCI60323

122. Cheresh P, Kim SJ, Tulasiram S, Kamp DW. Oxidative stress and pulmonary fibrosis. *Biochim Biophys Acta* (2013) 1832(7):1028–40. doi:10.1016/j.bbadis.2012.11.021

123. Veith C, Boots AW, Idris M, van Schooten FJ, van der Vliet A. Redox imbalance in idiopathic pulmonary fibrosis: a role for oxidant cross-talk between NADPH oxidase enzymes and mitochondria. *Antioxid Redox Signal* (2019) 31(14):1092–115. doi:10.1089/ars.2019.7742

124. Zhao W, Bai B, Li H, Feng Y, Sun J, Fang Y, et al. The role of oxidative stress-related genes in idiopathic pulmonary fibrosis. *Sci Rep* (2025) 15(1):5954. doi:10.1038/s41598-025-89770-y

125. Wang J, Chao J. Epithelial cell dysfunction in pulmonary fibrosis: mechanisms, interactions, and emerging therapeutic targets. *Pharmaceuticals (Basel).* (2025) 18(6):812. doi:10.3390/ph18060812

126. Camelo A, Dunmore R, Sleeman MA, Clarke DL. The epithelium in idiopathic pulmonary fibrosis: breaking the barrier. *Front Pharmacol* (2014) 4:173. doi:10.3389/fphar.2013.00173

127. Sakai N, Tager AM. Fibrosis of two: epithelial cell-fibroblast interactions in pulmonary fibrosis. *Biochim Biophys Acta* (2013) 1832(7):911–21. doi:10.1016/j.bbadis.2013.03.001

128. Sato N, Takasaka N, Yoshida M, Tsubouchi K, Minagawa S, Araya J, et al. Metformin attenuates lung fibrosis development *via* NOX4 suppression. *Respir Res* (2016) 17(1):107. doi:10.1186/s12931-016-0420-x

129. Jarman ER, Khambata VS, Cope C, Jones P, Roger J, Ye LY, et al. An inhibitor of NADPH oxidase-4 attenuates established pulmonary fibrosis in a rodent disease model. *Am J Respir Cell Mol Biol* (2014) 50(1):158–69. doi:10.1165/rcmb.2013-0174OC

130. Larson-Casey JL, Gu L, Kang J, Dhyani A, Carter AB. NOX4 regulates macrophage apoptosis resistance to induce fibrotic progression. *J Biol Chem* (2021) 297(1):100810. doi:10.1016/j.jbc.2021.100810

131. Martin-Garrido A, Brown DI, Lyle AN, Dikalova A, Seidel-Rogol B, Lassegue B, et al. NADPH oxidase 4 mediates TGF-beta-induced smooth muscle alpha-actin *via* p38MAPK and serum response factor. *Free Radic Biol Med* (2011) 50(2):354–62. doi:10.1016/j.freeradbiomed.2010.11.007

132. Liu RM, Desai LP. Reciprocal regulation of TGF-beta and reactive oxygen species: a perverse cycle for fibrosis. *Redox Biol* (2015) 6:565–77. doi:10.1016/j.redox.2015.09.009

133. Veith C, Hristova M, Danyal K, Habibovic A, Dustin CM, McDonough JE, et al. Profibrotic epithelial TGF-beta1 signaling involves NOX4-mitochondria cross talk and redox-mediated activation of the tyrosine kinase FYN. *Am J Physiol Lung Cell Mol Physiol* (2021) 320(3):L356–L67. doi:10.1152/ajplung.00444.2019

134. Hao B, Sun R, Guo X, Zhang L, Cui J, Zhou Y, et al. NOX4-Derived ROS promotes collagen I deposition in bronchial smooth muscle cells by activating noncanonical p38MAPK/Akt-Mediated TGF-beta signaling. *Oxid Med Cell Longev* (2021) 2021:6668971. doi:10.1155/2021/6668971

135. Hecker L, Logsdon NJ, Kurundkar D, Kurundkar A, Bernard K, Hock T, et al. Reversal of persistent fibrosis in aging by targeting Nox4-Nrf2 redox imbalance. *Sci Transl Med* (2014) 6(231):231ra47. doi:10.1126/scitranslmed.3008182

136. Kato K, Hecker L. NADPH oxidases: pathophysiology and therapeutic potential in age-associated pulmonary fibrosis. *Redox Biol* (2020) 33:101541. doi:10.1016/j.redox.2020.101541

137. Rodrigues SO, Cunha C, Soares GMV, Silva PL, Silva AR, Goncalves-de-Albuquerque CF. Mechanisms, pathophysiology and currently proposed treatments of chronic obstructive pulmonary disease. *Pharmaceuticals (Basel)* (2021) 14(10):979. doi:10.3390/ph14100979

138. Guo X, Fan Y, Cui J, Hao B, Zhu L, Sun X, et al. NOX4 expression and distal arteriolar remodeling correlate with pulmonary hypertension in COPD. *BMC Pulm Med* (2018) 18(1):111. doi:10.1186/s12890-018-0680-y

139. Liu X, Hao B, Ma A, He J, Liu X, Chen J. The expression of NOX4 in smooth muscles of small airway correlates with the disease severity of COPD. *Biomed Res Int* (2016) 2016:2891810. doi:10.1155/2016/2891810

140. Hollins F, Sutcliffe A, Gomez E, Berair R, Russell R, Szyndralewiez C, et al. Airway smooth muscle NOX4 is upregulated and modulates ROS generation in COPD. *Respir Res* (2016) 17(1):84. doi:10.1186/s12931-016-0403-y

141. Li M, Wang H, Lu Y, Cai J. Luteolin suppresses inflammation and oxidative stress in chronic obstructive pulmonary disease through inhibition of the NOX4-mediated NF-kappaB signaling pathway. *Immun Inflamm Dis* (2023) 11(4):e820. doi:10.1002/iid3.820

142. Wang X, Murugesan P, Zhang P, Xu S, Peng L, Wang C, et al. NADPH oxidase isoforms in COPD patients and acute cigarette smoke-exposed mice: induction of oxidative stress and lung inflammation. *Antioxidants (Basel)* (2022) 11(8):1539. doi:10.3390/antiox11081539

143. Fan X, Dong T, Yan K, Ci X, Peng L. PM2.5 increases susceptibility to acute exacerbation of COPD *via* NOX4/Nrf2 redox imbalance-mediated mitophagy. *Redox Biol.* (2023) 59:102587. doi:10.1016/j.redox.2022.102587

144. Orozco-Levi M, Colmenares-Mejia C, Ruiz J, Valencia-Baron YD, Ramirez-Sarmiento A, Quintero-Lesmes DC, et al. Effect of antioxidants in the treatment of COPD patients: scoping review. *J Nutr Metab* (2021) 2021:7463391. doi:10.1155/2021/7463391

145. Laleu B, Gaggini F, Orchard M, Fioraso-Cartier L, Cagnon L, Houngninou-Molango S, et al. First in class, potent, and orally bioavailable NADPH oxidase isoform 4 (Nox4) inhibitors for the treatment of idiopathic pulmonary fibrosis. *J Med Chem* (2010) 53(21):7715–30. doi:10.1021/jm100773e

146. Hikichi M, Hashimoto S, Gon Y. Asthma and COPD overlap pathophysiology of ACO. *Allergol Int* (2018) 67(2):179–86. doi:10.1016/j.alit.2018.01.001

147. Hudler A, Holguin F, Sharma S. Pathophysiology of asthma-chronic obstructive pulmonary disease overlap. *Immunol Allergy Clin North Am* (2022) 42(3):521–32. doi:10.1016/j.iac.2022.04.008

148. Michaeloudes C, Abubakar-Waziri H, Lakhdar R, Raby K, Dixey P, Adcock IM, et al. Molecular mechanisms of oxidative stress in asthma. *Mol Aspects Med* (2022) 85:101026. doi:10.1016/j.mam.2021.101026

149. Sturrock A, Huecksteadt TP, Norman K, Sanders K, Murphy TM, Chitano P, et al. Nox4 mediates TGF-beta1-induced retinoblastoma protein phosphorylation, proliferation, and hypertrophy in human airway smooth muscle cells. *Am J Physiol Lung Cell Mol Physiol* (2007) 292(6):L1543–55. doi:10.1152/ajplung.00430.2006

150. Wan WY, Hollins F, Haste L, Woodman L, Hirst RA, Bolton S, et al. NADPH Oxidase-4 overexpression is associated with epithelial ciliary dysfunction in neutrophilic asthma. *Chest* (2016) 149(6):1445–59. doi:10.1016/j.chest.2016.01.024

151. Al-Azzam N, Teegala LR, Pokhrel S, Ghebreigziabher S, Chachkovskyy T, Thodeti S, et al. Transient receptor potential vanilloid channel regulates fibroblast differentiation and airway remodeling by modulating redox signals through NADPH oxidase 4. *Sci Rep* (2020) 10(1):9827. doi:10.1038/s41598-020-66617-2

152. Thompson BT, Chambers RC, Liu KD. Acute respiratory distress syndrome. *N Engl J Med* (2017) 377(6):562–72. doi:10.1056/NEJMra1608077

153. Zeng L, Yan J. Mechanisms of alveolar type II epithelial cells' mitochondrial quality control during acute lung injury/acute respiratory distress syndrome: bridging the gap

between oxidative stress, inflammation, and fibrosis. *Front Physiol* (2025) 16:1684729. doi:10.3389/fphys.2025.1684729

154. Wang F, Ge R, Cai Y, Zhao M, Fang Z, Li J, et al. Oxidative stress in ARDS: mechanisms and therapeutic potential. *Front Pharmacol* (2025) 16:1603287. doi:10.3389/fphar.2025.1603287

155. Cao M, Wang Z, Wu H, Liu R, Kong D, Liu J, et al. Proinflammatory macrophage polarization is driven by NOX4/PPARgamma axis-mediated oxidative-inflammatory crosstalk in CEES-induced lung injury. *Int Immunopharmacol* (2025) 167:115701. doi:10.1016/j.intimp.2025.115701

156. Yu MH, Li X, Li Q, Mo SJ, Ni Y, Han F, et al. SAA1 increases NOX4/ROS production to promote LPS-induced inflammation in vascular smooth muscle cells through activating p38MAPK/NF-kappaB pathway. *BMC Mol Cell Biol* (2019) 20(1):15. doi:10.1186/s12860-019-0197-0

157. Harel S, Mayaki D, Sanchez V, Hussain SNA. NOX2, NOX4, and mitochondrial-derived reactive oxygen species contribute to angiopoietin-1 signaling and angiogenic responses in endothelial cells. *Vascul Pharmacol* (2017) 92:22–32. doi:10.1016/j.vph.2017.03.002

158. Lee CF, Qiao M, Schroder K, Zhao Q, Asmis R. Nox4 is a novel inducible source of reactive oxygen species in monocytes and macrophages and mediates oxidized low density lipoprotein-induced macrophage death. *Circ Res* (2010) 106(9):1489–97. doi:10.1161/CIRCRESAHA.109.215392

159. Johnson S, Sommer N, Cox-Flaherty K, Weissmann N, Ventetuolo CE, Maron BA. Pulmonary hypertension: a contemporary review. *Am J Respir Crit Care Med* (2023) 208(5):528–48. doi:10.1164/rccm.202302-0327SO

160. Tajsic T, Morrell NW. Smooth muscle cell hypertrophy, proliferation, migration and apoptosis in pulmonary hypertension. *Compr Physiol* (2011) 1(1):295–317. doi:10.1002/cphy.c100026

161. Kurakula K, Smolders V, Tura-Ceide O, Jukema JW, Quax PHA, Goumans MJ. Endothelial dysfunction in pulmonary hypertension: cause or consequence? *Biomedicines* (2021) 9(1):57. doi:10.3390/biomedicines9010057

162. Ranchoux B, Harvey LD, Ayon RJ, Babicheva A, Bonnet S, Chan SY, et al. Endothelial dysfunction in pulmonary arterial hypertension: an evolving landscape (2017 grover conference series). *Pulm Circ* (2018) 8(1):2045893217752912. doi:10.1177/2045893217752912

163. Tuder RM. Pulmonary vascular remodeling in pulmonary hypertension. *Cell Tissue Res* (2017) 367(3):643–9. doi:10.1007/s00441-016-2539-y

164. Jia Z, Wang S, Yan H, Cao Y, Zhang X, Wang L, et al. Pulmonary vascular remodeling in pulmonary hypertension. *J Pers Med* (2023) 13(2):366. doi:10.3390/jpm13020366

165. Dai J, Chen H, Fang J, Wu S, Jia Z. Vascular remodeling: the multicellular mechanisms of pulmonary hypertension. *Int J Mol Sci* (2025) 26(9):4265. doi:10.3390/ijms26094265

166. Ismail S, Sturrock A, Wu P, Cahill B, Norman K, Huecksteadt T, et al. NOX4 mediates hypoxia-induced proliferation of human pulmonary artery smooth muscle cells: the role of autocrine production of transforming growth factor-beta1 and insulin-like growth factor binding protein-3. *Am J Physiol Lung Cell Mol Physiol* (2009) 296(3):L489–99. doi:10.1152/ajplung.90488.2008

167. Wagner B, Ricono JM, Gorin Y, Block K, Arar M, Riley D, et al. Mitogenic signaling *via* platelet-derived growth factor beta in metanephric mesenchymal cells. *J Am Soc Nephrol* (2007) 18(11):2903–11. doi:10.1681/ASN.2006111229

168. Kim HJ, Kim CH, Ryu JH, Joo JH, Lee SN, Kim MJ, et al. Crosstalk between platelet-derived growth factor-induced Nox4 activation and MUC8 gene overexpression in human airway epithelial cells. *Free Radic Biol Med* (2011) 50(9):1039–52. doi:10.1016/j.freeradbiomed.2011.01.014

169. Lee DY, Wauquier F, Eid AA, Roman LJ, Ghosh-Choudhury G, Khazim K, et al. Nox4 NADPH oxidase mediates peroxynitrite-dependent uncoupling of endothelial nitric-oxide synthase and fibronectin expression in response to angiotensin II: role of mitochondrial reactive oxygen species. *J Biol Chem* (2013) 288(40):28668–86. doi:10.1074/jbc.M113.470971

170. Lee HY, Zeeshan HMA, Kim HR, Chae HJ. Nox4 regulates the eNOS uncoupling process in aging endothelial cells. *Free Radic Biol Med* (2017) 113:26–35. doi:10.1016/j.freeradbiomed.2017.09.010

171. Dennis KE, Aschner JL, Milatovic D, Schmidt JW, Aschner M, Kaplowitz MR, et al. NADPH oxidases and reactive oxygen species at different stages of chronic hypoxia-induced pulmonary hypertension in newborn piglets. *Am J Physiol Lung Cell Mol Physiol* (2009) 297(4):L596–607. doi:10.1152/ajplung.90568.2008

172. Wedgwood S, Lakshminrusimha S, Czech L, Schumacker PT, Steinhorn RH. Increased p22(phox)/Nox4 expression is involved in remodeling through hydrogen peroxide signaling in experimental persistent pulmonary hypertension of the newborn. *Antioxid Redox Signal* (2013) 18(14):1765–76. doi:10.1089/ars.2012.4766

173. Green DE, Murphy TC, Kang BY, Kleinhenz JM, Szyndralewiez C, Page P, et al. The Nox4 inhibitor GKT137831 attenuates hypoxia-induced pulmonary vascular cell proliferation. *Am J Respir Cell Mol Biol* (2012) 47(5):718–26. doi:10.1165/rcmb.2011-0418OC

174. Nisbet RE, Bland JM, Kleinhenz DJ, Mitchell PO, Walp ER, Sutliff RL, et al. Rosiglitazone attenuates chronic hypoxia-induced pulmonary hypertension in a mouse model. *Am J Respir Cell Mol Biol* (2010) 42(4):482–90. doi:10.1165/rcmb.2008-0132OC

EBM Experimental Biology and Medicine

TYPE Original Research
PUBLISHED 07 May 2026
DOI 10.3389/ebm.2026.10922

OPEN ACCESS

*CORRESPONDENCE
Zhiwen Fang,
fangzw@tsinghua.edu.cn

RECEIVED 03 December 2025
REVISED 25 March 2026
ACCEPTED 21 April 2026
PUBLISHED 07 May 2026

CITATION
Qian B and Fang Z (2026) Causal relationship between oral diseases and hypertension: a Mendelian randomization study.
Exp. Biol. Med. 251:10922.
doi: 10.3389/ebm.2026.10922

Causal relationship between oral diseases and hypertension: a Mendelian randomization study

Bofan Qian[1] and Zhiwen Fang[2]*

[1]Shanghai Engineering Research Center of Tooth Restoration and Regeneration and Tongji Research Institute of Stomatology, Shanghai Tongji Stomatological Hospital and Dental School, Tongji University, Shanghai, China, [2]Department of Statistics and Data Science, Tsinghua University, Beijing, China

Abstract

Current evidence supports the potential association between several common oral diseases and hypertension. The aim of the research is to clarify the causal relationship between these oral diseases and hypertension using Mendelian randomization (MR) analysis. Single nucleotide polymorphisms (SNPs) related to five oral traits (periodontitis, bleeding gums, loose teeth, periapical abscess and dental caries) were obtained from GWAS catalog, while those associated with hypertension (essential and secondary) were extracted from the FinnGen database. The SNPs were employed as instrumental variables (IVs) in the MR analysis. Assorted methods were applied, and inverse variance-weighted (IVW) analytical method was prioritized. Sensitivity analyses including MR-PRESSO method, MR Egger intercept test, Cochran's Q test, leave-one-out analysis and MR Steiger test were conducted. Our analysis identified the potential causal relationship between dental caries and essential hypertension. The forward MR analysis demonstrated a significant causal effect of dental caries on essential hypertension (OR = 1.036, 95%CI: 1.012–1.059, P = 0.003). The reverse analysis also indicated a significant causal effect (OR = 1.160, 95%CI: 1.016–1.323, P = 0.028). Additionally, we observed a causal effect of bleeding gums on essential hypertension (OR = 1.145, 95%CI: 1.019–1.288, P = 0.023). These findings support the potential causality between specific oral diseases and essential hypertension.

KEYWORDS
causal inference, essential hypertension, mendelian randomization, oral diseases, secondary hypertension

Impact statement

This paper addresses the issue of causal relationship between oral diseases and hypertension. Previous studies have shown that assorted oral diseases are possibly associated with hypertension. However, the results of these studies are biased. In addition, most of the studies are observational, which fail to reveal the causality and may be significantly affected by confounding factors and reverse causal relationship. In our study, we utilize Mendelian randomization analysis to investigate the causality between several oral diseases and hypertension, which minimizes the potential effect of confounders and reverse causality. Our study suggests that there is a bidirectional causal relationship between dental caries and essential hypertension, while gingival bleeding has a causal effect on essential hypertension. Our findings are significant as it can offer new insights into the association of the diseases, emphasizing the importance of oral health in the management of hypertension.

Introduction

Oral diseases are prevalent but neglected globally [1]. It is estimated that nearly half of the world's population suffers from oral diseases [2]. Among these diseases, dental caries and periodontal diseases are considered critical [3].

Hypertension is a common chronic disease which can be classified as essential or secondary [4]. In the cases of hypertension, essential hypertension accounts for the vast majority [5]. Several risk factors for essential hypertension have been identified, including diabetes, dyslipidemia, smoking and alcohol consumption [6]. However, the etiology of essential hypertension remains unclear.

In the previous research, the association between oral diseases and hypertension was described. Numerous studies have investigated the potential association between periodontitis and hypertension, and the results were polarized [7–11]. Evidence supports that severe periodontitis is associated with hypertension [12]. Gingival bleeding, as a surrogate for active periodontal inflammation, has been found to be positively correlated with hypertension [13]. In addition, loose teeth can also to some extent reflect the severity of periodontitis [14]. Another cross-sectional study has indicated that periapical abscess is closely associated with both essential and secondary hypertension, however, controversy still exists [15, 16]. Dental caries, with an extremely high prevalence, has also been linked to essential hypertension [17–19]. However, most of the studies are observational, indicating that confounding factors still exist and the direction of the relationships cannot be ascertained.

Mendelian randomization (MR) is an emerging innovative analytical approach similar to randomized controlled trials (RCTs), which uses genetic variance as instrumental variables (IVs), assessing the influence of risk factors on outcomes. MR analysis can overcome unmeasured confounding factors which may lead to deviation in traditional observational studies [20]. Additionally, it can effectively identify the direction of causal relationships and reduce the impact of reverse causality to a large extent [21]. Therefore, this study aims to utilize data extracted from GWAS catalog and FinnGen database to conduct two-sample MR analyses, offering insights into the correlation between several oral diseases and hypertension.

Materials and methods

Study design

This study was in full compliance with the STROBE-MR statement [22]. To conduct the MR analysis, three assumptions ought to be satisfied: (1) Selected IVs should be significantly related to the exposure; (2) Selected IVs must be independent of the confounding factors; (3) Selected IVs can only influence the outcome by exposure. The design of our study is depicted in Figure 1. First, a bidirectional MR analysis was implemented to investigate potential causal relationships between oral diseases and essential hypertension. Then, a unidirectional MR analysis was conducted to examine the effect of secondary hypertension on oral diseases.

Data sources

Data used in the research were extracted from two different genome-wide association study (GWAS) databases, effectively avoiding sample overlapping [23]. SNPs related to oral health conditions and hypertension were extracted from the GWAS catalog website[1] and the FinnGen website[2] respectively. The relevant features of samples are displayed in Table 1.

Selection of instrumental variables

Regarding instrumental variables for essential and secondary hypertension, the *P* value was set at 5×10^{-8}. Due to the insufficient number of SNPs for oral traits, we relaxed the threshold to 5×10^{-7} for bleeding gums and 5×10^{-6} for other traits [27–29]. Linkage disequilibrium (LD) was performed using standard clumping parameters ($r^2 < 0.001$, clumping window = 10,000 kb). Confounders were identified based on previous epidemiological and genetic studies, including well-established common risk factors for essential hypertension (e.g., body mass index, metabolite levels, and hemoglobin concentration) [30–32]. Subsequently, we imported the selected SNPs into the LDtrait tool[3] to assess their associations with the confounders, and any SNP exhibiting a significant association with any of these confounders was excluded [33]. To estimate the strength of the IVs, we calculated *F*-statistic in turn utilizing the following formula:

$$F = \left(\frac{\beta}{SE}\right)^2.$$

Normally, an *F*-statistic >10 implies no obvious bias generated by weak instrumental variable [34]. Considering the excessive quantity of SNPs for essential hypertension, we adopted a relatively strict *F*-statistic ($F > 50$). Finally, we acquired the IVs used for the subsequent MR analysis (Supplementary Material 1).

Mendelian randomization analysis

All the procedures were completed in R software (version 4.4.2), utilizing "TwoSampleMR" (version 0.6.8) and "MR-PRESSO" (version 1.0) R packages. First, records of exposure and outcome were merged, and missing SNPs were deleted. Then, duplicated and palindromic SNPs were excluded. The MR-PRESSO approach was employed to detect potential horizontal pleiotropy [35]. After manually excluding the outliers outputted by MR-PRESSO, the process was repeated until no outlier was identified. The SNPs undergoing these processes can be used in the subsequent analysis. In our analysis, inverse variance weighting (IVW) served as the main analytical approach [36]. IVW estimates the weighted average of Wald ratios for the SNPs, assuming the validity of each SNP, and provides the strongest statistical power. The IVW random-effect model was employed because it is robust even in the

1 https://www.ebi.ac.uk/gwas/

2 https://r12.finngen.fi/

3 https://ldlink.nih.gov/?tab=ldtrait

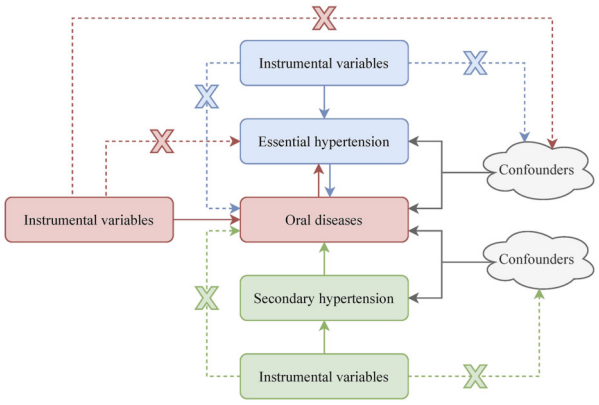

FIGURE 1
Study design of Mendelian randomization analysis.

presence of heterogeneity. Additionally, MR Egger and weighted median methods served as complementary methods. The former method is based on the assumption of instrument strength independent of direct effect (InSIDE), which can detect horizontal pleiotropy via the intercept term [37]. When the intercept term is not significantly different from zero, this suggests no evidence of horizontal pleiotropy, and the results are consistent with those from the IVW method. The weighted median method can provide a consistent causal estimate even when up to 50% of the IVs are invalid [38]. Collectively, these methods were used to evaluate the stability of the causal estimates. Consistent results across different approaches would strengthen the credibility of the causal association, whereas divergent results may indicate the presence of potential bias such as horizontal pleiotropy. The MR Egger intercept test was conducted to validate horizontal pleiotropy. In our test, a $P < 0.05$ indicates that horizontal pleiotropy existed in the results. In addition, Cochran's Q test was conducted to assess heterogeneity, and a $P < 0.05$ indicates the existence of heterogeneity. Leave-one-out sensitivity analysis was performed to assess the stability of the causal estimates. Although outliers had already been excluded by MR-PRESSO, the leave-one-out test verified that no single SNP predominantly influenced the overall effect, further supporting the robustness of our findings [39]. Furthermore, we conducted MR Steiger test to determine the direction of the causality by comparing the strength of association between IVs and the exposure versus the outcome [40]. In the Steiger test, a $P < 0.05$ supports the direction of causal relationship from exposure to outcome, with no evidence of reverse causality.

Results

Forest plots, scatter plots, funnel plots and the plot of leave-one-out sensitivity analysis were formed in R software (Supplementary Material 2). The results of Steiger test were shown in Supplementary Material 3. No heterogeneity or pleiotropy was discovered in the MR analysis (Table 2).

Causal effects of oral traits on essential hypertension

Our research revealed that bleeding gums (OR = 1.145, 95%CI: 1.019–1.288, $P = 0.023$) and dental caries (OR = 1.036, 95%CI: 1.012–1.059, $P = 0.003$) were positively correlated with essential hypertension. Although the weighted median analysis indicated the correlation between periodontitis and essential hypertension (OR = 1.038, 95%CI: 1.006–1.071, $P = 0.021$), it didn't serve as the major analytical approach. Therefore, no causal effects of other three oral traits on essential hypertension were identified. Detailed results were shown in Figure 2.

Causal effects of essential hypertension on oral traits

After reversing the exposure and outcome, we discovered the causal effect of essential hypertension on dental caries (OR = 1.160, 95%CI: 1.016–1.323, $P = 0.028$), which indicated that the causality between dental caries and essential hypertension was bidirectional. Detailed results were shown in Figure 3.

Causal effects of secondary hypertension on oral traits

We also conducted a unidirectional MR analysis to evaluate the causal effect of secondary hypertension on oral diseases. No causal

TABLE 1 Relevant features of samples used in MR analysis.

Trait	Consortium	GWAS ID	Population	Samplesize	N case
Periodontitis	GWAS catalog	GCST90436269 [24]	European	399358	1222
Bleeding gums	GWAS catalog	GCST90044343 [25]	European	454565	59211
Loose teeth	GWAS catalog	GCST90044344 [25]	European	454565	18545
Periapical abscess	GWAS catalog	GCST90436266 [24]	European	399313	1177
Dental caries	GWAS catalog	GCST90044098 [25]	European	456348	2906
Essential hypertension	FinnGen	finngen_R12_I9_HYPTENSESS [26]	European	478149	132515
Secondary hypertension	FinnGen	finngen_R12_I9_HYPTENSEC [26]	European	256198	3388

TABLE 2 The results of heterogeneity and pleiotropy.

Exposure	Outcome	$P_{Cochran's\ Q}$	$P_{MR\ Egger\ intercept}$	$P_{Global\ test}$
Periodontitis	Essential hypertension	0.284	0.280	0.322
Bleeding gums		0.142	0.734	0.181
Loose teeth		0.179	0.802	0.199
Periapical abscess		0.095	0.597	0.135
Dental caries		0.444	0.217	0.478
Essential hypertension	Periodontitis	0.266	0.479	0.230
	Bleeding gums	0.081	0.161	0.072
	Loose teeth	0.076	0.952	0.066
	Periapical abscess	0.261	0.459	0.228
	Dental caries	0.264	0.482	0.277
Secondary hypertension	Periodontitis	0.472	0.928	0.478
	Bleeding gums	0.605	0.686	0.392
	Loose teeth	0.127	0.405	0.200
	Periapical abscess	0.441	0.630	0.451
	Dental caries	0.573	0.384	0.492

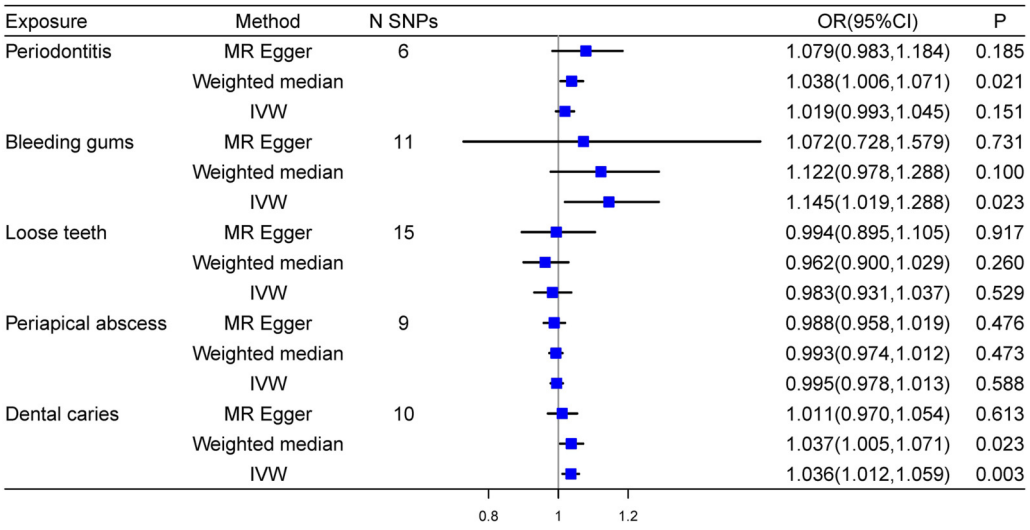

FIGURE 2
Forest plot of the causal effects of oral traits on essential hypertension.

effect of secondary hypertension on oral traits was identified in the analysis. Detailed results were shown in Figure 4.

Discussion

Oral diseases have already been found to be potentially associated with assorted systemic diseases in previous MR studies. Examples include kidney cancer, hypothyroidism and psychiatric disorders [41–43]. However, the majority of hypertension-related studies have placed emphasis on periodontitis [44, 45]. In fact, the oral health should be regarded as a whole. In our research, a comprehensive MR analysis was implemented to identify the causal relationship between several critical oral diseases and hypertension, eliminating the potential effect of confounders and reverse causal relationship to a great extent compared with observational studies. We stratified hypertension into two subtypes and examined the causality between oral diseases and each subtype separately. The results demonstrated the bidirectional causal relationship between dental caries and essential hypertension, and bleeding gums exerted a causal effect on essential hypertension.

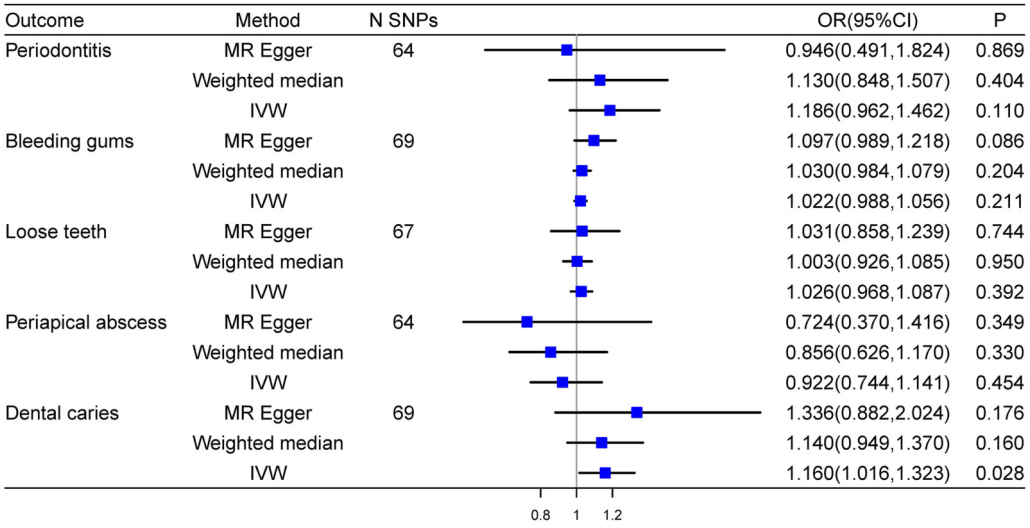

FIGURE 3
Forest plot of the causal effects of essential hypertension on oral traits.

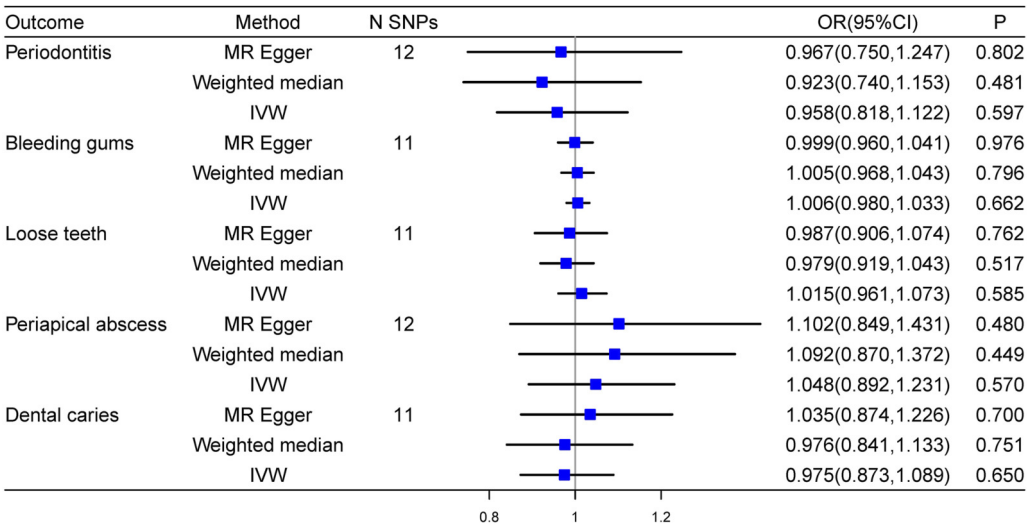

FIGURE 4
Forest plot of the causal effects of secondary hypertension on oral traits.

According to previous research, chronic inflammatory process possibly participates in the pathogenesis of hypertension [46, 47]. Periodontitis, defined as a chronic inflammation affecting the periodontal tissues, can result in systemic inflammation and elevate the levels of inflammatory mediators including interleukin-6 (IL-6) and C-reactive protein (CRP), which may serve as mediators underlying the association [3, 48–50]. Although numerous studies have suggested a potential association between periodontitis and hypertension, our result contradicts these studies. Loose teeth, as an indicator, was also not associated with hypertension in our research. Interestingly, the causal effect of bleeding gums on essential hypertension was identified. This is consistent with a recent study, and a plausible explanation is that gingival bleeding represents a status of active periodontal inflammation, which is more likely to be associated with systemic inflammation compared with stable periodontitis, indicating that active periodontal inflammation might increase the risk of essential hypertension [12, 13].

Different from periodontitis, periapical diseases are caused by the infection of root canal system with no apparent symptoms [51]. Recent evidence supports the potential association between periapical abscess and hypertension, but the views are controversial. A large-scale cross-sectional study has found that patients with secondary hypertension are more likely to suffer from periapical abscess than those with essential hypertension [15]. However, our MR analysis doesn't reveal such a relationship.

Dental caries, as a common oral disease both exist in primary and permament teeth, is also significantly correlated with essential

hypertension [18, 19]. Surprisingly, our study supports this viewpoint to some extent and reveals the direction of the relationship. The result turns out to be bidirectional, but the sample used in our analysis is merely described as dental caries without detailed subgroups.

The influence of dental caries on vascular health is mostly attributed to the nature of this disease, which is primarily a chronic bacterial infection. It exerts local effects such as compromised tooth structure and periodontal support, as well as systemic effects by increasing circulating inflammatory mediators, which contribute to endothelial dysfunction and arterial plaque formation [19]. In addition, hypertensive patients with poor oral health status show intensified oxidation of several plasma substrates, increased reactive oxygen species (ROS), lipid peroxidation, inactivation of prostacyclin and NO, as well as an imbalance in total antioxidant capacity [19]. In contrast, the reverse effect can be attributed to xerostomia induced by hypertension [52]. Saliva performs multiple physiological functions in the oral cavity, in which its clearance effect prevents tooth demineralization and ensures microbial homeostasis [53]. Degeneration of the salivary glands in hypertensive patients leads to hyposalivation, increasing the risk of caries on different tooth surfaces [54].

Emphasis should be laid on oral health, with extra attention paid to patients suffering from common oral diseases, as dental caries and bleeding gums are closely associated with essential hypertension according to our research. A prospective cohort study has discovered that nonsurgical periodontal treatment can significantly reduce the level of blood pressure in patients with periodontitis and prehypertension, stressing the importance of oral health from another angle [55]. Besides, the number of teeth may affect the level of blood pressure, which is not involved in our study due to data limitations [56, 57]. Further study needs to be conducted on a larger scale and can be extended to the association between oral disease and cardiovascular diseases instead of merely hypertension [58].

Limitations exist in our study. Though restricting data to European populations can effectively avoid sample overlap, it limits the generalizability of the results. Additionally, relaxed SNP selection thresholds were adopted for several oral traits due to the limited availability of genome-wide significant variants. The use of relatively weaker instrumental variables may introduce potential bias and influence the precision of causal estimates to some extent [34]. Therefore, the findings from these traits should be interpreted with appropriate caution. Moreover, the lack of detailed subgroup data (e.g., primary and permanent dental caries) represents another limitation. Larger-scale GWAS are urgently needed to further investigate and validate these associations.

Conclusion

In our research, we identified the bidirectional causal relationship between dental caries and essential hypertension, and also uncovered the causal effect of bleeding gums on essential hypertension. No causal associations were observed between other oral traits and essential hypertension. In addition, our results did not support the causal effect of secondary hypertension on oral diseases.

Author contributions

BQ designed the study, acquired the primary data, conducted statistical analyses and drafted the manuscript. ZF conducted statistical analyses and visualization, and performed manuscript editing and review. All authors contributed to the article and approved the submitted version.

Data availability

The original contributions presented in the study are included in the article/Supplementary Material, further inquiries can be directed to the corresponding author.

Ethics statement

All the data included in our study are publicly available. Ethics approval and consent to participate can be found in their corresponding original studies.

Funding

The author(s) declared that financial support was not received for this work and/or its publication.

Acknowledgements

We thank GWAS catalog Consortium and FinnGen Consortium for offerring GWAS data.

Conflict of interest

The author(s) declared no potential conflicts of interest with respect to the research, authorship, and/or publication of this article.

Generative AI statement

The author(s) declared that generative AI was not used in the creation of this manuscript.

Any alternative text (alt text) provided alongside figures in this article has been generated by Frontiers with the support of artificial intelligence and reasonable efforts have been made to ensure accuracy, including review by the authors wherever possible. If you identify any issues, please contact us.

Supplementary material

The Supplementary Material for this article can be found online at: https://www.ebm-journal.org/articles/10.3389/ebm.2026.10922/full#supplementary-material

References

1. Watt RG, Daly B, Allison P, Macpherson LMD, Venturelli R, Listl S, et al. Ending the neglect of global oral health: time for radical action. *Lancet* (2019) 394:261–72. doi:10.1016/S0140-6736(19)31133-X

2. Kassebaum NJ, Smith AGC, Bernabé E, Fleming TD, Reynolds AE, Vos T, et al. Global, regional, and national prevalence, incidence, and disability-adjusted life years for oral conditions for 195 countries, 1990-2015: a systematic analysis for the global burden of diseases, injuries, and risk factors. *J Dent Res* (2017) 96:380–7. doi:10.1177/0022034517693566

3. Peres MA, Macpherson LMD, Weyant RJ, Daly B, Venturelli R, Mathur MR, et al. Oral diseases: a global public health challenge. *Lancet* (2019) 394:249–60. doi:10.1016/S0140-6736(19)31146-8

4. Poulter NR, Prabhakaran D, Caulfield M. Hypertension. *Lancet* (2015) 386:801–12. doi:10.1016/S0140-6736(14)61468-9

5. Messerli FH, Williams B, Ritz E. Essential hypertension. *Lancet* (2007) 370:591–603. doi:10.1016/S0140-6736(07)61299-9

6. Unger T, Borghi C, Charchar F, Khan NA, Poulter NR, Prabhakaran D, et al. International society of hypertension global hypertension practice guidelines. *J Hypertens* (2020) 38:982–1004. doi:10.1097/HJH.0000000000002453

7. Aguilera EM, Suvan J, Buti J, Czesnikiewicz-Guzik M, Ribeiro AB, Orlandi M, et al. Periodontitis is associated with hypertension: a systematic review and meta-analysis. *Cardiovasc Res* (2020) 116:28–39. doi:10.1093/cvr/cvz201

8. Martin-Cabezas R, Seelam N, Petit C, Agossa K, Gaertner S, Tenenbaum H, et al. Association between periodontitis and arterial hypertension: a systematic review and meta-analysis. *Am Heart J* (2016) 180:98–112. doi:10.1016/j.ahj.2016.07.018

9. Kawabata Y, Ekuni D, Miyai H, Kataoka K, Yamane M, Mizutani S, et al. Relationship between prehypertension/hypertension and periodontal disease: a prospective cohort study. *Am J Hypertens* (2016) 29:388–96. doi:10.1093/ajh/hpv117

10. Torrungruang K, Vathesatogkit P, Mahanonda R, Thienpramuk L. Periodontitis and hypertension are linked through systemic inflammation: a 5-year longitudinal study. *J Clin Periodontol* (2024) 51:536–46. doi:10.1111/jcpe.13942

11. Rosa RAC, Rodrigues JVS, Cláudio MM, Franciscon JPS, Mulinari-Santos G, Cirelli T, et al. The relationship between hypertension and periodontitis: a cross-sectional study. *J Clin Med* (2023) 12:5140. doi:10.3390/jcm12155140

12. Aremu JB, Pérez CM, Joshipura KJ. Longitudinal association between periodontitis and the risk of hypertension. *Int J Dent* (2023) 2023:2644623. doi:10.1155/2023/2644623

13. Pietropaoli D, Monaco A, D'Aiuto F, Aguilera EM, Ortu E, Giannoni M, et al. Active gingival inflammation is linked to hypertension. *J Hypertens* (2020) 38:2018–27. doi:10.1097/HJH.0000000000002514

14. Tonetti MS, Greenwell H, Kornman KS. Staging and grading of periodontitis: framework and proposal of a new classification and case definition. *J Clin Periodontol* (2018) 45:S149–S61. doi:10.1111/jcpe.12945

15. Katz J, Rotstein I. Prevalence of periapical abscesses in patients with hypertension: a cross-sectional study of a large hospital population. *J Endod* (2021) 47:1070–4. doi:10.1016/j.joen.2021.04.006

16. Segura-Egea JJ, Jimenez-Moreno E, Calvo-Monroy C, Rios-Santos JV, Velasco-Ortega E, Sánchez-Domínguez B, et al. Hypertension and dental periapical condition. *J Endod* (2010) 36:1800–4. doi:10.1016/j.joen.2010.08.004

17. Cheng L, Zhang L, Yue L, Ling JQ, Fan MW, Yang DQ, et al. Expert consensus on dental caries management. *Int J Oral Sci* (2022) 14:17. doi:10.1038/s41368-022-00167-3

18. Ribeiro LSF, Santos JN, Vieira CLZ, Caramelli B, Ramalho LMP, Cury PR. Association of dental infections with systemic diseases in Brazilian native Indigenous: a cross-sectional study. *J Am Soc Hypertens* (2016) 10:413–9. doi:10.1016/j.jash.2016.02.012

19. Ostalska-Nowicka D, Paszynska E, Dmitrzak-Weglarz M, Neyman-Bartkowiak A, Rabiega A, Zachwieja J, et al. Dental caries-related primary hypertension in children and adolescents: cross-sectional study. *Oral Dis* (2021) 27:1822–33. doi:10.1111/odi.13700

20. Davies NM, Holmes MV, Smith GD. Reading Mendelian randomisation studies: a guide, glossary, and checklist for clinicians. *BMJ* (2018) 362:k601. doi:10.1136/bmj.k601

21. Richmond RC, Smith GD. Mendelian randomization: concepts and scope. *Cold Spring Harb Perspect Med* (2022) 12:a040501. doi:10.1101/cshperspect.a040501

22. Skrivankova V, Richmond R, Woolf B, Yarmolinsky J, Davies N, Swanson S, et al. Strengthening the reporting of observational studies in epidemiology using mendelian randomization: the STROBE-MR statement. *JAMA* (2021) 326:1614–21. doi:10.1001/jama.2021.18236

23. Burgess S, Davies NM, Thompson SG. Bias due to participant overlap in two-sample Mendelian randomization. *Genet Epidemiol* (2016) 40:597–608. doi:10.1002/gepi.21998

24. Zhou W, Nielsen JB, Fritsche LG, Dey R, Gabrielsen ME, Wolford BN, et al. Efficiently controlling for case-control imbalance and sample relatedness in large-scale genetic association studies. *Nat Genet* (2018) 50:1335–41. doi:10.1038/s41588-018-0184-y

25. Jiang LD, Zheng ZL, Fang HL, Yang J. A generalized linear mixed model association tool for biobank-scale data. *Nat Genet* (2021) 53:1616–21. doi:10.1038/s41588-021-00954-4

26. Kurki MI, Karjalainen J, Palta P, Sipilä TP, Kristiansson K, Donner KM, et al. FinnGen. FinnGen provides genetic insights from a well-phenotyped isolated population. *Nature* (2023) 613:508–18. doi:10.1038/s41586-022-05473-8

27. Wang YQ, Zhu JK, Zhou YL, Tang Y, Huang C. Exploring relationships between circulating interleukins and pulp and periapical diseases: a bidirectional mendelian randomization study. *J Endod* (2025) 51:132–9. doi:10.1016/j.joen.2024.11.010

28. Baurecht H, Freuer D, Welker C, Tsoi LC, Elder JT, Ehmke B, et al. Relationship between periodontitis and psoriasis: a two-sample Mendelian randomization study. *J Clin Periodontol* (2022) 49:573–9. doi:10.1111/jcpe.13620

29. Chen H, Peng LM, Wang ZX, He YJ, Zhang XA. Exploring the causal relationship between periodontitis and gut microbiome: unveiling the oral-gut and gut-oral axes through bidirectional Mendelian randomization. *J Clin Periodontol* (2024) 51:417–30. doi:10.1111/jcpe.13906

30. Bogaert YE, Linas S. The role of obesity in the pathogenesis of hypertension. *Nat Rev Nephrol* (2009) 5:101–11. doi:10.1038/ncpneph1022

31. Onuh JO, Qiu HY. Metabolic profiling and metabolites fingerprints in human hypertension: discovery and potential. *Metabolites* (2021) 11:687. doi:10.3390/metabo11100687

32. Lee SG, Rim JH, Kim JH. Association of hemoglobin levels with blood pressure and hypertension in a large population-based study: the Korea national health and nutrition examination surveys 2008-2011. *Clin Chim Acta* (2015) 438:12–8. doi:10.1016/j.cca.2014.07.041

33. Lin SH, Brown DW, Machiela MJ. LDtrait: an online tool for identifying published phenotype associations in linkage disequilibrium. *Cancer Res* (2020) 80:3443–6. doi:10.1158/0008-5472.CAN-20-0985

34. Burgess S, Thompson SG, Collaboration CCG. Avoiding bias from weak instruments in Mendelian randomization studies. *Int J Epidemiol* (2011) 40:755–64. doi:10.1093/ije/dyr036

35. Verbanck M, Chen CY, Neale B, Do R. Detection of widespread horizontal pleiotropy in causal relationships inferred from Mendelian randomization between complex traits and diseases. *Nat Genet* (2018) 50:693–8. doi:10.1038/s41588-018-0099-7

36. Burgess S, Scott RA, Timpson NJ, Smith GD, Thompson SG, Epic-Interact C. Using published data in Mendelian randomization: a blueprint for efficient identification of causal risk factors. *Eur J Epidemiol* (2015) 30:543–52. doi:10.1007/s10654-015-0011-z

37. Burgess S, Thompson SG. Interpreting findings from Mendelian randomization using the MR-Egger method. *Eur J Epidemiol* (2017) 32:377–89. doi:10.1007/s10654-017-0255-x

38. Bowden J, Smith GD, Haycock PC, Burgess S. Consistent estimation in Mendelian randomization with some invalid instruments using a weighted median estimator. *Genet Epidemiol* (2016) 40:304–14. doi:10.1002/gepi.21965

39. Burgess S, Bowden J, Fall T, Ingelsson E, Thompson SG. Sensitivity analyses for robust causal inference from mendelian randomization analyses with multiple genetic variants. *Epidemiology* (2017) 28:30–42. doi:10.1097/EDE.0000000000000559

40. Hemani G, Tilling K, Smith GD. Orienting the causal relationship between imprecisely measured traits using GWAS summary data. *Plos Genet* (2017) 13:e1007081. doi:10.1371/journal.pgen.1007081

41. Li BJ, Lin YF, Yang Y, Wang Z, Shi R, Zheng T, et al. Patients with periodontitis might increase the risk of urologic cancers: a bidirectional two-sample Mendelian randomization study. *Int Urol Nephrol* (2024) 56:1243–51. doi:10.1007/s11255-023-03858-w

42. Gao Y, Huang DH, Liu Y, Qiu YZ, Lu SH. Periodontitis and thyroid function: a bidirectional Mendelian randomization study. *J Periodontal Res* (2024) 59:491–9. doi:10.1111/jre.13240

43. Pi YY, Jiao ZM, Wang LN, Zhao Y, Hu WX, Chen F, et al. Genetic evidence strengthens the bidirectional connection between oral health status and psychiatric disorders: a two-sample Mendelian randomization study. *J Affective Disord* (2024) 351:661–70. doi:10.1016/j.jad.2024.01.232

44. Czesnikiewicz-Guzik M, Osmenda G, Siedlinski M, Nosalski R, Pelka P, Nowakowski D, et al. Causal association between periodontitis and hypertension: evidence from Mendelian randomization and a randomized controlled trial of non-surgical periodontal therapy. *Eur Heart J* (2019) 40:3459–70. doi:10.1093/eurheartj/ehz646

45. Zhou Y, Sun LY, Hu JY, Liu X, Ma YJ. Association of antihypertensive drugs with periodontitis: a comprehensive drug-target Mendelian randomization study. *Quintessence Int* (2024) 55:814–23. doi:10.3290/j.qi.b5754882

46. Zhang ZL, Zhao L, Zhou XY, Meng X, Zhou XL. Role of inflammation, immunity, and oxidative stress in hypertension: new insights and potential

therapeutic targets. *Front Immunol* (2023) 13:1098725. doi:10.3389/fimmu.2022.1098725

47. Jin NK, Huang L, Hong J, Zhao XC, Hu JN, Wang SS, et al. The association between systemic inflammation markers and the prevalence of hypertension. *BMC Cardiovasc Disord* (2023) 23:615. doi:10.1186/s12872-023-03661-6

48. Hajishengallis G, Chavakis T. Local and systemic mechanisms linking periodontal disease and inflammatory comorbidities. *Nat Rev Immunol* (2021) 21:426–40. doi:10.1038/s41577-020-00488-6

49. Aguilera EM, Leira Y, Catalina QM, Orlandi M, Czesnikiewicz-Guzik M, Guzik TJ, et al. Is systemic inflammation a missing link between periodontitis and hypertension? Results from two large population-based surveys. *J Intern Med* (2021) 289:532–46. doi:10.1111/joim.13180

50. Ozmeric N, Elgun S, Kalfaoglu D, Pervane B, Sungur C, Ergüder I, et al. Interaction between hypertension and periodontitis. *Oral Dis* (2024) 30:1622–31. doi:10.1111/odi.14543

51. Tibúrcio-Machado CS, Michelon C, Zanatta FB, Gomes MS, Marin JA, Bier CA. The global prevalence of apical periodontitis: a systematic review and meta-analysis. *Int Endod J* (2021) 54:712–35. doi:10.1111/iej.13467

52. Kawamoto M, Yamada S, Gibo T, Kajihara R, Nagashio S, Tanaka H, et al. Relationship between dry mouth and hypertension. *Clin Oral Invest* (2021) 25:5217–25. doi:10.1007/s00784-021-03829-4

53. Pedersen A, Belstrom D. The role of natural salivary defences in maintaining a healthy oral microbiota. *J Dent* (2019) 80:S3–S12. doi:10.1016/j.jdent.2018.08.010

54. Pedersen A, Sorensen C, Proctor G, Carpenter G, Ekström J. Salivary secretion in health and disease. *J Oral Rehabil* (2018) 45:730–46. doi:10.1111/joor.12664

55. Lanau N, Mareque-Bueno J, Zabalza M. Impact of nonsurgical periodontal treatment on blood pressure: a prospective cohort study. *Eur J Dent* (2023) 18:517–25. doi:10.1055/s-0043-1772246

56. Shin HS. Association between the number of teeth and hypertension in a study based on 13,561 participants. *J Periodontol* (2018) 89:397–406. doi:10.1002/JPER.17-0413

57. Da DX, Wang F, Zhang H, Zeng XL, Jiang YW, Zhao QH, et al. Association between tooth loss and hypertension among older Chinese adults: a community-based study. *BMC Oral Health* (2019) 19:277. doi:10.1186/s12903-019-0966-3

58. Sanz M, del Castillo AM, Jepsen S, Gonzalez-Juanatey JR, D'Aiuto F, Bouchard P, et al. Periodontitis and cardiovascular diseases: consensus report. *J Clin Periodontol* (2020) 47:268–88. doi:10.1111/jcpe.13189

EBM Experimental Biology and Medicine

TYPE Original Research
PUBLISHED 08 June 2026
DOI 10.3389/ebm.2026.10868

OPEN ACCESS

*CORRESPONDENCE
Ting Wang,
wangting198610@163.com
Xiaohan Ye,
cndgyxh@163.com

†These authors have contributed equally to this work and share first authorship

RECEIVED 20 October 2025
REVISED 28 April 2026
ACCEPTED 27 May 2026
PUBLISHED 08 June 2026

CITATION
Tang L, Yang B, Li P, Chen Y, Liu Y, Wang T and Ye X (2026) High systolic blood pressure and stroke: evidence from the NHANES 1999–2023 and global burden of disease 2021.
Exp. Biol. Med. 251:10868.
doi: 10.3389/ebm.2026.10868

High systolic blood pressure and stroke: evidence from the NHANES 1999–2023 and global burden of disease 2021

LuYi Tang†, BoWen Yang†, PeiWen Li†, YingQi Chen, Yi Liu, Ting Wang* and Xiaohan Ye*

Dongguan Hospital of Guangzhou University of Chinese Medicine, Dongguan, Guangdong, China

Abstract

High systolic blood pressure (HSBP) is a major modifiable risk factor for stroke, but trends in disease burden and causal associations related to HSBP in the United States require further investigation using multidimensional approaches. This study aims to elucidate this relationship by utilizing data from the Global Burden of Disease (GBD) database, the National Health and Nutrition Examination Survey (NHANES). This study integrated data from the GBD 2021 database and the NHANES. The GBD data provided macro-level estimates of stroke-related mortality and disability-adjusted life years (DALYs) attributable to various risk factors within the United States. By employing multivariable logistic regression models on individual-level NHANES data, the study assessed the association between HSBP history and stroke risk after adjusting for multiple confounding factors. GBD analysis revealed HSBP as the leading risk factor for U.S. stroke burden in 2021, with an increasing attributable burden since 2010, particularly among the elderly and women. NHANES analysis showed that HSBP significantly increased the risk of stroke (fully adjusted OR = 1.33, 95% CI: 1.17–1.51). Elevated SBP was additionally associated with increased all-cause mortality risk in stroke survivors (HR = 1.01). A novel U-shaped relationship emerged: stroke risk decreased below an SBP of 100 mmHg but increased sharply above this threshold. HSBP is the core driver and modifiable risk factor behind the persistently increasing stroke burden in the United States. The findings of this study highlight the critical importance of HSBP in stroke prevention and management.

KEYWORDS
EHANES, global burden of disease (GBD), high systolic blood pressure, stroke, stroke prevention and management

Impact statement

Multidimensional Data Integration: We combine macro-level population burden data (GBD) and individual-level epidemiological data (NHANES), enabling a comprehensive assessment of HSBP's role in stroke. Novel Epidemiological Insights: Our analysis revealed a Ushaped relationship between systolic blood pressure and stroke risk, identifying a threshold (<130 mmHg) below which stroke risk declines but above which it rises sharply. This nuanced finding contributes to understanding blood pressure management in stroke prevention. Updated and Longitudinal Data Analysis: Using the most recent and

extensive datasets spanning over two decades allows us to characterize temporal trends in stroke burden attributable to HSBP, particularly highlighting the rising impact among elderly individuals and women.

Introduction

Globally, stroke is the second leading cause of death after ischemic heart disease, with approximately 795,000 stroke events occurring annually in the United States, resulting in substantial economic burden, with estimated annual costs of $34 billion [1, 2] for health care services, medications, and work absenteeism. Established cerebrovascular risk factors, including hypertension, hyperlipidemia, atrial fibrillation, diabetes mellitus, smoking, and physical inactivity, significantly contribute to stroke risk. Given the significant impact stroke has on the lives and health of a large proportion of the population, there is an urgent need for timely and effective preventive interventions.

High systolic blood pressure (HSBP) is considered a major risk factor for stroke mortality [3, 4]. At the same time, it is a major risk factor for most cardiovascular diseases, including stroke, and is an even more important predictor than diastolic blood pressure, mean arterial pressure, and pulse pressure. Previous reports indicate that up to 60% of global stroke-related mortality may be associated with poorly controlled high systolic blood pressure, and blood pressure management has been proven to be the most effective intervention for stroke prevention [5].

Despite the heavy burden on the United States healthcare system, there are significant knowledge gaps regarding morbidity and mortality among people of different ages, genders, and economic levels [6]. Although the Global Burden of Disease (GBD) study provides extensive data on stroke risk factors in the United States, it lacks individual-level data on HSBP and stroke [7]. These models often rely on assumptions about the prevalence of high systolic blood pressure or simplistic ecological adjustments, which poses a significant potential for confusion [8, 9]. Therefore, this study aims to provide a more comprehensive assessment of the association between HSBP and stroke risk in the U.S. by integrating data from the GBD database and National Health and Nutrition Examination Survey (NHANES).

In addition, the study aims to identify potential differences in stroke prognosis, including differences in disease burden across socioeconomic groups, ethnicities, and geographic regions. Through this comprehensive analysis, this study is expected to provide valuable insights into reducing the burden of stroke due to HSBP in the United States. The results of this study will provide a scientific basis for strengthening HSBP interventions and early screening strategies, thereby improving the prognosis of stroke in high-risk groups.

Methods

Design

This study adopted a complementary two-level design by integrating GBD 2021 and NHANES data. The GBD database was used to quantify the population-level burden of stroke attributable to HSBP in the United States, including temporal and demographic patterns, whereas NHANES was used to assess the individual-level association between HSBP and stroke in a nationally representative sample. This combined design allowed us to examine both the public health significance and the individual-level relationship of HSBP with stroke.

Data sources and participants

GBD database

GBD 2021 is a comprehensive database that includes anonymized data encompassing 204 countries and territories, 7 regions, and 5 Socio-Demographic Index (SDI) quintiles, covering 371 diseases, 88 risk factors, and various types of injuries [4]. The data are publicly accessible through the Global Health Data Exchange (GHDx) (https://vizhub.healthdata.org/gbd-results/), an online platform developed and maintained by the Institute for Health Metrics and Evaluation (IHME) at the University of Washington [10]. Research involving GBD 2021 data was reviewed by the University of Washington's Institutional Review Board (IRB), which approved a waiver of the informed consent requirement [11]. This study strictly adhered to the GATHER (Guidelines for Accurate and Transparent Health Estimates Reporting) standards to ensure the precision and transparency of health assessment findings [12].

We applied a Bayesian age–period–cohort (BAPC) model fitted with integrated nested Laplace approximations (INLA) to generate predictive distributions of age-standardized mortality and DALY rates to 2045. BAPC explicitly estimates age, period, and cohort effects, and has been demonstrated as an effective approach for forecasting disease rates in large demographic datasets [13].

In the GBD database, the age-standardized mortality rate (ASDR) indicates the number of deaths per 100,000 people by age group. Age-standardized disability-adjusted life years (ASDAR) combine the years of life lost due to premature death and the years lived with disability per 100,000 population after age standardization. The study collected data on stroke and its subtypes attributable to HSBP, including mortality, disability-adjusted life-years (DALYs), age-standardized mortality rate (ASDR), and corresponding 95% uncertainty intervals (UIs). All data were stratified by age, sex, and other demographic variables.

NHANES database

NHANES is a stratified, multistage study program conducted by the National Center for Health Statistics (NCHS). It is designed to assess the health and nutritional status of the U.S. population by collecting nationally representative data. It has been widely used to investigate chronic diseases, nutrition, environmental exposures, and the relationships between health and behavior [14]. NHANES data collection and analysis procedures have been previously reported [15]. NHANES is conducted by the Centers for Disease Control and Prevention's National Center for Health Statistics. Written informed consent was obtained from all participants, and the protocol was approved by the National Center for

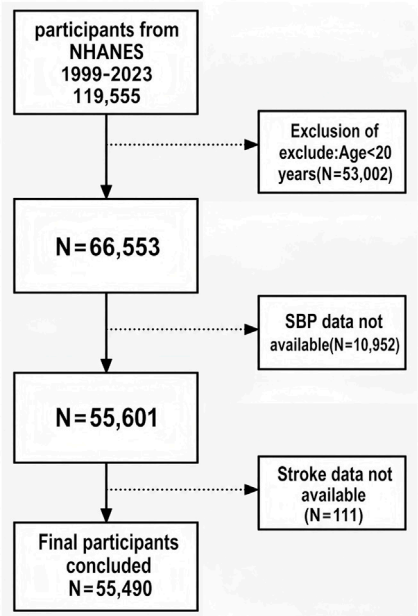

FIGURE 1
The flow chart of selection of included studies.

Health Statistics Institutional Review Board [16]. Representative survey subjects were selected by the method of stratified multi-stage probability sampling. Demographic data, questionnaire data, and dietary data were obtained, including demographics (age, gender, education, race), medical history, diet, and lifestyle habits (smoking, alcohol consumption, exercise). Detailed methods are available on the NHANES website[1].

This study analyzed data from 12 NHANES cycles (1999–2023). As shown in Figure 1, we initially included 119,555 participants from the NHANES database. This study focused on adults; thus, participants younger than 20 years were excluded. The definition of HSBP (SBP ≥130 mmHg) was based on the 2017 AHA/ACC adult guideline, whereas blood pressure classification in children and adolescents relies on age-, sex-, and height-specific criteria. Moreover, the low occurrence of stroke in individuals younger than 20 years in NHANES may limit the stability and interpretability of age-stratified analyses. After excluding participants aged <20 years (n = 53,002), those with fewer than 3 systolic blood pressure measurements (n = 10,952), and cases with missing stroke information (n = 111), we ultimately included 55,490 eligible participants in our final analysis.

Measures

Primary outcome

The primary outcome variable was stroke. The Medical Status Questionnaire was used to obtain a self-reported stroke diagnosis. Respondents were asked, "Have doctors or other health professionals ever told you about a stroke?" Based on their responses to this self-reported question, participants were divided into either the "stroke" or "non-stroke" groups. Previous studies have validated the use of self-reported stroke [17, 18].

Key variables

The primary exposure is the presence or absence of HSBP. In NHANES, all blood pressure measurements were taken by a certified examiner using a sphygmomanometer after the participant sat still for 5 min. According to the 2017 American Heart Association/American College of Cardiology (AHA/ACC) guidelines [19], individuals with SBP ≥130 mmHg were classified as having HSBP. To minimize random measurement error, we only included participants who had ≥3 SBP measurements, with the final SBP value calculated as the mean of three separate blood pressure readings.

Covariates

In the NHANES database, participant age was calculated from the date of interview to the date of birth, while gender was coded by NHANES personnel as either male or female following standardized protocols. Race is assessed through two questions: (1) "Do you identify as Hispanic, Mexican, or non-Hispanic?" (2) "What race do you consider yourself?" Based on responses to these questions, NHANES personnel categorized participants into five mutually exclusive racial/ethnic groups: Mexican American, Other Hispanic, Non-Hispanic White, Non-Hispanic Black, and Other Race. Education levels are grouped by the following question: "What is the highest grade or level of school you completed or the highest degree you earned?" According to the answer to this question, education is divided into three groups: below high school, high school, and above high school. Marital status is divided into married/partnered, divorced/widowed/separated, and never married. The PIR represents the ratio of a family's self-reported income to the appropriate poverty threshold. Participants were stratified into three groups based on PIR values: <1.3, 1.3–3.5, and ≥3.5. Body mass index (BMI) was calculated as weight in kilograms divided by the square of height in meters (kg/m^2). Participants were categorized into three BMI groups: <25 kg/m^2 (underweight/normal weight), 25 to <30 kg/m^2 (overweight), and ≥30 kg/m^2 (obese). Alcohol consumption, exercise, and smoking are divided into two categories: yes or no. Diabetes was defined as meeting any one of the following criteria: a documented history of diabetes, current use of insulin, use of oral hypoglycemic medications, glycated hemoglobin (HbA1c) ≥6.5%, fasting plasma glucose ≥126 mg/dL (7.0 mmol/L), or 2-h postprandial glucose ≥200 mg/dL (11.1 mmol/L). The diagnosis of hyperlipidemia was based on the National Cholesterol Education Program Adult Treatment Panel III (NCEP-ATP III) guidelines (2002). Participants were identified as having hyperlipidemia if they met any of the following criteria: (1) TC ≥ 200 mg/dL, (2) TG ≥ 150 mg/dL, (3) LDL-C ≥ 130 mg/dL, or (4) HDL-C ≤ 40 mg/dL

1 https://www.cdc.gov/nchs/nhanes/

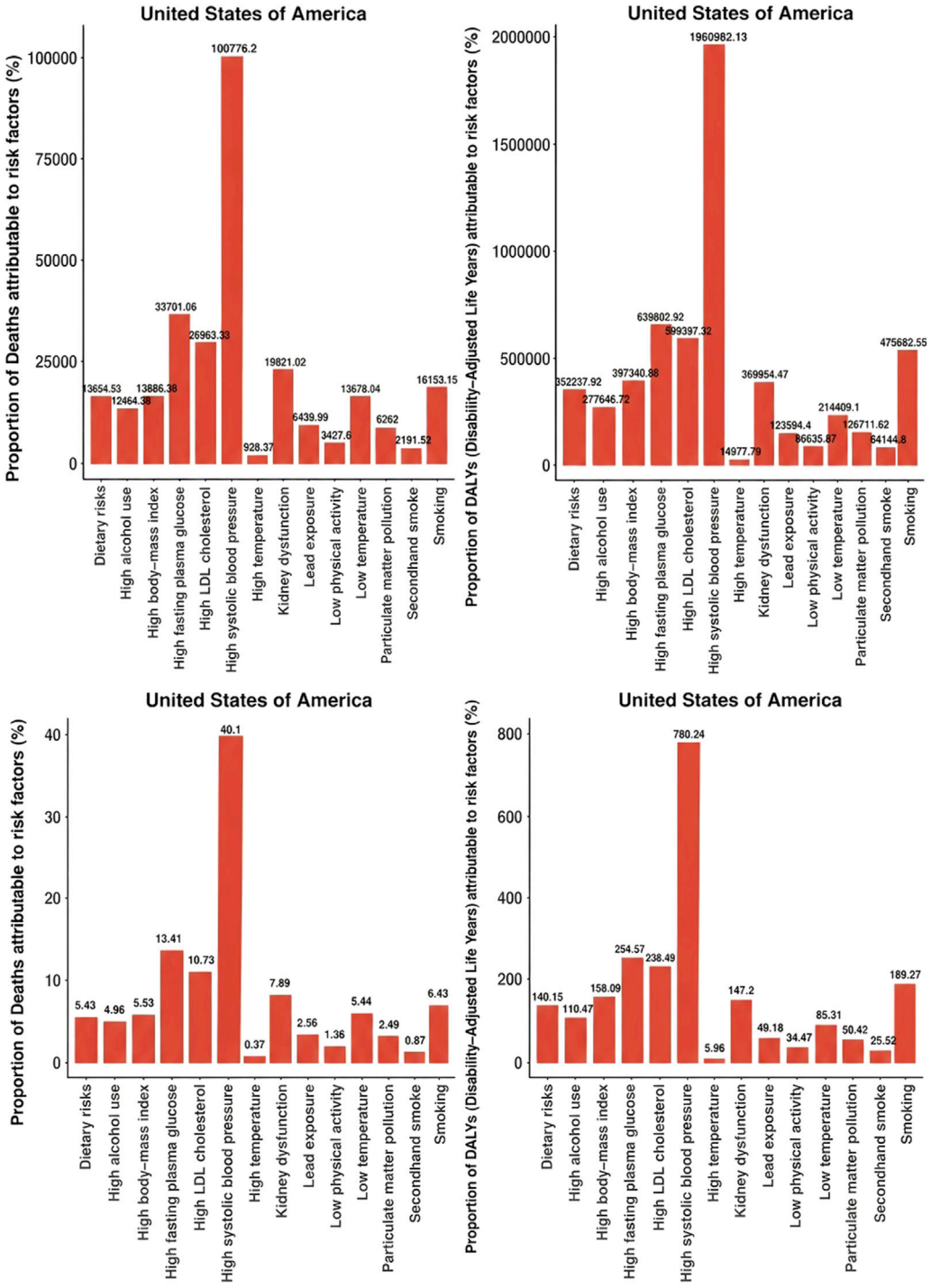

FIGURE 2
2021 US stroke burden by risk factors.

for males or ≤50 mg/dL for females. In addition, participants taking lipid-lowering drugs were also considered to have hyperlipidemia.

Participants were categorized into either low or high physical activity groups based on whether they met the National Physical Activity Guidelines (low physical activity: <500 MET-min/week; high physical activity: ≥500 MET-min/week) [20]. To ensure data quality, a comprehensive evaluation of missing data was conducted. For variables with a missing data rate of more than 10%, a multiple imputation approach was used.

This manuscript has been reported in line with the STROCSS criteria [21]. We utilized de-identified data from public databases, including the GBD and the NHANES. Ethical approval was obtained in the original surveys and was not required for this study.

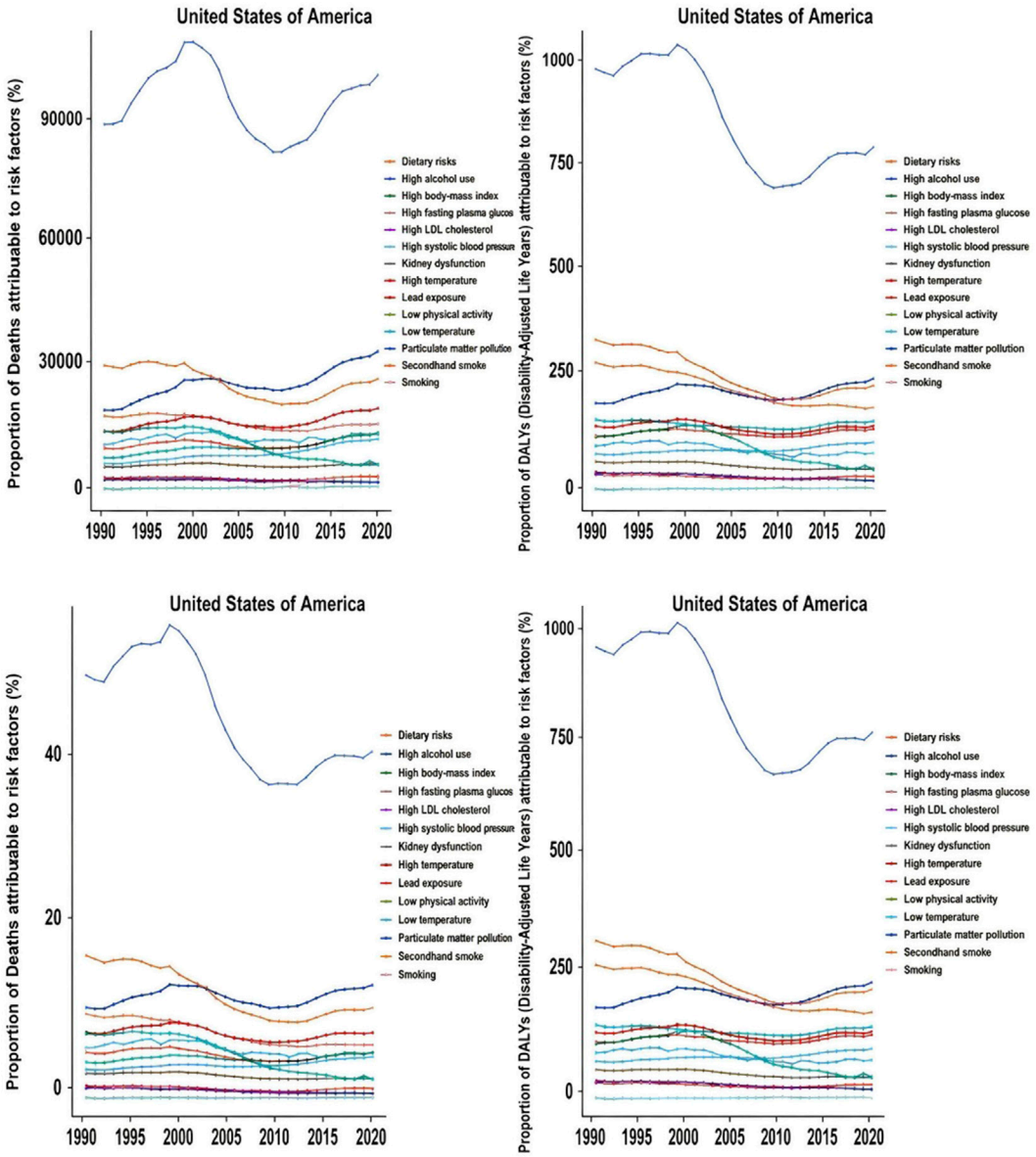

FIGURE 3
US time-stratified stroke burden from HSB.

Statistical analysis

This study utilized GBD 2021 data from the GBD database to analyze risk factors contributing to the stroke burden in the United States. We assessed each risk factor's attributable deaths, attributable DALYs, and age-standardized attributable DALY rates. NHANES data were utilized to analyze the association between HSBP and stroke incidence. Continuous variables were expressed as mean ± standard deviation, while categorical variables were presented as case numbers (percentages). Between-group comparisons were conducted using t-tests, Mann-Whitney U tests, or χ^2 tests. Multivariable logistic regression models were applied to examine the association between HSBP and stroke incidence.

Three multivariate logistic regression models were constructed to evaluate the linear relationship between HSBP and stroke: Model 1, unadjusted; Model 2, adjusted for age, gender, and race; and Model 3, further adjusted for education, marital status, smoking history, alcohol consumption, physical activity, diabetes, hyperlipidemia, and PIR based on Model 2. The results were presented as odds ratios (ORs) with corresponding 95% confidence intervals (CIs). Cox proportional hazards regression analysis was performed to evaluate the association between SBP and all-cause mortality among stroke survivors. Covariates included in the three models were consistent with those used in the multivariable regression analyses. Sensitivity analyses were additionally conducted treating systolic blood pressure as a continuous variable and stroke occurrence as the outcome, to assess the impact of each

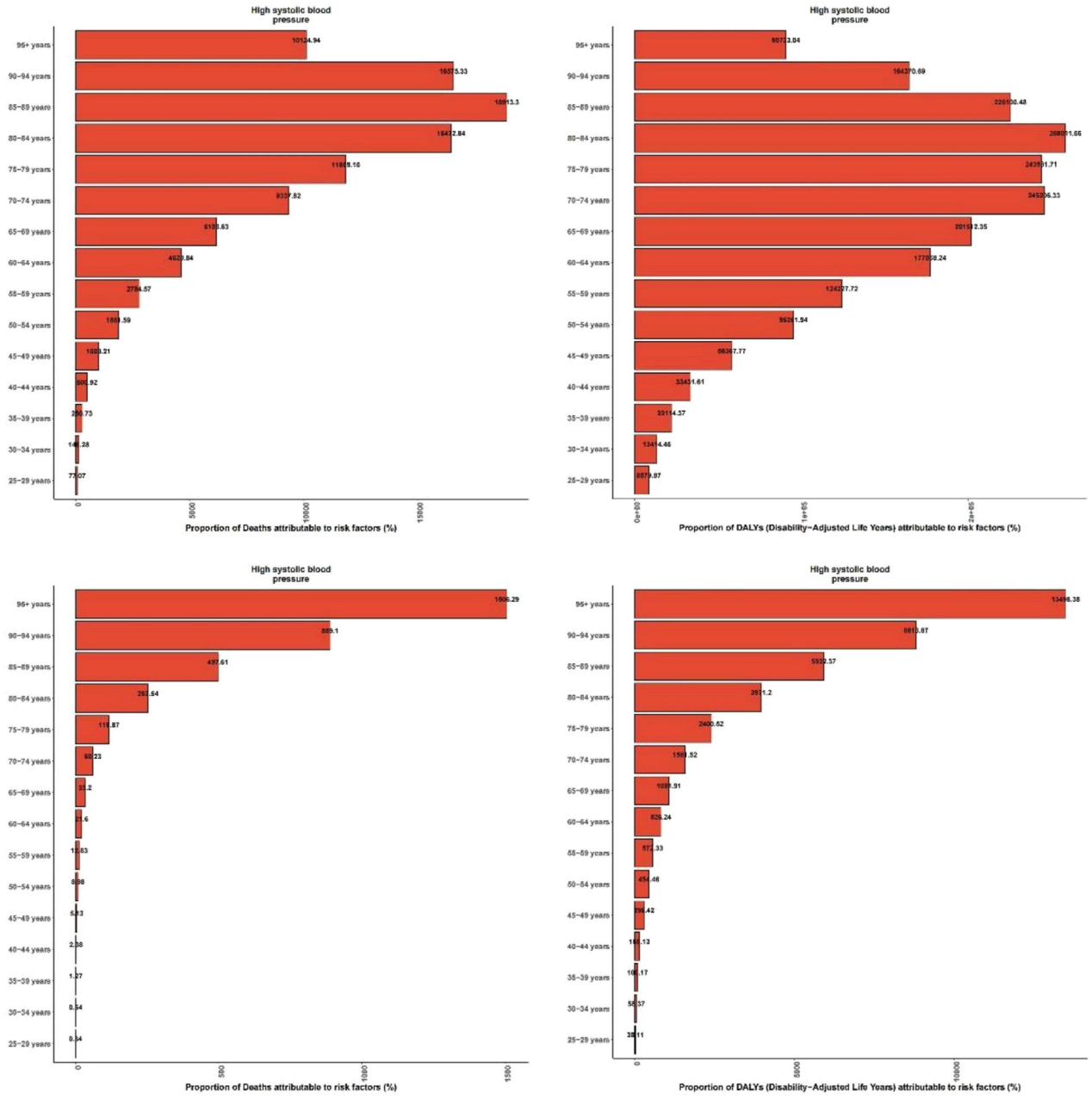

FIGURE 4
US age-stratified stroke burden from HSBP.

unit increase in systolic blood pressure on stroke incidence. Subgroup stratification and interaction tests were performed to investigate the association between HSBP and stroke across various demographic groups. The results of subgroup analyses were illustrated using forest plots. To account for NHANES's complex probability cluster sampling design, survey weights were incorporated in all statistical analyses. For covariates with less than 15% missing data, quantitative variables were imputed using the Predictive Mean Matching (PMM) method, while categorical variables were imputed via logistic regression imputation.

Results

HSBP is a major risk factor contributing to the stroke burden in the United States

Figure 2 summarizes the stroke burden attributable to various risk factors in the United States in 2021. In 2021, HSBP was the leading contributor among stroke risk factors, significantly exceeding all others. This dominance was consistently observed across all metrics: deaths (100,776.20; 95% uncertainty interval [UI]: 70,492.27–129,333.71), DALYs (1,960,982.13; 95% UI:

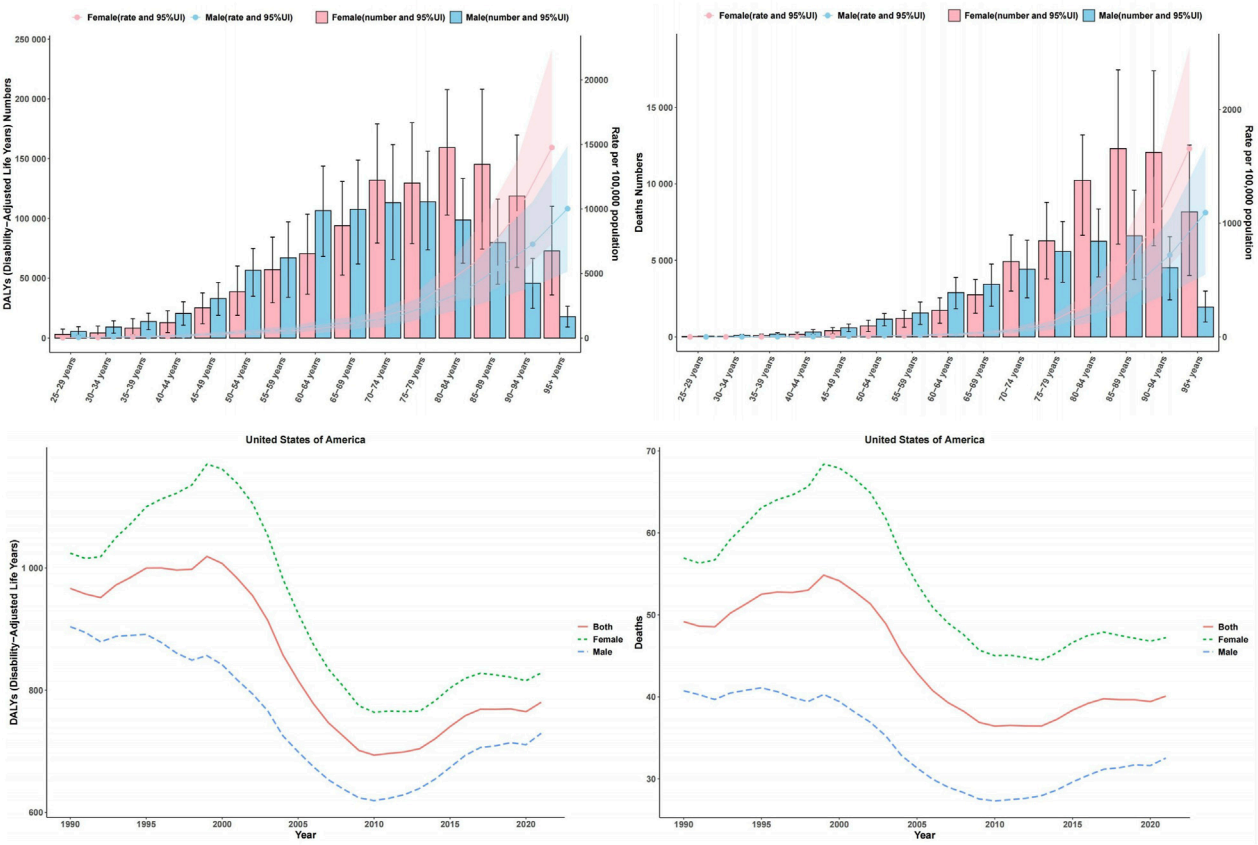

FIGURE 5
Gender-stratified analysis.

1,421,828.68–2,483,402.75), ASDR (40.10; 95% UI: 28.05–51.46), and ASDAR (780.24; 95% UI: 565.72–988.10).

Figure 3 presents a comprehensive temporal analysis of the stroke burden attributable to HSBP based on GBD study data. Results indicate that from 1990 to 1999, the stroke burden attributable to HSBP exhibited an overall increasing trend, followed by a consistent decline from 1999 to 2010. Subsequently, the trend reversed once more, rising after 2010. This pattern was consistently observed across all four metrics: deaths, DALYs, ASDR, and ASDAR.

Figure 4 presents an age-stratified analysis of the stroke burden attributable to HSBP in the United States. Results show that stroke deaths attributed to HSBP peaked in the 85–89 age group, with DALYs predominantly distributed among those aged 80–84 years; both ASDR and ASDAR reached their highest values in the population aged ≥95 years.

Gender-stratified analysis revealed male predominance in SBP-attributable stroke mortality, DALYs, and ASDAR among individuals aged 25–69 years in 2021, whereas female predominance was observed after age 70. Although ASDR was higher in males aged 25–79 years, females exhibited higher ASDR after age 80. From 1990 to 2021, females consistently exhibited higher ASDR and ASDAR than males (Figure 5).

In 2021, the ASDR for SBP-attributable stroke in the United States was 29.04 (95% UI: 28.86–29.22), with projections indicating a decline to 21.25 (95% UI: 14.05–28.45) by 2045. Similarly, the ASDAR was 613.48 (95% UI: 605.13–606.89) in 2021, with projections estimating a decrease to 518.46 (95% UI: 358.43–678.48) by 2045. The analysis predicts a consistent downward trend for both ASDR and ASDAR from 2021 through 2045 (Figure 6).

Characteristics of NHANES study participants

This study included data from 119,555 participants. After excluding subjects younger than 20 years or lacking mean SBP or necessary stroke data, a total of 55,490 participants were finally enrolled (see flow chart). The study population comprised 53,363 non-stroke individuals and 2,127 stroke patients. Table 1 presents the detailed demographic characteristics of the study population stratified by stroke status. Significant differences were observed between stroke and non-stroke subgroups in variables including race, education level, marital status, smoking history, alcohol consumption, METs, diabetes status, hyperlipidemia, mean SBP, age, and PIR. However, no statistically significant difference was found in sex distribution between the two groups. Compared to non-stroke individuals, stroke patients were significantly more likely to be older, of non-Hispanic White race, less educated, current smokers, alcohol consumers, diabetic, hyperlipidemic, and to have a lower PIR (all $P < 0.05$).

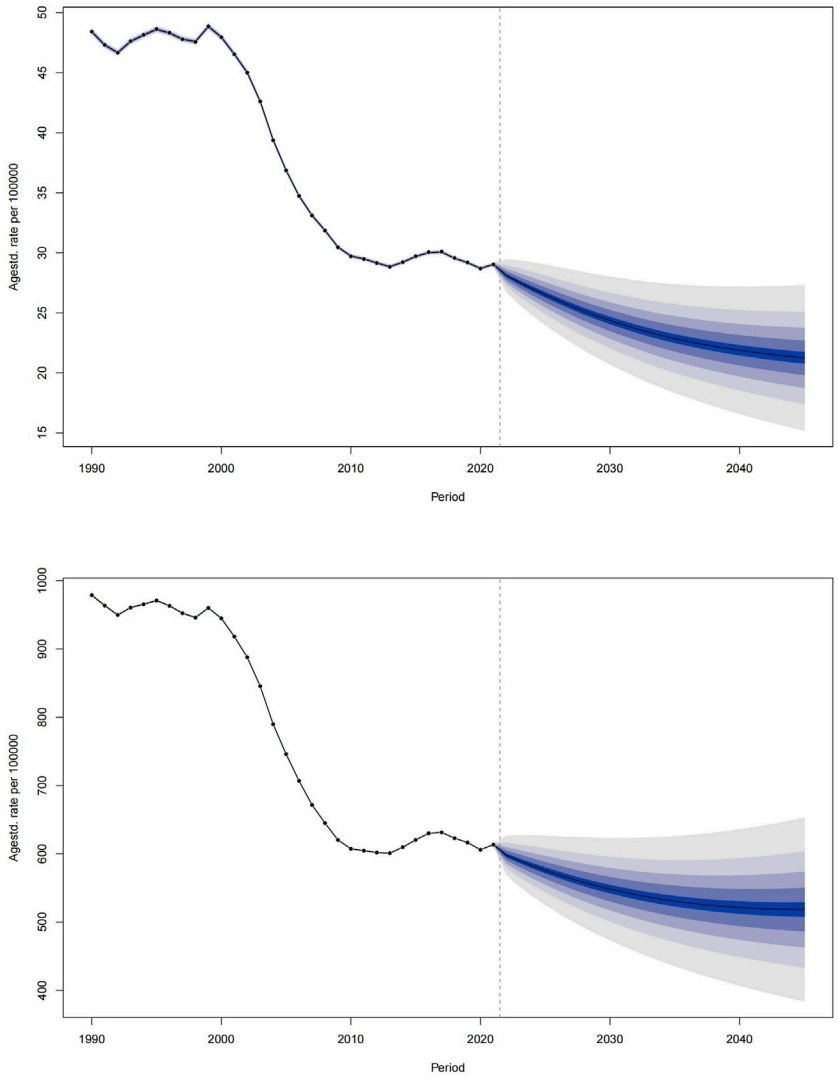

FIGURE 6
Predictive model.

Association between HSBP and stroke

All models consistently indicated that HSBP was associated with an increased incidence of stroke (Table 2). Specifically, Model 1 showed an odds ratio (OR) of 2.73 (95% confidence interval [CI]: 2.45–3.05); Model 2, OR = 1.52 (95% CI: 1.33–1.72); and Model 3, OR = 1.33 (95% CI: 1.17–1.51), indicating that individuals with HSBP had a 1.33-fold higher risk of stroke compared to those with normal blood pressure.

Association of HSBP and all-cause mortality in stroke survivors

Among 1,711 stroke survivors, 743 all-cause deaths occurred during the follow-up period. The unadjusted regression analysis (Table 3) indicated that HSBP was associated with an increased risk of all-cause mortality among stroke survivors (hazard ratio [HR] = 1.01; 95% CI: 1.01–1.02), suggesting a positive correlation between HSBP and mortality risk. This association remained statistically significant in the fully adjusted model (Model 3), with an HR of 1.01 (95% CI: 1.01–1.01). These results consistently demonstrate that elevated SBP significantly increases all-cause mortality risk among stroke survivors (Table 3).

Subgroup analysis

To assess the consistency of the association between HSBP and stroke across different populations, subgroup analyses and interaction tests stratified by gender, race, age, education level, marital status, alcohol consumption, physical activity, smoking history, diabetes mellitus, hyperlipidemia, mean SBP, and poverty-income ratio (PIR) were performed. As shown in Figure 7, no covariate significantly modified the association between HSBP and stroke.

TABLE 1 NHANES 1999-2023 participant baseline traits.

Variable	Total (n = 55,490)	0 (n = 53,363)	1 (n = 2,127)	Statistic	*P*
Sex, n (%)				χ^2 = 5.29	0.060
Male	26,849 (48.57)	25,767 (48.65)	1,082 (45.68)		
Female	28,641 (51.43)	27,596 (51.35)	1,045 (54.32)		
Age, n (%)				χ^2 = 1,352.06	**<0.001**
20–59	36,241 (74.68)	35,682 (75.83)	559 (34.47)		
≥60	19,249 (25.32)	17,681 (24.17)	1,568 (65.53)		
SBP, n (%)				χ^2 = 404.94	**<0.001**
<130	37,698 (73.04)	36,704 (73.68)	994 (50.59)		
≥130	17,792 (26.96)	16,659 (26.32)	1,133 (49.41)		
Race, n (%)				χ^2 = 53.34	**<0.001**
Mexican American	8,730 (7.94)	8,523 (8.04)	207 (4.35)		
Other hispanic	4,835 (6.05)	4,697 (6.09)	138 (4.57)		
Non-hispanic white	25,162 (67.69)	24,098 (67.65)	1,064 (68.80)		
Non-hispanic black	11,348 (10.95)	10,787 (10.84)	561 (14.82)		
Other race	5,415 (7.37)	5,258 (7.37)	157 (7.47)		
Education level, n (%)				χ^2 = 238.86	**<0.001**
Less than high school	13,591 (15.78)	12,848 (15.48)	743 (26.43)		
High school	12,788 (24.19)	12,205 (23.98)	583 (31.79)		
More than high school	29,111 (60.02)	28,310 (60.54)	801 (41.78)		
Martial status, n (%)				χ^2 = 232.80	**<0.001**
Married/living with partner	33,083 (63.84)	31,999 (64.05)	1,084 (56.69)		
Widowed/divorced/separated	14,997 (22.62)	14,073 (22.20)	924 (37.38)		
Never married	7,410 (13.54)	7,291 (13.76)	119 (5.93)		
Smoke, n (%)				χ^2 = 113.07	**<0.001**
No	30,481 (54.53)	29,636 (54.91)	845 (41.22)		
Yes	25,009 (45.47)	23,727 (45.09)	1,282 (58.78)		
Drinking, n (%)				χ^2 = 56.99	**<0.001**
No	16,549 (25.40)	15,813 (25.17)	736 (33.67)		
Yes	38,941 (74.60)	37,550 (74.83)	1,391 (66.33)		
Physical activity, n (%)				χ^2 = 284.52	**<0.001**
Low physical activity	21,248 (34.58)	20,023 (34.00)	1,225 (54.75)		
High physical activity	34,242 (65.42)	33,340 (66.00)	902 (45.25)		
Diabetes, n (%)				χ^2 = 842.34	**<0.001**
No	45,700 (86.79)	44,446 (87.49)	1,254 (62.07)		
Yes	9,790 (13.21)	8,917 (12.51)	873 (37.93)		
Hyperlipidemia, n (%)				χ^2 = 132.24	**<0.001**
No	17,902 (32.48)	17,452 (32.87)	450 (18.94)		
Yes	37,588 (67.52)	35,911 (67.13)	1,677 (81.06)		

(*Continued*)

TABLE 1 Continued

Variable	Total (n = 55,490)	0 (n = 53,363)	1 (n = 2,127)	Statistic	*P*
BMXBMI, n (%)				χ^2 = 63.07	**<0.001**
<25	16,125 (30.42)	15,613 (30.61)	512 (23.60)		
25–30	18,649 (33.31)	17,970 (33.37)	679 (31.00)		
≥30	20,716 (36.27)	19,780 (36.01)	936 (45.41)		
PIR, n (%)				χ^2 = 205.25	**<0.001**
<1.3	16,614 (21.29)	15,758 (20.96)	856 (32.58)		
1.3–3.5	21,049 (36.00)	20,187 (35.86)	862 (41.07)		
>=3.5	17,827 (42.71)	17,418 (43.18)	409 (26.34)		

SE: standard error.
t: t-test, χ^2: Chi-square test.

TABLE 2 The association between HSBP and stroke.

Variables	Model1		Model2		Model3	
	OR (95%CI)	*P*	OR (95%CI)	*P*	OR (95%CI)	*P*
SBP						
<130	1.00 (reference)		1.00 (reference)		1.00 (reference)	
≥130	2.73 (2.45–3.05)	**<0.001**	1.52 (1.33–1.72)	**<0.001**	1.33 (1.17–1.51)	**<0.001**
P for trend	**<0.001**		**<0.001**		**<0.001**	

OR: odds ratio, CI: confidence interval.
Model1: Crude.
Model2: Adjust: Adjusted for sex, age and race.
Model3: Adjusted for sex, age, race, education, marital status, smoking history, alcohol consumption, physical activity, diabetes, hyperlipidemia, and PIR.

TABLE 3 Association between SBP and all-cause mortality in stroke survivors.

Variables	Model1		Model2		Model3	
	HR (95%CI)	*P*	HR (95%CI)	*P*	HR (95%CI)	*P*
Systolic blood pressure	1.01 (1.01–1.02)	**<0.001**	1.01 (1.01–1.01)	**0.003**	1.01 (1.01–1.01)	**0.010**

HR: hazard ratio, CI: confidence interval.
Model1: Crude.
Model2: Adjusted for sex, age and race.
Model3: Adjusted for sex, age, race, education, marital status, smoking history, alcohol consumption, physical activity, diabetes, hyperlipidemia, and PIR.

Sensitivity analysis

In the sensitivity analysis, systolic blood pressure was treated as a continuous variable, and stroke occurrence was used as the outcome; multivariable logistic regression analysis was conducted to evaluate this relationship. In the fully adjusted model, HSBP remained significantly associated with increased stroke incidence ($P < 0.05$), with an adjusted OR of 1.01 (95% CI: 1.01–1.01). Weighted logistic regression models employed in the sensitivity analyses confirmed the robustness of these findings, demonstrating consistent associations between HSBP and stroke prevalence in alignment with primary analysis results (Table 4).

Nonlinear relationship between HSBP and stroke

Figure 8 illusrates the relationship between HSBP and stroke prevalence based on NHANES data. After adjustment for sex, race, education level, marital status, smoking history, alcohol consumption, METs, diabetes status, hyperlipidemia, BMI, age, and PIR, smoothed curve fitting revealed a U-shaped association between SBP and stroke prevalence. A piecewise regression model identified 100 mmHg as the critical threshold for SBP. Results demonstrated that within the lower SBP range (<100 mmHg), stroke risk decreased as blood pressure increased; conversely, above this threshold (>100 mmHg), higher SBP levels were associated with progressively increased stroke risk.

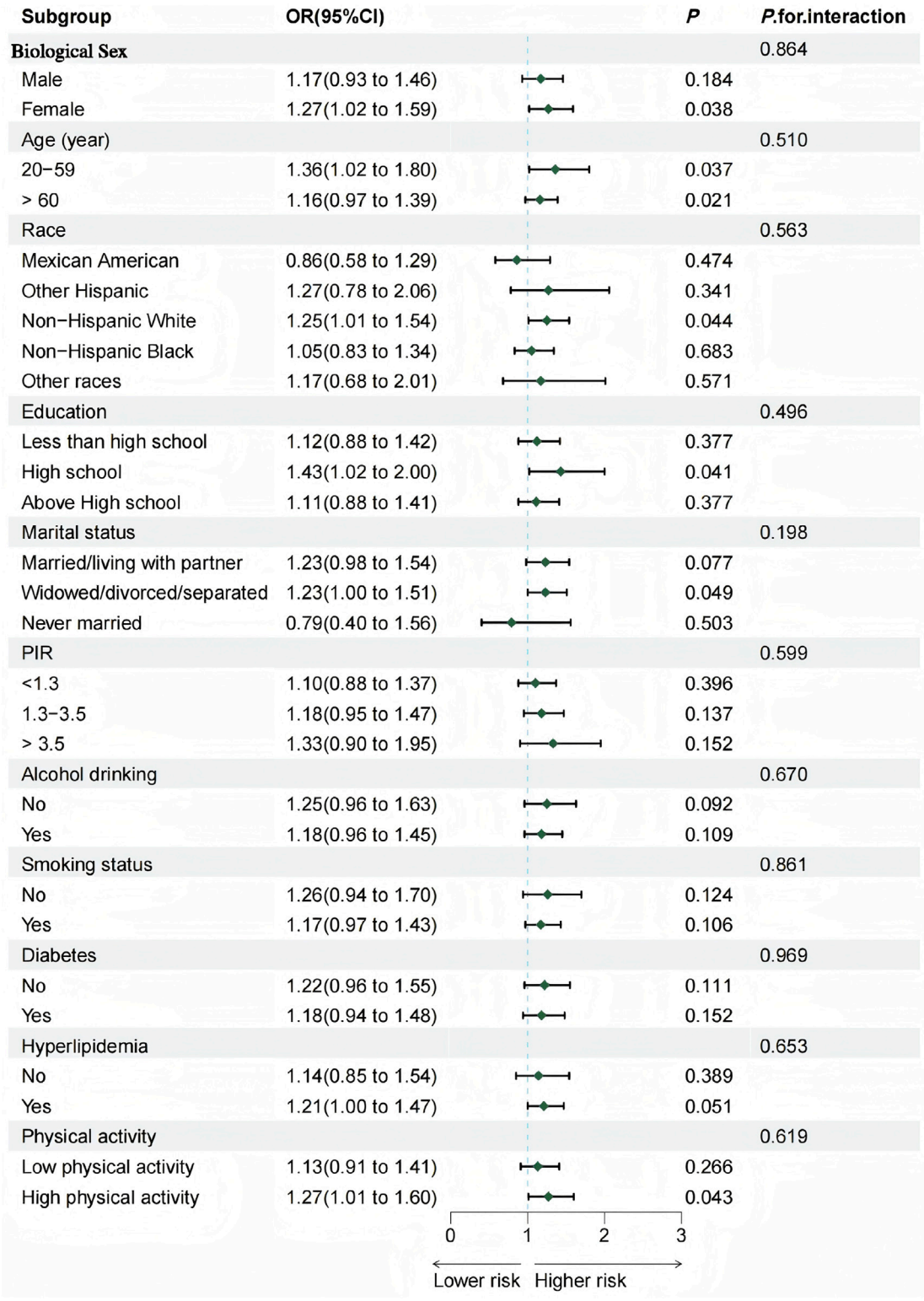

FIGURE 7
Subgroup analysis.

Discussion

A major strength of this study is the complementary use of GBD and NHANES data. The GBD analysis established the population-level context by showing that HSBP was the leading contributor to stroke burden in the United States, whereas the NHANES analysis extended these findings by demonstrating that HSBP was independently associated with stroke in a nationally

TABLE 4 Sensitivity analysis.

Variables	Model1		Model2		Model3	
	OR (95%CI)	*P*	OR (95%CI)	*P*	OR (95%CI)	*P*
Systolic blood pressure	1.03 (1.02–1.03)	**<0.001**	1.01 (1.01–1.01)	**<0.001**	1.01 (1.01–1.01)	**<0.001**

OR: odds ratio, CI: confidence interval.
Model1: Crude.
Model2: Adjusted for sex, age and race.
Model3: Adjusted for sex, age, race, education, marital status, smoking history, alcohol consumption, physical activity, diabetes, hyperlipidemia, and PIR.

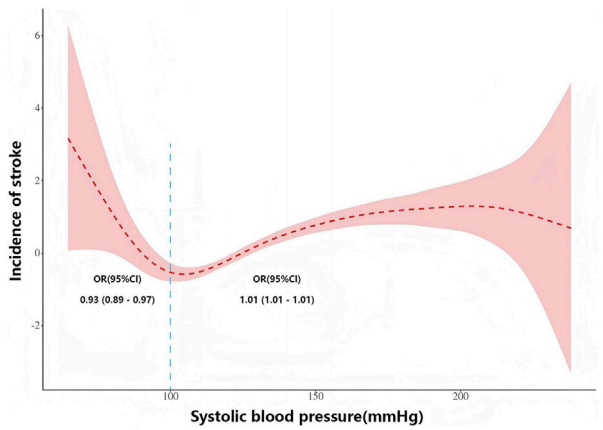

FIGURE 8
Nonlinear relationship between HSBP and stroke.

representative sample. Together, these results provide both epidemiological context and individual-level support for the role of HSBP as a major modifiable risk factor for stroke. Our findings demonstrate that HSBP remains the predominant risk factor for stroke-related deaths and DALYs in the U.S. Notably, the attributable burden has exhibited a consistent year-over-year increase since 2010. In the fully adjusted multivariable logistic regression model, individuals with HSBP demonstrated a 1.33-fold increased risk of stroke compared to those with normal blood pressure levels. Furthermore, each 1 mmHg increase in SBP was associated with approximately a 1% increase in the risk of stroke incidence (OR = 1.01, 95% CI: 1.01–1.01). These findings not only quantify the stroke disease burden attributable to SBP at the U.S. population level but also confirm HSBP as a key modifiable risk factor based on large-scale population data, thereby providing critical evidence for developing and optimizing targeted stroke prevention strategies, particularly in the U.S. where the burden continues to rise.

Our study confirms that HSBP is a key independent risk factor for stroke, a finding that is highly consistent with the extensive epidemiological evidence accumulated to date. A previous meta-analysis of the relationship between SBP and cardiovascular disease risk demonstrated that elevated SBP levels are the leading global cause of total mortality and a major contributor to long-term disability [22], with a greater predictive value than diastolic, mean arterial, and pulse blood pressure [23, 24]. The study data demonstrated that each 20 mmHg increase in SBP was associated with significantly increased risks across stroke subtypes: a 35% higher risk of ischemic stroke (95% CI: 1.28–1.42), 44% increased risk of intracerebral hemorrhage (95% CI: 1.32–1.58), and 43% greater risk of subarachnoid hemorrhage (95% CI: 1.25–1.63) [25]. Moreover, this level of blood pressure elevation more than doubled the risk of all-cause mortality [26].

Several underlying mechanisms may account for the observed positive association between HSBP and stroke. First, hypertension profoundly impacts the structure of cerebral blood vessels. Mechanical, neural, and humoral factors collectively contribute to structural alterations in the vascular wall. Under chronic high-pressure conditions, smooth muscle cells undergo hypertrophy, hyperplasia, and disorganized proliferation, which encroaches upon the arterial lumen. This pathological remodeling results in vascular narrowing, wall thickening, and arterial stiffening [27–29], thereby promoting atherosclerotic plaque formation and eventually leading to arterial occlusion and ischemic injury. Secondly, in patients with HSBP, decreased cerebral blood flow may precede cerebrovascular symptoms or white matter lesions. This reduction may be secondary to endothelial dysfunction, leading to increased vascular tone [30]. Furthermore, endothelial dysfunction impairs autoregulatory function [31], necessitating higher perfusion pressure to maintain normal cerebral blood flow. Concurrently, HSBP directly induces oxidative stress in the cerebrovasculature [32]. Such persistent oxidative stress depletes antioxidant molecules and inactivates antioxidant enzymes, compromising the endogenous antioxidant defense system and exacerbating both structural and functional vascular damage [33]. Moreover, inflammation constitutes a key pathological mechanism in vascular injury [34]. Inflammatory biomarkers have been shown to predict the risk of primary ischemic stroke [35]. Individuals predisposed to stroke consistently exhibit elevated levels of inflammatory markers—including C-reactive protein (CRP), interleukin-6 (IL-6), leukocyte elastase, lipoprotein(a), intercellular adhesion molecule-1 (ICAM-1), and E-selectin—compared to stroke-free individuals [36]. Finally, baroreflex sensitivity (BRS) is a key indicator of arterial baroreceptor function and plays a critical role in both the pathogenesis and prognosis of stroke [37]. After ischemic or hemorrhagic stroke, baroreflex dysfunction and blood pressure variability may significantly alter cerebral perfusion and exacerbate perihematoma edema [37, 38]. Therefore, in the absence of intervention, oxidative stress, inflammation, and baroreflex dysfunction may create a vicious cycle that ultimately culminates in stroke.

This study comprehensively evaluated the association between HSBP and stroke risk burden in the U.S. by integrating two complementary approaches: large-scale, nationally representative

NHANES data and GBD estimates. This study highlights the ongoing increase in the burden of HSBP-related stroke in the U.S. and confirms HSBP as a key modifiable risk factor for this disease. These findings provide a strong scientific basis for the urgent reinforcement of comprehensive blood pressure control measures in the U.S. In light of this rising and preventable disease burden, immediate, multidimensional, and targeted interventions are imperative. The restricted cubic spline analysis further suggests that the relationship between SBP and stroke is nonlinear, with a threshold near 100 mmHg, indicating that both elevated SBP and excessively low SBP in certain contexts may warrant clinical attention. These findings have important policy implications, as they support greater funding for blood pressure screening, early intervention, and long-term stroke prevention programs. Although based on U.S. data, the present results may also be informative globally, given that HSBP remains a leading modifiable risk factor for stroke worldwide and may represent a practical target for prevention across diverse healthcare settings.

However, this study has several limitations. Stroke inclusion criteria relied on self-reported stroke history, and the stroke subtypes were not identified, preventing further assessment of associations between HSBP and specific stroke subtypes. Furthermore, the findings are primarily applicable to individuals aged 20 years and above in the United States, limiting the generalizability of results. Future studies should consider more refined age stratification, such as 20–35 years, 36–45 years, and 46–60 years, to better characterize potential age-related heterogeneity in the association between HSBP and stroke. Nevertheless, the established association between HSBP and stroke is robust enough that it is unlikely to be substantially affected by unmeasured confounding factors. Future research should further investigate the long-term effects of HSBP on stroke using longitudinal designs and multicenter stroke registry data.

Conclusion

In summary, our findings demonstrate that HSBP is a core driver of the persistently increasing stroke burden in the United States and a crucial target for interventions aimed at preventing stroke-related morbidity. Our results hold significant implications for clinical stroke risk management and prevention. We anticipate that future longitudinal studies and multicenter stroke registry data analyses will further validate our conclusions.

Author contributions

All authors listed have made a substantial, direct, and intellectual contribution to the work and approved it for publication.

Data availability

The data sets generated and/or analyzed during the current study are available in the GBD repository (http://ghdx.healthdata.org/gbd-results-tool). The original contributions presented in the study are included in the article/supplementary material. Further inquiries can be directed to the corresponding author.

Ethics statement

Research involving GBD 2021 data was reviewed by the University of Washington's Institutional Review Board (IRB), which approved a waiver of the informed consent requirement. NHANES is conducted by the Centers for Disease Control and Prevention's National Center for Health Statistics. Written informed consent was obtained from all participants, and the protocol was approved by the National Center for Health Statistics Institutional Review Board.

Funding

The author(s) declared that financial support was not received for this work and/or its publication.

Acknowledgements

The authors appreciate the work by the GBD 2021 collaborators and all who helped with this study. The authors thank all the NHANES who participated in this study, and thank all investigators for making available their data.

Conflict of interest

The author(s) declared no potential conflicts of interest with respect to the research, authorship, and/or publication of this article.

Generative AI statement

The author(s) declared that generative AI was not used in the creation of this manuscript.

Any alternative text (alt text) provided alongside figures in this article has been generated by Frontiers with the support of artificial intelligence and reasonable efforts have been made to ensure accuracy, including review by the authors wherever possible. If you identify any issues, please contact us.

References

1. Global Regional. National burden of stroke, 1990-2016: a systematic analysis for the global burden of disease study 2016. *Lancet Neurol* (2019) 18(5):439–58.

2. Boehme AK, Esenwa C, Elkind MS. Stroke risk factors, genetics, and prevention. *Circ Res* (2017) 120(3):472–95. doi:10.1161/CIRCRESAHA.116.308398

3. Cao J, Eshak ES, Liu K, Arafa A, Sheerah HA, Yu C. Age-period-cohort analysis of stroke mortality attributable to high systolic blood pressure in China and Japan. *Sci Rep* (2021) 11(1):19083. doi:10.1038/s41598-021-98072-y

4. Global, regional, and national burden of stroke and its risk factors, 1990-2019: a systematic analysis for the global burden of disease study 2019. *Lancet Neurol*. (2021) 20(10):795–820. doi:10.1016/S1474-4422(21)00252-0

5. Lattanzi S, Brigo F, Silvestrini M. Blood pressure and stroke: from incidence to outcome. *J Clin Hypertens (Greenwich)* (2019) 21(5):605–7. doi:10.1111/jch.13525

6. Zhang D, Dong X, Meng Y, Yao Z, Wu X. Global, regional, and national burden of stroke and associated risk factors among adults aged ≥60 years, 1990-2021: a multidimensional analysis leveraging GBD, NHANES, and mendelian randomization. *Int J Surg* (2025). doi:10.1097/JS9.0000000000004336

7. He X, Zhu J, Liang W, Yang X, Ning W, Zhao Z, et al. Association of body roundness index with cardiovascular disease in patients with cardiometabolic syndrome: a cross-sectional study based on NHANES 2009-2018. *Front Endocrinol (Lausanne)* (2025) 16: 1524352. doi:10.3389/fendo.2025.1524352

8. Fischer U, Cooney MT, Bull LM, Silver LE, Chalmers J, Anderson CS, et al. Acute post-stroke blood pressure relative to premorbid levels in intracerebral haemorrhage *versus* major ischaemic stroke: a population-based study. *Lancet Neurol* (2014) 13(4): 374–84. doi:10.1016/S1474-4422(14)70031-6

9. Mant J, McManus RJ, Roalfe A, Fletcher K, Taylor CJ, Martin U, et al. Different systolic blood pressure targets for people with history of stroke or transient ischaemic attack: PAST-BP (prevention after Stroke--Blood pressure) randomised controlled trial. *Bmj* (2016) 352:i708. doi:10.1136/bmj.i708

10. Roth GA, Mensah GA, Johnson CO, Addolorato G, Ammirati E, Baddour LM, et al. Global burden of cardiovascular diseases and risk factors, 1990-2019: update from the GBD 2019 study. *J Am Coll Cardiol* (2020) 76(25):2982–3021. doi:10.1016/j.jacc.2020.11.010

11. Li XY, Kong XM, Yang CH, Cheng ZF, Lv JJ, Guo H, et al. Global, regional, and national burden of ischemic stroke, 1990-2021: an analysis of data from the global burden of disease study 2021. *EClinicalMedicine* (2024) 75:102758. doi:10.1016/j.eclinm.2024.102758

12. Ma Q, Li R, Wang L, Yin P, Wang Y, Yan C, et al. Temporal trend and attributable risk factors of stroke burden in China, 1990-2019: an analysis for the global burden of disease study 2019. *Lancet Public Health* (2021) 6(12):e897–e906. doi:10.1016/S2468-2667(21)00228-0

13. Hu T, Yang X, Du Y, Zhao Y, Chen L, Sun N, et al. Trends in the global, regional, and national burden of cardiovascular diseases attributed to high systolic blood pressure from 1990 to 2021 and projections to 2045: a systematic analysis based on GBD 2021 data. *BMC Cardiovasc Disord* (2025) 25(1):390. doi:10.1186/s12872-025-04807-4

14. Mao Y, Weng J, Xie Q, Wu L, Xuan Y, Zhang J, et al. Association between dietary inflammatory index and stroke in the US population: evidence from NHANES 1999-2018. *BMC Public Health* (2024) 24(1):50. doi:10.1186/s12889-023-17556-w

15. Yang B, Wang H, Tang L, Feng J, Hou S. Relative fat mass, A better predictor of erectile dysfunction: insights from the NHANES 2001-2004. *Am J Mens Health* (2025) 19(1):15579883241311218. doi:10.1177/15579883241311218

16. Cheng W, Bu X, Xu C, Wen G, Kong F, Pan H, et al. Higher systemic immune-inflammation index and systemic inflammation response index levels are associated with stroke prevalence in the asthmatic population: a cross-sectional analysis of the NHANES 1999-2018. *Front Immunol* (2023) 14:1191130. doi:10.3389/fimmu.2023.1191130

17. Parikh NS, Merkler AE, Iadecola C. Inflammation, autoimmunity, infection, and stroke: epidemiology and lessons from therapeutic intervention. *Stroke* (2020) 51(3): 711–8. doi:10.1161/STROKEAHA.119.024157

18. Jiang Y, Shen J, Chen P, Cai J, Zhao Y, Liang J, et al. Association of triglyceride glucose index with stroke: from two large cohort studies and Mendelian randomization analysis. *Int J Surg* (2024) 110(9):5409–16.

19. Whelton PK, Carey RM, Aronow WS, Casey DE, Collins KJ, Dennison Himmelfarb C, et al. ACC/AHA/AAPA/ABC/ACPM/AGS/APhA/ASH/ASPC/NMA/PCNA guideline for the prevention, detection, evaluation, and management of high blood pressure in adults: a report of the American college of cardiology/american heart association task force on clinical practice guidelines. *Hypertension* (2018) 71(6): e13–e115. doi:10.1097/JS9.0000000000001795

20. MacGregor KA, Gallagher IJ, Moran CN. Relationship between insulin sensitivity and menstrual cycle is modified by BMI, fitness, and physical activity in NHANES. *J Clin Endocrinol Metab* (2021) 106(10):2979–90. doi:10.1210/clinem/dgab415

21. Rashid R, Sohrabi C, Kerwan A, Franchi T, Mathew G, Nicola M, et al. The STROCSS 2024 guideline: strengthening the reporting of cohort, cross-sectional, and case-control studies in surgery. *Int J Surg* (2024) 110(6):3151–65. doi:10.1097/JS9.0000000000001268

22. Peters SA, Huxley RR, Woodward M. Comparison of the sex-specific associations between systolic blood pressure and the risk of cardiovascular disease: a systematic review and meta-analysis of 124 cohort studies, including 1.2 million individuals. *Stroke* (2013) 44(9):2394–401. doi:10.1161/STROKEAHA.113.001624

23. Inoue R, Ohkubo T, Kikuya M, Metoki H, Asayama K, Kanno A, et al. Stroke risk of blood pressure indices determined by home blood pressure measurement: the ohasama study. *Stroke* (2009) 40(8):2859–61. doi:10.1161/STROKEAHA.108.546499

24. Psaty BM, Furberg CD, Kuller LH, Cushman M, Savage PJ, Levine D, et al. Association between blood pressure level and the risk of myocardial infarction, stroke, and total mortality: the cardiovascular health study. *Arch Intern Med* (2001) 161(9):1183–92. doi:10.1001/archinte.161.9.1183

25. Rapsomaniki E, Timmis A, George J, Pujades-Rodriguez M, Shah AD, Denaxas S, et al. Blood pressure and incidence of twelve cardiovascular diseases: lifetime risks, healthy life-years lost, and age-specific associations in 1·25 million people. *Lancet* (2014) 383(9932):1899–911. doi:10.1016/S0140-6736(14)60685-1

26. Wang X, Carcel C, Woodward M, Schutte AE. Blood pressure and stroke: a review of Sex- and Ethnic/racial-specific attributes to the epidemiology, pathophysiology, and management of raised blood pressure. *Stroke* (2022) 53(4):1114–33. doi:10.1161/STROKEAHA.121.035852

27. Baumbach GL, Heistad DD. Cerebral circulation in chronic arterial hypertension. *Hypertension* (1988) 12(2):89–95. doi:10.1161/01.hyp.12.2.89

28. Benjo A, Thompson RE, Fine D, Hogue CW, Alejo D, Kaw A, et al. Pulse pressure is an age-independent predictor of stroke development after cardiac surgery. *Hypertension* (2007) 50(4):630–5. doi:10.1161/HYPERTENSIONAHA.107.095513

29. Laurent S, Boutouyrie P, Lacolley P. Structural and genetic bases of arterial stiffness. *Hypertension* (2005) 45(6):1050–5. doi:10.1161/01.HYP.0000164580.39991.3d

30. Barry DI. Cerebral blood flow in hypertension. *J Cardiovasc Pharmacol* (1985) 7(Suppl. 2):S94–98. doi:10.1097/00005344-198507002-00018

31. Castro P, Azevedo E, Sorond F. Cerebral autoregulation in stroke. *Curr Atheroscler Rep* (2018) 20(8):37.

32. Girouard H, Park L, Anrather J, Zhou P, Iadecola C. Cerebrovascular nitrosative stress mediates neurovascular and endothelial dysfunction induced by angiotensin II. *Arterioscler Thromb Vasc Biol* (2007) 27(2):303–9. doi:10.1161/01.ATV.0000253885.41509.25

33. Vaziri ND, Rodríguez-Iturbe B. Mechanisms of disease: oxidative stress and inflammation in the pathogenesis of hypertension. *Nat Clin Pract Nephrol* (2006) 2(10):582–93. doi:10.1038/ncpneph0283

34. Barungi S, Hernández-Camarero P, Moreno-Terribas G, Villalba-Montoro R, Marchal JA, López-Ruiz E, et al. Clinical implications of inflammation in atheroma formation and novel therapies in cardiovascular diseases. *Front Cell Dev Biol* (2023) 11: 1148768. doi:10.3389/fcell.2023.1148768

35. Tzoulaki I, Murray GD, Lee AJ, Rumley A, Lowe GDO, Fowkes FGR. Relative value of inflammatory, hemostatic, and rheological factors for incident myocardial infarction and stroke: the Edinburgh artery study. *Circulation* (2007) 115(16):2119–27. doi:10.1161/CIRCULATIONAHA.106.635029

36. McColl BW, Allan SM, Rothwell NJ. Systemic infection, inflammation and acute ischemic stroke. *Neuroscience* (2009) 158(3):1049–61. doi:10.1016/j.neuroscience.2008.08.019

37. Sykora M, Diedler J, Rupp A, Turcani P, Rocco A, Steiner T. Impaired baroreflex sensitivity predicts outcome of acute intracerebral hemorrhage. *Crit Care Med* (2008) 36(11):3074–9. doi:10.1097/CCM.0b013e31818b306d

38. Liu AJ, Ma XJ, Shen FM, Liu JG, Chen H, Su DF. Arterial baroreflex: a novel target for preventing stroke in rat hypertension. *Stroke* (2007) 38(6):1916–23. doi:10.1161/STROKEAHA.106.480061

EBM Experimental Biology and Medicine

TYPE Original Research
PUBLISHED 22 May 2026
DOI 10.3389/ebm.2026.11038

OPEN ACCESS

*CORRESPONDENCE
Mark T. Miedel,
mmiedel@pitt.edu
Jacquelyn A. Brown,
jab890@pitt.edu

†These authors share first authorship

‡These authors share senior authorship

RECEIVED 09 February 2026
REVISED 04 May 2026
ACCEPTED 14 May 2026
PUBLISHED 22 May 2026

CITATION
Gavlock DC, Castiglione MW, Wang A, Varmazyad M, Vernetti LA, Schurdak ME, Taylor DL, Brown JA and Miedel MT (2026) Scaling human liver microphysiological systems: implementing a higher-throughput liver acinus microphysiological system platform. *Exp. Biol. Med.* 251:11038. doi: 10.3389/ebm.2026.11038

Scaling human liver microphysiological systems: implementing a higher-throughput liver acinus microphysiological system platform

Dillon C. Gavlock[1†], Michael W. Castiglione[1†], Allen Wang[1], Mahboubeh Varmazyad[1,2,3], Lawrence A. Vernetti[1,2,3], Mark E. Schurdak[1,2,3], D. Lansing Taylor[1,2,3], Jacquelyn A. Brown[1,2,3*‡] and Mark T. Miedel[1,3,4*‡]

[1]Organ Pathobiology and Therapeutic Institute, University of Pittsburgh, Pittsburgh, PA, United States, [2]Department of Computational and System Biology, School of Medicine, University of Pittsburgh, Pittsburgh, PA, United States, [3]Pittsburgh Liver Research Center, University of Pittsburgh, Pittsburgh, PA, United States, [4]Department of Pharmacology and Chemical Biology, University of Pittsburgh, Pittsburgh, PA, United States

Abstract

The advancement in the use of all-human high content microphysiological systems (MPS) has enabled better *in vitro* modeling of liver function and disease progression as well as drug efficacy, metabolism and toxicity (ADME-Tox) testing. However, a continuing need in liver MPS development is balancing throughput without loss of the high-content biological complexity required for physiologically relevant modeling. Here, we present a scalable version of our well-established liver acinus microphysiological system (LAMPS). This higher-throughput format (ht-LAMPS) is designed to recapitulate the physiological complexity of the standard single-chamber LAMPS system while increasing experimental capacity through a seven-chamber microfluidic design. The ht-LAMPS is constructed using the same four key liver cell types as the LAMPS: primary hepatocytes and liver sinusoidal endothelial cells (LSECs) as well as Kupffer-like cells (THP-1) and hepatic stellate cells (LX-2). It recapitulates key physiological characteristics previously established in the LAMPS platform, including oxygen zonation–dependent liver phenotypes including model viability, secretion of functional and cytotoxicity markers, mitochondrial activity, and lipid accumulation, demonstrating reproducibility in the ht-LAMPS format. Finally, we also demonstrate that the ht-LAMPS model recapitulates key phenotypes associated with the progression of metabolic dysfunction–associated steatotic liver disease (MASLD), including increased steatosis and elevated production of inflammatory cytokines and profibrotic markers using our established MASLD media formulations. Overall, by increasing throughput while maintaining key high-content biological features of the LAMPS, ht-LAMPS

provides a scalable platform for investigating liver function, modeling disease progression, and enabling downstream drug testing in MASLD and other liver-related conditions.

KEYWORDS

in vitro liver model, liver-on-a-chip, metabolic dysfunction–associated steatotic liver disease, microphysiological systems, new approach methodologies

Impact statement

Developing more scalable human liver microphysiological systems while retaining biological complexity is essential for improving in vitro modeling of liver disease and therapeutic response. Here, we build upon our well-established liver acinus microphysiological system (LAMPS) to create a higher-throughput LAMPS (ht-LAMPS) platform that recapitulates key high-content physiological features of the original model while enabling the modeling of several key phenotypes of metabolic dysfunction-associated steatotic liver disease (MASLD) progression. This approach supports more scalable studies of liver function, disease progression, and drug responses, advancing the translational relevance of in vitro liver models.

Introduction

An important component of the FDA Modernization Act 2.0 is the elimination of the requirement for animal testing in the drug development process, allowing non-animal experimental data to be used for the evaluation of drug safety and efficacy [1, 2]. The goals of this change are to accelerate the drug development process and to reduce animal testing by promoting the use of non-animal experimental model systems. In further support of this shift, the National Institutes of Health (NIH) also recently announced that it will no longer award funding to grant proposals that rely solely on animal testing studies [3]. Thus, there is increased emphasis on implementing new approach methodologies (NAMs), human-relevant experimental and computational systems designed to replace or reduce animal testing while improving physiological relevance [4, 5]. NAMs include both complex *in vitro* models and *in silico* platforms such as organoids, spheroids, microphysiological systems (MPS), 3D bioprinting, and computational modeling approaches for modeling normal and pathological biological processes in a human-relevant context [6–8]. Human *in vitro* experimental models span a broad range of experimental throughput and biomimetic structure and functionality, including static 2D monocultures, static 3D spheroids and organoids, organoids in MPS, and both single organ and multi-organ coupled MPS [9, 10]. Biomimetic MPS are fluidic devices designed to reproduce key structural and spatial relationships among cells, physiological gradients, matrix environments, mechanical cues, and immune and neural interactions to approximate *in vivo* tissue and organ function [11].

Given the critical role of the liver in metabolism, drug-induced toxicity, and liver disease, numerous liver MPS platforms have been developed by academia and industry to model normal and pathological liver physiology, spanning a wide range of experimental throughput and biological complexity [11–29]. The unique organization of the liver sinusoid creates oxygen and metabolic gradients that drive zone-dependent hepatocyte functions [30–34]. Liver MPS platforms have therefore evolved to incorporate key aspects of liver architecture and function, enabling more biologically relevant modeling of both healthy and diseased liver physiology [10–18, 20–26, 35].

We have implemented a structured, biomimetic liver MPS platform, the liver acinus microphysiological system (LAMPS) (Figure 1) that is constructed with four key human liver cell types including hepatocytes, hepatic stellate cells (LX-2), liver sinusoidal endothelial cells (LSECs), and Kupffer-like cells (THP-1). The LAMPS can be constructed with multiple model configurations including a hybrid configuration consisting of both primary cells and immortalized cell lines, all-primary cells, and induced pluripotent stem cell (iPSC)-derived liver cells [20, 36–39]. The LAMPS is constructed through a combination of sequential cell layering and cell-to-cell self-organization between the 4 liver cell types and uses a single-chamber microfluidic design that supports sustained perfusion at controlled flow rates [37, 40]. This configuration enables maintenance of differential flow conditions that approximate the oxygen tensions characteristic of distinct liver zones (e.g., Zone 1 and Zone 3), allowing zone-dependent hepatocyte functions to be modeled within the same device [20, 37, 40]. The LAMPS includes a large set of phenotypic and molecular, secretome and fixed-endpoint readouts [20, 38, 39] and a database to capture and store the data and experimental metadata, as well as tools to analyze and model the data [41, 42]. A standard approach, the Pittsburgh Reproducibility Protocol (PReP), was developed that uses a set of common statistical metrics in a novel workflow to evaluate intra- and inter-study reproducibility of MPS performance across metrics [43].

The LAMPS has been validated by the National Center for Advancing Translational Sciences (NCATS) funded Tissue Chip Testing Centers (TCTC) and is being qualified as a drug development tool for hepatic clearance and toxicity in collaboration with the FDA as part of the Translational Centers for MPS (TraCe-MPS) program [37, 44, 45]. In addition, the LAMPS is also used as a disease progression and drug testing platform for metabolic dysfunction-associated steatotic liver disease (MASLD) [20, 36, 38, 39], to model the liver tumor microenvironment [46], and to evaluate biologics-induced liver injury [47].

As described above, human *in vitro* experimental models span a continuum of experimental throughput and biomimetic structure and functionality. There remains a need to further develop higher-throughput liver MPS that preserve biological complexity while supporting diverse experimental applications. Although the LAMPS

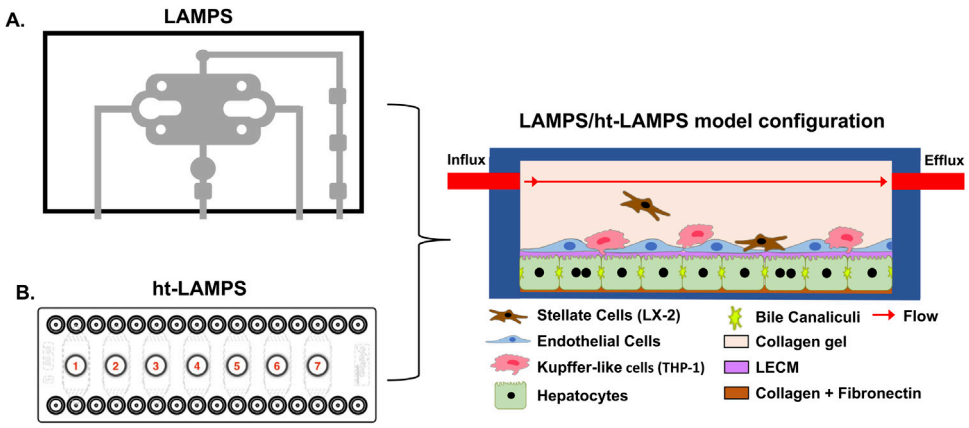

FIGURE 1
The LAMPS and higher throughput LAMPS (ht-LAMPS) platform overview. **(A)** Schematic diagram of the single chamber, PDMS-based Liver Acinus Microphysiological System (LAMPS) with glass bottom culture area. **(B)** Schematic of the higher throughput polystyrene based ht-LAMPS with 7 independent culture chambers. The two devices are constructed with four liver cell types (primary hepatocytes and liver sinusoidal endothelial cells (LSECS), as well as immortalized cell lines for hepatic stellate cells (LX-2) and Kupffer-like cells (THP-1). Both devices are maintained under continuous flow and can be maintained at various oxygen tensions corresponding to different liver zones. Representative 3D visualization of the multicellular architecture is provided in Supplementary Figure 1.

exhibits high model complexity, its current single-chamber configuration limits overall experimental throughput. To address this challenge, we adapted the LAMPS to a commercially available seven-chamber microfluidic device format, thereby increasing throughput while maintaining model complexity. This ht-LAMPS enables more scalable, high-content modeling of both normal and diseased liver physiology for downstream mechanistic and drug response studies. In this report, we demonstrate the reproducibility of ht-LAMPS and illustrate its performance using metabolic dysfunction–associated steatotic liver disease (MASLD) as a representative disease context.

Materials and methods

Cell sources and initial culture

The following lot of commercially available primary human hepatocytes was used in this study: hu8391 (ThermoFisher Scientific). Human liver sinusoidal endothelial cells (LSECs) were purchased from LifeNet Health (NPC-AD-LEC-P1). The THP-1 human monoblast cell line (ATCC, TIB-202) was used to generate Kupffer-like cells and was pretreated 48 h before seeding with 200 ng/mL phorbol 12-myristate 13-acetate (PMA; MilliporeSIgma, 524400) to induce macrophage-like differentiation and inhibit proliferation. Human hepatic stellate cells (LX-2) were obtained from MilliporeSIgma (SCC064). Cell culture conditions were as follows: LSECs: cultured in endothelial cell basal medium-2 (EBM-2; Lonza, CC-3162). THP-1 cells: maintained in suspension in RPMI 1640 (Cytiva, SH30096.FS) with 10% fetal bovine serum (FBS; Corning, MT35010CV), 100 µg/mL penicillin-streptomycin (Cytiva, SV30010), and 2 mM L-glutamine (Cytiva, SH30034.01). LX-2 cells: cultured in DMEM (ThermoFisher Scientific, 11965118) supplemented with 2% FBS, 100 U/mL penicillin, and 100 µg/mL streptomycin [20, 36–38, 40, 46].

LAMPS assembly and maintenance

ht-LAMPS were assembled and maintained as previously described [20, 36–38, 40, 46] except using the Fluidic 557 Reaction Chamber Chip (Microfluidic ChipShop #557). The ht-LAMPS were constructed using four liver cell types at the following cell densities: primary cryopreserved human hepatocytes (ThermoFisher lot hu8391 2.75 × 10^6 cells/mL), primary liver sinusoidal endothelial cells (LifeNet Health; LSECs 1.5 × 10^6 cells/mL), and THP-1 (ATCC; 0.4 × 10^6 cells/mL) and LX-2 (MilliporeSigma; 0.2 × 10^6 cells/mL). The percentages of hepatocytes (56%), THP-1 (18%), LSEC (22%), and LX-2 (4%) cells are consistent with the scaling used in our previously published models. The interior of the devices were coated for 2 h at RT or overnight at 4 °C with 100 µg/mL bovine fibronectin (MilliporeSigma, F1141) and 150 µg/mL rat tail collagen (Corning, 354249) in PBS prior to cell seeding. For all steps involving injection of media and/or cell suspensions into LAMPS devices, 90–100 µL per device was used to ensure complete filling of fluidic pathways and chamber. The devices were then overlayed with 1.5 mg/mL rat tail collagen I (Corning) and maintained with the perfusion of different conditions for 8 days at a flow rate of 5 µL/h to recapitulate zone 3 oxygen tension [38, 40].

Media formulation; normal fasting, early metabolic syndrome, and late metabolic syndrome media

MASLD disease phenotypes in LAMPS were driven using defined media formulations to mimic disease progression from normal fasting (NF) to early metabolic syndrome (EMS) and then late metabolic syndrome (LMS) for 8 days [20, 38]. These media formulations were developed using glucose-free Williams E base medium (ThermoFisher, ME18082L1) supplemented with physiologically relevant levels of glucose (MilliporeSIgma,

G8644), insulin (ThermoFisher, 12585014), and glucagon (MilliporeSIgma and molecular drivers of fibrosis including TGF-β1 (ThermoFisher, PHG9214) and lipopolysaccharide (MilliporeSIgma, L2654). The specific concentrations of all media components used for the NF, EMS, and LMS formulations are provided in Supplementary Table 1.

LipidTOX staining and immunofluorescence

Devices were stained using established protocols [8, 20, 37]. Cells were fixed with 4% paraformaldehyde (ThermoFisher Scientific, AA433689M) in PBS for 30 min, followed by two washes with PBS. For lipid staining, LipidTOX Deep Red Neutral Lipid Stain (1:500; Invitrogen, H34477) was perfused into devices and incubated overnight at 4 °C. For immunofluorescence, chambers were labeled with either rabbit polyclonal anti-cytokeratin 18 (CK-18) antibody (ThermoFisher Scientific, PA5-14263; 1:200) and mouse monoclonal anti-α-smooth muscle actin (αSMA) antibody (Sigma-Aldrich, A2547; 1:100), or with rabbit polyclonal anti-collagen 1A1 (COL1A1) antibody (Proteintech, 14695; 1:100), and incubated overnight at 4 °C. The following day, devices were washed twice with PBS and then incubated for 2 h at room temperature with Alexa Fluor goat anti-rabbit 488 (1:250; Invitrogen, A-11029) and Alexa Fluor goat anti-mouse 568 (1:250; Invitrogen, A-11004) secondary antibodies, along with Hoechst (5 μg/mL; Invitrogen, H1399). Devices were washed three times with PBS prior to imaging.

TMRE and calcein AM staining

Mitochondrial membrane potential was assessed in live LAMPS using tetramethylrhodamine ethyl ester (TMRE; ThermoFisher Scientific, Cat. No. T669). Devices were equilibrated in pre-warmed culture medium containing 100 nM TMRE for 15 min at 37 °C. Following incubation, channels were gently rinsed with fresh medium to remove excess dye and immediately imaged under live-cell conditions using confocal fluorescence microscopy (ex/em = 549/575 nm). For endpoint live cell imaging, cultures were stained with Calcein AM (ThermoFisher C1430) and Hoechst nuclear dye (ThermoFisher 62249). A 1 mg/mL Calcein AM stock solution was prepared in DMSO and diluted 1:1000 in normal fasting medium to yield a final concentration of approximately 1 μM, together with Hoechst (1:2000; ~9 μM final). Following chip disconnection, 50 μL of staining solution was applied to both the inlet and outlet, and chips were incubated for 45 min at 37 °C. Imaging was performed at ×10 magnification using the FITC (Calcein AM) and DAPI (Hoechst) channels.

Confocal imaging and analysis

Imaging was conducted on the Phenix High-Content Imaging system (Revvity) using a 20×/0.4 NA air objective. Z-stacks covering 35 μm depth (5 μm steps) were acquired across 7 × 15 adjacent fields (total area: 44 mm^2; 105 total fields per chamber). All images were collected using consistent exposure and laser power settings to maintain signal intensity within 50–90% of the dynamic range. Image analysis was performed using Harmony software (Revvity, v5.1).

Quantification of calcein-positive cells

Live cell quantification was performed on Day 8 using an automated image analysis workflow implemented in Harmony (PerkinElmer). The analysis utilized the DAPI (nuclear) (ex: 405/em: 435–480) and calcein (live cell) (ex: 488/em: 500–550) fluorescence channels to identify total and live cell populations. Nuclei were segmented using the "Find Nuclei" block set to method M in the Harmony 5.1 software, and calcein-positive regions were detected using optimized intensity thresholding within the "Find Image Region" block. Then nuclei not overlapping with calcein-positive regions were excluded using the "Select Population" block. The percentage of live cells was determined as:

$$\%\,\text{Calcein-positive cells} = \left(\frac{Calcein-positive\,nuclei}{Total\,Hoechst-positive\,nuclei}\right) \times 100$$

Mitochondrial activity quantification (TMRE)

Mitochondrial membrane potential was quantified on Day 8 from TMRE fluorescence images using automated segmentation and intensity-based analysis. Nuclei were first identified using the DAPI channel using the "Find Nuclei" block in the Harmony 5.1 software, and the corresponding perinuclear cytoplasmic regions were defined for each cell using the "Find Surrounding Region" block on method A. TMRE-positive (ex: 561/em: 570–630) signal intensity and area were measured within these regions, and integrated density was calculated as the product of TMRE-positive area and mean fluorescence intensity to represent mitochondrial activity per cell.

LipidTOX staining and quantification

Steatosis was quantified on Day 8 from LipidTOX-stained images using automated segmentation and object detection workflows (Harmony). Nuclei were identified from the DAPI channel, and lipid-positive regions were segmented based on LipidTox fluorescence (ex: 640/em: 650–760). Individual lipid droplets between 5 and 30 μm in diameter were detected and counted. Lipid accumulation was report both in terms of the average number of lipid droplets per cell (total droplets divided by total nuclei) and the mean lipid-positive area per imaging field.

Efflux collection and functional analysis

Albumin (ALB), blood urea nitrogen (BUN), lactate dehydrogenase (LDH), and pro-collagen Iα1 (COL 1A1) levels were assessed as previously described [20, 36, 37, 46]. Efflux from the LAMPS was collected on days 2, 4, 6, and 8 for analysis. ALB levels were quantified using an enzyme-linked immunosorbent assay (ELISA) on 1:100 efflux dilutions with commercial antibodies (Bethyl Laboratories, A80-129A and A80-129P) and an ELISA accessory kit (Bethyl Laboratories, E101), with a human albumin standard prepared in-house (MilliporeSigma, 126658). Secreted COL 1A1 was quantified using the human pro-collagen Iα1 ELISA kit (R&D Systems, cat. no. DY6220-05) in a 1:50 efflux dilution. BUN levels were determined using the Stanbio

BUN Liquid Reagent for Diagnostic Set (Stanbio Laboratory, cat. no. SB-0580–250), while LDH levels were assessed using the CytoTox 96 Non-Radioactive Cytotoxicity Assay (Promega, cat. no. G1780). The BUN and LDH assays were adapted to a 384-well microplate format without efflux dilution.

Multiplex immunoassays

The levels of IL-6, IL-8, and MCP-1 were determined in efflux collected on Day 8 using a custom version of the Human XL Cytokine Performance Panel (R&D systems). Assays were completed according to the manufacturer's instructions at The University of Pittsburgh Cancer Proteomics Facility Luminex® Core Laboratory on the xMAP platform.

Oxygen tension modeling and validation

Oxygen tension was quantified in the ht-LAMPS as previously described [10, 16, 40] and validated via ratio imaging using oxygen-sensitive and oxygen-insensitive fluorescent beads. Oxygen supply in the sealed microfluidic LAMPS device was modeled to determine the flow rate required to achieve target oxygen tension. Using a 3D COMSOL Multiphysics model (v5.2a) [10, 16, 40], flow was described by Brinkman equations through the ECM and cell layer, and oxygen transport/consumption was modeled using the "transport of diluted species" module with a maximum primary hepatocyte OCR of 450 pmol s^{-1} 10^6 $cells^{-1}$. The model predicted that 5 μL h^{-1} would maintain 6–8% oxygen tension, which was confirmed experimentally with oxygen-sensitive beads (Bangs Laboratories). PdTFPP-loaded oxygen-sensitive beads (ex/em 405/706 nm) and polystyrene oxygen-insensitive beads (Bangs Laboratories) (ex/em 405/455 nm) were obtained from Bangs Laboratories and prepared as previously described [10, 16, 40]. Validation was performed in simplified ht-LAMPS containing only hepatocytes and the bead mixture. This configuration was used to isolate the dominant oxygen-consuming hepatocyte cell population [48, 49] and enable controlled calibration of the bead-based oxygen measurements. At the seeding ratios used here, hepatocytes are the primary drivers of oxygen consumption in the system, and prior experimental and computational studies support hepatocyte-driven oxygen gradients under these conditions. Chips were pre-treated with ECM overnight, seeded with hepatocytes, and incubated for 4 h. The bead mixture were added in LECM and allowed to settle overnight. Chips were overlaid with collagen, polymerized after 4 h, and perfused at 5 μL/h in NFM (18% dissolved oxygen) for 7 days. Imaging was performed using the IN-Cell Analyzer 6000. Calibration was done using the same chips: Max O_2 (18%): Achieved by increasing flow to 50 μL/h. Min O_2 (0%): Achieved by adding 200 μg/mL glucose oxidase (MilliporeSigma) to the media. Final oxygen tension was determined as ratio between the oxygen sensitive and insensitive beads [40].

Statistical analysis

For comparisons between two groups, the student's t-test with Welch's Correction was used, while multigroup comparisons used a One-Way ANOVA with Tukey's test for multiple comparisons. For all statistical analyses, a p-value of 0.05 was used as criteria for statistical significance. Reproducibility analysis was assessed using the Eve Analytics™ platform following the Pittsburgh Reproducibility Protocol (PReP) [43]. Intraclass correlation coefficient (ICC) was used to assess both intra- and inter-study reproducibility over time for the efflux metrics. Model performance reproducibility was classified as: Excellent: ICC ≥0.8 Acceptable: 0.2 ≤ ICC <0.8 Poor: ICC <0.2. The coefficient of variation (CV) was used to assess the reproducibility of the single time point measurements model performance reproducibility was classified as: Excellent: CV ≤ 5%; Acceptable: 5% ≤ CV < 20%; Poor: CV ≥ 20%.

Results

Development of a higher-throughput liver acinus microphysiological system (ht-LAMPS)

To increase experimental throughput while preserving the biological complexity of the original LAMPS platform, the single-chamber device (Figure 1A) was adapted to a commercially available seven-chamber microfluidic format (Figure 1B). The resulting higher-throughput LAMPS (ht-LAMPS) maintains the same layered, multicellular architecture as the original LAMPS, as confirmed by 3D imaging of cell-type distribution within the device using CellTracker labeling (Supplementary Figure 1), and supports continuous perfusion under flow conditions corresponding to Zone 1 and Zone 3 oxygen tensions. Each chamber functions as an independent model, enabling parallel experimental conditions within a single device. This configuration increases experimental capacity while using the same cell composition, media formulations, and perfusion parameters established for the standard LAMPS platform.

Oxygen zonation modeling and validation

A key functional feature of the LAMPS platform is the ability to reproduce hepatic zonation through controlled oxygen tension through defined media flow conditions [19, 31, 46]. Computer Solutions (COMSOL) modeling was used to estimate the perfusion rates required to achieve zone-specific oxygen levels in the ht-LAMPS platform (Figure 2A) [19, 31, 46]. Liver zonation was induced in ht-LAMPS by modulating oxygen tension through controlled perfusion rates. COMSOL simulations predicted that a flow rate of 5 μL/h produces zone 3–like oxygen tension (~6% O_2), whereas 15 μL/h yields zone 1–like oxygen tension (~15% O_2) (Figure 2A).

These predictions were validated experimentally using oxygen-sensitive beads in hepatocyte-containing chips, which serve as a simplified model for the full system given the dominant contribution of hepatocytes to oxygen consumption [16, 40, 48, 49], with oxygen levels quantified by ratiometric imaging based on the ratio of oxygen-sensitive to oxygen-insensitive fluorescence intensity (Figure 2B; $p < 0.0001$, $n = 21$chambers) [19, 31, 46]. In addition, ht-LAMPS model viability under both oxygen conditions was comparable after 8 days of culture under flow, as

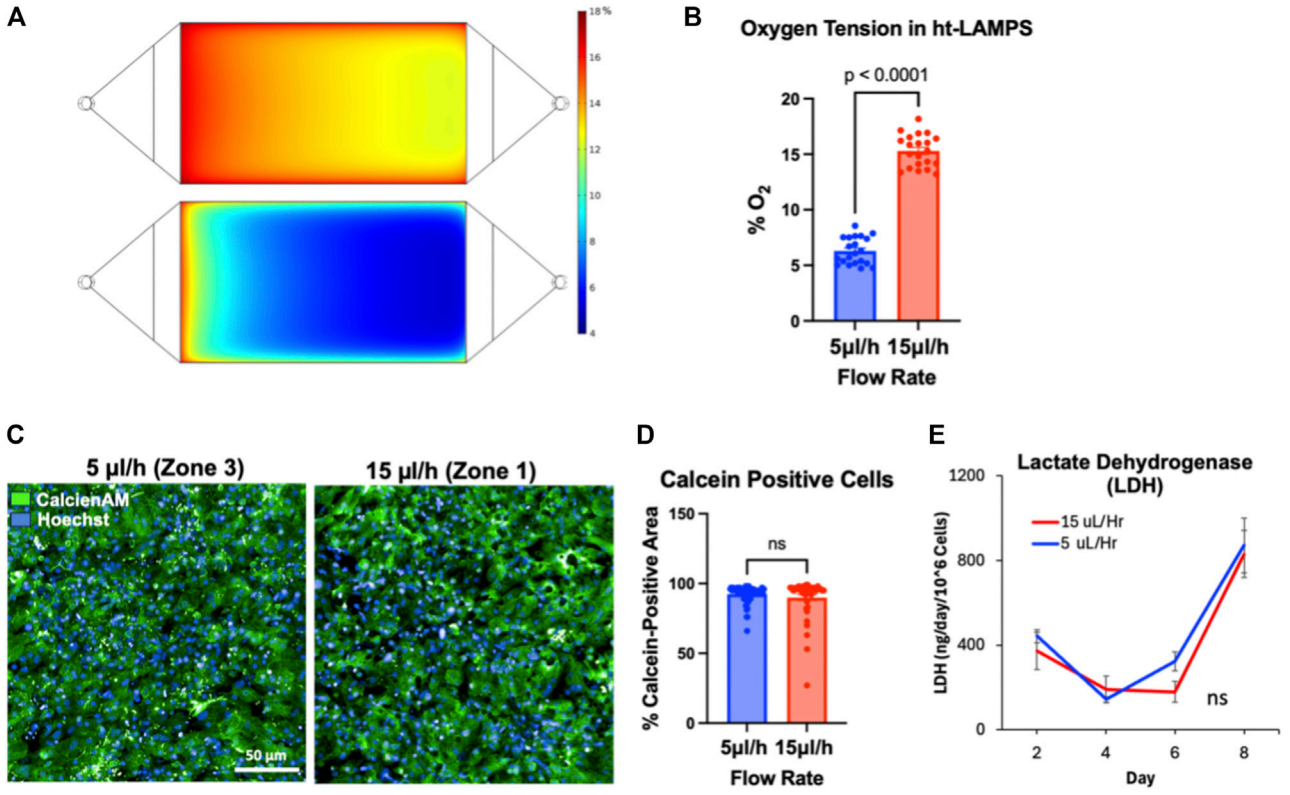

FIGURE 2
Validation of oxygen tension, viability, and cytotoxicity in ht-LAMPS. **(A)** COMSOL modeling predicted oxygen tension profiles in ht-LAMPS at perfusion rates of 5 µL/h (Zone 3) and 15 µL/h (Zone 1). **(B)** Experimental quantification using oxygen-sensitive beads in hepatocyte-only ht-LAMPS confirmed significantly higher oxygen levels at 15 µL/h (~15% O_2) compared with 5 µL/h (~6% O_2) ($p < 0.0001$, n = 21 chambers). **(C)** Representative fluorescence images of ht-LAMPS after 8 days under flow show calcein-positive viable cells and Hoechst-labeled nuclei (20x; scale bar = 50 µm). **(D)** Quantification on Day 8 of calcein-positive area demonstrated no significant difference in model viability between Zone 1– and Zone 3–like flow conditions after 8 days in culture (n = 21 chambers). **(E)** Lactate dehydrogenase (LDH) secretion did not differ significantly between zones, indicating comparable cytotoxicity under both oxygen conditions (one-way ANOVA; n = 21 chambers). Data are presented as mean ± SEM.

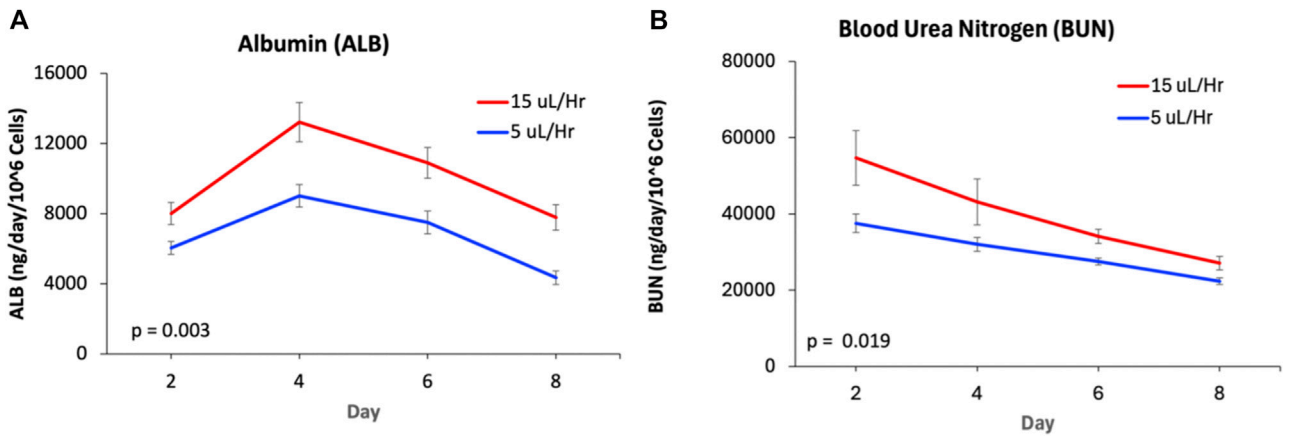

FIGURE 3
Zone-specific differences in albumin and blood urea nitrogen secretion are recapitulated in ht-LAMPS. Albumin (ALB) and blood urea nitrogen (BUN) secretion were quantified over an 8-day time course in ht-LAMPS maintained under perfusion rates of 15 µL/h (Zone 1) or 5 µL/h (Zone 3). ht-LAMPS maintained at 15 µL/h exhibited significantly higher ALB **(A)** and BUN **(B)** secretion compared with those maintained at 5 µL/h (one-way ANOVA: ALB, $p = 0.003$, n = 21 chambers; BUN, $p = 0.019$, n = 21 chambers). Data are presented as mean ± SEM.

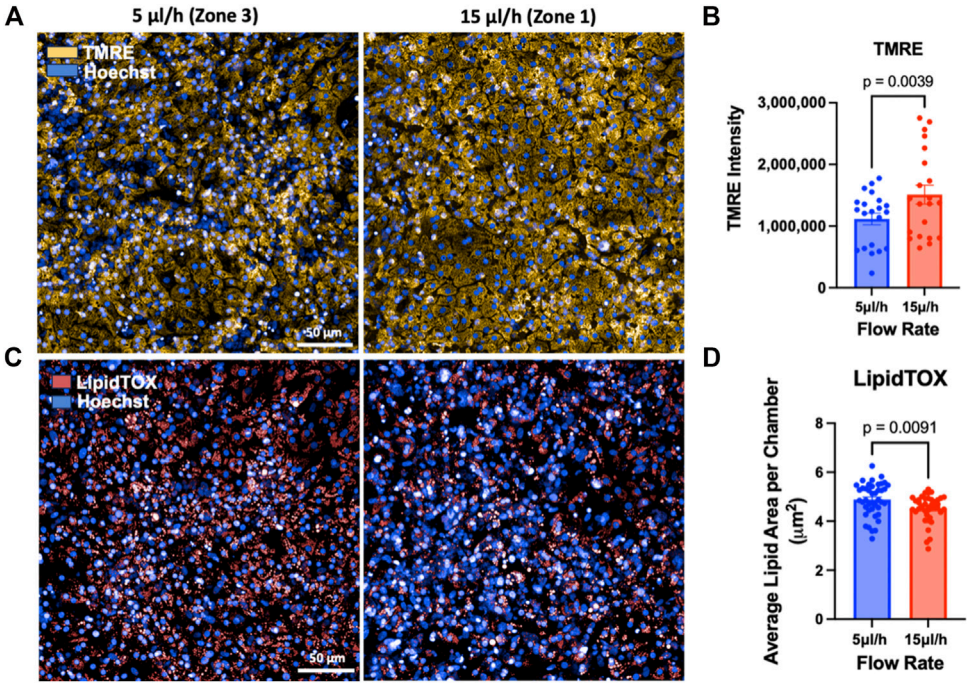

FIGURE 4
Zone-specific differences in mitochondrial activity and steatosis in ht-LAMPS. Representative Day 8 fluorescence images **(A)** and quantification **(B)** of tetramethylrhodamine ethyl ester (TMRE) staining demonstrate significantly higher mitochondrial activity in Zone 1–like ht-LAMPS compared with Zone 3–like conditions (20×; scale bar = 50 µm; p = 0.0039, n = 21 chambers). Representative images **(C)** and quantification **(D)** of LipidTOX staining demonstrate significantly greater lipid accumulation in Zone 3–like ht-LAMPS compared with Zone 1–like conditions (20x; scale bar = 50 µm; p = 0.0091, n = 21 chambers). Data are presented as mean ± SEM.

assessed by Calcein AM staining, with no significant difference in the percentage of Calcein-positive cells (Figures 2C,D; n.s., n = 21 chambers) nor in lactate dehydrogenase (LDH) secretion, a marker of cytotoxicity (Figure 2E; n.s., n = 21chambers). Together, these data confirm that stable, zone-specific oxygen conditions can be established in ht-LAMPS without adverse effects on model viability or cytotoxicity.

Functional validation of hepatic zonation

Oxygen gradients across the liver lobule drive zonation-dependent differences in hepatocyte function and protein secretion [16, 31, 40, 50]. To evaluate whether the ht-LAMPS recapitulates zone-specific hepatocyte functions, effluent media were collected and analyzed for albumin and urea nitrogen as indicators of hepatocyte secretory and metabolic activity. Consistent with clinical observations [51], albumin secretion was significantly higher in Zone 1 than in Zone 3 throughout the experimental time course (Days 2–8) (Figure 3A; p = 0.003, n = 21chambers). Similarly, urea nitrogen secretion was significantly greater in Zone 1 ht-LAMPS compared with Zone 3 over the same period (Figure 3B; p = 0.019, n = 21 chambers), consistent with zonation-dependent secretion patterns previously reported for *in vivo* human liver and the LAMPS platform [20, 38, 40, 52].

To further assess zonation-dependent phenotypes, mitochondrial activity and steatosis, which are known to differ by liver zone [24, 46, 53], were quantified in ht-LAMPS maintained at Zone 1 or Zone 3 flow rates for 8 days. Tetramethylrhodamine ethyl ester (TMRE) staining intensity was significantly higher in Zone 1 ht-LAMPS compared with Zone 3 on Day 8 (Figures 4A,B; p = 0.0039, n = 21 chambers), consistent with increased mitochondrial activity in Zone 1 [40]. In contrast, lipid accumulation, assessed using the neutral lipid dye LipidTOX, was significantly greater in Zone 3 ht-LAMPS than in Zone 1 on Day 8 (Figures 4C,D; p = 0.0091, n = 21 chambers), consistent with known zone-specific patterns of hepatic steatosis and with our prior LAMPS-based studies [20, 40, 54]. Together, these results demonstrate that ht-LAMPS reproduces physiologically relevant, zone-specific functional phenotypes consistent with those previously observed in the LAMPS platform [20, 40].

ht-LAMPS demonstrates reproducibility across multiple assay metrics

Reproducibility was assessed in the ht-LAMPS for the experimental metrics used to generate Figures 2–4 using the Pittsburgh Reproducibility Protocol (PReP) [43] in combination with the EveAnalytics™ platform [41, 42]. Multi–time point metrics (albumin, urea nitrogen, and lactate dehydrogenase as well as single–time point metrics collected on Day 8 (Calcein AM, TMRE, and LipidTOX) were analyzed to quantify both intra- and inter-study reproducibility (Table 1). For multi–time point metrics, intraclass correlation coefficients (ICC) indicated strong intra- and inter-study reproducibility for albumin and urea nitrogen secretion. In contrast, LDH exhibited poor inter-study reproducibility overall, although intra-study reproducibility was

TABLE 1 **ht-LAMPS demonstrate intra- and inter-study reproducibility across multiple key metrics.**

Metric	Flow rate (μL/hr)	Intra-study reproducibility											
		Study 1			Study 2			Study 3			Inter-study reproducibility		
		Metric	Value	Status	Metric	Value	Status	Metric	Value	Status	Metric	Value	Status
Albumin	15	ICC	0.35	Acceptable	ICC	0.29	Acceptable	ICC	0.42	Acceptable	ICC	0.58	Acceptable
	5	ICC	0.2	Acceptable	ICC	0.55	Acceptable	ICC	0.49	Acceptable	ICC	0.83	Excellent
BUN	15	ICC	0.07	Poor	ICC	0.64	Acceptable	ICC	0.44	Acceptable	ICC	0.86	Excellent
	5	ICC	0.26	Acceptable	ICC	0.63	Acceptable	ICC	0.39	Acceptable	ICC	0.81	Excellent
LDH	15	ICC	0.71	Acceptable	ICC	0.05	Poor	ICC	0.66	Acceptable	ICC	−0.05	Poor
	5	ICC	0.82	Excellent	ICC	0.61	Acceptable	ICC	0.5	Acceptable	ICC	0.11	Poor
Calcein	15	CV	7.11	Acceptable	CV	13.41	Acceptable	CV	3.37	Excellent	CV	1.17	Excellent
	5	CV	7.7	Acceptable	CV	2.54	Excellent	CV	4.66	Excellent	CV	1.68	Excellent
TMRE	15	CV	23.17	Poor	CV	22.6	Poor	CV	11.75	Acceptable	CV	15.7	Acceptable
	5	CV	66.35	Poor	CV	26.5	Poor	CV	51.21	Poor	CV	17.3	Acceptable
LipidTOX	15	CV	8.81	Acceptable	CV	14.47	Acceptable	CV	5.36	Acceptable	CV	3.623	Excellent
	5	CV	12.67	Acceptable	CV	7.94	Acceptable	CV	7.26	Acceptable	CV	13.03	Acceptable

For multi-time point measurements model reproducibility was classified as: Excellent: ICC ≥0.8; acceptable: 0.2 ≤ ICC <0.8; poor: ICC <0.2. For single time point measurements model reproducibility was classified as: Excellent: CV ≤ 5%; acceptable: 5% ≤ CV < 20%; poor: CV ≥ 20%.

10.3389/ebm.2026.11038

generally acceptable except for Study 2. For single–time point metrics (Day 8), coefficients of variation (CV) indicated high inter-study reproducibility for Calcein AM, TMRE, and LipidTOX measurements. Calcein AM and LipidTOX also showed high intra-study reproducibility, while TMRE exhibited greater variability within individual studies. Together, these results indicate that ht-LAMPS exhibits reproducible performance for several key functional and phenotypic assay metrics, while also revealing greater variability in selected readouts, including LDH and TMRE. Notably, TMRE measurements showed higher intra-study variability but consistent directional trends across studies, whereas LDH exhibited variability across both intra- and inter-study comparisons. These findings highlight both the strengths of the platform and areas where additional assay optimization may be beneficial.

To directly compare the performance of the ht-LAMPS with the previously published single-chamber LAMPS platform [20, 40, 42, 47], zonation-dependent functional metrics measured at Day 8 were compared across platforms using ht-LAMPS data generated in this study and single-chamber LAMPS datasets from prior studies (Supplementary Table 2; Supplementary Figure 2). Supplementary Figure 2 shows these comparisons, allowing for the visualization of the zonation-dependent trends wthin each platform. Ratios of Zone 3 to Zone 1 responses for albumin, urea nitrogen, mitochondrial activity (TMRE), and steatosis (LipidTOX) showed consistent directional trends between the two platforms. Across these metrics, ht-LAMPS recapitulated key zone-specific patterns previously observed in the single-chamber LAMPS, including higher metabolic activity in Zone 1 and increased steatosis in Zone 3. While these comparisons are not derived from fully matched head-to-head experiments, they indicate that scaling the LAMPS setup to a multi-chamber format recapitulates key zonation-dependent functional relationships for the metrics evaluated in this study.

ht-LAMPS recapitulates key MASLD-associated phenotypes

We have previously developed and published a series of media formulations, normal fasting media (NF), early metabolic syndrome media (EMS), and late metabolic syndrome media (LMS), to experimentally model lifestyle-driven progression of MASLD (Supplementary Figure 1) [20, 38]. These formulations were designed based on clinical blood chemistries and have been used to characterize multiple MASLD-associated phenotypes, including steatosis, secretion of pro-inflammatory cytokines, and pro-collagen 1α1 (COL 1A1) in the LAMPS platform.

To determine whether the ht-LAMPS recapitulates these MASLD-associated phenotypes, models were cultured in NF, EMS, and LMS media (Supplementary Figure 1) and evaluated on Day 8. Because MASLD-associated injury and lipid accumulation are most pronounced in the pericentral (Zone 3) region of the liver [53, 55], ht-LAMPS were maintained under Zone 3–like flow conditions, consistent with the experimental design used in our previous MASLD studies with the LAMPS platform [20, 36, 38]. Both EMS and LMS media induced significantly greater lipid accumulation compared with NF media (Figure 5A; $p < 0.0001$, n = 7 chambers). In parallel, secretion of inflammatory cytokines increased under disease-inducing conditions, with IL-6 showing a significant elevation in the LMS condition relative to NF (Figure 5B; $p = 0.0001$, n = 7 chambers). CCL2 and IL-8 also exhibited increasing trends in the LMS condition compared with NF (Figure 5B). These cytokines (IL-6, IL-8, and CCL2) were selected as representative inflammatory mediators based on their established roles in MASLD progression and hepatic inflammatory responses [56, 57], and their use in prior LAMPS studies [20, 36, 38]. In addition, secretion of the pro-fibrotic marker COL 1A1 increased in a stepwise manner from EMS to LMS (Figure 5D; $p < 0.0001$, n = 7 chambers). Complementing these efflux-based measurements, immunofluorescence imaging of ht-LAMPS (Figure 5C) demonstrated increased expression of α-smooth muscle actin (αSMA) and COL1A1 under EMS and LMS conditions relative to NF. These data provide cell-associated evidence of increased stellate cell–associated and fibrogenic marker expression under disease-inducing conditions.

To assess whether MASLD-associated phenotypes observed in ht-LAMPS are consistent with those previously reported in the single-chamber LAMPS [20, 36, 38], disease-response metrics measured at Day 8 were compared between platforms under matched media conditions (Supplementary Table 3). Both platforms exhibited similar increases in steatosis and secretion of the pro-fibrotic marker COL 1A1 in response to EMS and LMS media, indicating preserved induction of key metabolic and fibrotic MASLD progression phenotypes in the ht-LAMPS configuration. Cytokine responses were also broadly comparable between platforms under LMS conditions, with both systems showing increased IL-6 secretion and increasing trends in CCL2 and IL-8. While cytokine induction under EMS conditions was attenuated in ht-LAMPS relative to the single-chamber LAMPS, the overall pattern of MASLD-associated metabolic, fibrotic, and inflammatory responses was consistent between platforms.

Discussion

In this study, we demonstrate that our previously established, high-content liver MPS, the liver acinus microphysiological system (LAMPS) [11, 20, 36–40, 46], can be adapted from a single-chamber format to a multi-chamber (7 chambers per chip) configuration while recapitulating its key physiological and functional characteristics. The higher-throughput LAMPS (ht-LAMPS), compared to the original single-chamber device, maintained controlled oxygen zonation, reproduced zone-dependent hepatocyte functions, and recapitulated key MASLD progression phenotypes, including steatosis, inflammatory cytokine secretion, and pro-fibrotic marker production. Across these readouts, ht-LAMPS exhibited reproducible performance for several key metrics (Table 1) and recapitulated key biological features previously observed in the single-chamber LAMPS platform for the metrics evaluated in this study [20, 37, 38, 40, 45]. Despite differences in device design, material properties, and chamber configuration, the same underlying biological system produced broadly similar functional, metabolic, and disease-associated phenotypes in both the single-chamber LAMPS and the seven-chamber ht-LAMPS formats. The single-chamber LAMPS

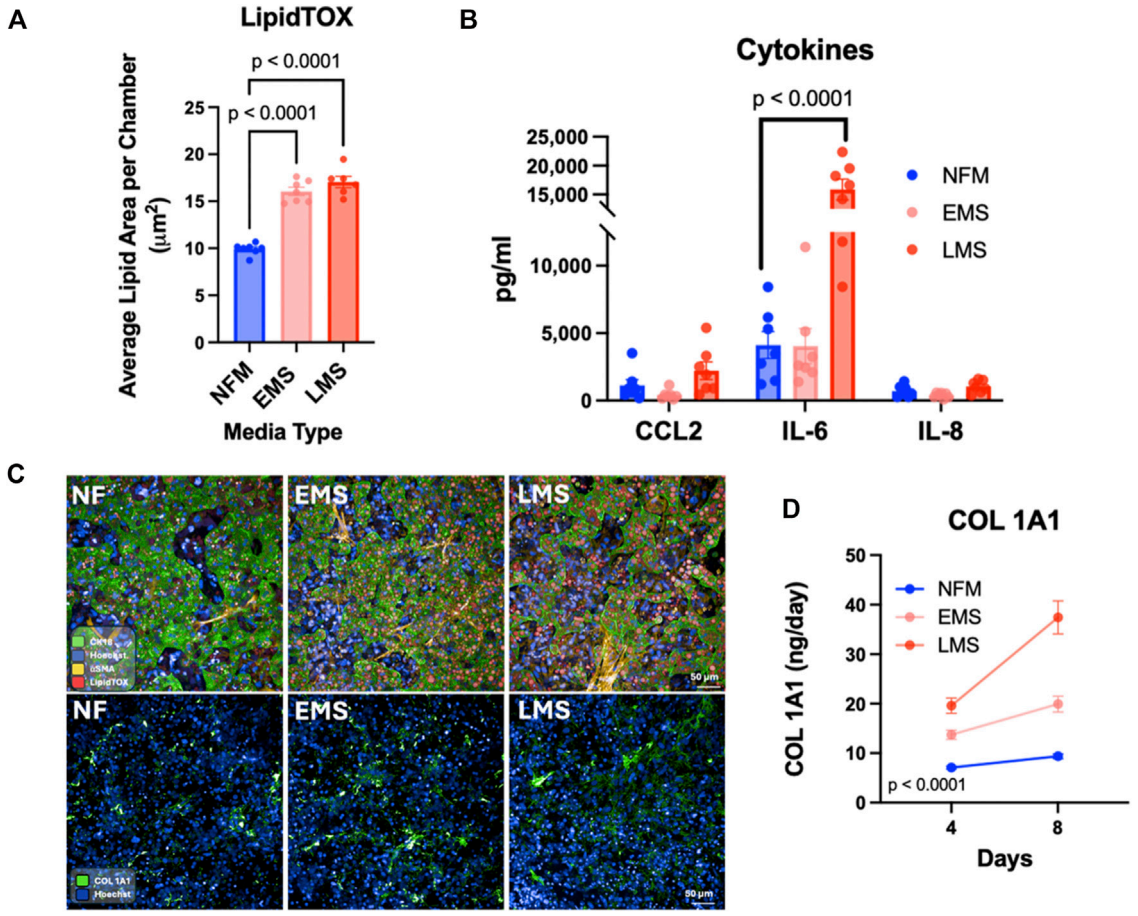

FIGURE 5
ht-LAMPS recapitulates key MASLD-associated phenotypes under disease-inducing media conditions. ht-LAMPS were maintained for 8 days under Zone 3 flow conditions and cultured in normal fasting (NF), early metabolic syndrome (EMS), or late metabolic syndrome (LMS) media formulations previously established to model MASLD progression in the LAMPS platform [20, 36, 38]. **(A)** Steatosis, assessed by LipidTOX staining, was significantly increased in both EMS- and LMS-treated ht-LAMPS compared with NF controls, indicating enhanced steatosis under disease-inducing conditions on Day 8 ($p < 0.0001$, n = 7 chambers). **(B)** Evaluation of inflammatory cytokine secretion showed increased levels across cytokines in the LMS condition compared with NF, with IL-6 exhibiting a statistically significant increase on Day 8 ($p < 0.0001$, n = 7 chambers). **(C)** Representative Day 8 immunofluorescence images demonstrating expression of LipidTOX and α-smooth muscle actin (αSMA; top panels) and collagen 1α1 (COL 1A1; bottom panels) in ht-LAMPS cultured under NF, EMS, and LMS conditions. In the top panels, hepatocytes are labeled with cytokeratin-18 (CK-18) as a marker of hepatocytes. Increased αSMA and COL 1A1 staining is observed under EMS and LMS conditions relative to NF, consistent with increased stellate cell–associated and fibrogenic marker expression. Nuclei are labeled with Hoechst. Scale bars = 50 μm. The spatial organization of hepatocytes (CK-18 and LipidTOX) and stellate cells (αSMA) in ht-LAMPS under these MASLD-inducing conditions is shown in Supplementary Figure 3, which illustrates both cell distribution and disease-associated changes in marker expression. **(D)** Secretion of the pro-fibrotic marker COL 1A1 was significantly elevated in EMS and LMS conditions relative to NF, with a stepwise increase from EMS to LMS on Day 8 (one-way ANOVA; $p < 0.0001$ for both EMS and LMS, n = 7 chambers). Data are presented as mean ± SEM.

employs a square PDMS-based chamber, whereas the ht-LAMPS utilizes a polystyrene device with trapezoidal prism–shaped chambers, and the two platforms also differ substantially in chamber height (approximately 170 μm versus ~700 μm, respectively). Despite these differences in geometry, material composition, and chamber dimensions, controlled oxygen zonation and zone-dependent functional outputs were maintained under the conditions evaluated. Direct cross-platform comparisons demonstrated similar zonation-dependent functional patterns across both platforms, as assessed by metabolic activity, mitochondrial function, and steatosis (Figures 2–4; Supplementary Table 2). Comparisons of MASLD-associated phenotypes further showed that steatosis and pro-fibrotic responses between platforms were similar (Figure 5; Supplementary Table 3), with only modest differences in inflammatory cytokine responses observed under early disease (EMS) conditions. Together, these findings indicate that the biological performance of the LAMPS model is recapitulated across differences in device architecture and material properties, supporting its adaptability for use across distinct microfluidic formats.

Recent advances in liver MPS have increasingly emphasized incorporation of vascular structures, immune components, and multicellular spheroid/organoid designs to better recapitulate aspects of native liver physiology and disease [27–29]. These platforms demonstrate the ability to capture complex cell–cell interactions, including vascular perfusion and immune cell

recruitment, representing important advances in modeling higher-order liver physiology. In this context, ht-LAMPS is designed as a complementary approach that prioritizes controlled zonation, reproducible performance, and longitudinal functional readouts. The platform enables defined and tunable oxygen and flow conditions that reproducibly generate zone-specific phenotypes. In addition, the relatively low perfusion rates support collection of concentrated effluent, enabling sensitive longitudinal analysis of secreted factors, which can be more challenging in higher-flow or highly vascularized systems. Accordingly, ht-LAMPS occupies a distinct position within the current MPS landscape, bridging simplified high-throughput systems and more complex vascularized models, and is particularly well-suited for applications requiring controlled perturbation of metabolic and zonation-dependent processes.

The primary technical advance of this study is a practical increase in experimental throughput while preserving model complexity. Adaptation of LAMPS to a multi-chamber format enables an approximately four-fold increase in experimental capacity relative to the original single-chamber system, while maintaining the established biological architecture, cell composition, and experimental framework of the platform. Across the broader landscape of MPS models, platform selection reflects a balance between throughput and biological complexity that is driven by the specific question and context of use. While higher-throughput liver MPS platforms are employed for various applications [14, 58–62], these often rely on simplified tissue architectures or emphasize different aspects of physiological complexity and control. In this context, the ht-LAMPS represents a meaningful increase in capacity within a human-relevant liver MPS that retains the complexity required for zonated liver function, disease modeling, and downstream mechanistic and therapeutic studies.

The development of ht-LAMPS also aligns with the increasing emphasis on human-based experimental systems in biomedical research. Recent policy and funding initiatives, including the FDA Modernization Act 2.0 and updated NIH guidance, underscore the need for experimentally tractable human-relevant models that complement traditional animal studies and improve the translational relevance of preclinical research [1, 3, 6, 63]. By preserving physiological complexity while increasing experimental capacity, ht-LAMPS contributes to this evolving landscape by providing a human liver MPS with enhanced experimental capacity suitable for disease-relevant mechanistic studies and therapeutic evaluation.

Although the ht-LAMPS represents a meaningful step forward, additional scalability remains an important area for future development of this platform. In addition, future studies will evaluate how varying the number of active chambers within a device influences flow distribution, oxygen gradients, and assay performance, to further define the operating range and scalability of the platform. Further gains in overall model scalability may be achieved through device-level refinements, including increasing chamber number per chip without compromising assay sensitivity, implementing fluidic designs that evenly distribute flow across parallel chambers from a single inlet, miniaturizing culture volumes to enable higher-density layouts, integrating multiplexed real-time sensors to reduce manual sampling, and adopting device formats compatible with the robotic liquid-handling systems used in high-throughput laboratories. In parallel, advances in automation, including bioprinting-based approaches for controlled cell and matrix deposition, could reduce operator time and improve reproducibility; however, because ht-LAMPS is implemented in a closed-chip format, these approaches will need to be adapted for enclosed microfluidic environments. These developments must balance increased scalability with preservation of the spatial organization, flow control, and multicellular interactions that underpin the biological performance of the LAMPS model.

The observed differences in inflammatory cytokine responses between the single-chamber LAMPS and ht-LAMPS under EMS conditions highlight the value of direct cross-platform comparisons. While cytokine responses under LMS conditions were broadly similar between formats, the attenuated response under EMS conditions may reflect differences in the experimental platforms or biological variability, including cell sourcing. These findings motivate future studies to more systematically characterize how experimental design parameters, such as disease stage, chamber format, and cell source, influence inflammatory readouts across device formats.

In summary, this work establishes ht-LAMPS as a more scalable extension of our validated LAMPS platform that recapitulates key physiological and functional characteristics while increasing experimental capacity. The ht-LAMPS maintained controlled oxygen zonation, reproduced zone-dependent hepatocyte functions, and exhibited reproducible performance consistent with the original single-chamber LAMPS. In addition, ht-LAMPS recapitulated core MASLD progression phenotypes, including steatosis, inflammatory cytokine secretion, and pro-fibrotic marker production, supporting its use for downstream mechanistic studies and drug development applications.

Author contributions

Original draft writing: DG, MC, JB, and MM; Review and editing: DG, MC, AW, MV, LV, MS, DT, JB, and MM; Conceptualization: LV, MS, DT, JB, and MM; Investigation: MC, AW, MV, and JB; Data curation: DG and MC; Methodology: DG, MC, and AW; Supervision: JB and MM; Formal analysis: DG, MC, AW, MV, MS, and JB; Validation: DG, MC, AW, MV, and JB; Funding acquisition: LV, MS, DT, and MM; Visualization: DG, MC, AW, LV, and JB. All authors contributed to the article and approved the submitted version.

Data availability

The datasets generated and analyzed during the current study are available from the corresponding author on reasonable request. In addition, the data from experimental studies performed in this work are available at: https://eveanalytics.com/accounts/login/?next=https%3A//eve.eveanalytics.com/assays/assaystudyset/53/.

Ethics statement

Ethical approval was not required for the studies on humans in accordance with the local legislation and institutional requirements because only commercially available established cell lines were used.

Funding

The author(s) declared that financial support was received for this work and/or its publication. We acknowledge the following grants from the National Institutes of Health: S10OD12269 (DT), 5RO1DK135606 (MM), and 1U2CTR004863 (MS, DT, MM, and LV).

Acknowledgements

The authors would like to thank all members of their laboratories for supporting the research efforts reported here. The cytokine data was obtained using the University of Pittsburgh Cancer Institute (UPCI) Cancer Biomarkers Facility: Luminex Core Laboratory.

Conflict of interest

The author(s) declared no potential conflicts of interest with respect to the research, authorship, and/or publication of this article.

Generative AI statement

The author(s) declared that generative AI was not used in the creation of this manuscript.

Any alternative text (alt text) provided alongside figures in this article has been generated by Frontiers with the support of artificial intelligence and reasonable efforts have been made to ensure accuracy, including review by the authors wherever possible. If you identify any issues, please contact us.

Supplementary material

The Supplementary Material for this article can be found online at: https://www.ebm-journal.org/articles/10.3389/ebm.2026.11038/full#supplementary-material

References

1. Ahmed SM, Shivnaraine RV, Wu JC. FDA modernization act 2.0 paves the way to computational biology and clinical trials in a dish. *Circulation* (2023) 148:309–11. doi:10.1161/CIRCULATIONAHA.123.065585

2. Stewart A, Denoyer D, Gao X, Toh YC. The FDA modernisation act 2.0: bringing non-animal technologies to the regulatory table. *Drug Discov Today* (2023) 28:103496. doi:10.1016/j.drudis.2023.103496

3. Gerke S, Balamut J, Wagner JK. The FDA's plan to phase out animal testing. *Trends Biotechnol* (2026). doi:10.1016/j.tibtech.2025.12.011

4. Sewell F, Alexander-White C, Brescia S, Currie RA, Roberts R, Roper C, et al. New approach methodologies (NAMs): identifying and overcoming hurdles to accelerated adoption. *Toxicol Res (Camb)* (2024) 13:tfae044. doi:10.1093/toxres/tfae044

5. Schmeisser S, Miccoli A, von Bergen M, Berggren E, Braeuning A, Busch W, et al. New approach methodologies in human regulatory toxicology - not if, but how and when. *Environ Int* (2023) 178:108082. doi:10.1016/j.envint.2023.108082

6. Han JJ. FDA Modernization Act 2.0 allows for alternatives to animal testing. *Artif Organs* (2023) 47:449–50. doi:10.1111/aor.14503

7. Mansouri M, Lam J, Sung KE. Progress in developing microphysiological systems for biological product assessment. *Lab Chip* (2024) 24:1293–306. doi:10.1039/d3lc00876b

8. Taylor DL, Gough A, Schurdak ME, Vernetti L, Chennubhotla CS, Lefever D, et al. Harnessing human microphysiology systems as key experimental models for quantitative systems pharmacology. *Handbook Experimental Pharmacology* (2019) 260:327–67. doi:10.1007/164_2019_239

9. Ingber DE. Human organs-on-chips for disease modelling, drug development and personalized medicine. *Nat Rev Genet* (2022) 23:467–91. doi:10.1038/s41576-022-00466-9

10. Aleman J, Wiegand C, Schurdak ME, Vernetti L, Gavlock D, Reese C, et al. A metabolic dysfunction-associated steatotic liver acinus biomimetic induces pancreatic islet dysfunction in a coupled microphysiology system. *Commun Biol* (2024) 7:1317. doi:10.1038/s42003-024-07006-7

11. Gough A, Soto-Gutierrez A, Vernetti L, Ebrahimkhani MR, Stern AM, Taylor DL. Human biomimetic liver microphysiology systems in drug development and precision medicine. *Nat Reviews Gastroenterol & Hepatology* (2021) 18:252–68. doi:10.1038/s41575-020-00386-1

12. Feaver RE, Cole BK, Lawson MJ, Hoang SA, Marukian S, Blackman BR, et al. Development of an *in vitro* human liver system for interrogating nonalcoholic steatohepatitis. *JCI Insight* (2016) 1:e90954. doi:10.1172/jci.insight.90954

13. Kermanizadeh A, Valli J, Sanchez K, Hutter S, Pawlowska A, Whyte G, et al. Particulate and drug-induced toxicity assessed in novel quadruple cell human primary hepatic disease models of steatosis and pre-fibrotic NASH. *Arch Toxicol* (2022) 96:287–303. doi:10.1007/s00204-021-03181-2

14. Kostrzewski T, Snow S, Battle AL, Peel S, Ahmad Z, Basak J, et al. Modelling human liver fibrosis in the context of non-alcoholic steatohepatitis using a microphysiological system. *Commun Biol* (2021) 4:1080. doi:10.1038/s42003-021-02616-x

15. Kukla DA, Khetani SR. Bioengineered liver models for investigating disease pathogenesis and regenerative medicine. *Semin Liver Dis* (2021) 41:368–92. doi:10.1055/s-0041-1731016

16. Li X, George SM, Vernetti L, Gough AH, Taylor DL. A glass-based, continuously zonated and vascularized human liver acinus microphysiological system (vLAMPS) designed for experimental modeling of diseases and ADME/TOX. *Lab Chip* (2018) 18:2614–31. doi:10.1039/c8lc00418h

17. Liu JS, Madruga LYC, Yuan Y, Kipper MJ, Khetani SR. Decellularized liver nanofibers enhance and stabilize the long-term functions of primary human hepatocytes *in vitro*. *Adv Healthc Mater* (2023) 12:e2202302. doi:10.1002/adhm.202202302

18. Ouchi R, Togo S, Kimura M, Shinozawa T, Koido M, Koike H, et al. Modeling steatohepatitis in humans with pluripotent stem cell-derived organoids. *Cell Metab* (2019) 30:374–84. doi:10.1016/j.cmet.2019.05.007

19. Qi L, Matsuo K, Pereira A, Lee YT, Zhong F, He Y, et al. Human iPSC-Derived proinflammatory macrophages cause insulin resistance in an isogenic white adipose tissue microphysiological system. *Small* (2023) 19:e2203725. doi:10.1002/smll.202203725

20. Saydmohammed M, Jha A, Mahajan V, Gavlock D, Shun TY, DeBiasio R, et al. Quantifying the progression of non-alcoholic fatty liver disease in human biomimetic liver microphysiology systems with fluorescent protein biosensors. *Exp Biol Med (Maywood)* (2021) 246:2420–41. doi:10.1177/15353702211009228

21. Slaughter VL, Rumsey JW, Boone R, Malik D, Cai Y, Sriram NN, et al. Validation of an adipose-liver human-on-a-chip model of NAFLD for preclinical therapeutic efficacy evaluation. *Sci Rep* (2021) 11:13159. doi:10.1038/s41598-021-92264-2

22. Strobel S, Kostadinova R, Fiaschetti-Egli K, Rupp J, Bieri M, Pawlowska A, et al. A 3D primary human cell-based *in vitro* model of non-alcoholic steatohepatitis for efficacy testing of clinical drug candidates. *Sci Rep* (2021) 11:22765. doi:10.1038/s41598-021-01951-7

23. Telles-Silva KA, Pacheco L, Komatsu S, Chianca F, Caires-Junior LC, Araujo BHS, et al. Applied hepatic bioengineering: modeling the human liver using organoid and Liver-on-a-Chip technologies. *Front Bioeng Biotechnol* (2022) 10:845360. doi:10.3389/fbioe.2022.845360

24. Wang Y, Wang H, Deng P, Tao T, Liu H, Wu S, et al. Modeling human nonalcoholic fatty liver disease (NAFLD) with an Organoids-on-a-Chip system. *ACS Biomater Sci Eng* (2020) 6:5734–43. doi:10.1021/acsbiomaterials.0c00682

25. Yang J, Hirai Y, Iida K, Ito S, Trumm M, Terada S, et al. Integrated-gut-liver-on-a-chip platform as an *in vitro* human model of non-alcoholic fatty liver disease. *Commun Biol* (2023) 6:310. doi:10.1038/s42003-023-04710-8

26. Yuan Y, Cotton K, Samarasekera D, Khetani SR. Engineered platforms for maturing pluripotent stem cell-derived liver cells for disease modeling. *Cell Mol Gastroenterol Hepatol* (2023) 15:1147–60. doi:10.1016/j.jcmgh.2023.01.013

27. Bonanini F, Dinkelberg R, Torregrosa MC, Kortekaas N, Hagens TMS, Treillard S, et al. A microvascularizedin vitroliver model for disease modeling and drug discovery. *Biofabrication* (2024) 17 (1). doi:10.1088/1758-5090/ad818a

28. Tevonian EN, Kan EL, Maniar KK, Wang AJ, Datta A, Kamm RD, et al. A vascularized liver microphysiological system captures key features of hepatic insulin resistance and monocyte infiltration. *Nat Commun* (2026) 17:950. doi:10.1038/s41467-025-68031-6

29. Wesseler MF, Taebnia N, Harrison S, Youhanna S, Preiss LC, Kemas AM, et al. 3D microperfusion of mesoscale human microphysiological liver models improves functionality and recapitulates hepatic zonation. *Acta Biomater* (2023) 171:336–49. doi:10.1016/j.actbio.2023.09.022

30. Beckwitt CH, Clark AM, Wheeler S, Taylor DL, Stolz DB, Griffith L, et al. Liver 'organ on a chip. *Exp Cell Res* (2018) 363:15–25. doi:10.1016/j.yexcr.2017.12.023

31. Colnot S, Perret C. Liver zonation. In: Monga S, editor. *Molecular Pathology of Liver Diseases*. Boston, MA: Springer (2011).

32. Rui L. Energy metabolism in the liver. *Compr Physiol* (2014) 4:177–97. doi:10.1002/cphy.c130024

33. Soto-Gutierrez A, Gough A, Vernetti LA, Taylor DL, Monga SP. Pre-clinical and clinical investigations of metabolic zonation in liver diseases: the potential of microphysiology systems. *Exp Biol Med (Maywood)* (2017) 242:1605–16. doi:10.1177/1535370217707731

34. Trefts E, Gannon M, Wasserman DH. The liver. *Curr Biol* (2017) 27:R1147–R51. doi:10.1016/j.cub.2017.09.019

35. Qi L, Zushin PH, Chang CF, Lee YT, Alba DL, Koliwad SK, et al. Probing insulin sensitivity with metabolically competent human stem cell-derived white adipose tissue microphysiological systems. *Small* (2022) 18:e2103157. doi:10.1002/smll.202103157

36. Lefever DE, Miedel MT, Pei F, DiStefano JK, Debiasio R, Shun TY, et al. A quantitative systems pharmacology platform reveals NAFLD pathophysiological states and targeting strategies. *Metabolites* (2022) 12:528. doi:10.3390/metabo12060528

37. Vernetti LA, Senutovitch N, Boltz R, DeBiasio R, Shun TY, Gough A, et al. A human liver microphysiology platform for investigating physiology, drug safety, and disease models. *Exp Biol Med (Maywood)* (2016) 241:101–14. doi:10.1177/1535370215592121

38. Xia M, Varmazyad M, Pla-Palacin I, Gavlock DC, DeBiasio R, LaRocca G, et al. Comparison of wild-type and high-risk PNPLA3 variants in a human biomimetic liver microphysiology system for metabolic dysfunction-associated steatotic liver disease precision therapy. *Front Cell Dev Biol* (2024) 12:1423936. doi:10.3389/fcell.2024.1423936

39. Miedel MT, Schurdak ME, Stern AM, Soto-Gutierrez A, Strobl EV, Behari J, et al. Integrated patient digital and biomimetic twins for precision medicine: a perspective. *Semin Liver Dis* (2025) 45:458–75. doi:10.1055/a-2649-1560

40. Lee-Montiel FT, George SM, Gough AH, Sharma AD, Wu J, DeBiasio R, et al. Control of oxygen tension recapitulates zone-specific functions in human liver microphysiology systems. *Exp Biol Med (Maywood)* (2017) 242:1617–32. doi:10.1177/1535370217703978

41. Gough A, Vernetti L, Bergenthal L, Shun TY, Taylor DL. The microphysiology systems database for analyzing and modeling compound interactions with human and animal organ models. *Appl In Vitro Toxicol* (2016) 2:103–17. doi:10.1089/aivt.2016.0011

42. Schurdak M, Vernetti L, Bergenthal L, Wolter QK, Shun TY, Karcher S, et al. Applications of the microphysiology systems database for experimental ADME-tox and disease models. *Lab Chip* (2020) 20:1472–92. doi:10.1039/c9lc01047e

43. Miedel MT, Varmazyad M, Xia M, Brooks MM, Gavlock DC, Reese C, et al. Validation of microphysiological systems for interpreting patient heterogeneity requires robust reproducibility analytics and experimental metadata. *Cell Rep Methods* (2025) 5:101028. doi:10.1016/j.crmeth.2025.101028

44. Sakolish C, Luo YS, Valdiviezo A, Vernetti LA, Rusyn I, Chiu WA. Prediction of hepatic drug clearance with a human microfluidic four-cell liver acinus microphysiology system. *Toxicology* (2021) 463:152954. doi:10.1016/j.tox.2021.152954

45. Vernetti LA, Vogt A, Gough A, Taylor DL. Evolution of experimental models of the liver to predict human drug hepatotoxicity and efficacy. *Clin Liver Dis* (2017) 21:197–214. doi:10.1016/j.cld.2016.08.013

46. Miedel MT, Gavlock DC, Jia S, Gough A, Taylor DL, Stern AM. Modeling the effect of the metastatic microenvironment on phenotypes conferred by estrogen receptor mutations using a human liver microphysiological system. *Sci Rep* (2019) 9:8341. doi:10.1038/s41598-019-44756-5

47. Beaudoin JJ, Clemens L, Miedel MT, Gough A, Zaidi F, Ramamoorthy P, et al. The combination of a human biomimetic liver microphysiology system with BIOLOGXsym, a quantitative systems toxicology (QST) modeling platform for macromolecules, provides mechanistic understanding of Tocilizumab- and GGF2-Induced liver injury. *Int J Mol Sci* (2023) 24:9692. doi:10.3390/ijms24119692

48. Haque A, Gheibi P, Gao Y, Foster E, Son KJ, You J, et al. Cell biology is different in small volumes: endogenous signals shape phenotype of primary hepatocytes cultured in microfluidic channels. *Sci Rep* (2016) 6:33980. doi:10.1038/srep33980

49. Nishikawa M, Ito H, Tokito F, Hirono K, Inamura K, Scheidecker B, et al. Accurate evaluation of hepatocyte metabolisms on a noble oxygen-permeable material with low sorption characteristics. *Front Toxicol* (2022) 4:810478. doi:10.3389/ftox.2022.810478

50. Gebhardt R, Matz-Soja M. Liver zonation: novel aspects of its regulation and its impact on homeostasis. *World J Gastroenterol* (2014) 20:8491–504. doi:10.3748/wjg.v20.i26.8491

51. Ben-Moshe S, Veg T, Manco R, Dan S, Papinutti D, Lifshitz A, et al. The spatiotemporal program of zonal liver regeneration following acute injury. *Cell Stem Cell* (2022) 29:973–89. doi:10.1016/j.stem.2022.04.008

52. Haussinger D. Nitrogen metabolism in liver: structural and functional organization and physiological relevance. *Biochem J* (1990) 267:281–90. doi:10.1042/bj2670281

53. Paolini E, Longo M, Meroni M, Dongiovanni P. Hepatic zonation in MASLD: old question, new challenge in the era of spatial omics. *Int J Mol Sci* (2025) 26:10701. doi:10.3390/ijms262110701

54. Schleicher J, Dahmen U, Guthke R, Schuster S. Zonation of hepatic fat accumulation: insights from mathematical modelling of nutrient gradients and fatty acid uptake. *J R Soc Interf* (2017) 14. doi:10.1098/rsif.2017.0443

55. Miller DM, McCauley KF, Dunham-Snary KJ. Metabolic dysfunction-associated steatotic liver disease (MASLD): mechanisms, clinical implications and therapeutic advances. *Endocrinol Diabetes Metab* (2025) 8:e70132. doi:10.1002/edm2.70132

56. Duan Y, Pan X, Luo J, Xiao X, Li J, Bestman PL, et al. Association of inflammatory cytokines with non-alcoholic fatty liver disease. *Front Immunol* (2022) 13:880298. doi:10.3389/fimmu.2022.880298

57. Glass O, Henao R, Patel K, Guy CD, Gruss HJ, Syn WK, et al. Serum Interleukin-8, osteopontin, and monocyte chemoattractant protein 1 are associated with hepatic fibrosis in patients with nonalcoholic fatty liver disease. *Hepatol Commun* (2018) 2:1344–55. doi:10.1002/hep4.1237

58. Meyer SR, Zhang CJ, Garcia MA, Procario MC, Yoo S, Jolly AL, et al. A high-throughput microphysiological liver chip system to model drug-induced liver injury using human liver organoids. *Gastro Hep Adv* (2024) 3:1045–53. doi:10.1016/j.gastha.2024.08.004

59. Kostrzewski T, Maraver P, Ouro-Gnao L, Levi A, Snow S, Miedzik A, et al. A microphysiological system for studying nonalcoholic steatohepatitis. *Hepatol Commun* (2020) 4:77–91. doi:10.1002/hep4.1450

60. Ewart L, Apostolou A, Briggs SA, Carman CV, Chaff JT, Heng AR, et al. Performance assessment and economic analysis of a human liver-chip for predictive toxicology. *Commun Med (Lond)* (2022) 2:154. doi:10.1038/s43856-022-00209-1

61. Bircsak KM, DeBiasio R, Miedel M, Alsebahi A, Reddinger R, Saleh A, et al. A 3D microfluidic liver model for high throughput compound toxicity screening in the organoPlate(R). *Toxicology* (2021) 450:152667. doi:10.1016/j.tox.2020.152667

62. Tan K, Keegan P, Rogers M, Lu M, Gosset JR, Charest J, et al. A high-throughput microfluidic microphysiological system (PREDICT-96) to recapitulate hepatocyte function in dynamic, re-circulating flow conditions. *Lab Chip* (2019) 19:1556–66. doi:10.1039/c8lc01262h

63. Zushin PH, Mukherjee S, Wu JC. FDA modernization act 2.0: transitioning beyond animal models with human cells, organoids, and AI/ML-based approaches. *J Clin Invest* (2023) 133:e175824. doi:10.1172/JCI175824

Experimental Biology & Medicine Conference

Orlando, FL - October 13 -16, 2024

Please visit **exbiomedcon.org** or scan the QR code for more info.

Keynote Lecturers

Namandjè Bumpus, Ph.D.
Chief Scientist - US Food and Drug Administration

Advancing Emerging Technologies in Regulatory Science

Michael Friedlander, Ph.D.
Vice President - Health Sciences and Technology at Virginia Tech

All events will take place at the Embassy Suites by Hilton, Orlando Lake Buena Vista South

Cardiovascular

Delphine Gomez, Ph.D.
University of Pittsburgh

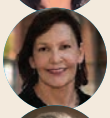

Karen Hirschi, Ph.D.
University of Virginia

Jay Humphrey, Ph.D.
Yale University

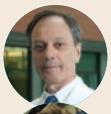

Ali J. Marian, M.D.
The University of Texas Health Science Center at Houston

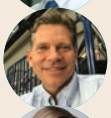

Joseph Miano, Ph.D.
Medical College of Georgia

Dianna Milewicz, M.D., Ph.D.
University of Texas Heath Science Center Houston

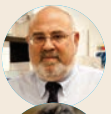

Robert Schwartz, Ph.D.
University of Houston

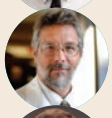

George Taffet, M.D.
Baylor College of Medicine

David Zawieja, Ph.D.
Texas A&M University Health Science Center

Neuroscience

Lique Coolen, Ph.D.
Kent State university

Michael Fehlings, M.D.
University of Toronto

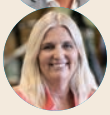

Susan Harkema, Ph.D.
University of Louisville

Maria Lehtinen, Ph.D.
Harvard University

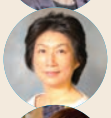

Fang Liu, Ph.D.
NCTR/US Food and Drug Administration

Agnes Luo, Ph.D.
University Cincinnati

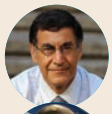

Mervyn Maze, MBChB
University of California San Francisco

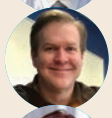

Dorian McGavern, Ph.D.
National Institute of Neurological Diorders and Stroke

Vesna Jevtovic-Todorovic, M.D., Ph.D.
University of Colorado School of Medicine

Regenerative Medicine

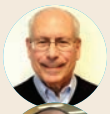

Arnold I. Caplan, Ph.D.
Case Western Reserve

Jian Feng, Ph.D.
State University of New York at Buffalo

Joshua Hare, M.D.
University of Miami

Karen Hasty, Ph.D.
University of Tennessee Health Science Center

Rajasingh Johnson, Ph.D.
University of Tennessee Health Science Center

Y. James Kang, DVM, Ph.D.
Sichuan University

Kwang-Soo Kim,Ph.D.
Harvard University

Joanne Kurtzberg, M.D.
Duke University

Jun Wu, Ph.D.
UT Southwestern

Trainees

Justin Boyd, Ph.D.
Vaxxinity

Udayan Apte, Ph.D.
U of Kansas Medical Center

Ram Kumar, Ph.D.
U of Kansas Medical Center

And More

Career Development
Short Talks
Poster Sessions
Member Blitz

SEBM SOCIETY FOR EXPERIMENTAL BIOLOGY AND MEDICINE

EBM Experimental Biology and Medicine

Scope

Experimental Biology and Medicine (EBM) is a global, peer-reviewed journal dedicated to the publication of multidisciplinary and interdisciplinary research in the biomedical sciences. The journal covers the spectrum of translational research from T0, basic research, to T4, population health. Articles in EBM represent cutting edge research at the overlapping junctions of the biological, physical and engineering sciences that impact upon the health and welfare of the world's population. EBM is particularly appropriate for publication of papers that are multidisciplinary in nature, are of potential interest to a wide audience, and represent experimental medicine in the broadest sense of the term. However, manuscripts reporting novel findings on any topic in the realm of experimental biology and medicine are most welcome.

EBM publishes Research, Reviews, Mini Reviews, and Brief Communications in the following categories.

- Anatomy/Pathology
- Artificial Intelligence/ Machine Learning Applications to Biomedical Research
- Biochemistry and Molecular Biology
- Bioimaging
- Biomedical Engineering
- Bionanoscience
- Cell and Developmental Biology
- Clinical Trials
- Endocrinology and Nutrition
- Environmental Health/Biomarkers/ Precision Medicine
- Genomics, Proteomics, and Bioinformatics
- Immunology/Microbiology/Virology
- Mechanisms of Aging
- Neuroscience
- Pharmacology and Toxicology
- Physiology and Pathophysiology
- Population Health
- Stem Cell Biology
- Structural Biology
- Synthetic Biology
- Systems Biology and Microphysiological Systems
- Translational Research

EBM Experimental Biology and Medicine

EBM is the official journal of the Society for Experimental Biology and Medicine

Experimental Biology and Medicine (EBM) is a global, peer-reviewed journal dedicated to the publication of multidisciplinary and interdisciplinary research in the biomedical sciences.

Discover more of our Special Issues

See more →

Contact

development@ebm-journal.org

See more

ebm-journal.org

publishingpartnerships.frontiersin.org/our-partners